Titre: Title:	Low-Cost Integrated Waveguide Antenna Front-End Solutions for Fifth Generation Cellular Systems and Beyond
Auteur: Author:	Ajay Babu Guntupalli
Date:	2014
Type:	Mémoire ou thèse / Dissertation or Thesis
Référence: Citation:	Guntupalli, A. B. (2014). Low-Cost Integrated Waveguide Antenna Front-End Solutions for Fifth Generation Cellular Systems and Beyond [Ph.D. thesis, École Polytechnique de Montréal]. PolyPublie. https://publications.polymtl.ca/1666/

UNIVERSITÉ DE MONTRÉAL

LOW-COST INTEGRATED WAVEGUIDE ANTENNA FRONT-END SOLUTIONS FOR FIFTH GENERATION CELLULAR SYSTEMS AND BEYOND

AJAY BABU GUNTUPALLI

DÉPARTEMENT DE GÉNIE ÉLECTRIQUE

ÉCOLE POLYTECHNIQUE DE MONTRÉAL

THÈSE PRÉSENTÉE EN VUE DE L'OBTENTION

DU DIPLÔME DE PHILOSOPHIAE DOCTOR

(GÉNIE ÉLECTRIQUE)

DÉCEMBRE 2014

UNIVERSITÉ DE MONTRÉAL

ÉCOLE POLYTECHNIQUE DE MONTRÉAL

Cette thèse intitulée :

LOW-COST INTEGRATED WAVEGUIDE ANTENNA FRONT-END SOLUTIONS FOR FIFTH GENERATION CELLULAR SYSTEMS AND BEYOND

présentée par : GUNTUPALLI Ajay Babu

en vue de l'obtention du diplôme de : Philosophiae Doctor

a été dûment acceptée par le jury d'examen constitué de :

M. KASHYAP Raman, Ph. D., président

M. Wu Ke, Ph. D., membre et directeur de recherche

M. FRIGON Jean-François, Ph. D., membre

M. SEBAK Abdel, Ph. D., membre externe

DEDICATION

To my mother Rani

To my father Satyanarayana.

To my Sister, Brother-in-law and Niece

ACKNOWLEDGMENT

I would like to thank my PhD research director, Prof. Ke Wu for giving me the opportunity to pursue my Doctorate study at Ecole Polytechnique of Montreal. His motivation helped me to understand and think solutions for some of the bottleneck problems in millimeter-wave communication.

I would like to thank technical personnel Mr. Jules Gauthier, Mr. Steve Dubé, Mr. Traian Antonescu and Mr. Maxime thibault in Poly-grames Research Centre for realizing the simulated prototypes. I would like to thank Mr. Jean-Sébastien Décarie for assistance with software problems and also Mrs. Ginette Desparois and Mrs. Nathalie Lévesque for administrative procedures of the department.

I would like to my master thesis director Prof. Substrata Sanyal at Indian Institute of Technology, Kharagpur (IIT-KGP) for teaching me RF and microwave basics and motivating me to choose my career in the microwave field. I specially want to thank Dr. Mrinal Kanti Mondal and Dr. Priyanaka Mondal for helping me to settle in Montreal and for all the encouragement. My special thanks go to my master thesis co-supervisor Dr. Vamsi Krishna Velidi for teaching me microwave filter design.

I specially want to thank Dr. Tarek Djerafi for introducing me to millimeter-wave frequency antenna array design. I would like to thank my friends Divyabrahmam Kandimalla (at IIT-KGP), Dr. Nasser Ghasemi, Dr. Sulav Adhiakri, Dr. Farshad Sarbachi, Dr. Shabnam Ladan, Lydia Chioukh, Pascal Burasa, Ya Deng, Babak Nikfal, Dr. Ali Doghri, Yang Ping, Tariq sha Mohammed, who made my stay at Poly-Grames Research Center memorable. I would like to thank Pascal Burasa and Bilel Mnasri for helping me to write the French version of Abstract.

I specially would like to thank Dr. Shabnam Ladan for her great help in revising my PhD thesis. Dr. Ladan was very helpful and supportive during my PhD. The ideas we shared during common discussion were significantly improved the quality of thesis.

Finally, I would like to extend my gratitude to my mother Rani Guntupalli and father Satyanayana Guntupalli who supported my decision at every stage of my life and encouraged to pursue Ph.D. degree in Canada. I would like thank my sister Vijaya sri Guntupalli, brother-in-law Naveen kode and my niece Kundana for all their encouragement during my graduate studies. I also want to thank my extended family members Vanaja Guntupalli, Sethaiah Vootla, Vijay anna, Laxmi vadina for all support during the final stage of writing of PhD thesis.

RÉSUMÉ

Les réseaux d'antennes en bande millimétrique ayant une polarisation rectiligne simple, une polarisation rectiligne double, ou une polarisation circulaire double ont été largement exploités dans plusieurs applications comme les réseaux de transmission de données sans fils, les radars, l'imagerie passive, et les systèmes de radio cognitive. La structure guide d'onde représente le candidat idéal pour implémenter les réseaux d'alimentation à faible pertes ainsi que les réseaux d'antennes ayant des gains importants dans la bande de fréquences millimétriques. Ces antennes basées sur des structures guide d'onde présentent de très bonnes performances mais elles sont difficilement intégrables avec les composants actifs. Dans la bande millimétrique, la technologie GIS (guide d'onde intégré au substrat) représente une excellente alternative pour la conception et l'implémentation des réseaux d'alimentation à faible couts et a faibles pertes. Les antennes alimentées à l'aide des structures GIS sont capables d'offrir une excellente efficacité de radiation ainsi qu'une large bande d'opération. Dans cette thèse, la technologie GIS a été choisie dans le but de concevoir des réseaux de distribution de puissance et de phase dans le but d'implémenter des antennes a grande efficacité.

Les contributions scientifiques principales de cette thèse peuvent être divisées en deux catégories. La première partie étant consacrée a la présentation des solutions pour des structures a rayonnement efficace tels que les réseaux d'antennes LP, DLP et DCP. Le choix de l'élément rayonnant est une étape vitale et cruciale pour le design de réseaux d'antennes a gain élevé et qui peuvent être contrôlés électroniquement. Dans la deuxième partie de cette thèse, des nouvelles techniques seront proposées dans le but de contrôler la direction du rayonnement suivant plusieurs directions dans les plans d'élévation et azimut.

A la fréquence 60 GHz, l'antenne a diélectrique fuselé a été choisie pour avoir une polarisation rectiligne et l'antenne patch 'a cavité ont été choisie afin d'avoir une polarisation circulaire. En effet, l'antenne a diélectrique fuselé est utilisée par la suite pour faire la conception d'un réseau d'antennes 4x4 ayant une polarisation rectiligne a un angle de 45^{o}.Ensuite, l'antenne a diélectrique a été l'unité élémentaire pour l'implémentation d'un réseau a polarisation rectiligne double dont les deux polarisations sont orthogonales ce qui constitue un avantage important par rapport 'a un réseau a simple polarisation vu qu'on est capable de multiplier par 2 le débit de données a

transmettre par notre nouvelle architecture. Finalement, l'antenne a diélectrique fuselé a été sélectionnée dans le but de concevoir un réseau d'antennes planaire ayant la capacité de faire un balayage unidimensionnel seulement (1-D).

La matrice de Butler BFN a été modifiée et intégrée au sein d'un réseau d'antennes patch 2x2, permettant d'avoir un pattern de polarisation rectiligne dans les plans élévation et azimut simultanément. La matrice de Butler a une taille réduite et permet l'alimentation d'un réseau d'antennes planaire. Le réseau d'antennes est conçu suivant la technique multicouche. Le prototype a été validé expérimentalement autour de la bande de fréquences Ka.

Dans la technique suivante, un faisceau CP est dirigé en 2-D en espace. À 60 GHz, un faisceau circulairement polarisée est obtenu en alimentant une matrice d'antenne patch en utilisant une topologie d'alimentation SIW. Dans un premier temps, les caractéristiques de l'antenne CP sont obtenues par l'insertion de deux encoches sur la circonférence extérieure d'un patch LP. Dans l'étape suivante, une matrice 2 x 2 CP patch, ayant une taille compacte et une excellente performance de rapport axial (AR) est réalisée à 60 GHz. Le faisceau rayonne avec des caractéristiques de CP en élévation et en azimut en utilisant trois dimensions construit à partir de la matrice de Butler. Ce réseau d'antennes est facilement utilisable dans un système radio intelligent.

Les mécanismes de balayage 2-D utilisant la phase et la fréquence simultanément, ont été démontrés dans cette thèse. Dans un premier temps, une technique pour la réalisation de faisceaux directionnels balayant une région limitée, est introduite et implémentée en technologie SIW. Le balayage 2-D est réalisé par le balayage de phase d'une antenne à onde de fuite. Un réseau de faisceau basé sur la lentille Rotman et une matrice de d'antenne à onde de fuite sont intégrés sur le contour de sortie, pour réaliser un réseau d'antenne de balayage 2-D.

Dans la dernière technique, une matrice d'antenne à balayage 3-D (toute l'espace) est proposée pour couvrir une région de 320^{o} en azimut et 20^{o} en élévation. Dans cette configuration, l'un des faisceaux peuvent être utilisé pour l'émission tandis que l'autre faisceau est simultanément utilisé pour la réception. Dans la phase finale, la plage de balayage du faisceau est en outre étendue pour couvrir toute l'espace en plaçant deux MBAs indépendants et orthogonales l'un à l'autre. La

technique proposée est adaptable pour diverses applications allant de la bande de fréquence W et au-delà.

Dans cette thèse, un ensemble complet de solutions d'antenne pour future génération de communication cellulaire (5e génération) est proposé et validé. L'étude approfondie des techniques d'antenne sont discutés en détail dans cette thèse. Tous les antennes sont simulées à l'aide de HFSS et mesurées dans la chambre anéchoïque. Les résultats présentés dans cette thèse sont publiés dans les brevets américains (en attente), des revues internationales de haut niveau et également présentés lors de conférences internationales tenues en Amérique du Nord, Europe et Asie-Pacifique.

ABSTRACT

Millimeter-wave (or simply mm-wave) antenna arrays with single linear polarization (LP), dual linear polarization (DLP) and dual circular polarization (DCP) characteristics are widely being used for numerous applications including wireless data communication, radar sensors, passive imaging, energy harvesting and cognitive radio systems. Among different types of feeding structure, waveguide presents an excellent candidate to implement low-loss feeding networks and high-gain antenna arrays over mm-wave frequency range. Those waveguide-based antennas have been exhibiting excellent radiation characteristics, but they are not easy to integrate with active components. At mm-wave frequency, SIW (substrate integrated waveguide) is an emerging outstanding candidate to implement low loss and low cost feeding networks. SIW-fed antenna is able to yield high radiation efficiency and broadband impedance behavior. In this thesis, SIW feeding transmission technology is chosen to implement power and phase distributing networks for realizing high efficiency antenna front ends.

The main scientific and technical contributions can be summarized into two parts. In the first part, solutions for efficiently radiating apertures have been proposed such as high gain LP antenna arrays, pencil beam antenna arrays, DLP antenna arrays and DCP antenna arrays. The radiating element choice with excellent radiation characteristics is vital in realising high gain antenna array and electronically steerable phased arrays. In the second part, new techniques have been proposed to steer the fixed beam into multiple directions in elevation and azimuth utilizing passive phase shifting network.

At 60 GHz frequency, dielectric rod antenna is selected for linearly polarized radiation and cavity backed metallic circular patch antenna is selected to obtain circular polarization radiation. Single rod antenna element is experimentally characterized to validate the proposed concept. In the next stage, high gain antenna array with 45^{o} linear polarization utilizing rod antenna radiating element is demonstrated and feeding implemented in three dimensional (3-D) architecture is integrated along with the 4 × 4 antenna array. The data handling capability of single polarization antenna array is increased up to two fold by integrating two orthogonal polarized antenna arrays with an aperture area of one single polarized array. The Rod antenna application is also extended to obtain phase steered beams in horizontal plane in a planar 1-D phased array antenna configuration. The

demonstrated 1-D scan phased array is simple to manufacture but the scanned patterns exists only in horizontal plane.

The Butler matrix BFN is modified and integrated under the 2 × 2 patch array, resulting LP scanned pattern in elevation and azimuth simultaneously. The Butler matrix is compact in size and feeding planar antenna array. The compact 2-D scan phased array is realized in multi-layer configuration and experimentally validated at Ka-band frequency range.

In the next technique, CP beam is steered in 2-D scans space. At 60 GHz frequency, circularly polarized radiated beam is obtained by feeding an array of patch antenna using SIW feeding topology. At first, CP antenna characteristics are obtained by inserting two notches on the outer circumference of a LP patch. In the next stage, 2 x 2 CP patch array occupying compact size and excellent axial ratio (AR) performance is realized in the SIW technology. The radiated beam with CP characteristics is phase steered in elevation and azimuth using three dimensionally constructed Butler matrix BFN. The two dimensional scan CP phased array antenna system is readily usable to implement antenna front end in a cognitive radio system.

The 2-D scan mechanisms utilizing phase and frequency scan simultaneously have been demonstrated in the work. In the first technique, a technique for achieving simultaneous multiple scanned directional beams limited scan region is introduced and its development is enabled by the substrate integrated waveguide (SIW) technology. The 2-D scanning is achieved by phase steering each beam of frequency scanned leaky wave array. Rotman lens based BFN and array of LWA sources are integrated on the output contour to realize the 2-D scan conformal phased array antenna.

In the last technique, full-space scanning 3-D phased array antenna is proposed to cover 320^{o} scan region in azimuth and 20^{o} scan region in elevation. Two-layered feed part is implemented by the combination of 90^{o} H-plane coupler and two similar 4 × 4 Butler matrices. In this configuration, one of the beams can be used for transmit operation while the other beam can be used for receive operation simultaneously. Measured S-parameters and directional pattern measurements have confirmed the multi-dimensional scanning capability of the proposed MBA. In the final stage, the beam scanning range is further extended to cover the full-plane region by placing two independent MBAs orthogonal to each other. The proposed technique is scalable for various system applications up to W-band frequency range and beyond.

In this PhD thesis, complete set of antenna front-end solutions are proposed and validated in a low-cost integrated waveguide technology for future 5th generation cellular communication. The comprehensive study of the antenna techniques are discussed in detail in PhD thesis. The antenna radiating part is designed and simulated in full-wave electromagnetic software Ansoft high simulation software (HFSS) and experimentally verified in far-field MI technology anechoic chamber. The results presented in this PhD thesis are published in US patents (pending), reputed international journals and also presented in international conferences held in North America, Europe and Asia-Pacific regions.

TABLE OF CONTENTS

LIST OF FIGURES

LIST OF TABLES

LIST OF APPENDICES

LIST OF ACRONYMS AND ABBREVIATIONS

1-D	One-Dimensional
2-D	Two-Dimensional
3-D	Three-Dimensional
ALSTA	Antipodal Linearly Tapered Slot Antenna
AR	Axial Ratio
BFN	Beam Forming Network
CR	Cognitive Radio
CBCPW	Conductor-Backed Co-Planar Waveguide
CPW	Coplanar Waveguide
CP	Circular Polarization
DCP	Dual Circular Polarization
DLP	Dual Linear Polarization
EIRP	Equivalent Isotropic Radiated Power
HFSS	High Frequency Structure Simulator
HMSIW	Half Mode Substrate Integrated Waveguide
LP	Linear Polarization
LWA	Leaky Wave Antenna
MBA	Multi Beam Antenna
MMICs	Microwave Monolithic Integrated Circuits
MPT	Microwave Power Transmission
Mm-wave	Millimeter-wave
PCB	Printed Circuits Board
SIW	Substrate Integrated Waveguide
SICs	Substrate Integrated Circuits
SINRD	Substrate Integrated Non-Radiative Dielectric Guide
SIIG	Substrate Integrated Image Guide
TE	Transverse Electric
TEM	Transverse Electric Magnetic

INTRODUCTION

1.1 Background and Motivation

Research interests towards the development of millimeter-wave (mm-wave) communication and sensing techniques and applications are increasing due to abundant and natural advantages that exist around the highly publicized 60 GHz frequency band and beyond compared to the low-frequency ranges. The 60-GHz frequency band can be employed to realize the next-generation wireless high-speed communication system that is capable of handling data rates of multiple gigabits per second. The unlicensed band of 7 GHz at 60 GHz, for example, is useful and attractive for establishing high-speed wireless personnel area network (W-PAN) with a speed of at least 7 Gbps [1]. Still, in order to obtain a mm-wave link-budget that is required for wireless gigabit-per-second communication, antenna arrays are needed that should have sufficient gain and support beam-forming. The development of antenna arrays that can maintain high gain and high radiation efficiency is much anticipated for future 5G cellular communication systems and beyond. Moreover, antenna array and RF front-end should be integrated into a low-cost system on substrate that can be realized with a standard production process. The high permittivity of silicon would limit the antenna performance in terms of radiation and bandwidth. Nevertheless, the antenna designed on such a high permittivity can readily be integrated with the other silicon based platforms. The use of current wireless frequency bands limits further evolvement to higher data rates and shorter distances for two main reasons. First, the bandwidth available for these systems are limited that fundamentally limits the achievable data rate. Second, radiofrequency interference limits the operation of parallel systems within a limited range of each other. Mm-wave communication system can overcome these two hurdles. However, related link budget analysis demands for antenna arrays that have high gain and high aperture efficiency. Also, antenna arrays with multiple polarization signatures may be used to double the system data rate capability.

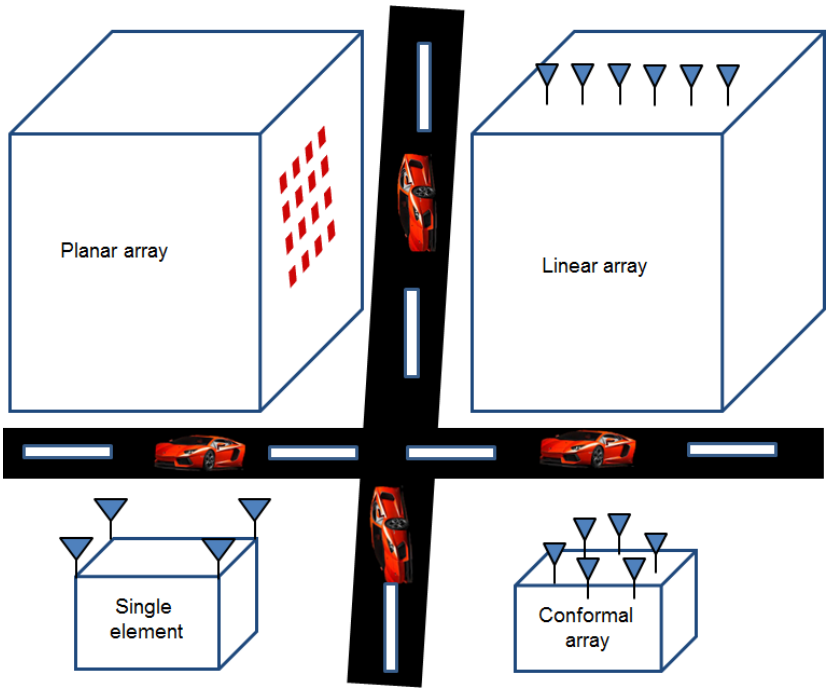

(a)

(b)

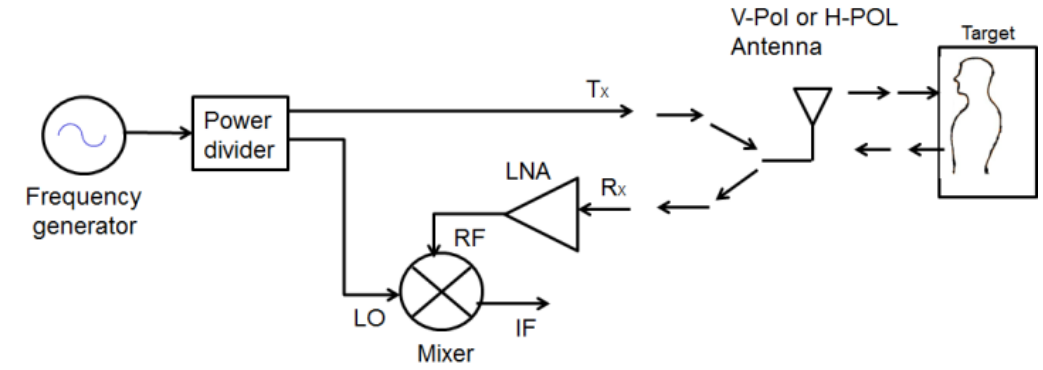

(c)

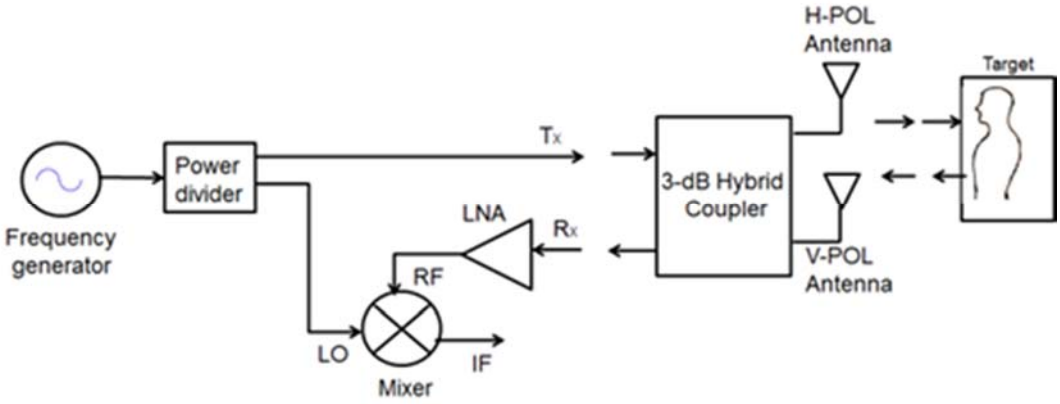

(d)

Figure.1.1 (a) Typical base station antenna architecture of cellular communication, (b) Indoor application of ultra-high-speed short range communication system, simplified block diagram of a radar sensor using (c) single circular, (d) dual circular polarization antenna to detect human heart beat and respiration rates.

Mm-wave base station antenna architecture is shown in Figure 1.1a. The typical antenna configuration in a cellular communication can be linear, planar, non-planar and conformal shape. In addition, beam steering capability of the base station antenna minimizes interference between adjacent users and reduces power consumption. The application of mm-wave frequency for short range ultra-high-speed communication is show in Figure 1.1b. In addition antenna with single linear and dual circular polarization characteristics are widely being used for numerous applications including radar sensors, passive imaging, energy harvesting and cognitive radio systems. The simplified block diagram of a radar transceiver using single LP antenna and CP antenna is shown in Figure. 1.1c, d. The radar with CP antenna can detect chest and heart displacement irrespective of the patient position [2]-[4]. The sensor can always detect amplitude

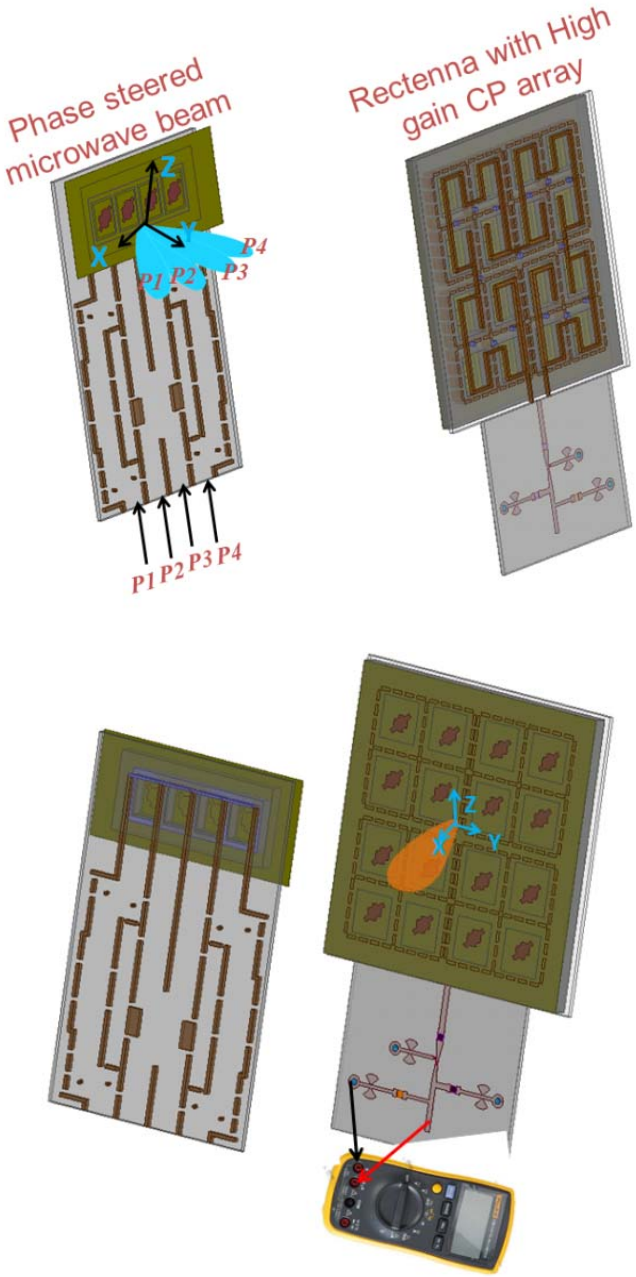

Figure. 1.2. Microwave power transmission (MPT) system with phase steered microwave beam on the transmission side and rectenna with high gain CP array on the receiving side. The phased array system and antenna array are using the SIW feeding network technology.

variations even the polarization of patient is not matched with the transmitting antenna. To satisfy front-end requirements of these systems, different techniques have been proposed to obtain circular polarization at mm-wave frequency.

The typical application of multi-functional antenna front end using dual circular polarization, dual linear polarization and phased array antenna are explained here. A circular polarization system can receive data or power signals with vertical and horizontal polarizations simultaneously. The applications of CP antennas include secured communication in space mission, high-resolution sensor, portable imaging device [5] and microwave energy harvesting [6]. In the development of energy harvesting techniques, the rectified output voltage would become constant when compared with the scenario of an LP antenna. All these aforementioned applications are highly dependent on CP purity, gain and pattern bandwidth. In the case of energy harvesting applications, CP antenna connected to rectifier is generally expected to covert RF to DC power independent of source polarization [7]. The received DC voltage is maximum and constant for CP over linearly polarized (LP) rectenna configuration.

The 60 GHz frequency band as one special mm-wave hotspot can be employed to realize the next-generation wireless short-haul high-speed communication link between inter-satellite systems [8]-[9]. The shorter wavelengths of electromagnetic waves at 60 GHz (5 mm or 0.2 inch wavelength) interact with oxygen molecules and absorbs the radiated energy. In the higher altitudes (above 43,000 kms) where there is no oxygen, 60 GHz band can offer longer communication link [8], free from electromagnetic interferences from earth over the same band. Polarization diversity antennas can transport double the data rate and offer greater flexibility in terms of size and cost of satellite antennas. For this purpose, high gain DLP antenna array is proposed and experimentally validated in this work.

The application of 1-D scan phased array antenna and high efficiency antenna array is explained using an example of microwave power transmission (MPT) system. As illustrated in Figure. 1.2, a typical MPT system consists of a phased array antenna on the transmitting side and a rectenna array on the receiving side. In the development of an efficient MPT system, antenna plays a vital role in focusing the radiating beam in a specific direction. MPT over mm-wave frequency range has been under investigation from many years [10]. General architecture of MPT consists of signal generator, power amplifier and antenna array or phase steered antenna array in the back-end. Antenna array will be able to transmit the power in only one direction and antenna array combined with phased array techniques results in multiple simultaneous directional beams. High-efficiency phased array systems were used to transmit power in multiple directions [11-13].

The choice of a mm-wave frequency range has advantages in terms of shorter wavelength and smaller antenna aperture size. However, the path losses between the transmitting and receiving antennas also increase with the operating frequency. In this case, high-gain antenna array should be designed to satisfy all requirements of mm-wave power-budget. In [14], an antenna synthesis was developed for dedicated wireless MPT and it demonstrated the maximum beam efficiency capability of the circular and rectangular planar arrays.

In addition to the typical application mentioned above, electronically steerable millimeter-wave antenna systems with 2-D scan capability have found numerous applications including radar, high-data rate communication systems, synthetic vision schemes for weapon detection and automotive collision avoidance systems [84], and cognitive radio [16]-[19]. These systems require a high-speed elevation and azimuth two-dimensional (2-D) scanning of the radiation beam to increase the performance in term of capacity, precision (resolution) and to reduce the number of the system building blocks.

First technique of 2-D scan phased array antenna utilizing phase-controlled BFN for azimuth plane scanning, and frequency controlled leaky wave sources for elevation plane scanning is demonstrated in [20]. However, many antenna front-end applications require a fixed outgoing beam in the operating frequency range. Second technique of 2-D scan phased array system utilizing phase only steered antenna system in elevation and azimuth have been studied in [21]-[24].

The 2-D scanning can be enabled in planar array by the use of phase shifters [25] or a switching beam (Butler matrix or lens-enabled techniques) which can be stacked or (volumetric) multiple-beam-forming lens as proposed in [26]. To enable a continuous scanning, the electronically steered antenna array generally are complex with a prohibitively high cost because of a large number of phase shifters involved in the system design and their considerable RF losses [27]-[30]. This is in particular true for mm-wave systems.

The concept of substrate integrated waveguide (SIW) technology offers various advantages over the conventional microstrip technology and metallic hollow waveguide. The passive beamforming techniques are mainly fixed beamforming techniques, where the numbers of output beamforming states are limited and the adaptive steering of beam can be obtained by the integration of the active components on the same system but the power distribution network adds the extra complexity to

the system. The technology plays a vital role while designing a high performance phased array system. The millimeter-wave interconnects have been mostly used for traditional transmission lines such as microstrip, co-planar wave guide and planar substrate integrated waveguide only. However, a significant parasitic effect of the wire bonding method not only limits the bandwidth but also contributes to the undesired radiation loss. The SIW technology allows the convenient integration of all the active components on the single substrate resulting in low cost, light weight, highly compact phased array systems with the active control. The SIW technology is suitable candidate to implement low profile beam forming network and easy to integrate along with the active components. At millimeter-wave (mm-wave) frequency, the selection of substrate integrated waveguide (SIW) in the design and development of a beam forming network topology has proven to be excellent [31]. The SIW feeding antenna arrays were realized on a silicon substrate to implement system on chip [32].

For certain applications, operating frequency should be kept constant, while the phase gradient is varied to steer the beam in elevation and azimuth simultaneously. 1-D scan system can have phase-controlled beams only in one direction where a linear phase gradient is varied along the array input contour. A beamforming network (BFN) driven linear array involves more freedom, which can be fed from an edge of array. In 2-D scan systems feeding planar arrays, phase-controlled beams are scanning in azimuth and elevation planes. The selection of a beam forming network is, nevertheless, critical in such 2-D scan systems because of the phase gradients varied along the two directions.

In this PhD thesis, phase only steered 2-D scan antenna system technique is proposed and validated at Ka-band frequency range. Such two-dimensional (2-D) scanning phased array antenna with low-cost, high-performance are highly in demand for high data-rate wireless radio links, and mm-wave imaging applications[33]-[36]. The performance of a 2-D beam-forming antenna system depends on the design of its beam-forming network (BFN) to produce constant beam direction angle θ_0, beam shape and low side lobe level. Various BFN topologies to feed 1-D linear array were summarized in [87]. In 1-D beam-forming systems, the antenna placement allows to place the BFN and an array in the same plane. In 2-D beam-forming systems, phase gradient between two elements is different in horizontal and vertical directions which impose a strict requirement on the design of the BFN.

The metallic waveguide fed microstrip array has been proposed in [88] to alleviate the radiation loss problem of the microstrip feed network. The SIW fed planar microstrip array has also been proposed in [39] to overcome the limitations of conventional metallic waveguide, where a higher radiation efficiency of 79% was obtained. Nevertheless, the feed network and patch array were integrated onto the same layer, the spurious radiation from the feed network was thus not completely suppressed. The SIW cavity-backed 2 × 2 antenna arrays have been proposed to enhance the radiation efficiency up to 70% in [40] and impedance bandwidth up to 11.7% in [41]. The standing-wave SIW fed aperture-coupled microstrip array has been proposed in [42] and achieved an impedance bandwidth up to 22% at 60 GHz. The previously proposed SIW fed array applications were generally limited to only one fixed beam direction [38]-[42]. Planar and non-planar forms of various beamforming matrices like Butler, Blass and Nolen matrices were already studied in SIW technology to scan one dimensional (1-D) linear array. Recently, a 2-D scanning of planar 2 × 4 array employing a planar switched beam network that consists of two 4 × 4 Butler matrices and four hybrid couplers using the microstrip technology has been proposed for 60-GHz radio applications [91]. The loss of BFN in combination with array decreases the total radiation efficiency. The SIW based 2-D scan beam forming network has been studied and developed in [92], where single resonant slot antenna has narrow bandwidth and low radiation efficiency, and its applications are limited for feeding the 2 × 2 antenna array only.

As shown in Figure. 1.3, the basic architecture for a traditional electronically scanned array consists of transmit and receive components, a power dividing network, a phase shifting network, and an array of antennas. Phased arrays can be classified as either active or passive category. Passive arrays make use of a central transmitter and receiver, and they are able to apply a progressive phase difference to each antenna element. The passive beam-forming can be obtained by using the fixed beam forming techniques such as Butler matrix, where a better control of the radiated beams can be obtained by increasing the number of inputs to the butler matrix. With respect to active arrays, there is an individual transmit/receive module (TRM) at each antenna element that is comprised of an amplifier for high-power transmission, an amplifier for low-noise reception, and a phase shifter device.

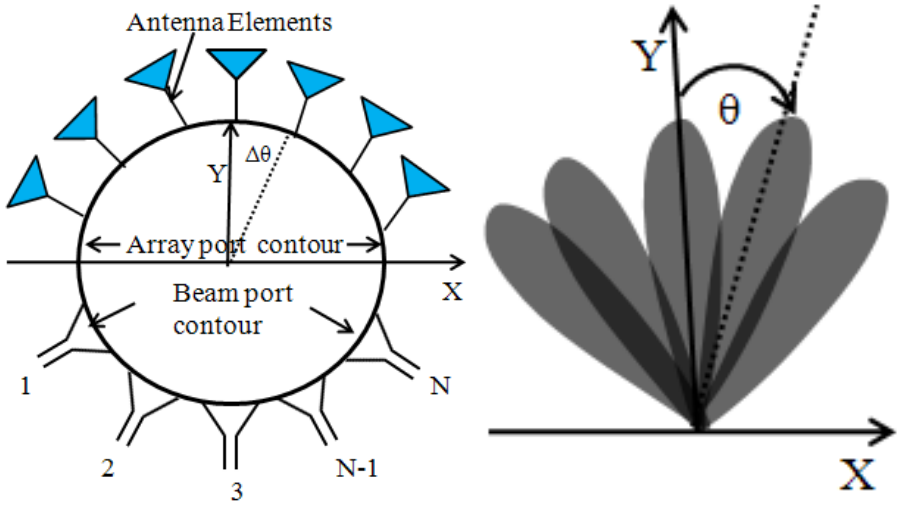

Figure. 1.3.Beam forming network (BFN) feeding conformal array for upper hemisphere coverage, where θ is the main beam steering angle, $\Delta\theta$ is the required phase shift, N=the number of beam ports.

The passive beamforming techniques are mainly fixed beamforming techniques, where the numbers of output beamforming states are limited and the adaptive steering of beam can be obtained by the integration of the active components on the same system but the power distribution network adds the extra complexity to the system.

The basic operation principle of the phased array technique (using a receiver as an example) is depicted in Figure. 1.4b. The phased array receiver consists of N separate signal paths that connect to separate antennas. The desired signal from certain incident angle(s) (θ) arrives at these antennas with different time delays. In a one-dimensional antenna array receiver, the progressive time delay between two adjacent antennas is

$$\tau = d \sin\theta / c$$

Where d is the antenna spacing and c is the speed of light. The signal received by the first antenna of a phased array receiver can be represented as

$$S_o(t) = A(t)\cos(w(t) + \phi)$$

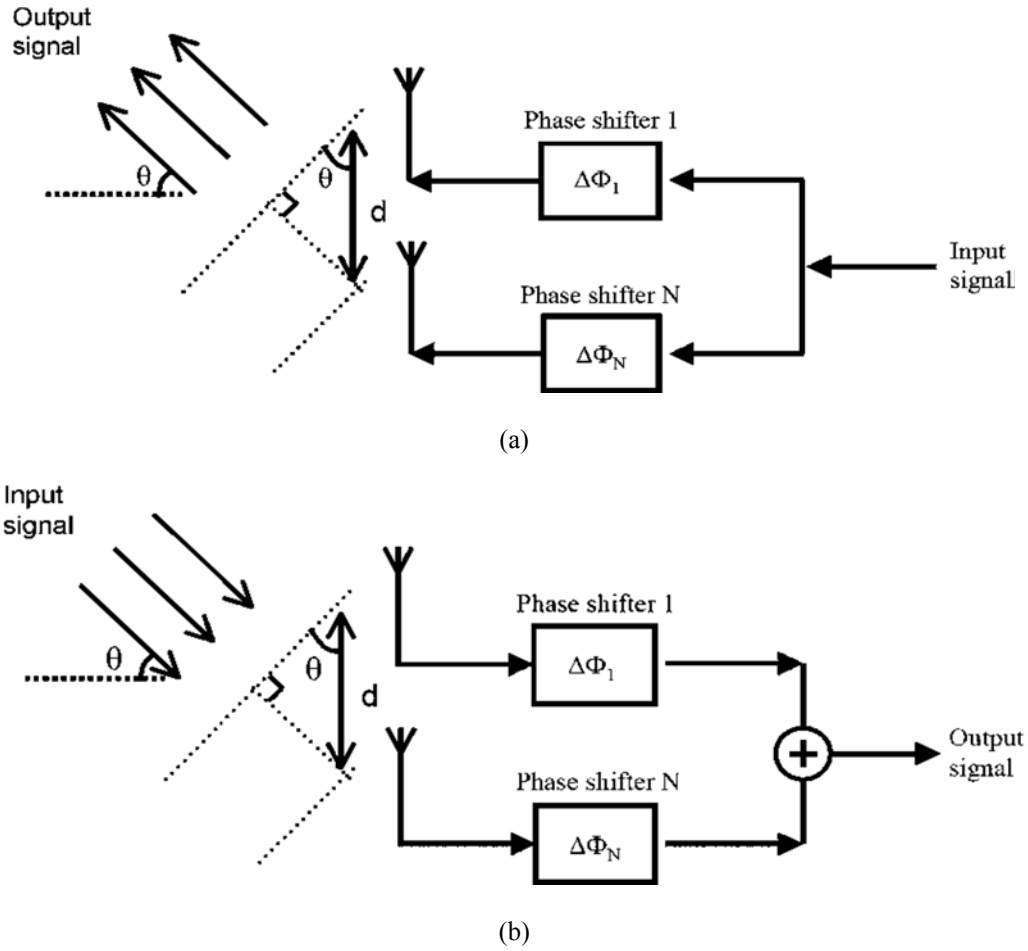

Figure. 1.4. (a) Principle of a phased array transmitter (b) Principle of a phased array receiver.

The time delays among the different signals paths can be compensated in the receiver so that the signals are combined coherently at the output, then the combined signal at the output can be expressed as: $S_{out}(t) = S_o(t) * N$, where N is the number of antenna elements.

1.1.1 Benefits of Phased Arrays

Phased arrays bring several advantages to the wireless system.

- First of all, in a phased array receiver, the signals received by the multiple antennas can be added up coherently. As a result, the output signal-to noise ratio and therefore the sensitivity of the receiver can be improved by 10log10 (N) dB.

- Secondly, in a phased array transmitter (Figure. 1.4a), the signals transmitted by the multiple antennas can be added up coherently in certain direction(s) in space through spatial power combining. In comparison to a single-antenna transmitter that transmits an output power of P0, each path of the phased-array transmitter can transmit an output power of P0/N and keep the sum of the output power equal to *P0*. The equivalent isotropic radiated power (EIRP) of the phased-array transmitter will be $P0 \times N$, which is increased by 10 log10 (N) dB in comparison to a single-antenna transmitter. Besides, the output power of a phased array transmitter can be controlled by simply turning on or off a certain number of transmitter paths.
- Thirdly, a phased array system can place nulls in undesired direction(s), which improves channel multipath profile and reduces interference to/from other systems.

1.2 Outline of thesis

This PhD thesis proposes solutions to design high-performance antenna front-end systems for obtaining single broadside beam and electronically steerable directional beam. The comprehensive work flow is organized, which covers multiple aspects of beam antenna system exploration from single broadside beam, narrow directional beam, simultaneous orthogonal directional beam, circularly polarized directional beam and then electronically steering the single beam in both azimuth and elevation simultaneously.

The second chapter of PhD thesis covers different antenna front-end systems using rod antenna as radiating element At first, planar dielectric rod antenna is proposed and used as radiating element to design high gain 45^{o} linearly polarized antenna array. In the subsequent step, dual polarization antenna array is designed using the rod antenna as radiating element. The planar phased array antenna using rod antenna is discussed and validated in SIW technology.

The third chapter of the PhD thesis presents and discusses the technique to obtain phase steered beams in elevation and azimuth beams simultaneously. Phase steering obtained by using analog beam forming technique is integrated under the aperture area of 2 × 2 planar array.

The fourth chapter of the thesis is dedicated to obtain circularly polarized beams in single direction and also in multiple phase steered directions. At first, single CP beam is radiated from 2 × 2 sub

array and exhibits excellent CP radiation characteristics. Dual circularly polarized antenna is designed using rod antenna as radiating element. At the end, single CP beam is phase- steered in elevation and azimuth directions simultaneously by integrating compact Butler matrix under 2 × 4 array aperture.

The fifth chapter of PhD thesis introduces and discusses phase and frequency scanning array antennas operating at E-band frequency range. Leaky wave antenna (LWA) designed in SIW technology is used as radiating element to design 2D scan phased array antennas. The frequency scanning behaviour of LWA is combined with phase scanning behaviour of Rotman lens based phase shifter to obtain multiple beam in limited scanning range. In the second part, the multi-beam antenna deploys a Butler matrix phase shifting network proposed to cover 320^{o} scan range with multiple beams in azimuth and 20^{o} range in elevation simultaneously.

The conclusion and future work are given in the sixth chapter.

CHAPTER 2 MILLIMETER-WAVE ANTENNA ARRAY AND PHASED ARRAY ANTENNA WITH LINEAR POLARIZATION DIVERSITY

This chapter introduces new techniques to design low profile planar rod antenna, single linearly polarized (LP) high gain antenna array, dual linearly polarized (DLP) antenna array and 1-D scan phased array antenna operating at 60 GHz frequency range. The research results reported in the thesis are already published in the international journals and conferences. At first, dielectric rod antenna is proposed and characterized in SIW technology. The application of rod antenna in the realization of high performance antenna front-ends is discussed in detail.

2.1 60 GHz Planar Dielectric Rod Antenna

Among different types of antenna, dielectric rod antenna has widely been used due to its simplicity in architecture [45] and easy to integrate along with the milli-meter-wave integrated circuits on the single platform. The inherent wide-band nature of the rod antenna has been used for different applications including the wide bandwidth ground penetrating radar in [46]. Different techniques to design the linearly polarized antenna and antenna array were proposed in [46-51]. In [47], 60 GHz multi-layer aperture-coupled antenna array was proposed and peak gain was measured at 32 dBi with 256 radiating elements. The efficiency of array was measured to be 70%. In [48], planar SIW fed 60GHz slot array antenna was proposed and the peak gain was measured to be 23 dBi. However, the inherent narrow-band nature of the slot limits the impedance bandwidth and the series feeding method limits the pattern bandwidth. The antenna array efficiency was measured to be 68% at 60 GHz. To improve the antenna impedance and pattern bandwidth, dielectric rod antenna has been proposed in this work.

Dielectric rod antenna has been studied extensively in the literature [49-51]. Among the substrate integrate circuits (SICs) family, both substrate integrated image guide (SIIG) and integrated non-radaitive waveguide (SINRD) have been used respectively in [49] and [50] to feed dielectric rod antenna. These two families of SICs require an additional transition to communicate with the other parts of circuit. The third and well-known family member of SICs, is substrate integrated waveguide (SIW) that has also used for the design of feeding networks in [51] and to

develop high-gain dielectric rod antenna arrays. In this case, antipodal linearly tapered slot antenna (ALTSA) antenna was loaded by polyflon material to increase the gain. But, all these methods were not suitable for integration along with active circuits on a single planar platform.

2.1.1 Antenna design

The rod antenna is fabricated by using a simple printed-circuit board (PCB) process on single Rogers 3006 substrate with $\varepsilon_r = 6.3$, $\tan \delta = 0.0012$@10 GHz, and thickness = 0.635 mm. The rod Antenna is characterized in full wave electromagnetic software HFSSv14 developed by ANSYS.

2.1.1.1 ALTSA antenna architecture

Among the end-fire radiating antenna structures, antipodal linearly tapered slot antenna (ALTSA) has widely been used in various applications thanks to its simplicity in architecture. Recently, 60 GHz ALTSA was proposed in [52] and a radiation behavior was obtained over the full band of frequencies from 55 GHz to 67 GHz. The antenna was designed on dielectric substrate (RO 4003) with $\varepsilon_r = 3.38$. As substrate permittivity value increases, most of the electrical fields will be concentered inside the dielectric region. Antenna radiation efficiency will then be decreased.

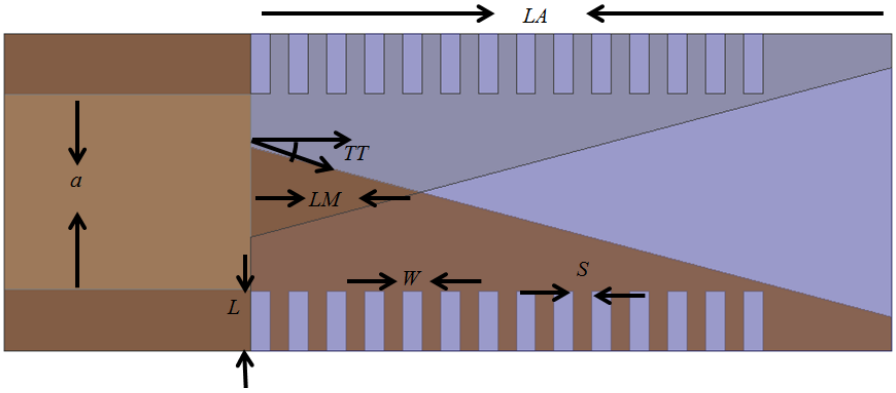

Figure. 2.1. ALTSA antenna as feed element

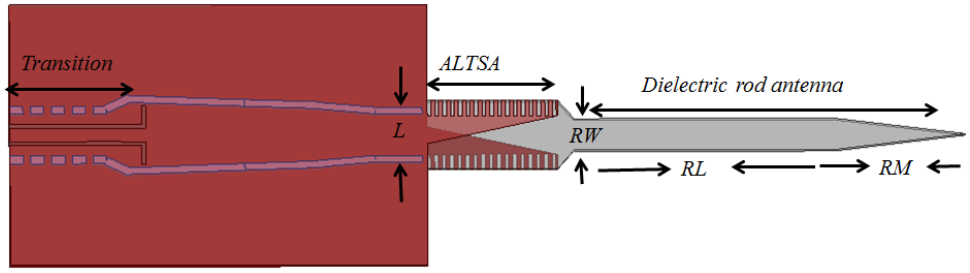

Figure. 2.2. ALTSA is loaded by a tapered dielectric rod.

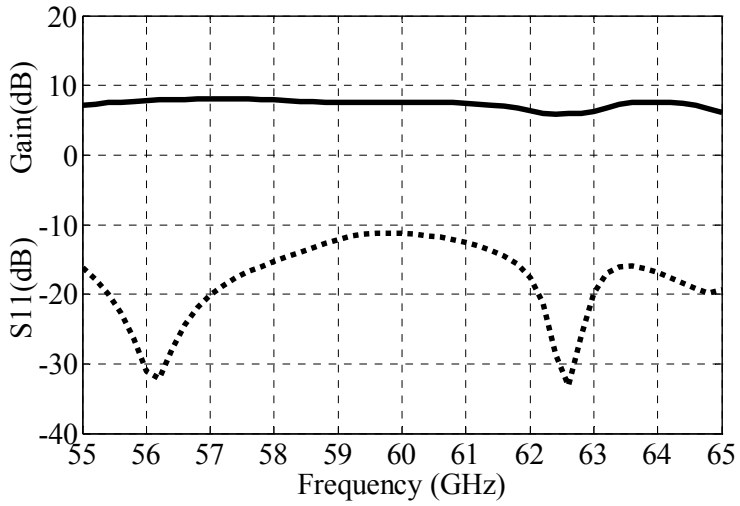

Figure. 2.3. ALTSA antenna impedance matching and gain as a function of frequency.

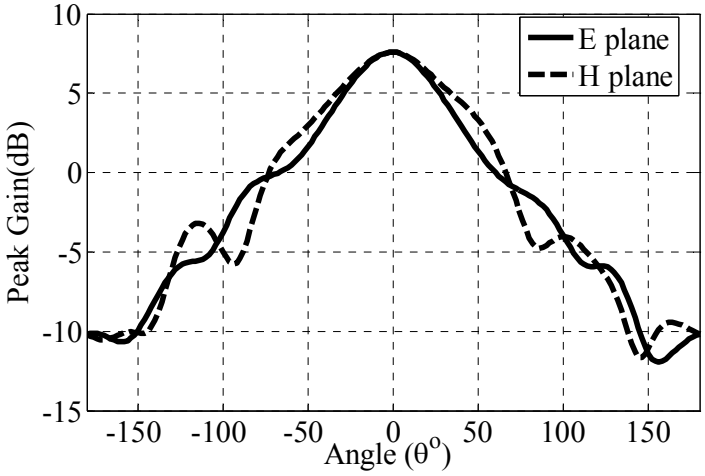

Figure. 2.4. ALTSA antenna simulated radiation behavior in E and H-planes at 60 GHz.

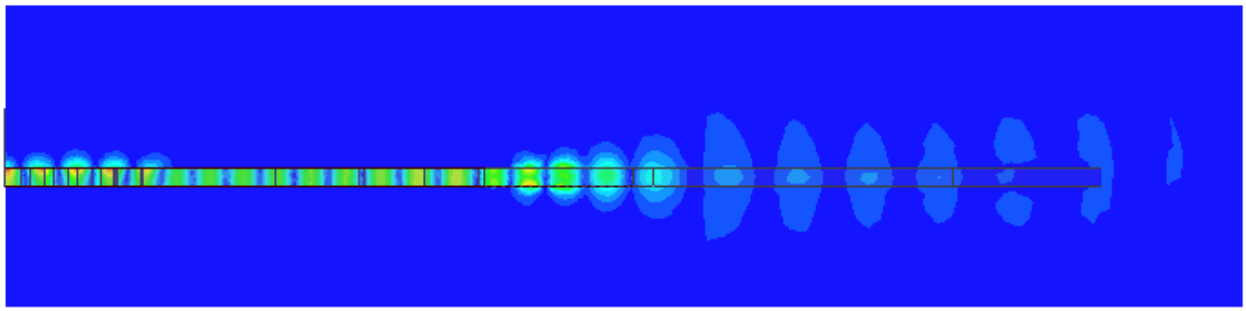

Figure. 2.5. Electric field strength inside the dielectric guide.

As shown in Figure. 2.1, ALTSA antenna is initially designed on dielectric substrate with ε_r =6.3 and all the physical parameters are given in the same Figure. Slots near H-plane of the dielectric are corrugated to improve the cross-polarization and also the input matching of the ALTSA. All the physical parameters are optimized to obtain a good radiation pattern performance. Antenna return loss and gain as a function of frequency are shown in Figure. 2.3. Return loss of the antenna $|S11| \leq -10$ dB is obtained over 16.6% of bandwidth at 60 GHz. Peak gain is better than 6 dBi over the entire desired frequency band.

As shown in Figure. 2.4, antenna gain pattern is symmetrical in E and H-planes and the half-power beam width (HPBW) in E and H-planes is of 70º. The cross-polarization value is lower than -15 dB. Peak gain of the ALTSA antenna is 7.4 dBi only. The antenna gain can be increased by changing the value of LA, but parameters TT and LM are set to be maximum possible values at this frequency on the chosen dielectric permittivity value.

2.1.1.2 Rod antenna architecture

To further enhance the gain of ALTSA antenna, dielectric rod antenna shown in Figure. 2.2 is proposed. The dielectric rod is loaded at the output and the matching at the junction is obtained by tapering the end-fire edge of the ALTSA. The output end of rod antenna is tapered to make the sharp edge and the length *RM* is chosen as one quarter wavelength for matching the junction discontinuities. The electric field strength is mainly concentrated inside the high permittivity dielectric of ALTSA antenna.

The thickness of substrate is chosen to be 0.635mm, so the width of microstrip line is relatively thick. To obtain the better matching condition, a grounded coplanar waveguide (GCPW) to SIW transition is designed and used to measure the cascaded section of ALTSA and rod antenna. The transition behavior is similar to the principle of diploe antenna. So, the final architecture of the proposed antenna is a series combination of dipole, linearly tapered slot antenna and the dielectric rod antenna. In Figure. 2.5, field propagation inside the high-permittivity dielectric is given at the design frequency of 60 GHz.

Table 1 Antenna physical parameters

Variable	Value (in mm)	Variable	Value (in mm)
RW	1.2	TT	12º
RL	10	LM	1.9
RM	5	W	0.14
L	1.6	S	1.16
LA	5.1	a	1.6

The rod antenna peak gain is as a function of rod length *RL* at the design frequency of 60 GHz. As the length of the rod increases, the gain also increases. Simulated Antenna radiation efficiency with and without considering losses is compared in Figure. 2.6. The ideal antenna radiation efficiency is close to 95% over the entire frequency band. When losses are taken into account for the dielectric rod, the dielectric loss tangent is set as 0.0025 for simulations at 60 GHz. The metallic sidewalls are filled up with the copper, the metallic sheet thickness is also considered to be 17 um. The antenna efficiency including all the losses is 85% at the frequency of 60 GHz.

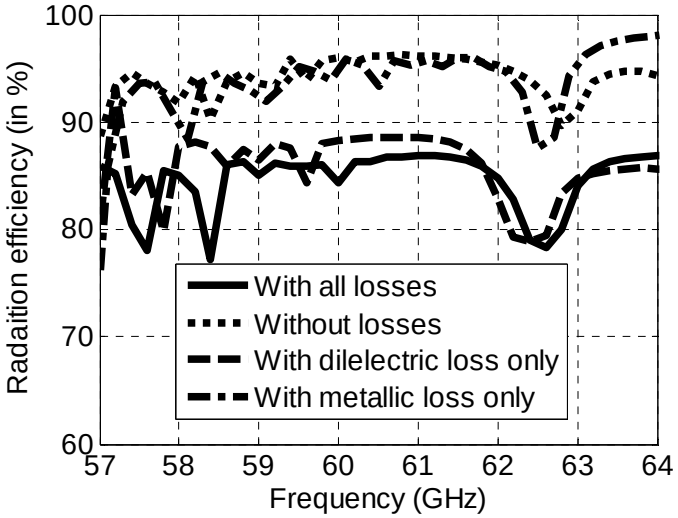

Figure. 2.6. Simulated radiation efficiency (with and without considering metallic and dielectric losses) of the final prototype including the input transition.

2.1.1.3 Antenna cross-pol and side lobe levels

Antenna cross-pol and side lobe level as a function of substrate thickness is given in Figure. 2.7. As the substrate thickness increases, the cross pol level and side lobe levels also increase. As the thickness increases, the fields become loosely bonded within the substrate dielectric, so the polarization purity gets also reduced. For 10 mil thickness, the cross-pol value is less than -29.35 dB and the worst side lobe value is -26 dB. Finally, the antenna thickness is considered to be 25 mil for the fabricated prototype.

2.1.1.4 Measured antenna impedance bandwidth

The rod antenna is manufactured by using a simple low-cost fabrication process. The experimental prototype is shown in Figure. 2.8a. V-connector is used to measure the return loss of the antenna with Antitsu 3739C vector network analyzer. The total length of the fabricated antenna is $4\lambda_o$ excluding the length of feed waveguide and transition. Measured and simulated reflection coefficients are compared in Figure. 2.8b. Antenna reflection coefficient $|S11| \leq -10$ dB from 55 GHz to 65 GHz.

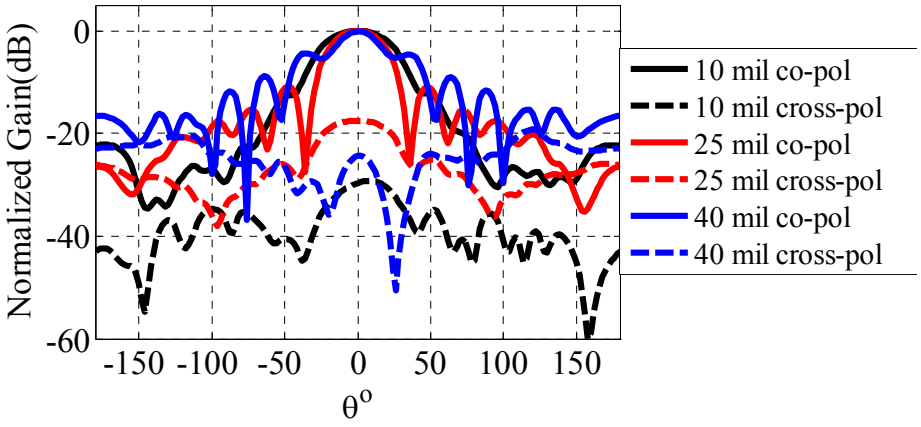

Figure. 2.7. E-plane co-pol and cross-pol radiation pattern as a function of substrate thickness.

2.1.2 Antenna radiation pattern performance

Far field antenna pattern is measured in the MI technology anechoic chamber. Experimental prototype of the antenna is considered as receiver and the transmitting horn antenna is set a transmitter. Antenna radiation pattern is measured from 57 GHz to 64 GHz at an interval of 0.5 GHz for frequency and 1º of interval for gain patterns. Figure. 2.9, plots the normalized radiation patterns in the E and H-planes at three different frequency points 57 GHz , 60 GHz and 64 GHz. Simulated and measured results are compared and also measured cross polarization is shown in the same Figure. Both results are well in agreement and similar behavior is observed for all the remaining frequency points.

The measured gain is extracted to be 12.5 dBi at the design frequency of 60 GHz. The peak gain values are measured to be 11.5 dBi, 12.5 dBi and 12.8 dBi at 57GHz , 60 GHz and 64 GHz, respectively. Antenna HPBW is calculated to be 40º in both the E and H-plane radiation cut planes. The HPBW value of antenna is almost half when compared to the ALTSA.This is due to the loading of the ALTSA with the dielectric rod antenna. The worst side-lobe level (SLL) value is measured to be 10.5 dB lower than the maximum peak gain value. This value can be further lowered by decreasing the thickness of dielectric to 10 mil from the chosen 25 mil thickness. The measured cross polarization is lower than -17 dB at 60 GHz. The antenaa performance for different thickness is shown in Figure. 2.7. The measured gain difference or fluctuation over the bandwidth from 57 GHz to 64 GHz is less than 1.8 dBi.

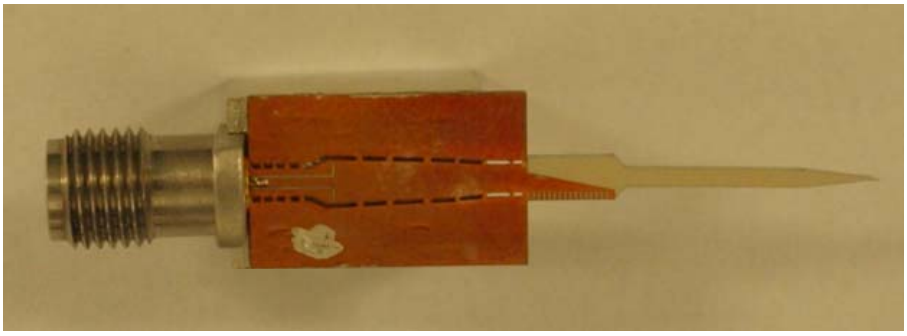

(a)

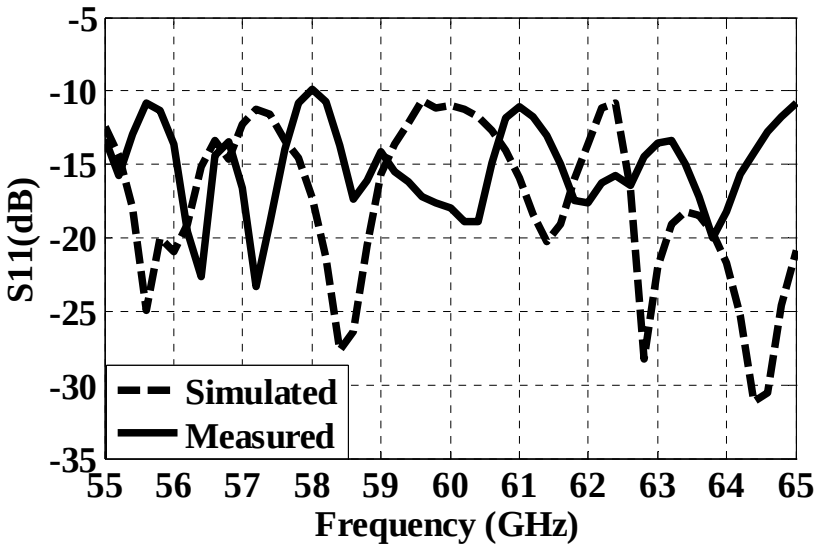

(b)

Figure. 2.8. (a) Manufactured prototype of the rod antenna. (b) Simulated and measured return losses of the dielectric rod antenna.

The proposed antenna makes use of a simple transmssion line model of SICs family, exhibiting a good radation behavoir over the entire frequency band from 57 GHz to 64 GHz. Antenna radation efficiency of 85% is calculated from the measured peak gain and simulated directivity at 60 GHz . The efficiency is primarily effected by the dielectric loss of the substrate.

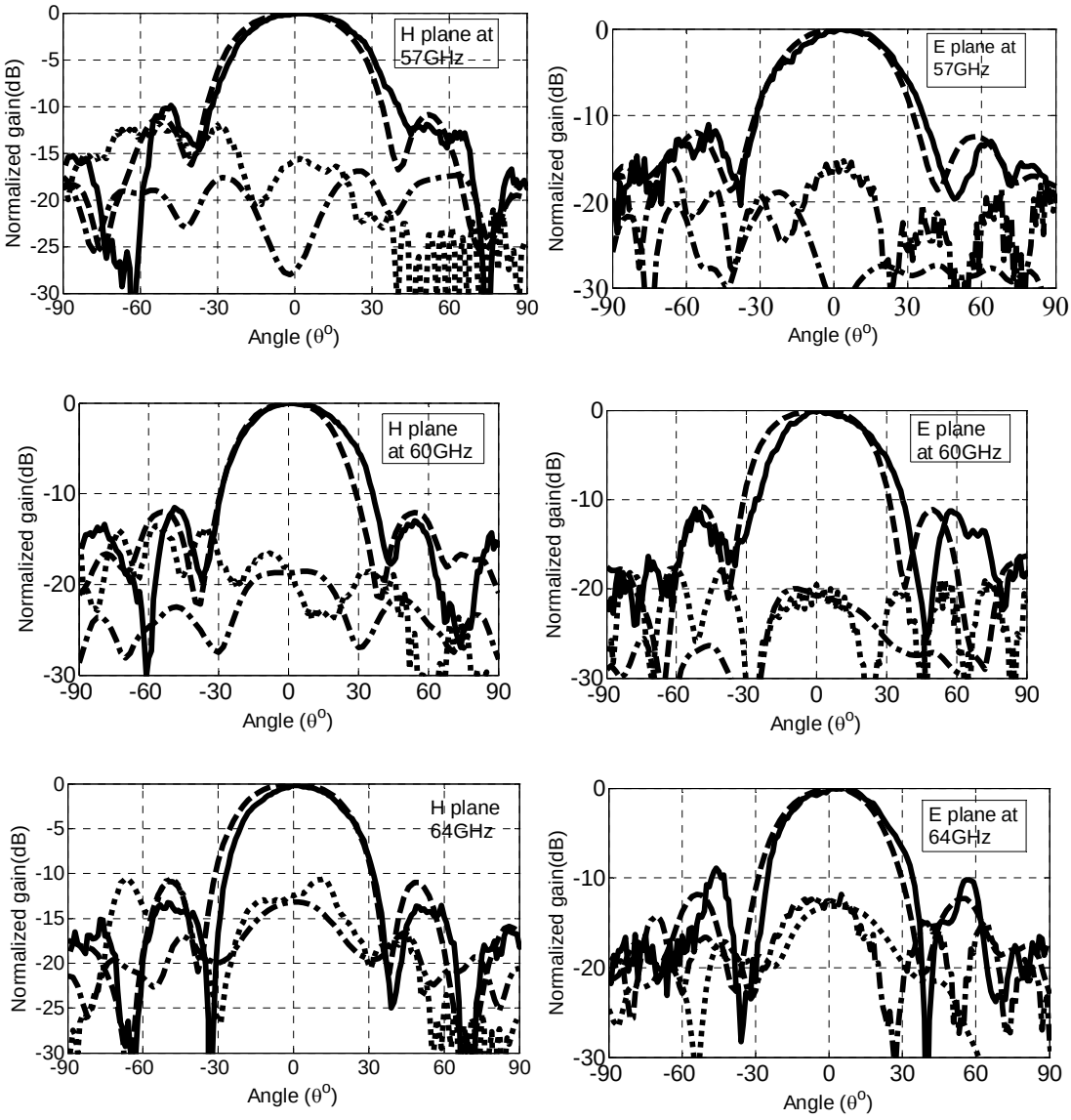

Figure. 2.9. E-plane and H-plane measured co-pol simulation (dotted), measurement (solid) and simulated cross-pol (sash-dot), measured cross-pol pattern (dash) for the rod antenna at 57 GHz, 60 GHz and 64 GHz.

In [48], 128 slot antennas were contributing to the gain of 22 dB . Also, slot antena has inherent narrowband nature When compared with SIC family of the rod antennas developed in [49]-[50] , the proposed antenna is using SIW feed type instead of SIIG or SINRD. SIW feed structre was proposed in [51], but dilelectric loading of the ALTSA makes antenna non-planar and relatively complicated to manufacture. Antenna developed in [52], was a corrugated ALTSA

but prototype was printed on a substrate permitivity vlaue of 3.3. Antenna physical size will not allow to implement antenna arrays with different polarization signatures.

Table 2 Comparison of rod antennas within substrate integrated circuits (SICs) family

	SIIG	SINRD guide	SIW
Fundamental mode	TE_{11}	LSM_{10} and/or LSE_{10}	TE_{10}
Transition design	Uneasy to integrate with microstrip and CPW structures	Uneasy to integrate with microstrip and CPW structures	Easy to integrate with microstrip and CPW structures
Cut-off frequency dependence	Substrate thickness	Substrate thickness and dielectric width	Waveguide width only
Useful for frequency range	Limited lower frequency use for because of unacceptable leakage and radiation at discontinuities	For *W*-band and beyond	From low GHz applications and above
Fabrication complexity	Moderate	Limitation on substrate thickness	Easy
Bandwidth of fundamental mode	< 20%	< 20%	≤ 50%
Remarks	Limited use because SIIG open waveguide structure contributes to radiation loss.	Limited use because SINRD fundamental mode bandwidth may be narrow.	Widely used

2.2 45º linearly polarized high gain antenna array for 60 GHz radio

In this section, the dielectric rod antenna is used as raiding element to implement high gain antenna array at 60 GHz frequency. Millimeter-wave antenna arrays are widely studied and developed for short-range communications, automotive radar, sensing and imaging systems.

Antenna arrays with high gain are needed to satisfy the link-budget at the V-band frequency range [53]. In most cases, allocated unlicensed frequency range from 57 GHz to 64 GHz is chosen to design high performance antenna arrays with linear and circular polarizations [54]-[55]. At 60 GHz, high efficiency antenna arrays fed by using SIW transmission line were reported in [56]-[61]. The SIW slot array proposed in [56] makes use of 128 slots to generate a peak gain of 22 dBi. Generally, resonant nature of the SIW slots limits operating bandwidth to 4.1% at 60.5 GHz. To increase the bandwidth, multiple slots were etched on the top ground plane of the SIW and achieved 15% of bandwidth in [57]. The solution proposed in [58] utilizes a narrow wall coupling to excite the slots etched on the top ground plane of SIW cavity. Antenna has achieved 12.6% of impedance bandwidth with 12 dBi peak gain. Multi-layer stacked Yagi-antenna with a small footprint was proposed in [59], and achieved 10.5% of impedance bandwidth with 18 dBi gain at 60 GHz. At 35 GHz, 3-D antenna array proposed in [60], has a gain of 27 dBi with 128 radiating elements.

Low temperature co-fired ceramic (LTCC) technology has been used to implement broadband high gain antennas [53]. In the dielectric rod antenna radiated beam peak gain is a function of rod length. To implement high gain and high efficiency antenna arrays, SIW-fed rod antenna has been proposed in [61] and [62]. SIW transmission line has low-loss nature at millimeter-wave frequencies due to perfect shielding nature. Therefore, low-cost antenna with high gain is studied and developed in this work.

The millimeter-wave interconnects have been mostly used for traditional transmission lines such as microstrip, co-planar wave guide and planar substrate integrated waveguide only. Among the existing techniques, wire-bonding method is the most common way to connect different transmission lines [63]. However, a significant parasitic effect of the wire bonding method not only limits the bandwidth but also contributes to the undesired radiation loss. To mitigate the radiation loss, non-planar interconnects were proposed in SIW technology for realizing non-planar magic T and dual polarization antenna array in [60] and [61].

In this work, a 45^{o} LP planar array utilizing non-planar interconnect and SIW fed rod antennas is proposed to construct high gain antenna array at 60 GHz frequency band. Array occupies a total volume of 2.8 $\lambda \times 3.2\ \lambda \times 5.1\ \lambda$ with an average peak gain of 17.5 dBi over 8.3% of pattern bandwidth.

2.2.1 3-D Antenna array design

Antenna prototype is simulated in Ansoft HFSS software and fabricated on Rogers's 3006 substrate with 10 mil dielectric thickness. Antenna and feeding network are designed on dielectric substrate with ε_r =6.3 and $tan\delta$=0.003.

2.2.2 Vertical InterConnect

A vertical interconnect operating in an upper *Ka*-band over 14% and 28.5% of bandwidth (with |S11|≤ -15 dB) at 35GHz was respectively proposed in [60] and [61]. The slot etched on a broad wall waveguide is narrow band with only 4% at the design frequency. The equivalent circuit is represented with shunt admittance. As explained in [8], slot is replaced by a waveguide so that bandwidth of transition is increased to 11.3%. Feed network shown in Figure. 2.10a, makes use of a vertical interconnect operating at 60 GHz. The feed part consists of slot placed at a distance $D_{sh}= \lambda_g/4$ from shorted end of the wall, so that maximum electric field is excited in center of the slot. The parameter D_{sh} controls bandwidth and input impedance of the interconnect. The vertical waveguide is connected to feed guide using this slot. The power is being transferred to vertical waveguide from input waveguide. Input port 1 is placed on the feed guide and output port 2 is placed on the vertical guide. The foot print of the vertical waveguide is fit within the feed guide width. Impedance matching bandwidth is improved by selecting vertical guide width *S* is less than feed guide width *W*. The field is coupling smoothly from horizontal guide to the vertical guide without any reflections coming back to input port. As shown in Figure. 2.10b, simulated magnitude of reflection coefficient (with |S11| ≤ -20) without input transitions is covering the frequency band from 57 GHz to 63 GHz. The design and fabrication complexity has been reduced when compared to the technique proposed in [60]. The proposed vertical interconnect is used to connect feeding network and antenna elements. The Rod antenna shown in Figure. 2.11, is used radiating element to design high gain antenna array at 60 GHz frequency range. The antenna element is experimentally validated in the previous section.

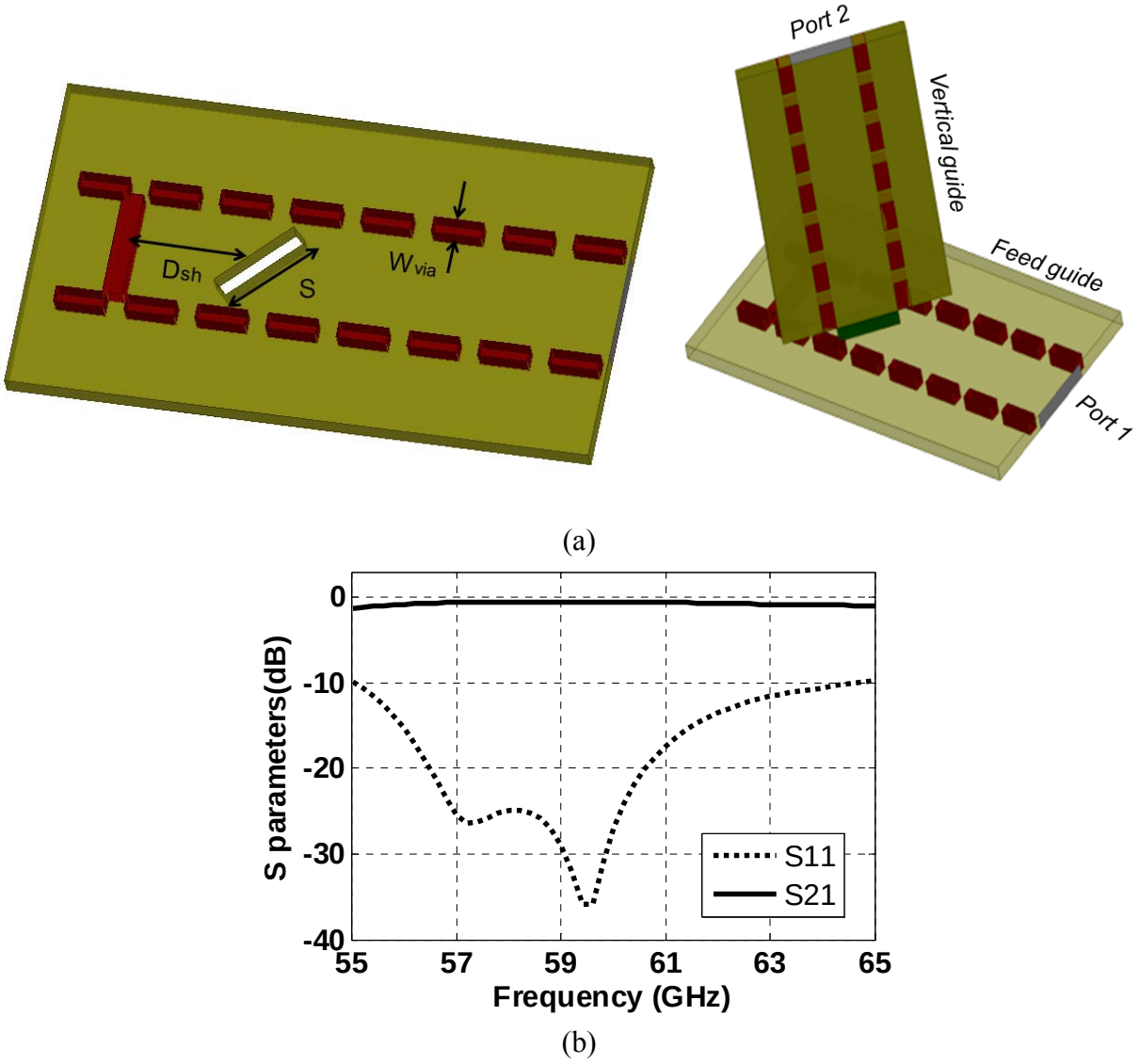

Figure. 2.10. 45^{o} rotated vertical interconnect (a) architecture (where D_{sh}=1.92 mm, S=1.1 mm, W_{via}=0.2 mm), (b) performance.

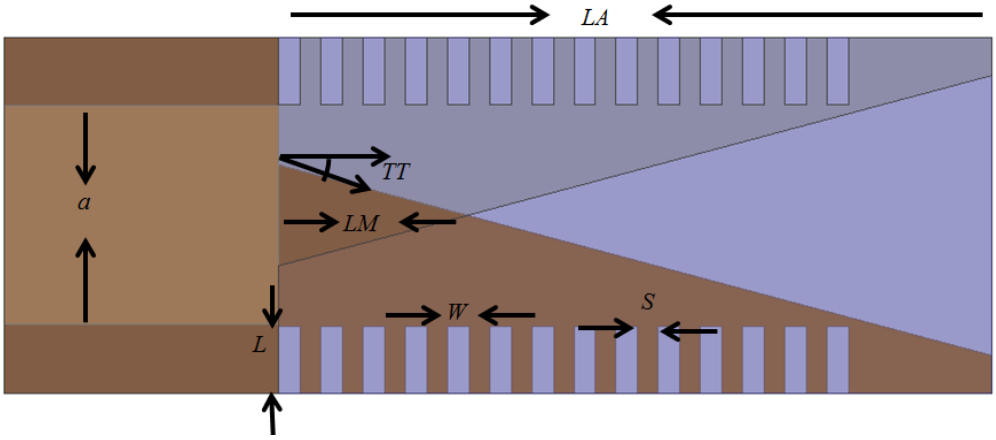

(a)

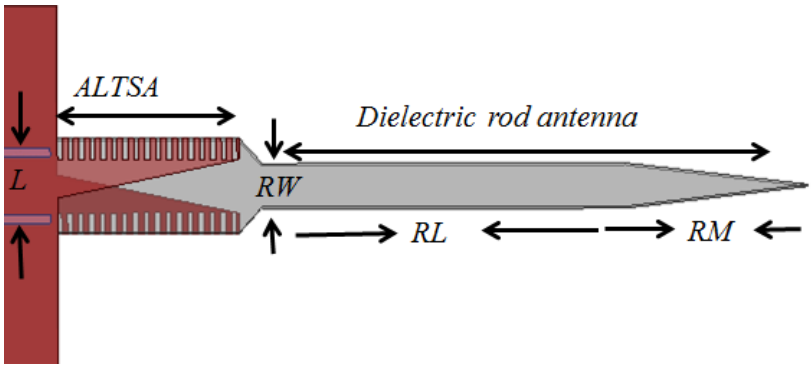

(b)

Figure. 2.11. (a) ALTSA antenna architecture, (b) dielectric rod antenna, where RW=1.2, RL=10, RM=5, L=1.6, LA=5.1, TT=12^{o}, LM=1.9, W=0.14, S=1.16 and a=1.6 (all dimension are in mm).

2.2.3 Feed network of 4×4 planar array

To begin with, a planar 1:16 power divider is optimized over a desired frequency range. The simulated 3-D power divider is shown in the Figure. 2.12a. Input impedance (with |S11|< -20 dB) is matched over a frequency range from 58 GHz to 62 GHz. When fed from input port *P1,* power is distributed uniformly among all the 16 output ports. The vector representation of the Electric field is given in the Figure. 2.12b. The amplitude and phase performance of the proposed 3-D power divider is shown in the Figure. 2.13c, d. For example, phase difference between ports *P2* and *P3* is 180^{o}, because of electric field orientation is opposite in the slots located in the feed guide. The similar phase distribution is observed between the pairs of remaining feeding ports.

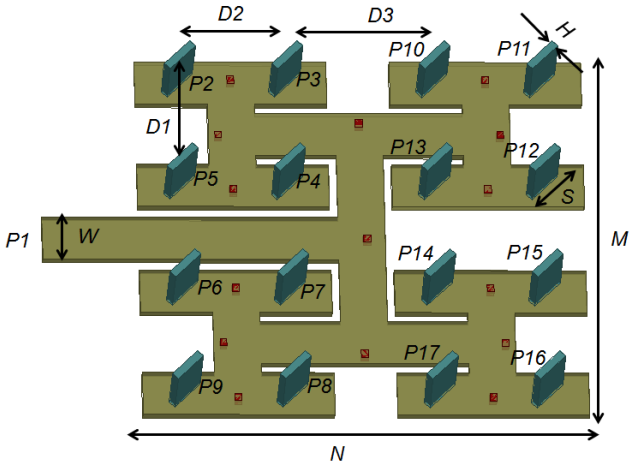

(a)

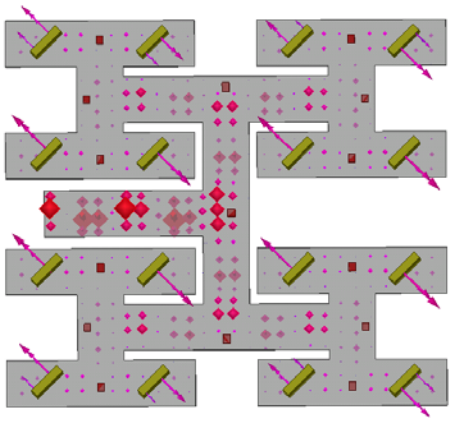

(b)

Figure. 2.12. (a) 3-D view of the feed network, where input port on the *XY*-plane and 16 output ports are located on the vertically placed waveguides, (where $C = 2, 3, \ldots 16$), W=1.47, $D1$=3.65, $D2$=3.36, $D3$=4.5, H=0.254, S=1.1, M=12.3, and N=14 (all dimensions are in mm), (b) Vector representation of E-field inside the 3-D feed network.

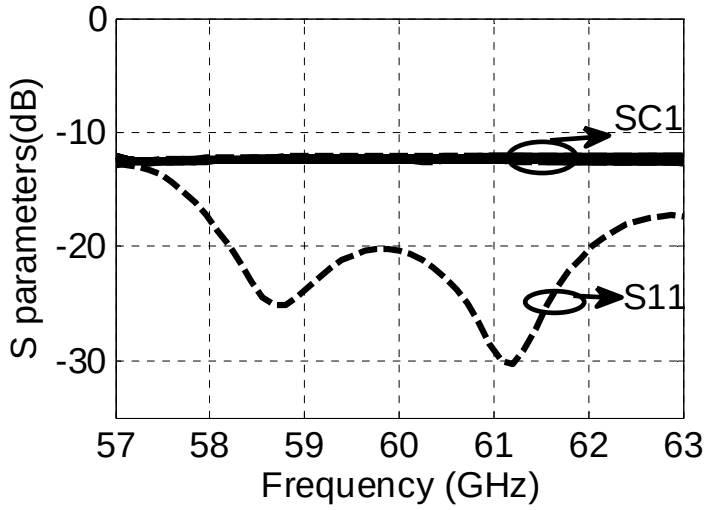

(c)

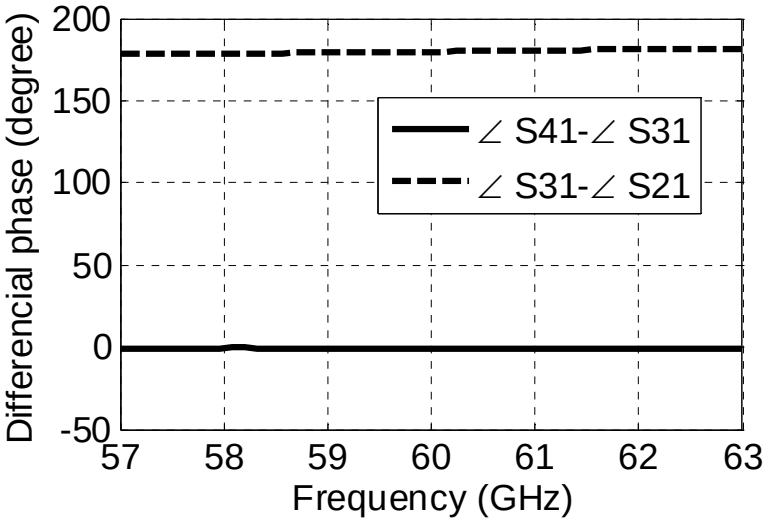

(d)

Figure. 2.13. S-parameters (c) amplitude performance, (d) differential phase between ports *P2, P3* and *P3*, *P4.*

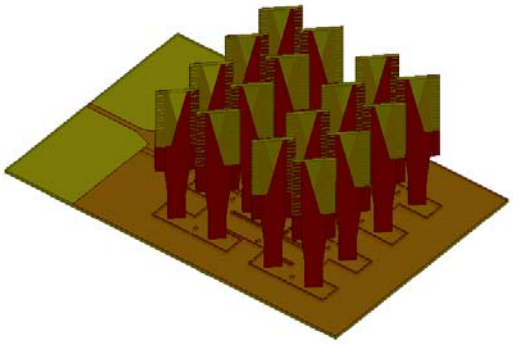

(a)

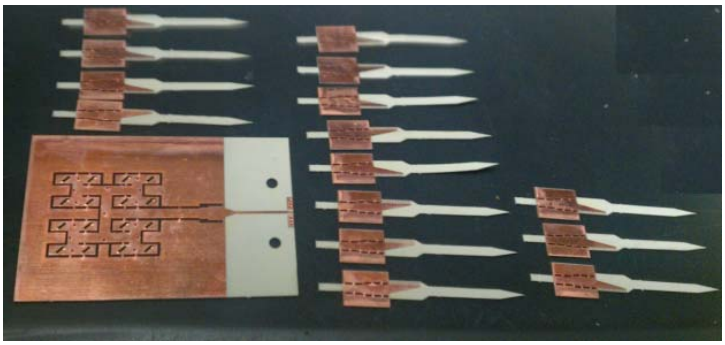

(b)

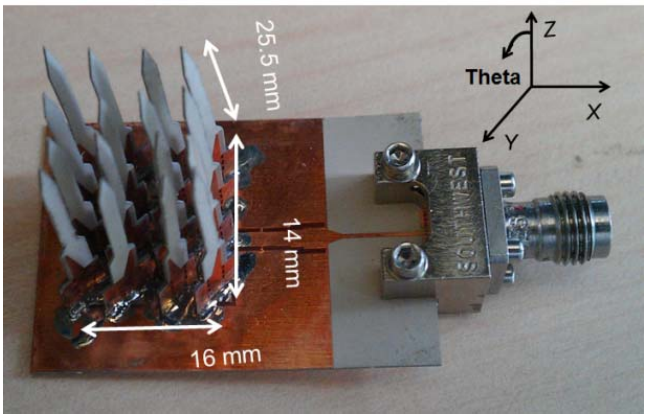

(c)

Figure. 2.14. (a) Antenna array simulated prototype showing only *ALTSA* antenna. (b) Fabricated prototypes of the 16 rod antennas and feeding network, (c) final array prototype.

2.2.4 Antenna array architecture

The simulated prototype of the ALTSA antenna array fed by using 3-D power divider is shown in the Figure. 2.14a. The 180^{o} phase shift offered by the feeding network is compensated

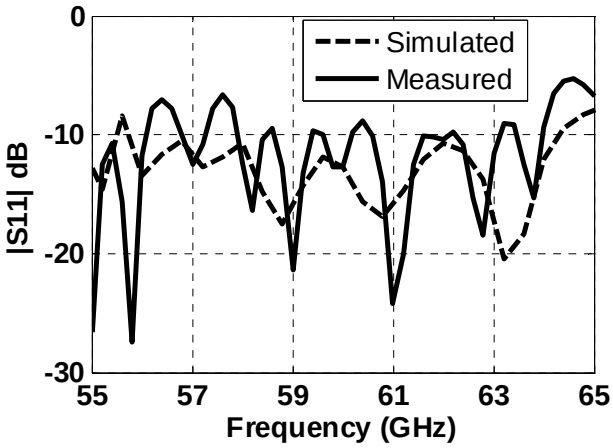

(a)

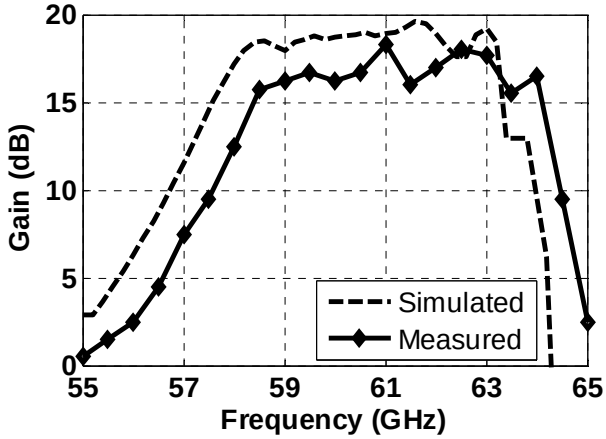

(b)

Figure. 2.15. Magnitude of S11 and peak gain comparison between simulated (dotted line) and measured (solid line) results.

by altering the slots of ALTSA antenna. Eight antenna elements fed by the feeding ports P2,P5,P6,P9,P10,P13,P14,P17 are mirrored to remaining eight elements fed by the feeding ports P3,P4,P7,P8,P11,P12,P15,and P16. As shown in the Figure. 2.14b, sixteen rod antenna elements and feeding network are fabricated individually. Rod antenna and vertical interconnect has

broadband matching performance over the frequency range from 55 GHz to 65 GHz. The rod antenna feeding points are made longer to ensure a proper alignment into slots and then antenna is soldered on the top side. After that, extra part of the rod antenna is removed and bottom side opening of the SIW fed rod antennas are covered with conductive epoxy to have perfect ground plane. The SIW feeding radiating elements are integrated into 45° rotated slots on feeding waveguide to implement 45° linearly polarized antenna array. Experimental prototype of the 3-D antenna array is shown in Figure. 2.14c.

2.2.5 Impedance and radiation performances

One port antenna impedance and radiation pattern measurements are measured through a South West Microwave end-launch connector. Antenna radiation pattern is measured in the MI technology anechoic chamber when the source polarization is set at 45° angle. Antenna measured gain is extracted from the calibrated data of the two standard horn antennas.

Antenna impedance is measured by using Anritsu vector network analyzer 37397. As shown in Figure. 2.15a, simulated and measured input impedances (with |S11| < -8 dB) are well matched over a bandwidth from 57 GHz to 64 GHz. Measured |S11| level is effected due to additional reflections from the used end-launch connector and also microstrip to SIW transition at the input of antenna array. Antenna radiation pattern is measured over the frequency band from 57 GHz to 64 GHz with 0.2 GHz frequency interval. Simulated and measured peak gain as a function of frequency is compared in Figure. 2.15b. Antenna gain is measured as 16.5 dBi, 17 dBi and 17.5 dBi at 59 GHz, 60 GHz and 62 GHz, respectively. Antenna measured gain is 1.5 dB lower the simulated value of gain. This is mainly due to the loss introduced by soldering at each of the interconnection point between vertical guide and feed guide. Figure. 2.16 compares simulated and measured radiation pattern in principal *XZ*-plane and *YZ*-plane. Antenna measured half power beam width is 14° and 13.5° in *XZ*-plane and *YZ*-plane respectively.

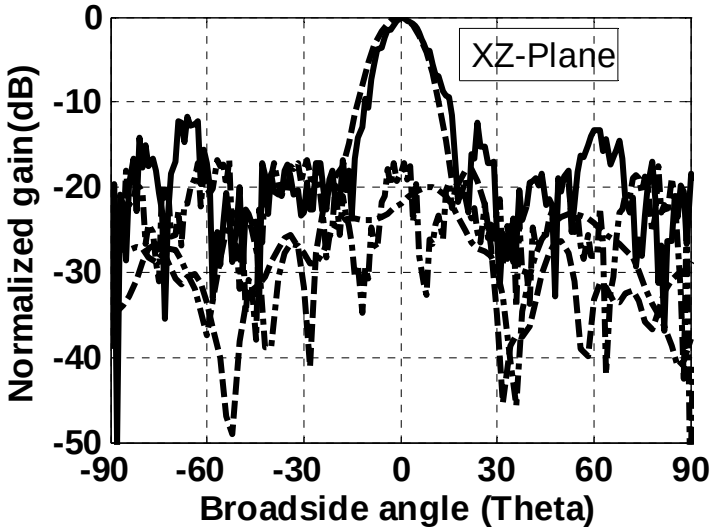

(a)

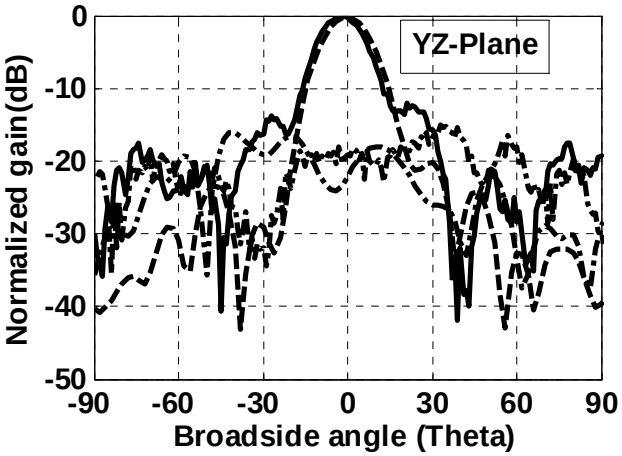

(b)

Figure. 2.16. Antenna radiation pattern at 60 GHz frequency in (a) E-plane (*XZ*-plane) and (b) in H-plane (*YZ*-plane). Dash line: co-pol simulated, solid line: co-pol measured, dotted: cross-pol simulated and dot-dash: cross-pol measured.

Rod antenna cross-polarization level is lower for 10 mil when compared to 25 mil thickness. However, in SIW feeding mechanism metallic loss is lower for thick substrates. In this design, rod antenna with 10 mil thickness is chosen to obtain good cross polarization characteristics. Nevertheless, antenna mechanical strength is reduced and also end-points are slightly misaligned along Z-axis of orientation**.** The amount of power radiating in the side lobe levels is 10 dB lower

than the main beam direction. An increase in measured side lobe levels in *XZ*-plane is caused by misalignment effect and large inter-element spacing in array. This problem can be mitigated by using foam spacer between antenna elements, so that overall mechanical strength will be improved without affecting the radiation pattern. When antenna has polarization mismatch amount of power received is 18 dB lower than the perfect polarization match.

In this sub-section, 45^{o} linearly polarized antenna array is proposed and implemented at 60 GHz frequency range. Antenna occupies a volume of 14 mm × 16 mm × 25.5 mm. Antenna peak gain of 17.5 dBi is obtained with 16 rod antenna elements. The gain enhancement is achieved without increasing any feed network size. Gain can be further increased by utilizing the rod antenna length in the third dimension. The three-dimensional antenna is fed by using SIW transmission line and fabricated by using a low-cost PCB process.

2.3 Milli-meter wave linear polarization diversity antenna array at 35 GHz

The ALTSA antenna is used as a radiating element to realize dual polarization antenna array operating at 35 GHz frequency. The application of DLP array in wireless power transmission is discussed in this work. Wireless communication systems have evolved from cellular telephony with data rates of kilobits per second (kbps) over distance of kilometers to wireless local area networks (WLANs) and wireless personal area networks (WPANs) that communicate with megabits per second (Mbps) over distance of meters. Research activities towards millimeter-wave communications are being intensified due to numerous advantages offered by this portion of electromagnetic spectrum [64]. Smaller physical size and inherent high gain of antenna are the two determinant advantages at the higher-end of millimeter-wave frequencies. On the other hand, short range communication with high data rate over a smaller distance is of main interest in the millimeter-wave frequency band [65].

The DLP antenna array is vital component for an application of simultaneous wireless power and data transmission. The high gain antenna with maximum aperture efficiency can collect the maximum incident power and provides the sufficient RF input power to operate the rectifier at the maximum conversion efficiency region. Integrated antenna arrays with high gain and polarization agility are highly in demand due to the advantages including simultaneous high data transmission and high angular resolution for short range wireless links. Such SIW-based DLP

systems can find numerous applications including imaging systems [66]-[67]. Particularly, the speed at which image is re-constructed depends on the number of simultaneous beams for imaging systems. Also, image quality depends on antenna system that can receive single or dual polarization signatures, simultaneously. Quasi-planar arrays with a combination of microstrip patch arrays and waveguide feed network were proposed in [68].The complexity of such feed networks and the power loss due to the microstrip feeds which is printed along with the arrays, make these techniques unsuitable to scale up for millimeter-wave frequencies. In [69], a waveguide fed ortho-mode transducer and in [70], planar interdigital structure was proposed to achieve dual polarizations. Nevertheless, all these solutions are using metallic waveguide and using corporate feeding network to feed antenna arrays.

Simultaneous microwave power and data transmission systems are an emerging area of research that allows sharing passive and active sources effectively. The circular and dual linear polarization antennas have always two independent horizontal and vertical polarization components. In [71], circular polarization (CP) antenna was used to demonstrate the same principle. Those proposed techniques were benefitting from the advantages of planar nature of the microstrip technology and low-cost fabrication cost. But, those techniques were not scalable to mm-wave frequency range mainly due to low antenna radiation efficiency. Also, the rectennas were using only one antenna element and providing low input power to the rectifier. The conversion and energy efficiency of the rectennas can be improved by using polarization agile antenna array instead of single polarization antenna element [72]-[73].

Initially, horizontal polarization (HP) and vertical polarization (VP) arrays are simulated, measured and then integrated into single aperture area to realize the proposed DLP antenna array. All the radiation patterns of HP linear array, VP linear array and DLP array are obtained at several frequencies in an indoor far-field MI technology laboratory. The transition from the grounded coplanar waveguide to the SIW is made to measure the impedence and radaition pattern bandwidth. The antipodal linearly tapered slot antenna (ALTSA) is chosen as radiating element due to its simple architecture and high gain characteristics. The ALTSA antenna is chosen as a radiating element to implement the DLP antenna array at 35 GHz frequency.

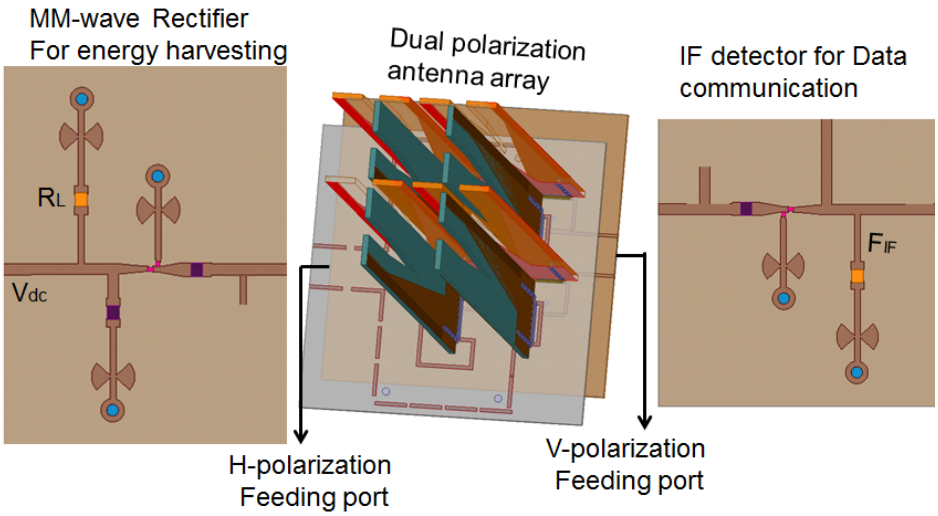

Figure. 2.17. Illustrative diagram showing the operation of simultaneous power and data communication system.

2.3.1 Radiating element performance

Among the end-fire radiating structures ALTSA antenna is widely used for numerous applications. Here, linear tapering of the slots on the broad wall of waveguide and corrugated side walls are used to obtain good radiation from the ALTSA antenna element. The antenna physical structure is shown in the Figure. 2.18a. Side walls of the linearly tapered slots are corrugated to reduce side lobe levels and to improve the cross polarization of antenna. The ALTSA antenna element was experimentally characterized in [60].

Antenna impedance matching is shown in the Figure. 2.18b. Magnitude of reflection coefficient with $|S11| \leq -10$ is from 30 GHz to 40 GHz frequency band. Antenna radiation performance is given in Figure. 2.18c. Simulated antenna gain is of 14.5 dB, cross polarization level is lower than -25 dB and side lobe levels are lower than 20 dB in both the E and H planes.

2.3.2 Feed network performance of HP and VP arrays

Initially, planar feed network parameters are optimized to obtain good impedance matching from 33.5 GHz to 35.7 GHz. The physical and scattering parameters of the planar SIW feed network are shown in the Figure. 2.19a. Power divider is using the parallel feed topology to

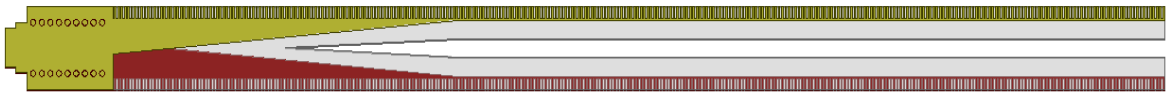

(a)

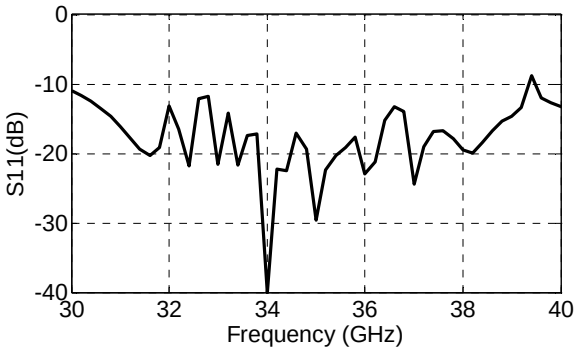

(b)

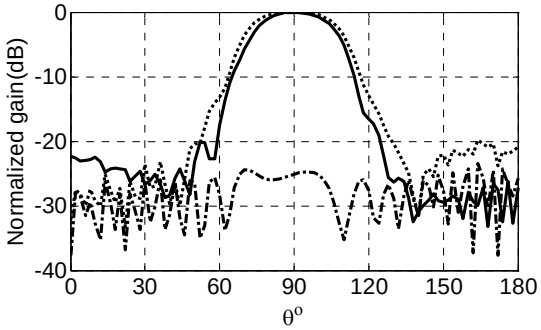

(c)

Figure. 2.18. (a) The linearly tapered ALTSA antenna and feed portion of the radiating element, (b) simulated antenna impedance matching as function of frequency and (c) Low side lobe level radiation pattern of the ALTSA antenna. E-plane and H-plane are symmetrical and the cross polarization also shown.

feed 2 × 2 planar array. As shown in the Figure. 2.19 c, d transmission loss (|S21|) ≤1.5 dB and reflection coefficient magnitude (|S11|) ≤ 20 over the frequency band from 33 GHz to 38 GHz. The power divider is used to feed the high aperture efficiency HP and VP antenna arrays.

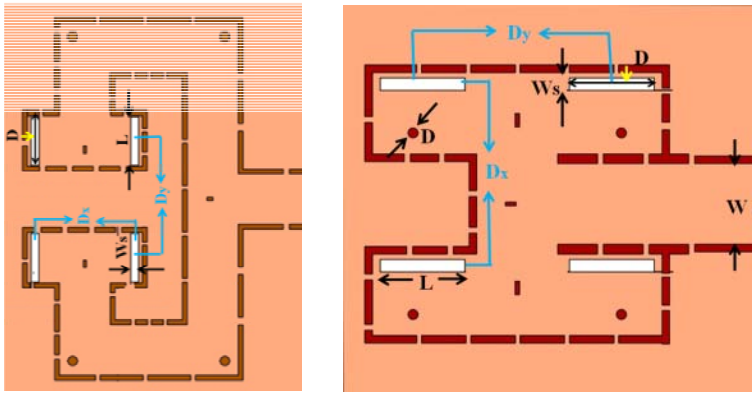

(a) (b)

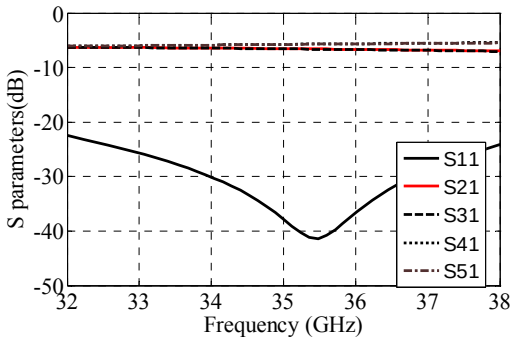

(c)

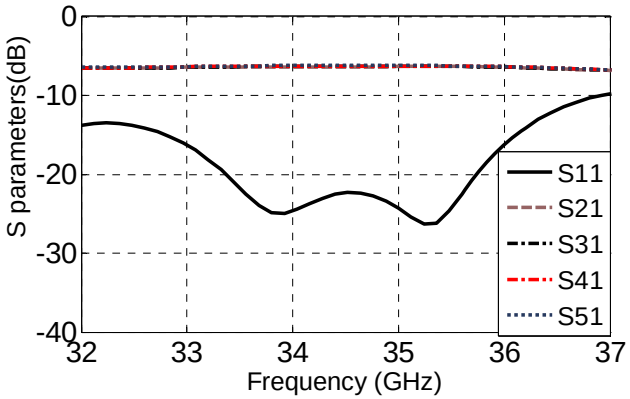

(d)

Figure. 2.19. Feed network part of (a) HP polarization, where the physical parameters are D_x= 0.84λ, D_y= 0.85λ, W=3.3mm, D=0.2mm, Ws=0.508mm, and DL=3.44mm, and (b) VP polarization, where the physical parameters are D_x= 0.84λ, D_y= 0.85λ., S-parameters of the feeding network for (c) HP array, and (d) VP array.

2.3.3 HP linear array performance

At first, HP linear array is constructed with four anti-podal linearly tapered slot antennas (ALTSA) and parallel feeding network. The feed part and four ALTSA antennas are fabricated independently. The input port is located on the horizontal plane and the output ports are located on the output plane. The optimized physical parameters of the array feed network are shown in the Figure. 2.19a. The 3-dB beam widths are approximately 16° and 15° for both E-plane and H-plane patterns, respectively. The side lobes are lower in the E-plane compared to the H-plane. Simulated antenna gain at 35 GHz is about 21 dBi and measured gain of 19.2 dBi. The cross-polarization level is found to be better than 20 dB thanks to the overlapped flaring metal in the SIW version. The measured radiation patterns are stable when the operating frequency is changing from 33.5 GHz to 36.5 GHz. For the HP array Distance between antenna elements in *X*- and *Y*- direction is set as $0.65\lambda_o$ and $0.67\lambda_o$. Measured maximum side-lobe levels are -17dB lower than peak gain value. The array cross- polarization levels are -21 dB below the main lobe in the band.

2.3.4 VP linear array performance

The optimized physical parameters of the VP linear array feed network are shown in the Figure. 2.19b. The orientation of ALTSA antennas on the feed network is orthogonal to the HP linear array. The radiation behavior is similar to the earlier discussed V-polarized array. For the proposed V-polarized array, measured radiation patterns are stable when the operating frequency is changing from 33 GHz to 37 GHz. For the VP array, distance between antenna elements in *X*- and *Y*- direction is set as $0.75\lambda_o$ and $0.77\lambda_o$. Measured maximum side-lobe levels are -17dB lower than peak gain value. The array cross- polarization levels are -21dB below the main lobe in the band.

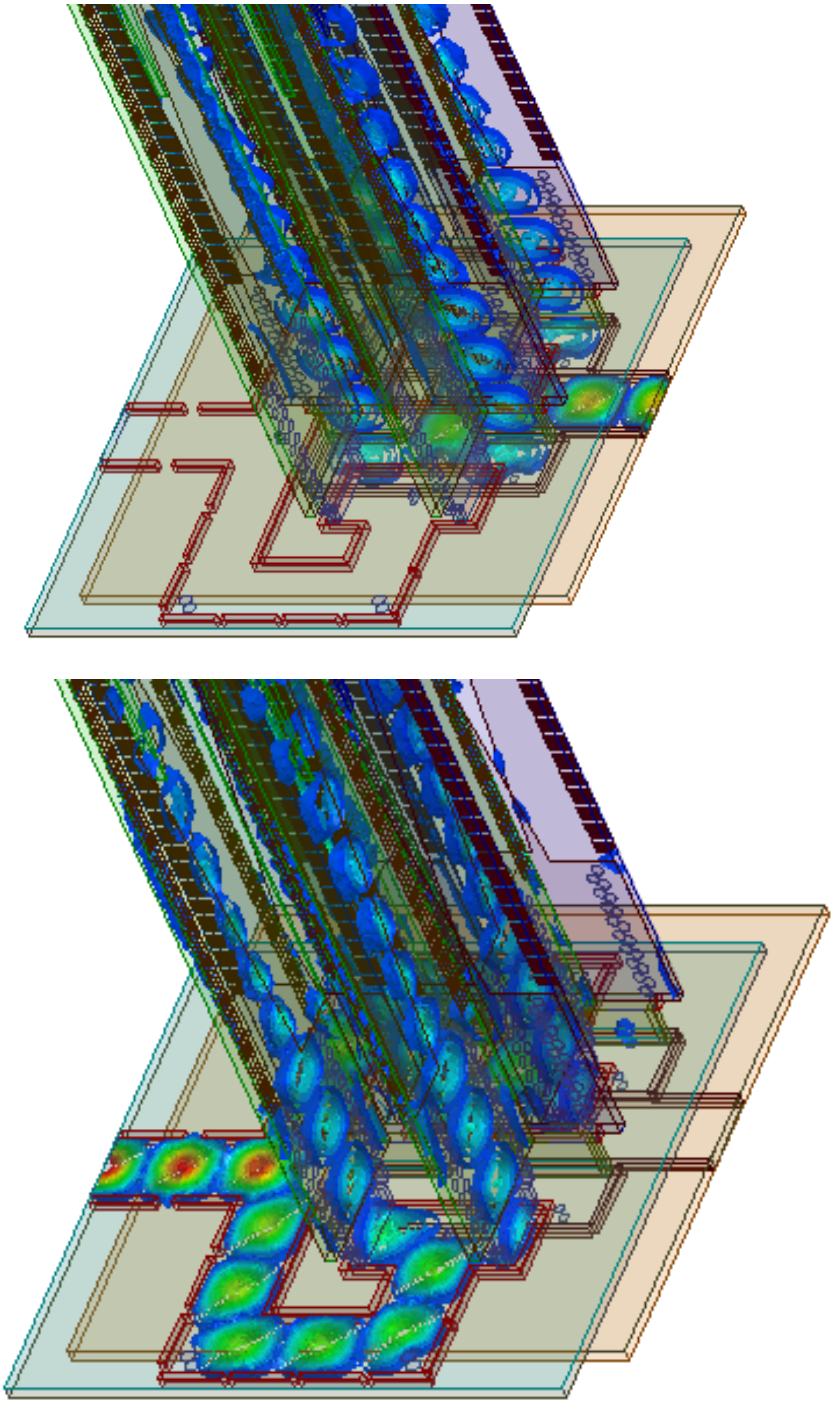

(a) (b)

Figure. 2.20. Simulated power flow inside the DLP array when fed (a) from port 1, and (b) from port 2.

2.3.5 DLP array performance

Electric field distribution inside DLP is shown in Figure. 2.20 a, b. When excited H-polarized array alone, almost no field is being coupled to V-polarized array. The SIW structure presents a naturally self-shielding feature for its transmission. Therefore, SIW feeder can minimize any potential interference to a negligible level. This is a very important advantage compared microstrip or co-planar waveguide planar transmission lines. The experimental prototype of the VP array and DLP array are shown in the Figure 2.21.

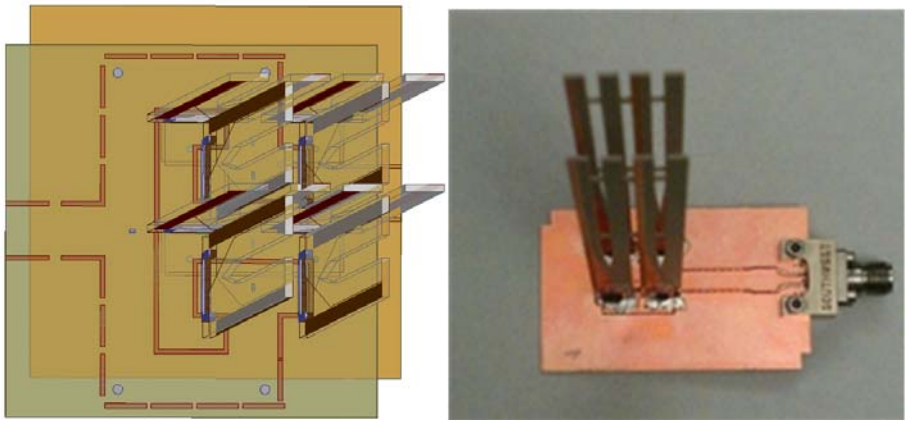

(a) (b)

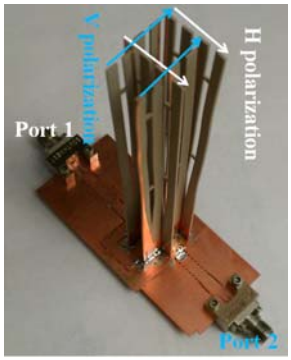

(c)

Figure. 2.21. DLP array (a) architecture in HFSS, and the experimental prototype of (b) single VP array, and (c) DLP array, (where the horizontal and vertical polarization array are integrated into single aperture area).

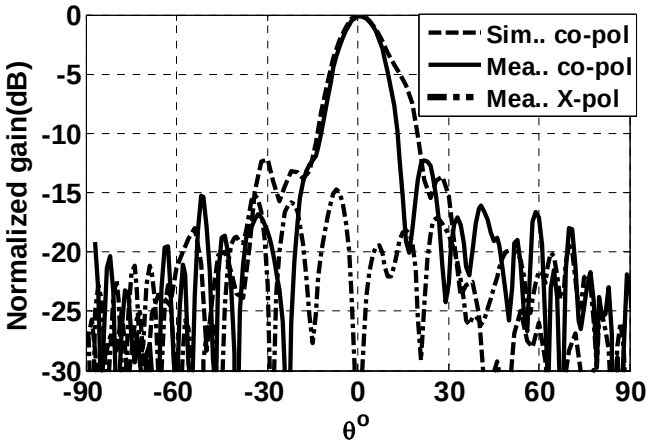

(a)

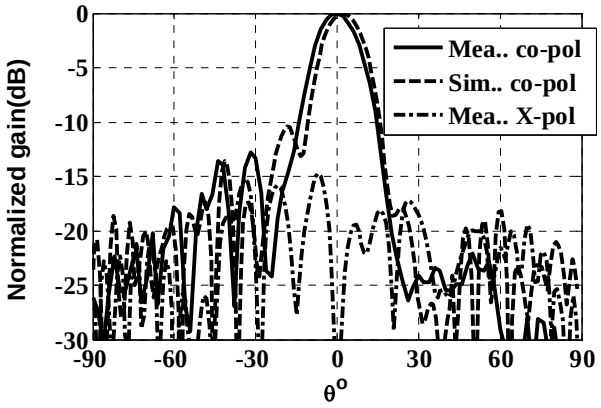

(b)

Figure. 2.22. Measured H-pol array performance at 35 GHz (a) in E plane (b) in H plane, where simulated co-pol (dotted), measured co-pol (solid) and measured cross pol (dotted dash).

For DLP array, port 1 corresponds to H-polarization and port 2 corresponds to V-polarization. Simulated and measured E-plane and H-plane co-pol radiation patterns along with the cross-polarization pattern are plotted in Figure. 2.22 and Figure. 2.23. Also, the Figure compares the measured and simulated co-pol pattern for H and V polarization states in the dual array environment. The simulated and measured results are well in agreement. The increased side lobe levels for the measured results are mainly due to intersection of H- and V- polarisation

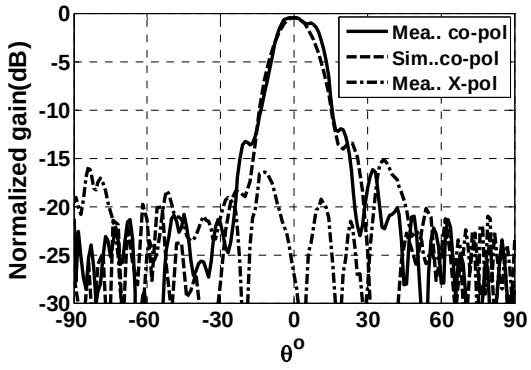

(a)

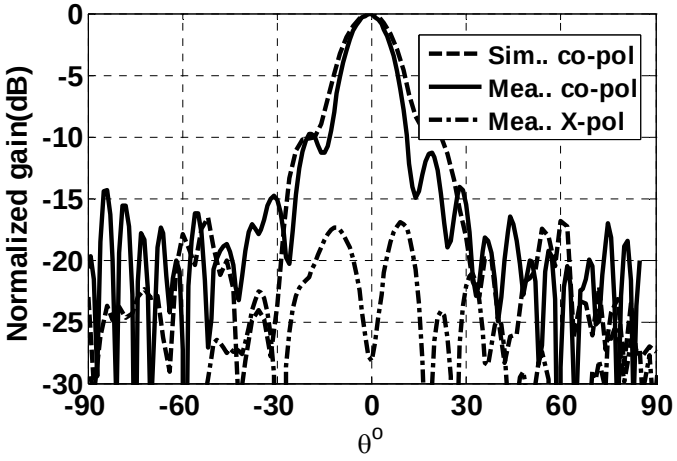

(b)

Figure. 2.23. V-pol array performance at 35 GHz (a) in E plane (b) in H plane, where simulated co-pol (dotted), measured co-pol (solid) and measured cross pol (dotted dash).

arrays in the feed part of DLP array. The undesired peaks can be avoided by choosing the array spacing larger than 0.75λ.

At 35 GHz, V-polarized and H-polarized array gain is about 19.4 dBi based on our simulations and almost 18.4 dBi is obtained in the measurement. The cross-polarization level is lower than 21 dB from co-pol value. Because, the proposed arrays are using perfect 0º and 90º slots on their respective feed structures. Normally, slot has perfect aperture distribution and it will avoid any cross-talk between the two perpendicular arrays. Also, the radiating element is having excellent cross-polarization characteristics due to the overlapped flaring metal in the SIW version. The feed

network is using parallel topology instead of series feeding topology. The two different types of vertical interconnects are used to realize DLP array architecture. The beam squint effect normally occurs in series type of feeding is removed by using parallel feed topology. Since antenna element gain is a function of aperture length, vertical plane dimension can be explored to increase the gain further. This concept can be scalable to higher millimeter-wave frequencies up to 94 GHz, particularly for Terahertz imaging applications.

The high gain, negligible mutual coupling, small foot print and low cross-polarization are main highlights of the DLP antenna array. This proposed DLP array can found application in simultaneous power and data transmission at 35 GHz. Where one polarization is dedicated for power transmission and orthogonal polarization is dedicated for data transmission. The other applications include imaging system for improving image reconstruction speed and to obtain improved image resolution.

2.4 Polarization Diversity Antenna with High Gain and Small Foot Print for Millimeter-wave Inter-Satellite Communication at 60 GHz Frequency

The DLP array feeding proposed in section 2.3, is suitable to feed 2 × 2 planar array only. To realize higher order arrays such as N × N planar array with dual-polarization signatures, new feeding network topology is required to obtain pure orthogonal polarizations without grating lobes in the radiating space. In this section, DLP antenna array of 4 × 4 array size with two independent horizontal and vertical polarization components is proposed for intended application in mm-wave satellite communication.

Novel techniques were proposed in literature to design linear polarization diversity antenna for wide variety of applications [74]-[81]. Orhto mode transducer (OMT) is a passive feeding network that generates two orthogonal linearly polarized components [76]-[78]. Two orthogonally located horn antennas were excited with substrate integrated OMT in [78]. However, complexity of OMT design further increases to feed large antenna arrays with higher gain levels. Another technique, is to excite two orthogonally oriented radiators both sharing common aperture area. The DLP antenna array with excellent radiating characteristics has been demonstrated in [79]-[80]. The feeding network was implemented in low-loss waveguide technology and achieved

very high radiation efficiency. In [81], single DLP antenna element has been proposed in SIW technology. But, the feeding network for large antenna arrays has not

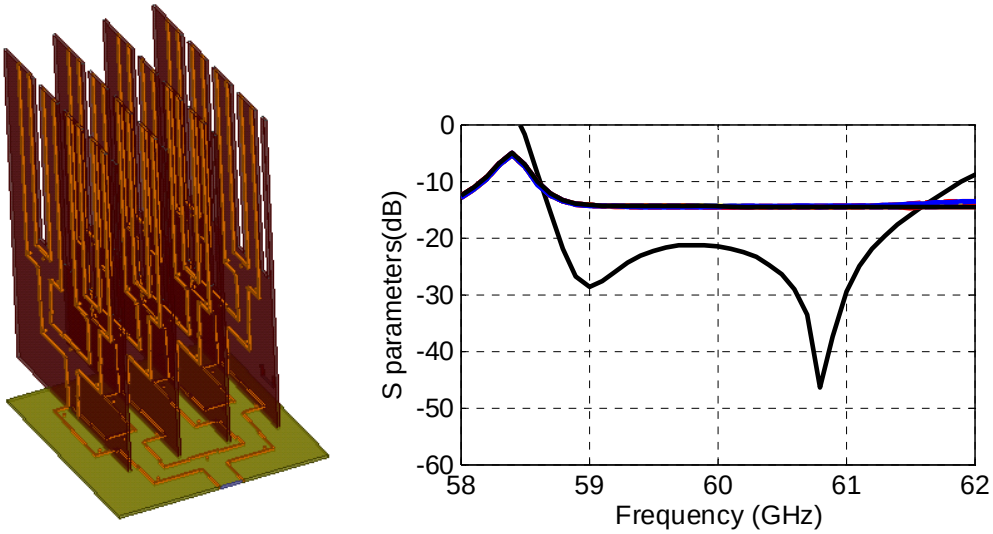

(a) (b)

Figure. 2.24. H-polarized feeding network (a) proposed architecture, (b) S-parameters.

provided. In this work, a technique is proposed to design higher order linear polarization diversity antenna arrays at 60 GHz frequency range.

The complete 3D architecture of DLP antenna array is detailed in this section. Two orthogonal LP components are excited simultaneously using two different topology of SIW feeding network. Initially, horizontal polarization (HP) and vertical polarization (VP) arrays are optimized to have best radiation performance, and later integrated into common aperture area to realize the DLP antenna array. For the measurement purposes, transition from microstrip to SIW transmission line is integrated at each input ports

2.4.1 Feed network performance of HP and VP arrays

As shown in the Figure. 2.24a feeding network for HP antenna array is designed in two steps. At first, a planar 1 × 4 Y-junction power divider is designed and each output port is connected to another set of four 1 × 4 Y-junction power dividers. In the second step, horizontal

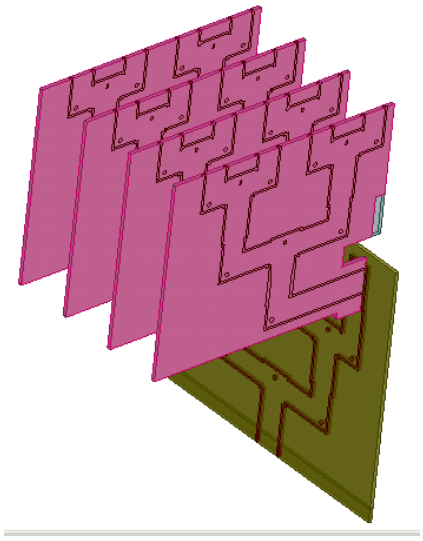

(a)

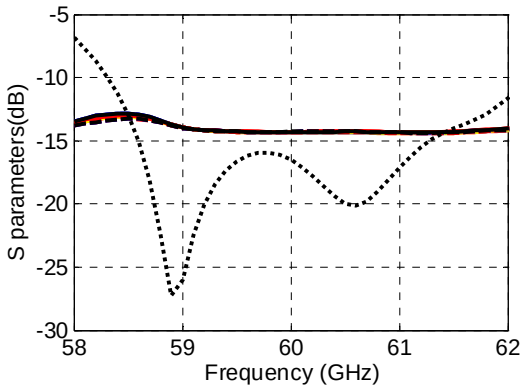

(b)

Figure. 2.25. V-polarized feeding network, (a) architecture (b) S-parameters

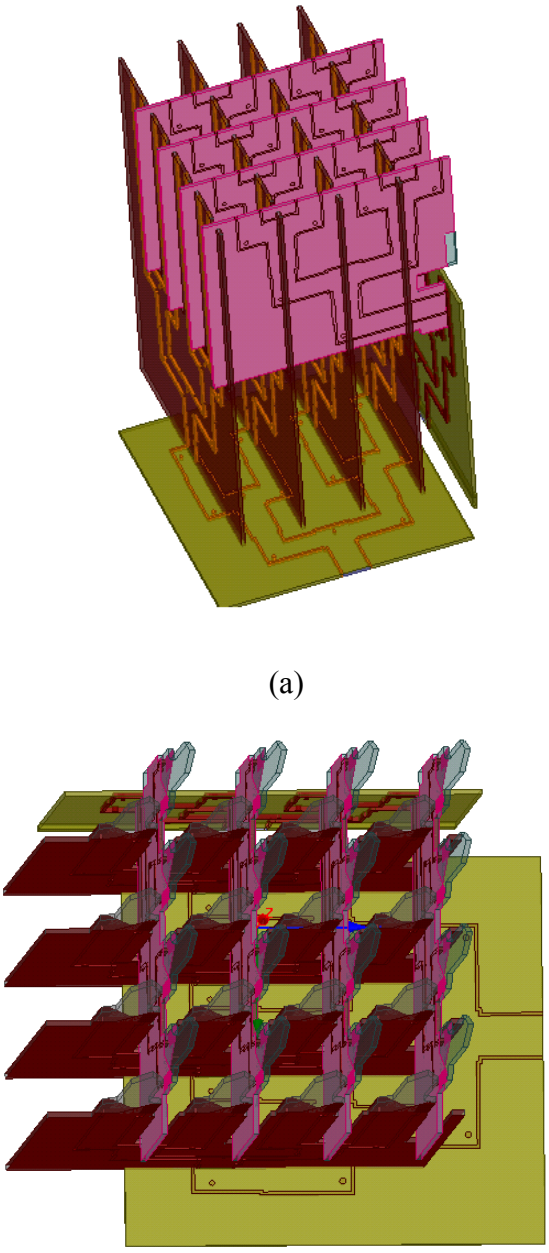

(a)

(b)

Figure. 2.26. Dual linearly polarized antenna array (a) three dimensional architecture, (b) top view showing the antenna array.

and vertical guides are connected through a SIW vertical interconnect at each junction [81]. The S-parameters of the 3-D feeding network are given in Figure. 2.24b. The input port is on horizontal guide and output ports are located in the vertical guide.

The transmission coefficient magnitude |S21|, |S31|, |S41|, |S51| ≤ 1.5 dB and reflection coefficient magnitude |S11| ≤ 20 over the frequency band from 58.8 GHz to 61.3 GHz. The 3-D power divider is then integrated along with the sixteen rod antennas to design 4 × 4 HP antenna array.

As shown in Figure. 2.25a, special topology adopted for VP array is different from HP array feeding network and extended in three dimensions. The main 1 × 4 power divider is acting as vertical feeding part and each output is connected to another set of 1 × 4 power divider. The feeding network is consisting of one input port and sixteen output ports. The S-parameters plotted in Figure. 2.25b, shows that power is distributing uniformly among 16 output ports and input matching condition is satisfied in the feeding network.

2.4.2 DLP array architecture and fabrication

As depicted in Figure. 2.26a, HP and VP feeding network are orthogonally placed each other to realize the compact DLP array. The feeding network has two input ports and 32 output ports. The electromagnetic fields are guided smoothly in the SIW from the input to output without any cross-coupling between any two closely spaced transmission lines. The anti-podal linearly tapered slot antenna (ALTSA) antenna loaded with tapered dielectric substrate to enhance the gain of the total combination. The DLP array simulated in Ansoft High Frequency Simulation software is shown in the Figure. 2.26b. The feeding network and 32 antenna elements are integrated together to realize the final prototype.

The distance between two elements in *X*- direction and *Y*-direction at 60 GHz frequency is fixed at 4.4 mm (0.88 λ_o) for HP and VP polarization respectively. The DLP feeding network and antenna array are integrated on the Rogers 3006 substrate (10 mil thickness, ε_r = 6.3, *tan* δ = 0.003). The array is free from the grating lobes in the visible space. The feeding network is designed with effective utilization of three dimensions. The foot print of the array is occupying size of 5.4 λ_o × 6.8 λ_o in the horizontal plane. The DLP array height is 10.4λ_o including the feeding network size.

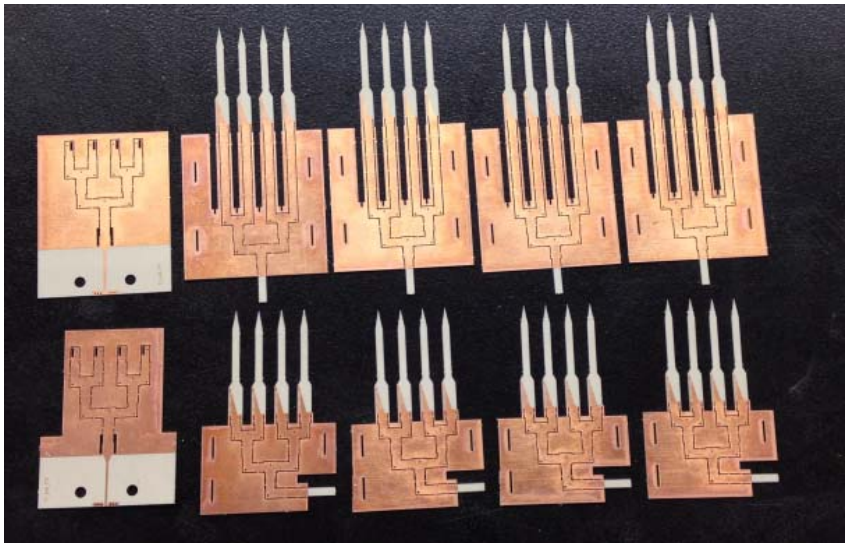

(a)

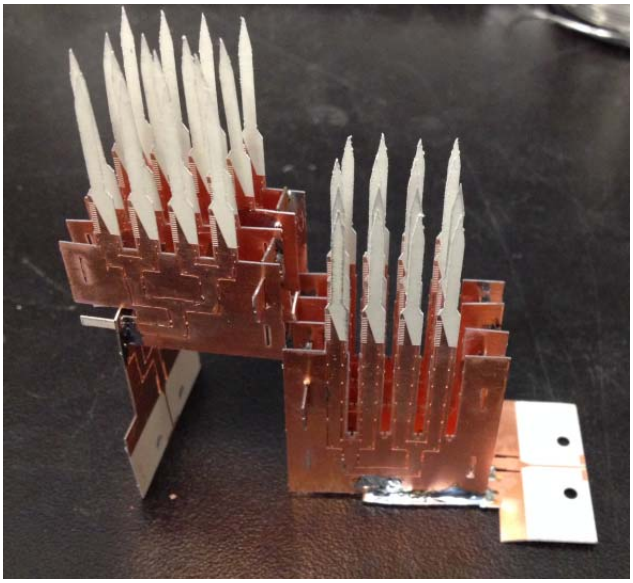

(b)

Figure. 2.27. Dual linearly polarized antenna array (a) individual parts, (b) HP and VP arrays are constructed independently.

The complex feeding network of array is fabricated in easy printed circuit board process. The HP and VP array feeding network and antenna array fabricated parts are shown in the Figure. 2.27a. The individual parts are used to construct both the arrays independently as shown in the

Figure. 2.27b. In the final step, both the arrays are integrated in the common aperture area. The feeding network and array are benefiting from the self-shielding nature of the SIW. The DLP

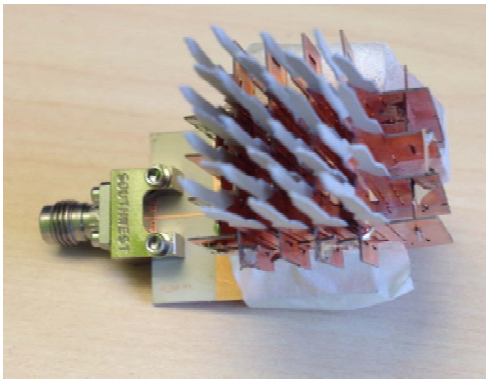

(a)

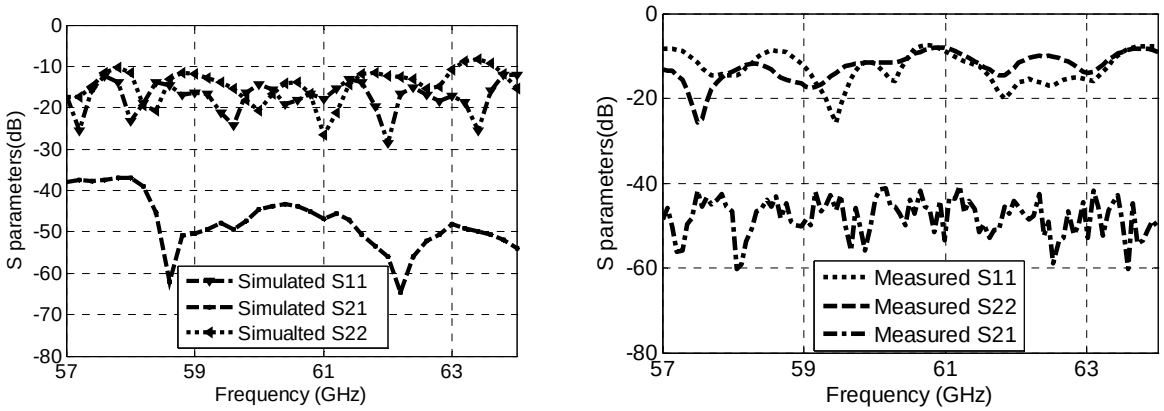

(b)

Figure. 2.28. Dual linearly polarized antenna array (a) three dimensional architecture, S-parameters (b) simulated, (c) measured as a function of frequency.

antenna array fabricated prototype is shown in the Figure. 2.28a. The array is measured by using V-band end launch connectors from South West Microwave company. The Rod antenna gain is a function of tapered rod length. Here, the rod length is fixed at 3 λo to keep better rigidity in the structure.

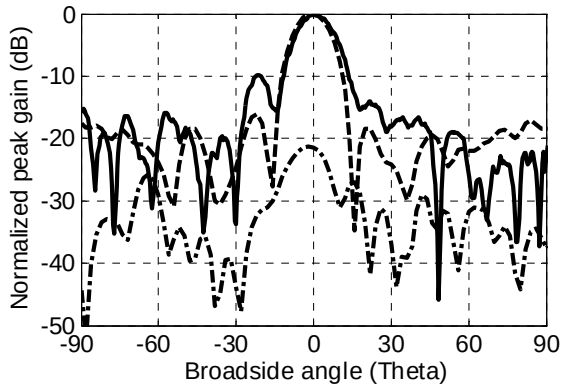

(a)

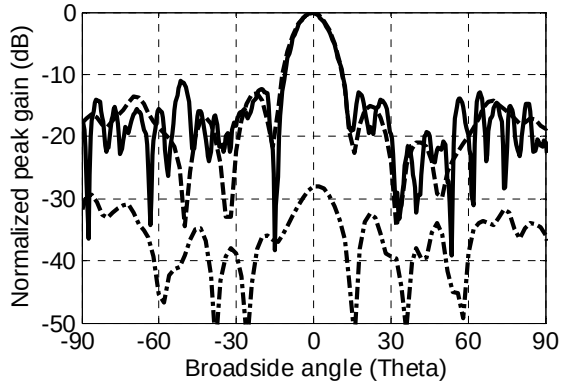

(b)

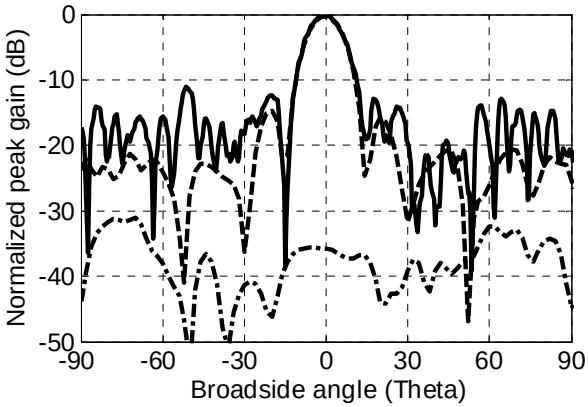

(c)

Figure. 2.29. Simulated and measured V-pol array performance in H-plane at (a) 58 GHz (b) 60 GHz, (c) 62 GHz, where simulated co-pol (dotted), measured co-pol (solid) and measured cross pol (dotted dash).

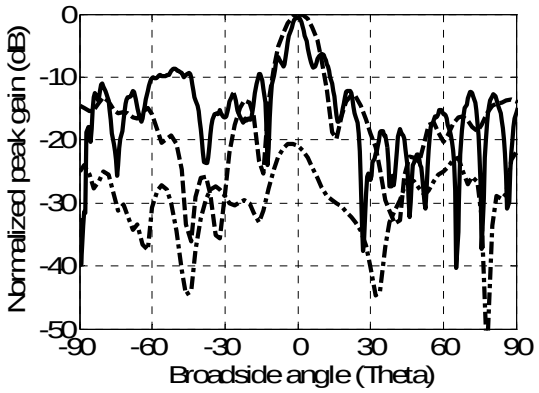

(a)

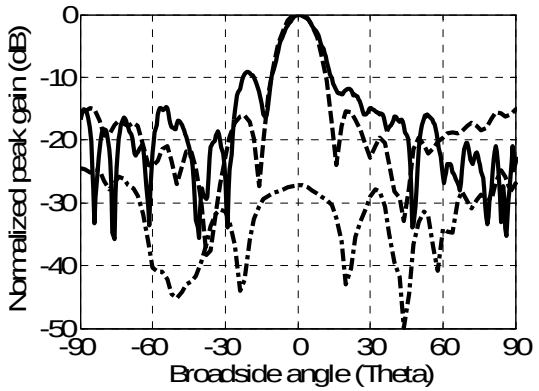

(b)

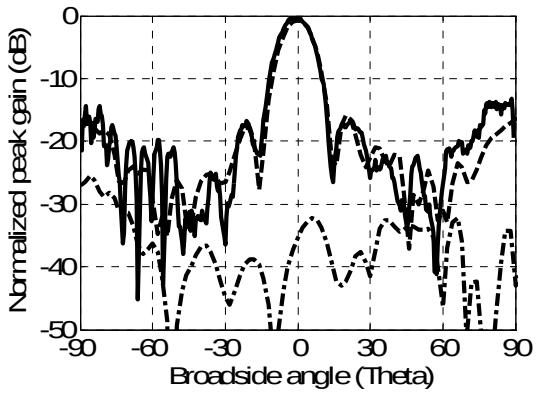

(c)

Figure. 2.30. Simulated and measured V-pol array performance in E-plane at (a) 58 GHz (b) 60 GHz, (c) 62 GHz, where simulated co-pol (dotted) , measured co-pol (solid) and measured cross pol (dotted dash).

The end points of the rod antenna array are kept at 0.88 λo in X- and Y- directions using the substrate spacers inserted between the walls of the HP and VP array feeding network. The S-parameters of the DLP array are shown in the Figure. 2.28b. The array mutual coupling coefficient (S21) is less than -40 dB and the input matching condition is satisfied in the frequency band from 58 GHz to 62 GHz. When excited from port 1 and 2, HP and VP electromagnetic waves are radiated respectively.

2.4.3 HP linear array performance in the DLP array radiating environment

The DLP antenna array radiation pattern is measured in the far-field MI technology laboratory. The standard radiation pattern cuts in the principal planes are measured for HP and VP linear array independently. Antenna array radiation pattern is measured from 58 GHz to 62 GHz with 0.2 GHz frequency interval and 0.5^{o} radiation angle interval. The HP antenna array radiation pattern in H-plane and E-plane at 58 GHz, 60 GHz and 62 GHz is plotted in Figure. 2.29. The simulated and measured results are good in agreement at all frequency bandwidth from 58 GHz to 62 GHz. The HP array is excited by using parallel type of feeding network and hence there is no beam squints observe in the 4 GHz bandwidth operating around 60 GHz frequency. The DLP array is radiating HP wave in the broadside direction for all the frequency bandwidth.

At 60 GHz frequency, HP array 3-dB beam widths are approximately 14^{o} and 15^{o} in H-plane and E-plane patterns, respectively. The array has symmetric beam width in both planes and measured gain is around 18 dBi at 60 GHz frequency band. The side lobes are lower than -11 dB in E-plane and H-plane respectively. The higher side lobes are due to large inter-element distance between antenna elements. The side-lobe levels can be suppressed by applying tapered amplitude distribution instead of uniform distribution. The cross-polarization level is -20 dB lower than the co-polarization level in all the frequency points in both the planes. The array radiation performance can be enhanced by inserting foam spacers between rod antenna edge points, so the overall mechanical strength of the antenna will be improved. Measured maximum side-lobe levels are -10 dB lower than peak gain value in E-plane at 60 GHz frequency band. The single linearly polarized array performance is not affected in the dual linearly polarized environment.

2.4.4 VP linear array performance in the DLP array radiating environment

Antenna array radiation pattern is measured from 58 GHz to 62 GHz with 0.2 GHz frequency interval and 0.5^{o} radiation angle interval. The VP antenna array radiation pattern in H-plane and

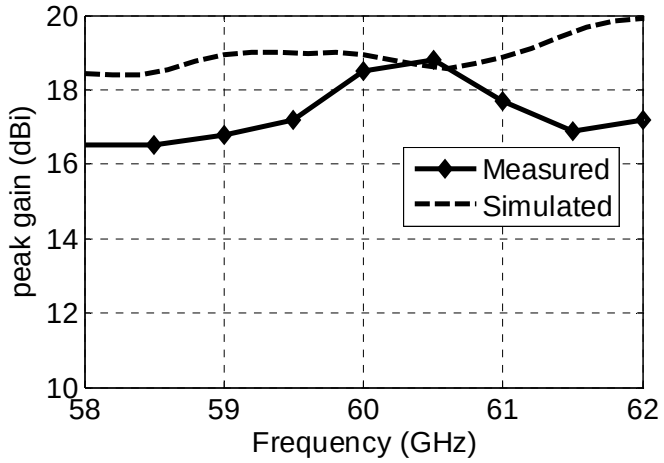

(a)

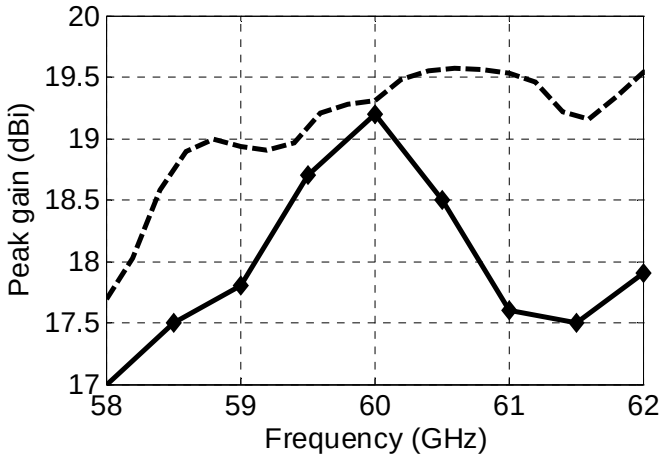

(b)

Figure. 2.31. Simulated and measured peak gain in H-plane for (a) H-pol array only, and (b) V-pol array only.

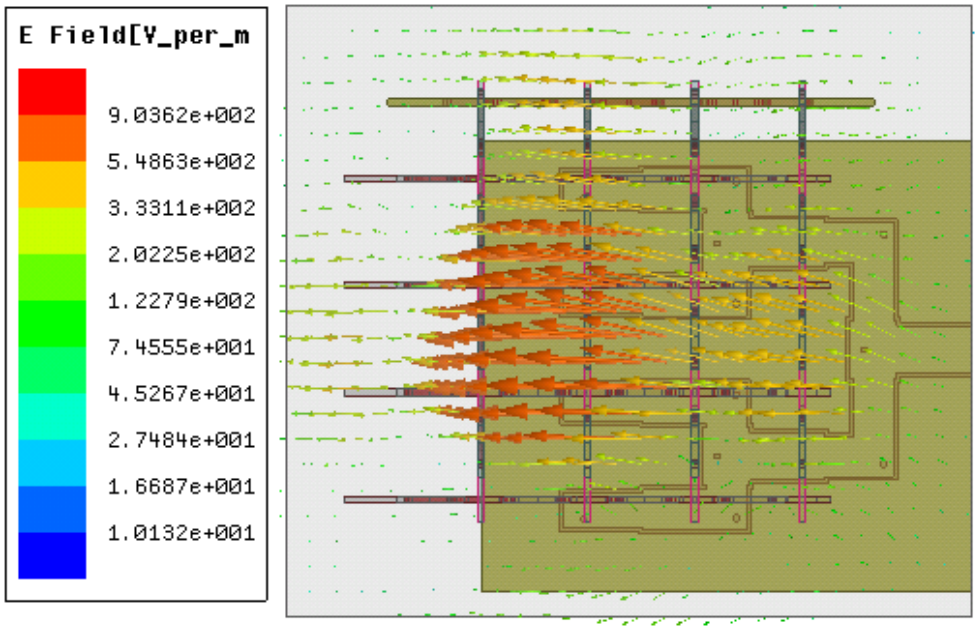

(a)

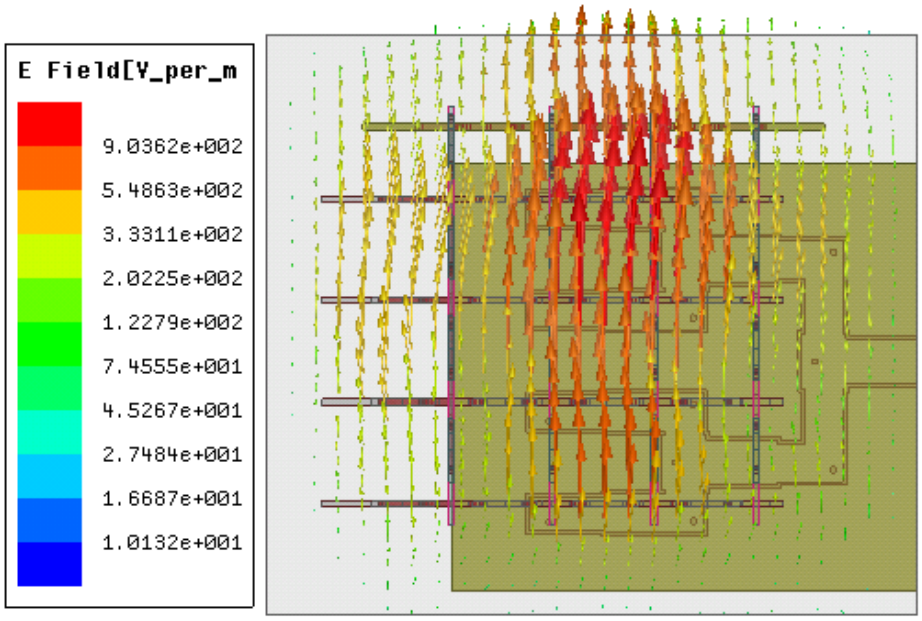

(b)

Figure. 2.32. Simulated electric field component for (a) H-pol array only, and (b) V-pol array only.

E-plane at 58 GHz, 60 GHz and 62 GHz is plotted in Figure. 2.30. The simulated and measured results are good in agreement at all frequency bandwidth from 58 GHz to 62 GHz. The VP array is excited by using parallel type of feeding network and hence there is no beam squint observes in the 4 GHz bandwidth operating around 60 GHz frequency. The DLP array is radiating VP wave in the broadside direction for all the frequency bandwidth. At 60 GHz frequency, VP array 3-dB beam widths are approximately 14o and 15o in H-plane and E-plane patterns, respectively.

The DLP array polarization purity and electric field inside SIW feeding array is shown in the Figure. 2.32. It can be concluded that, when port 1 excited only HP mode is radiating and when port 2 I excited only VP mode is radiating in the DLP array environment. The feeding network is acting as polarization diplexer and feeding the corresponding array only without any mutual coupling effects.

2.4.5 HP and VP linear array peak gain

Figure. 2.31 compares the simulated and measured DLP antenna peak gain as a function of frequency for each polarization mode. In the anechoic chamber, DLP array is measured in the receiving mode and horn antenna is radiating power. When fed from port 1, HP array received the maximum transmitted power and no power is being coupled to the VP array. Simulated antenna gain at 60 GHz is about 18.5 dBi and measured gain of 17 dBi. The peak gain is extracted after the standard calibration performed using two standard horn antennas. When fed from port 2, VP array alone is receiving maximum radiated power and almost no power is being coupled to the orthogonal polarization mode. The average simulated gain is 19 dBi and measured peak gain is 18 dBi around the 60 GHz frequency. The difference between simulated and measured peak gain values is attributed to the additional metallic losses, soldering losses at the interconnecting points and antenna misalignment errors inside the anechoic chamber.

2.5 Planar 1-D Scan Phased array antenna at 60 GHz

The dielectric rod antenna discussed above, is used as radiating element to implement phased array system, where each beam is electronically steered in the azimuth scan space. The

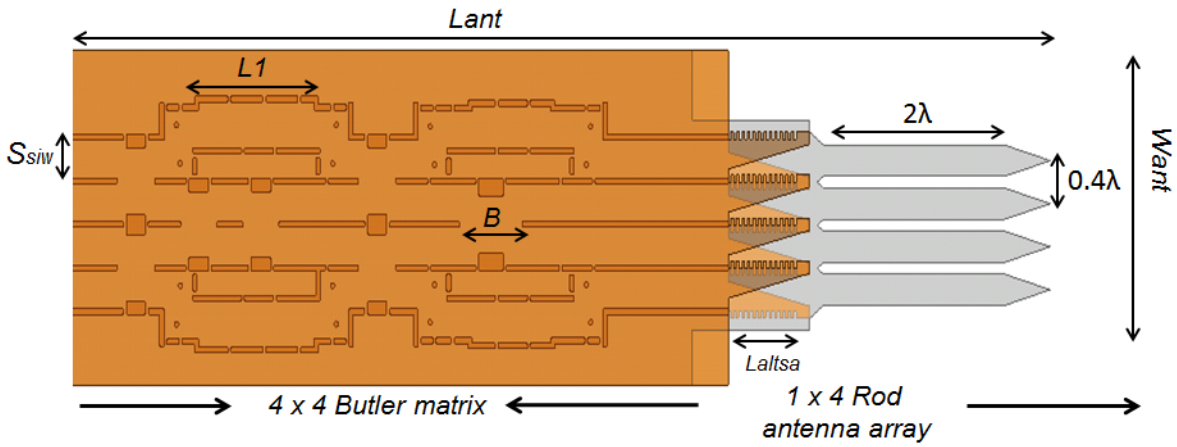
Lant
L1
Ssiw
B
2λ
0.4λ
Want
Laltsa
4 x 4 Butler matrix
1 x 4 Rod
antenna array

(a)

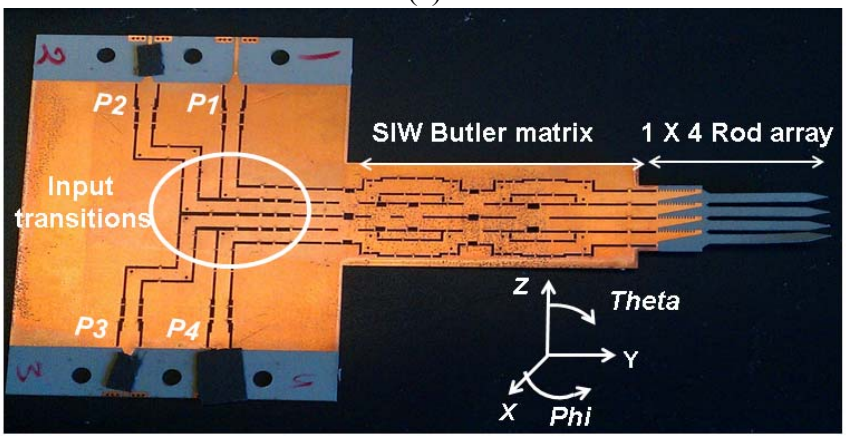
P2
P1
SIW Butler matrix
1 X 4 Rod array
Input
transitions
P3
P4
Z
Theta
Y
X
Phi

(b)

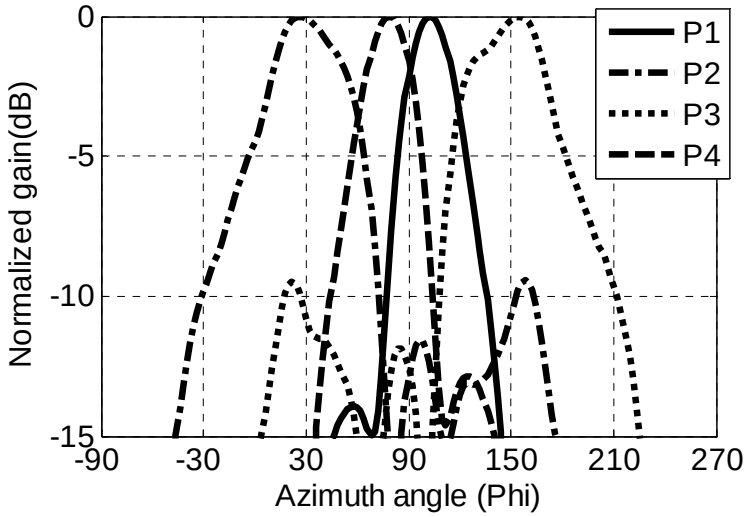
0
-5
-10
-15
Normalized gain(dB)
-90
-30
30
90
150
210
270
Azimuth angle (Phi)
P1
P2
P3
P4

(c)

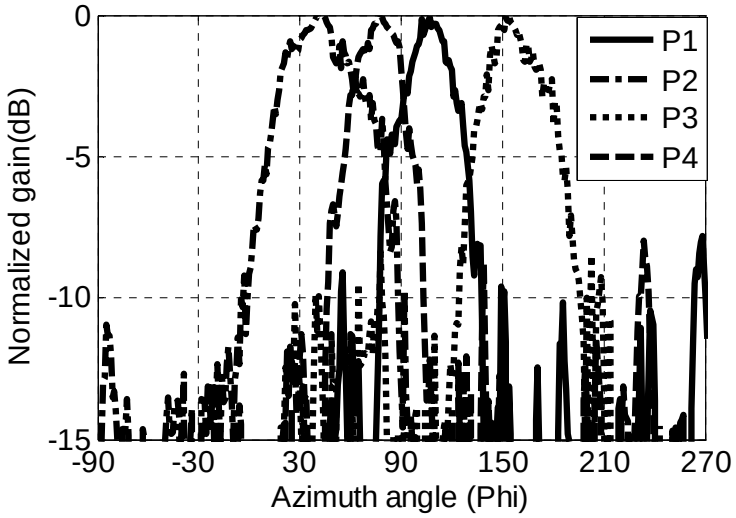

(d)

Figure. 2.33. 1-D scan phased array antenna (a) simulated model (S_{siw}=1.57,L_1=6.58, L_{altsa}=4.5, L_{ant}=56,W_{ant}= 14,B=3.46, where all dimensions are in mm), (b) fabricated prototype, azimuth plane radiation pattern at 60 GHz frequency (c) simulated, and (d) measured for four input ports *P1* to *P4* (where *P* = port number).

proposed 1-D scan phased array is planar and simple to manufacture in low-cost SIW technology.

Butler matrix based on H-plane coupler was proposed to scan directional beam in four fixed directions [82]. The BFN prototype is shown in Figure. 2.33a. The simulated phase and amplitude distributions in the BFN are close to the expected theoretical values. The linear phase gradient at the input of array has four beam forming states, namely +45º, -135º, -45º and +135º for four input ports P1 to P4 respectively and the amplitude distribution is uniform for all the input ports. Experimental prototype of the phased array antenna is shown in Figure. 2.33b.

The simulated and measured radiation patterns in the azimuth plane for four input ports are shown in Figure. 2.33c, d. When the input port is changed from P1 to P4, outgoing beam directions are simulated at four fixed directions as -45º,-10º, +10º, +45º and measured at -46º,-12º, +12º and +47º, respectively. The comparison between the simulated and measured beam directions is in a good agreement. The half power beam width (HPBW) for + 135º phase shift is close to 50º and for + 45º phase shift is close to 30º at 60 GHz. The phased array has a constant beam direction for each input port when frequency is changed from 59 GHz to 62 GHz. This is because phase dispersion in the BFN is minimized and antenna impedance is matched over a broadband frequency range. The beam pointing error is measured as 5º between the simulated

and measured results. Over the 60 GHz frequency band of interest, the measured gain for port 1, port 2, port 3 and port 4 is 14.5 dB, 12.2 dB, 12.3 dB and 14.5 dB, respectively. The rod antenna gain is a function of the dielectric rod length. The 1-D phased array antenna is designed on a 10 mil thickness substrate. The rod antenna element length is set to be 2λ so that single element has a wider half-power beam width and also a better mechanical stability. The single element has 10.5 dBi peak gain at 60 GHz and 1 dB gain difference between lower and higher operating frequency. The phased array is constructed by using the combined structure of BFN and 1 × 4 rod antenna array. The measured gain of the 1-D phased array includes the losses of the BFN, and input transitions. The measured average peak gain value is 13 dBi whereas the expected directivity is around 16.5 dBi. The metallic and dielectric losses of substrate decrease the peak gain value by 3.5 dB. For the end user applications, the feeding network loss can be compensated by integrating low-noise/power amplifier in the receiver/transmitter front-end.

2.6 Conclusions of rod antenna applications

In this chapter, four antenna front-end systems have been studied, analyzed and demonstrated in detail and each antenna or array radiation behavior is different.

In this chapter, 60 GHz linearly polarized antenna element is proposed and its application in the design of an antenna array is also discussed. An antenna solution is presented that meets the requirements for 60GHz unlicensed band and it can also be used as a radiating element for 60 GHz phased array system design. Simulated and measured results are compared to validate the proposed concept. Finally, antenna performance is compared with the best reported results. Here, the proposed SIW feed technique can be used to implement high gain linearly polarized planar arrays.

In addition, a 45^{o} linearly polarized antenna array is proposed and implemented at 60 GHz frequency range. Antenna occupies a volume of 14 mm × 16 mm × 25.5 mm. Antenna peak gain of 17.5 dBi is obtained with 16 rod antenna elements. The gain enhancement is achieved without increasing any feed network size. Gain can be further increased by utilizing the rod antenna length in the third dimension. The three-dimensional antenna is fed by using SIW transmission line and fabricated by using a low-cost PCB process.

Furthermore, this unlicensed frequency range from 57 GHz to 64 GHz was chosen to design high performance antenna arrays with dual linear and dual circular polarizations. A new technique was proposed to design 4 × 4 dual linearly polarized antenna array with high gain and good radiation characteristics at 60 GHz frequency. The techniques proposed were easily scalable to higher mm-wave frequency. The peak gain can be further increased by utilizing the rod antenna length in the third dimension. The three-dimensional antenna are integrated in SIW technology and fabricated in low-cost fabrication process. The proposed antenna is readily usable to satisfy bandwidth and gain requirements of cognitive radio front end at 60 GHz frequency range.

Finally, a linearly polarized phased array with 1-D scanning is introduced and experimentally characterized over the 60 GHz frequency range. A 1 × 4 linear rod antenna array is fed by using a Butler matrix and a complete phased array is integrated in a single layer substrate. The 1-D scan phased array is fully planar and has four beam forming states for four inputs. The physical size is $3\lambda \times 12\lambda \times 0.01\lambda$ and each phase steered beam has gain of 13 dBi.

CHAPTER 3 TWO-DIMENSIONAL SCANNING ANTENNA ARRAY DRIVEN BY INTEGRATED WAVEGUIDE PHASE SHIFTER

A planar phased array antenna demonstrated in chapter 2, is radiating beams in the azimuth scan space only. In this chapter, phase steered 2-D scan antenna array radiating beams in elevation and azimuth scan space is discussed in detail.

The performance of a 2-D beamforming antenna system depends on the design of its beamforming network (BFN) to produce constant beam direction angle θ_0, beam shape and low side lobe levels. Various BFN topologies to feed 1-D linear array were summarized in [87]. In 1-D beamforming systems, the antenna placement allows to place the BFN and an array in the same plane. In 2-D beamforming systems, the phase gradient between two elements is different in horizontal and vertical directions which impose a strict requirement on the design of the BFN. Although the array has a compact layout, the use of a microstrip feed network increases the attenuation by 0.3dB/cm with the dimension of a given array which decreases the radiation efficiency. The metallic waveguide fed microstrip array has been proposed in [88] to alleviate the radiation loss of the microstrip feed network. The SIW fed planar microstrip array has been proposed in [89] to overcome the limitations of conventional waveguide where a higher radiation efficiency of 79% can be obtained. Nevertheless, the feed network and patch array were integrated onto the same layer; hence the spurious radiation from the feed network was not completely suppressed. The standing wave SIW fed aperture-coupled microstrip array has been proposed in [90] and it has achieved an impedance bandwidth up to 22%. All these SIW fed array applications are limited to only one fixed beam direction [68] and [88-90]. Planar and non-planar forms of various beamforming matrices like Butler, Blass and Nolen matrices were already studied in SIW technology to scan one dimensional (1-D) linear array. Recently, a 2-D scanning of planar 2 × 4 array employing a planar switched beam network consists of two 4 × 4 Butler matrices and four hybrid couplers using the microstrip technology has been proposed for 60-GHz radio applications [91]. The SIW based 2-D scan beam forming network has been proposed in [92], where single resonant slot antenna has narrow bandwidth and low radiation efficiency, and its applications are limited for feeding the 2 × 2 antenna array only.

In this work, SIW based eight-port BFN is designed to feed 2 × 2 antenna array to obtain ensure 2-D scanned beam patterns. The aperture coupling method is used to excite wideband antenna element and to completely isolate the feed network. The desired beam direction obtained in the measurements of a fabricated prototype in the standard printed circuit board (PCB) technology has validated the proposed concept.

3.1 Single element design and characterization

The selection of radiating element in an array depends on operating frequency, polarization, bandwidth, scan angle, power handling, and array construction compatibility. To satisfy pre-designated requirements, SIW fed aperture-coupled annular ring antenna (ACARA) was selected as radiating element in [93] and [94]. In this work, similar antenna topology is adopted and designed on high permittivity feed substrate. As shown in Figure. 1, the antenna architecture of interest consists of 3 layers stacked on top of each other. The substrate in layer 1 is chosen to be of high permittivity Rogers RT/Duriod 6010 with ε_r =10.5, $tan\delta$ = 0.0023@10 GHz and thickness *H1*=20 mil (0.044λ_o), so to decrease the dimension of feed network and to fit well within the antenna array grid. The SIW feed is realized on this layer. The substrate in layer 2 is chosen to be of low cost dielectric foam Rohacell31 IG/A with ε_r =1.05, *tan* δ=0.0034@26.5 GHz and *H2*=60 mil (0.134λ_o), in order to achieve a wide 2:1 VSWR bandwidth around the operating frequency of 26.5 GHz. The layer 3 substrate is chosen as Rogers Ultralam 3850 with ε_r=2.9, *H3*=1 mil (0.0022λ_o), *tan* δ=0.0025 @10 GHz, in order to lower the surface wave losses and equivalent effective permittivity between the feed layer and the annular ring. Peak gain and input matching as a function of frequency is shown in Figure. 3.2. The radiating element is integrated on ultrathin layer 3. All the antenna parameters are optimized, and achieved 14.15% of 2:1 voltage standing wave ratio (VSWR) bandwidth, peak gain of 8.63 dB, radiation efficiency of 90% and symmetrical *E* and *H*-plane half power beam width (HPBW) of 75°, at the operating frequency of 26.5 GHz. The three layered antenna element explored in vertical dimension occupies a compact size of 0.693λ_o×0.835λ_o×0.176 λ_o very well suitable for a beam scanning antenna array where the radiator size is crucial.

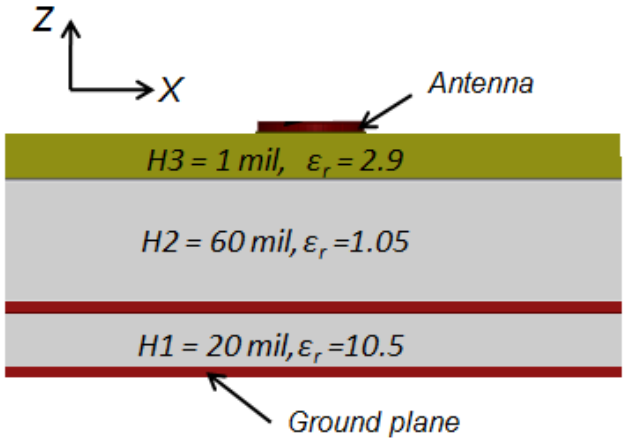

(a)

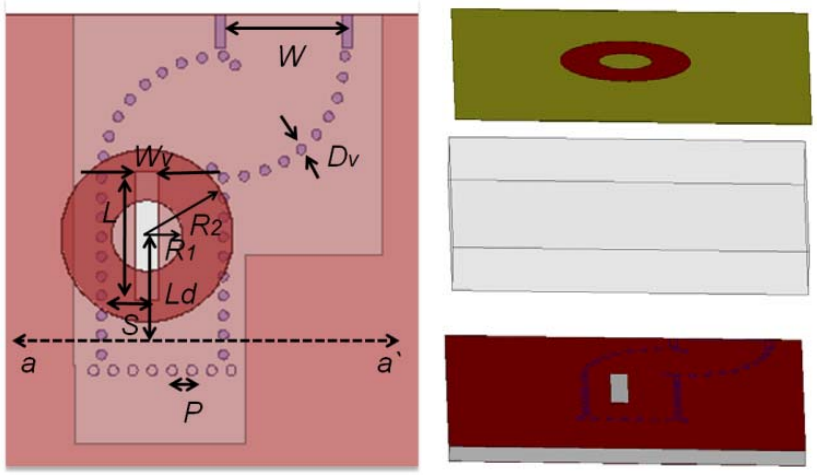

(b)

Figure. 3.1. (a) Basic cross section (a-a') of antenna stack up in XZ – plane (b) Antenna top view and exploded view (W = 2.96, Wv = 0.6, L=3.3, $R1$ = 0.9, $R2$ = 2.19, S = 1.15625, Ld = 3.427, P = 0.5, Dv = 0.254. Where antenna dimension are in mm).

3.2 Beamforming network design

The new configuration of 4 × 4 Butler matrix makes use of SIW cruciform directional couplers. The directional coupler used here was proposed in [95] and used to implement Butler matrix in [96]. Subsequently, a design method for this coupler was proposed in [97]. The equivalent rectangular waveguide model of the proposed Butler matrix is given in Figure. 3.3a. All coupler parameters are optimized for equal power division with 90° phase shift between

coupled and direct ports. The coupler exhibits 30% of bandwidth over which isolation between coupling ports is better than -20 dB and magnitude of reflection coefficient for input ports is less than -25 dB over the designed frequency range. This planar Butler matrix is modified to

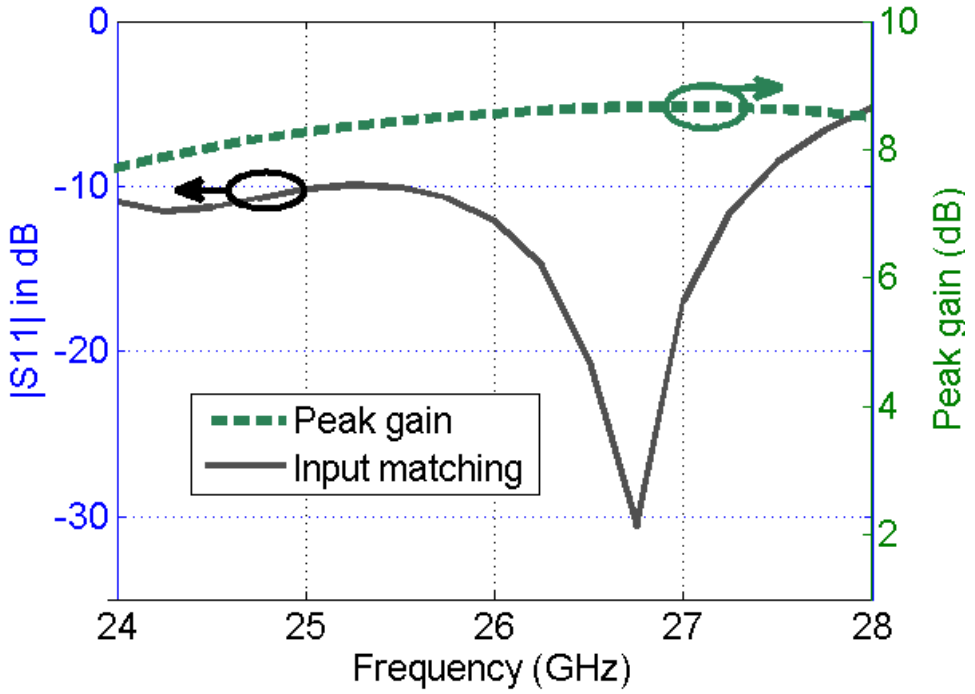

Figure. 3.2. Simulated reflection coefficient magnitude and peak gain as a function of frequency.

feed 2 × 2 array, as illustrated in Figure. 3.3b. The two-layered SIW BFN has four input ports 1-4 on layer 1 and four output ports P5-P8 on layer 2. The layer 1 of Butler matrix is constructed by using four 3-dB H-plane directional couplers and two unequal length 45° differential phase shifters. The crossover-free BFN produces the required theoretical amplitude distribution of -6.02 dB and phase difference of 45°, -135°, -45°, and 135° when fed from ports *P1*, *P2*, *P3* and *P4*, respectively. The layer 2 is used as connecting layer formed by two different bends (S shape and L shape), to feed the four radiating elements. The amplitude and phase profile of BFN is not affected by the connecting layer. The layer 1 and layer 2 are connected through a slot. The coupling slot parameters are optimized to minimize reflection and insertion losses due to the lateral transition.

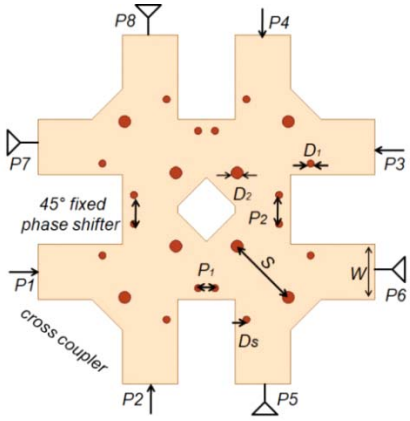

(a)

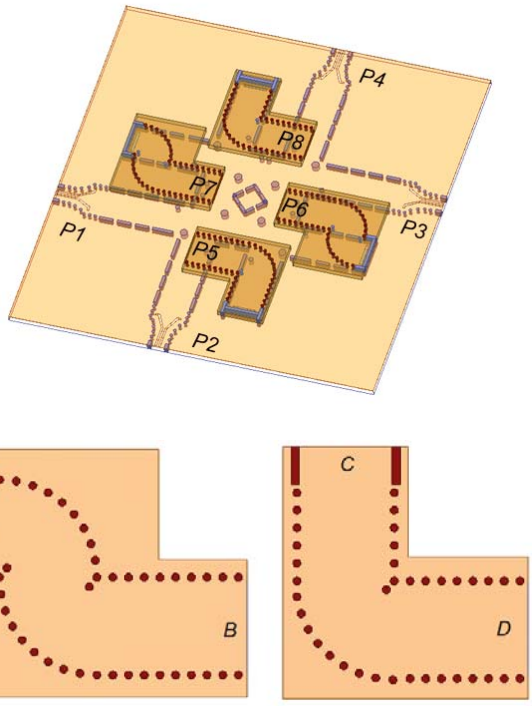

(b)

Figure. 3.3. (a) Planar 4×4 butler matrix with four hybrid couplers and two 45° phase shifters, where D_1 = 0.19, D_2 = 0.32, P_1 = 0.9, P_2 = 1.47, D_s = 0.47, S = 3.87, W = 2.96, where all dimension are in mm, and **(**b) Two layer eight port hybrid using two different shape bends. The coupling slot dimensions are width Wc = 0.16 mm, distance from end wall Sc = 0.275 mm, and length Lc = 2.56 mm. Ports *P1-P4* on layer 1 and *P5-P8* on layer 2.

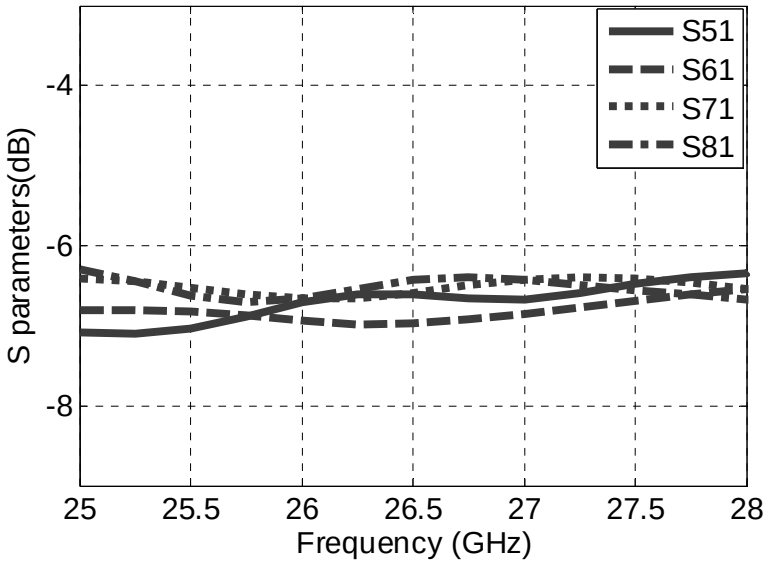

(a)

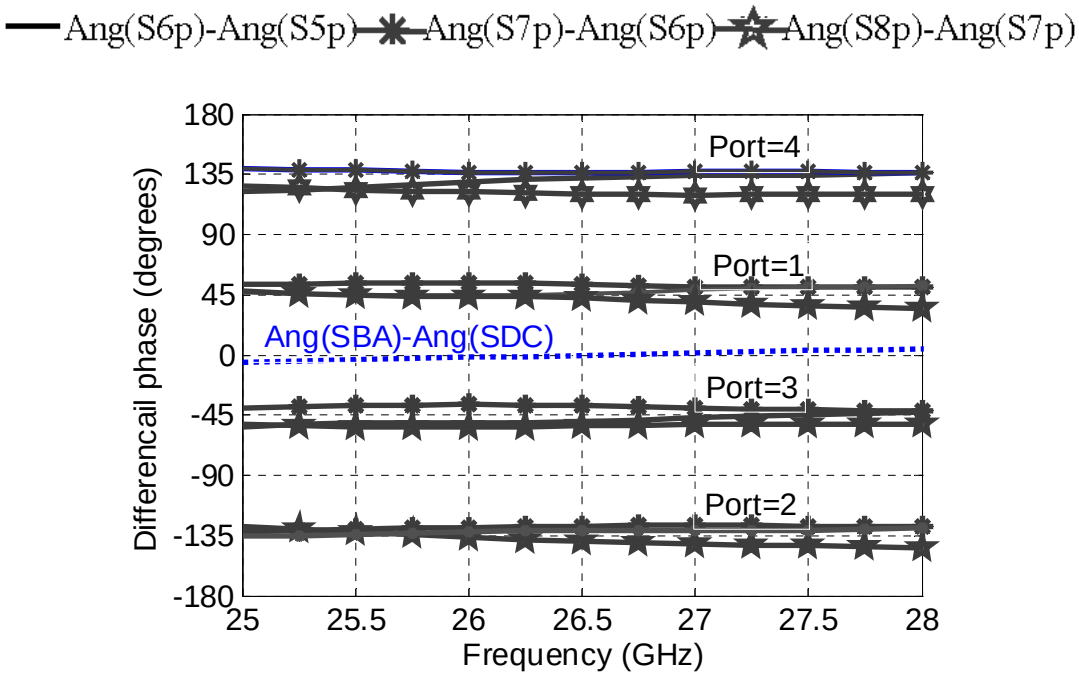

(b)

Figure. 3.4. BFN (a) Simulated transmission coeffceints fed from port 1, and (b) differential phase for all four ports, the blue dotted curve is the differencial phase shift between two bends. Here, *P* is the input port number.

Table 3 Theoretical phase difference of Butler Matrix

Port 1		ϕ_x	ϕ_y	θ_o, ϕ_o
135° port8	45° port 6	45°	90°	(21°, 61°)
90° port7	0° port5			
Port 2				
-45° port8	-135° port6	-135°	90°	(-38°, -31°)
90° port7	0° port5			
Port 3				
-135° port8	-45° port6	-45°	-90°	(-21°, 61°)
-90° port7	0° port5			
Port 4				
45° port8	135° port6	135°	-90°	(38°, -31°)
-90° port7	0° port5			

3.2.1 BFN S-parameter performance

Simulated transmission magnitude and phase parameters versus frequency are shown in Figure. 3.4. The transmission magnitudes are about 1.26 dB more than the theoretical values of -6.02 dB and phase dispersion with peak to peak error of 12°, around the theoretical values of -45°, 135°, 45° and -135° respectively. The phase difference is a combined phase dispersion of unequal length phase shifter in layer 1 and unequal width different shape bends in layer 2. The maximum amplitude dispersion is within + 0.75 dB over the frequency range of 25 GHz to 28 GHz. As shown in Figure. 3.4b, optimized peak to peak phase dispersions of two different shape bends are less than 7° over the frequency range of 25 GHz - 28 GHz. The phase difference between two different bends is plotted in Figure. 3.4b. The proposed matrix has better phase and amplitude performance while maintaining a more compact size than in [98].

3.2.2 Theoretical beam pointing angles

The phase profile of the theoretical Butler matrix is given in Table 3.

$$\phi_x = -kd_x \sin(\theta_o)\cos(\phi_o), \phi_y = -kd_y \sin(\theta_o)\sin(\phi_o) \quad (1)$$

$$\phi_o = \tan^{-1}\left(\frac{\phi_y d_x}{\phi_x d_y}\right), \theta_o = \sin^{-1}\sqrt{(\frac{\phi_x}{kd_x})^2 + (\frac{\phi_y}{kd_y})^2} \quad (2)$$ Where,

θ_o, ϕ_o = main beam scanning angle.

ϕ_x, ϕ_y = progressive phase shift in *X*- and *Y*- direction.

$\phi_x = \angle S5p - \angle S6p = \angle S7p - \angle S6p = \angle S8p - \angle S7p$

$\phi_y = \angle S8p - \angle S6p = \angle S7p - \angle S5p$

P= port number.

k = propagation constant in the free space.

d_x, d_y = distance between two neighboring antenna elements in *X*- and *Y*- direction.

The Butler matrix consists of four 90° hybrid couplers and two 45° fixed differential phase shifters. This combination produces linear phase gradients, in X-direction and Y-direction at output ports [37]. For a rectangular array of size M × N in *XY*-plane, to direct the beam towards direction such that the progressive phase shifts between the elements be equal to (1) and (2).

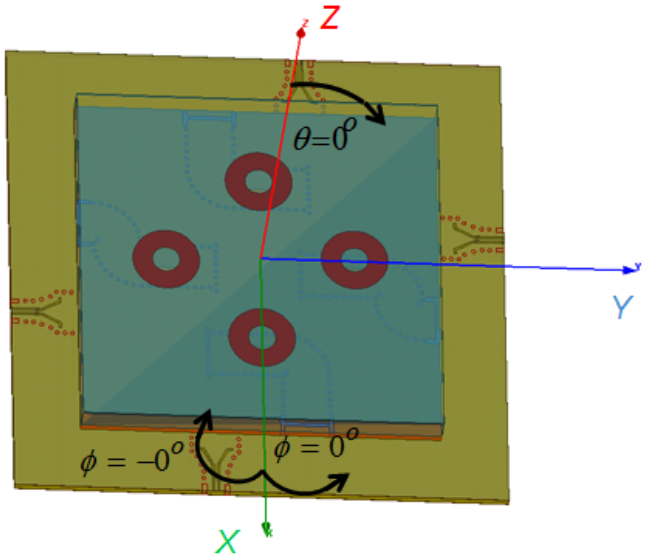

(a)

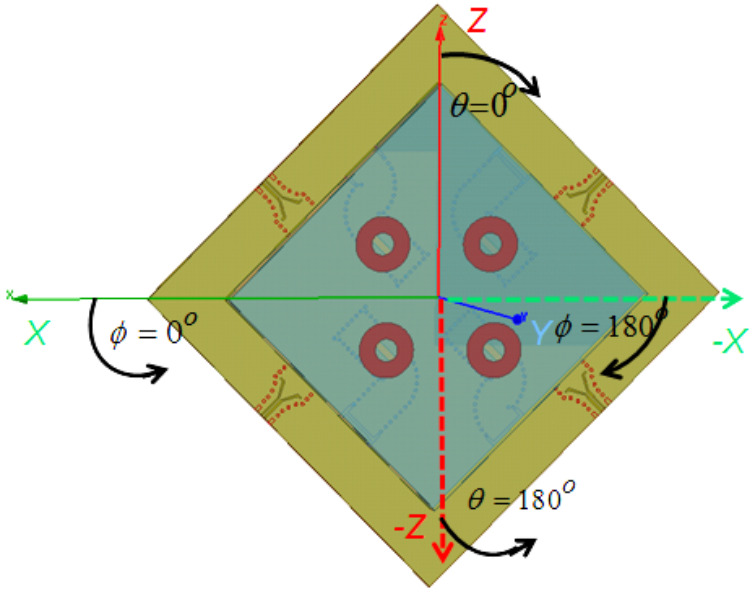

(b)

Figure. 3.5. Co-ordinate system definition (a) on 0° degree rotated array, and (b) on 45° degree rotated array.

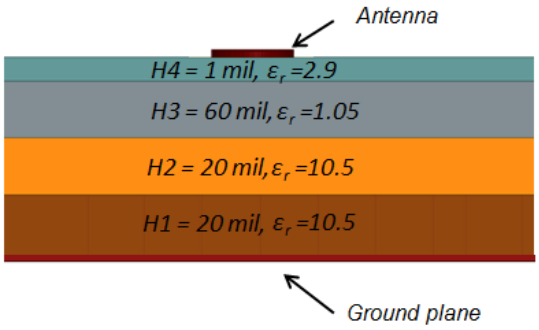

(a)

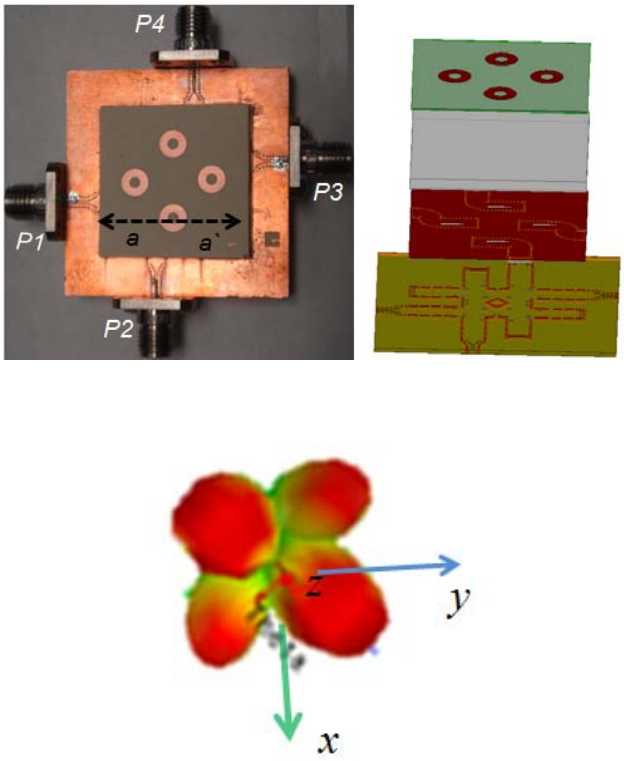

(b)

Figure. 3.6. *Ka*-band phased array (a) Basic cross section of array stacked up (a-a`) (where the BFN is synthesized on layer 1, 2, foam is on layer 3 and antenna is integrated on layer 4), and (b) Experimental proof-of-concept prototype, multi-layered diagram and 2-D scanned beams.

The theoretical phase difference between output ports P5, P6, P7 and P8 in X- direction is 45°,-135°,-45°,135° and in Y-direction is 90°, 90°, -90°,and -90° when fed from input ports P1, P2, P3 and P4, respectively, as given in Table 3. An output beam pointing direction is calculated according to the standard co-ordinate system defined in Figure. 3.5a. Then, theoretical beam angle direction is calculated as (21°, 61°), (-38°, -31°), (-21°, 61°) and (38°, -31°) when fed from port 1 to port 4, respectively. Here, four beams are located in four quadrants of the array. The new coordinate system is defined in Figure. 5b. Then, new beam angle direction from Figure. 3.5b is calculated as (66°, 106°), (97°, 104°), (114°, 70°) and (82°, 76°) when fed from port 1 to port 4, respectively. An array dimension in X-direction and Y-direction is described with reference to Figure. 3.5b. Inter-element distances for arrays in *X*-direction d_x = 0.7 and *Y*-direction d_y = 0.8, both are normalized to free space wavelength at 26.5 GHz.

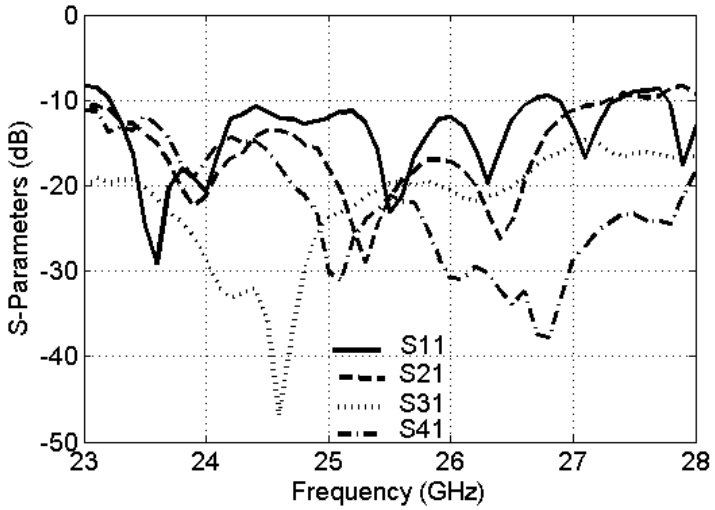

Figure. 3.7. Measured reflection coefficient for port 1 and isolation from 1 to 2, 3 and 4.

3.2.3 2×2 Antenna Array beamforming results

A single wideband (14.15% of impedance bandwidth) antenna element presented in Section II can produce symmetrical *E*-plane and *H*-plane half power beam width over the operating bandwidth. The new configuration of wideband BFN (with good performance over 11.3% of frequency bandwidth) described in Section III is used to feed an array of four ACARA arranged in a triangular lattice. Each element in annular metallic ring array is aperture-coupled

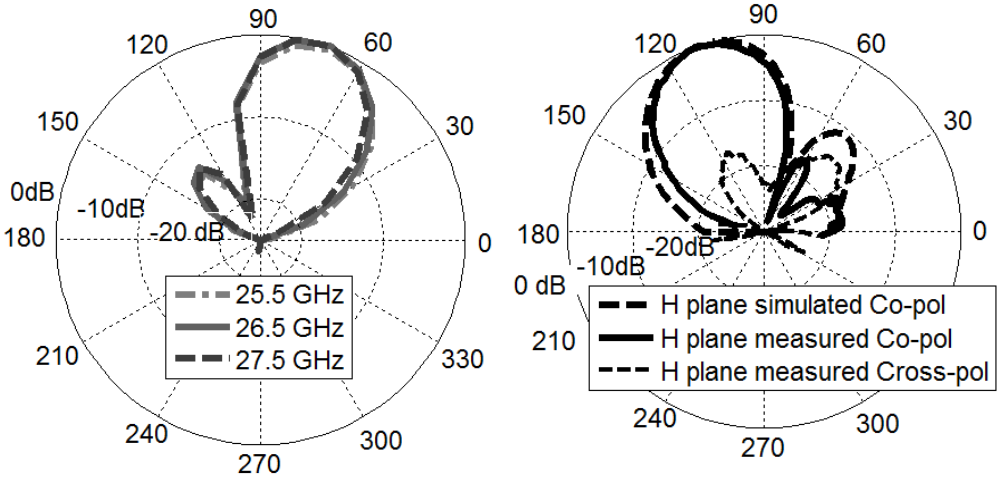

(a) (b)

Figure. 3.8. (a) Simulated normalized *E* plane radiation patterns as a function of θ (in degrees) when fed from port 1, and (b) comparison between simulated and measured normalized *H* plane radiation patterns as a function of ϕ (in degrees) when fed from port 1 at 26.5 GHz.

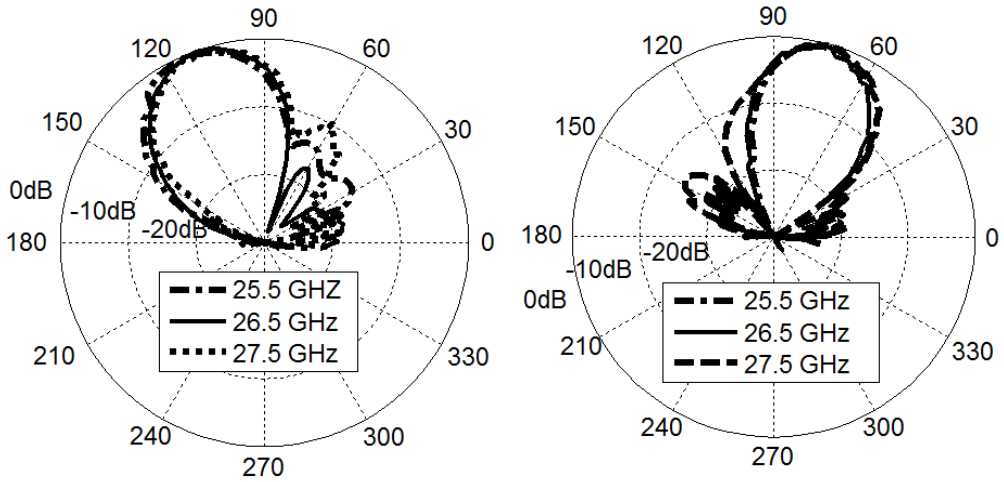

(a) (b)

Figure. 3.9. Measured normalized *H* plane radiation patterns as a function of ϕ (in degrees) when fed from (a) port 2, and (b) port 3.

through a wider slot etched on top of the SIW. Figure. 3.6a shows the top view and cross sectional view of the four layer layout stacked up for 2×2 metallic ring array (ARA) in the multi-layer structure. The two-layered SIW BFN is integrated inside the 2×2 array grid. The whole triangular array grid dimension is optimized to maximize single element performance in

an array radiating environment. The opposite feeding of the antennas from ports P5, P8 and P6, P7 causes 180° phase shift, so slots are etched on the opposite side of each bend in BFN to give an additional 180° phase shift. In this way, all the currents in an array are added in phase. The combined antenna system can yield four very directive fixed beams in four quadrants around the center of array axis. The complete configuration is simulated in full wave electromagnetic based simulator Ansoft High frequency simulation (HFSS) software.

3.2.4 Scattering Parameters

The proposed four layer structure of phased array is fabricated by using the multilayer fabrication facility developed within our Poly-Grames Research Centre. The photograph of a manufactured prototype is shown in Figure. 3.6b.

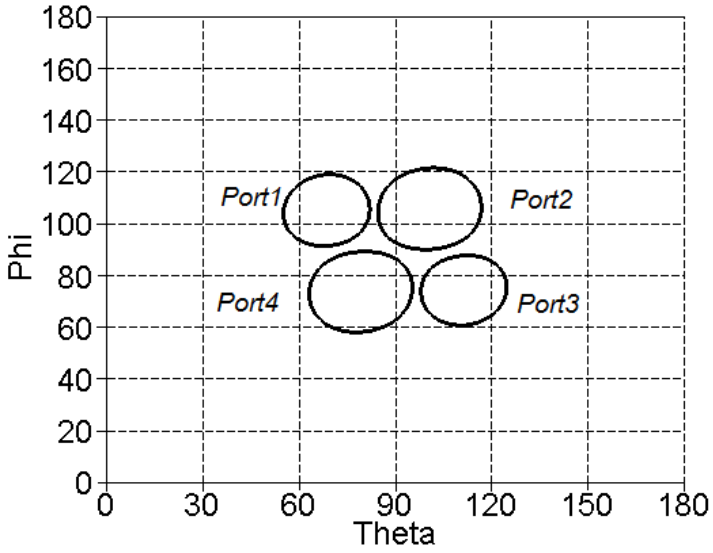

Figure. 3.10. Simulated 3-dB beam widths at 26 GHz.

The four port antenna array is measured by using vector network analyzer Anritsu 37369D with a standard short-open-load-thru calibration. Figure. 3.7 plots the measured S-parameters from port 1 to ports 2, 3 and 4. A similar behavior is observed for all the remaining 3 ports. The simulated and measured magnitude of reflection coefficient for input ports and isolation between input ports are lower than -10 dB over the frequency band of interest (25 GHz to 28 GHz).

3.2.5 Directional pattern measurements

The radiation pattern and gain measurements are conducted in our MI Technology anechoic chamber. The far field radiation pattern for a whole hemisphere (-90° to 90° in orthogonal planes) at an interval of 1° is measured by moving horn antenna along with the array. The simulated *E*-plane pattern given in Figure. 8a shows that array has peak gain at an angle of 20° from the array center axis and it has stable radiation pattern with side lobe levels lower than -13 dB over the operating frequency. Figure. 3.8b compares simulated and measured *H*-plane radiation patterns and it can be observed that both are in a very good agreement, and measured cross-polarization level in the direction of scanned beam is found to be lower than -17 dB over the entire band of frequency in both *E*-plane and *H*-planes. The beam direction obtained in azimuth plane has side lobe levels observed because of a larger inter element distance between antenna elements. The gain difference is attributed to the phase and amplitude dispersion of the BFN in an array.

Figure. 3.9a, b plots the measured *H*-plane radiation pattern over the frequency band of 25 GHz to 28 GHz when ports 1 and 2 are excited alone, which are obtained during azimuth scan when the array is placed in the horizontal plane. Similar radiation pattern is obtained for ports 3 and 4 due to the symmetry of the structure but in the orthogonal direction. A slightly distorted radiation pattern is observed at 27.5 GHz. This distortion can arise from the obstructions caused by the extended height of K-connector used above the antenna ground plane. The measured beam direction is (theta, phi) (75°, 105°), (97°, 104°), (112°, 70°), (75°, 75°), and measured side lobe level are -13.4 dB, -16 dB, -14 dB, -15.1 dB when fed from ports *P1* - *P4* at 26.5 GHz. The final array prototype was fabricated in the multi-layer fabrication process. Misalignment errors between BFN layer and array layer result in increased side lobe levels. Also, measured side-lobe levels are affected by the *K*-connector used for the measurement

3.2.6 Array Gain and HPBW

Simulated 2-D contour plot of the HPBW is shown in Figure. 3.10. As described in Section I, each metallic ring antenna provides an ideal gain of 8.3 dBi and theoretical directivity of 2×2 array would be 14.3 dBi. The measured gain is calculated as 11.9 dBi, 12.1 dBi, 12.9 dBi, 12.9 dBi, and measured radiation efficiency is calculated as 57.5%, 60%, 72.4 % and 72.4 % for ports P1, P2, P3 and P4 at 26.5 GHz. Various losses that are accounted for the calculation of radiation

efficiency are summarized in Table 4. The measured HPBW is approximately 39°, 30°, 38° and 28° in H-plane for ports P1, P2, P3 and P4, respectively at 26.5 GHz. The gain increases with frequency due to a larger electrical length of antenna at higher frequency and gain variation is less than 1 dB over the operating bandwidth from 25 GHz to 28 GHz. An array physical size without considering the input port lengths is 17mm×17mm×2.54mm. Aperture efficiency is calculated as 54.6 %, 57.19 %, 68.76 % and 68.76 % for ports P1, P2, P3 and P4 at 26.5 GHz.

Table 4 Summary of losses for 2 × 2 ACARA

Loss type	Transmission loss (dB)	Multiplication Factor (×n)
One Coupler (x n = 3)	0.100	0.30
One vertical coupling slot (x n = 4)	0.100	0.40
One bend (x n = 4)	0.165	0.66
Conductor, dielectric and radiation	0.500	0.50
GCPW to SIW Transition(x1)	0.300	0.30
Input Connector Loss (x1)	0.200	0.20
Total		2.36

3.2.7 Beam squint effect

The parallel feeding topology of the proposed BFN has little or no effect on beam squint. As shown in Figure. 3.8, measured beam squint is less than 3° because squint introduced by an array in one direction is cancelled by the element in the opposite direction. The measurements have confirmed that the array can produce four clearly defined fixed, wide beamforming states. A usable bandwidth of the array is 7.6% at the operating frequency.

Table 5 Performance highlights of high-efficiency 2-D scan antenna array system

Feature	Specification
Frequency band	25.5 GHz – 27.5 GHz
Operating Frequency	26.5 GHz
Polarization	Single linear
Total number of Elements	4

Gain at 20° scan angle	12 dBi
Side lobe levels (with respect to main lobe and no grating lobes)	≤ -13 dB
Aperture efficiency	68.7%
Number of beamforming states	4
Total number of simultaneous independent beams	1
Number of inputs	4
Beam pointing error	5°
Phase shifter type and technology	Inexpensive passive and substrate integrated
Insertion loss of phase shifter	1.26 dB
Input connector	*K*
Input matching and coupling coefficients	≤ -12dB
Weight	≤ 0.1 Kg
Physical size	2.86 λ_o × 2.86 λ_o × 0.22 λ_o

Table 6 Comparison of 2D scan Antenna Systems

Parameter	Reference		
	[11]	[12]	This work
Feed network technology	Microstrip	SIW	SIW
Operating frequency	60 GHz	30 GHz	26.5 GHz

3.2.8 Conclusion

In this chapter, 2-D scan 2 × 2 planar array fed by an eight port hybrid BFN for four independent orthogonal beams is proposed, studied, fabricated and validated. The measured results confirm that the concept of SIW technology has brought superb benefits to 2-D steering antenna systems including light weight, high integration profile into mm-wave system-in-package, low radiation loss and cost effective design. Table 5 summarizes the key performance parameters of the proposed passive 2-D scan antenna array system. The BFN is highly compact and it occupies the same size as antenna array grid. As given in Table 6, proposed BFN performance is compared to the other reported 2-D scan antenna systems.

Measured aperture efficiency up to 68% is obtained with the SIW technology. The conductor, dielectric and metallic losses of the dielectric substrate will cause significant RF loss inside SIW BFN, hence the radiation efficiency and gain are reduced. The selection of low loss substrate will make the proposed scanning array system highly efficient. The antenna GCPW to SIW transition for the BFN allows measuring through a K-connector as an interface. The proposed 2 × 2 planar array can effectively scan in four quadrants with four independent orthogonal beams.

CHAPTER 4 MILLI-METER WAVE ANTENNA DESIGN WITH CIRCULAR POLARIZATION DIVERSITY

In this chapter, circularly polarized (CP) antenna array is proposed and validated in SIW technology. The 2-D scan phased array antenna proposed in chapter 3, is useful for linearly polarized antenna front end systems. To further enhance data handling capability, circularly polarized 2-D scan phased array system is proposed and demonstrated at 60 GHz frequency. At first, fixed beam radiating CP antenna array is demonstrated and then phase shifting network is integrated under the radiating aperture to steer the CP beam electronically in elevation and azimuth scan regions. The dual circularly polarized antenna element is also demonstrated in this chapter.

4.1 60 GHz Circularly Polarized Antenna Array Made in Low-Cost Fabrication Process

Various SIW feeding microstrip antenna arrays have been well documented in [99]-[102]. At 60 GHz, high performance antennas with excellent CP purity fabricated in low temperature co-fired ceramic (LTCC) technology were reported in [103]-[104]. For certain applications, antennas developed in low-cost printed circuit board (PCB) technology will be useful for single substrate integration. A CP antenna with 4.0 % of 3-dB axial ratio (AR) bandwidth was described in [105]. The reported two layered prototype consists of a dielectric resonator antenna (DRA) on the top layer and cross-slot on the bottom layer. However, narrow band nature of slots limiting the operating bandwidth of the antenna.

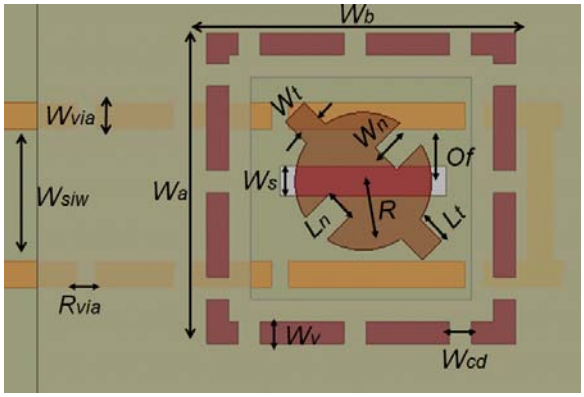

(a)

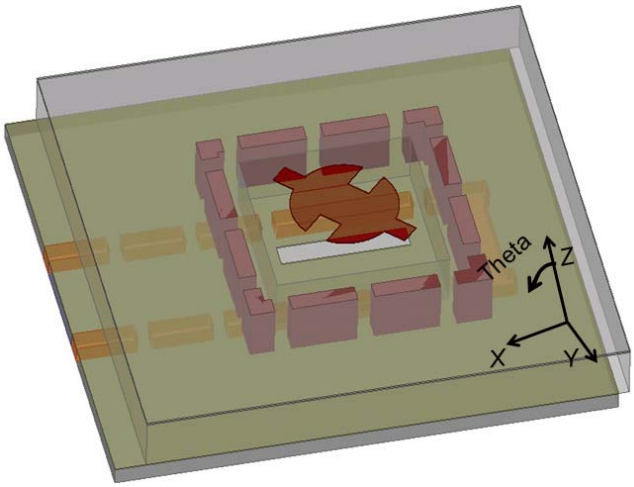

(b)

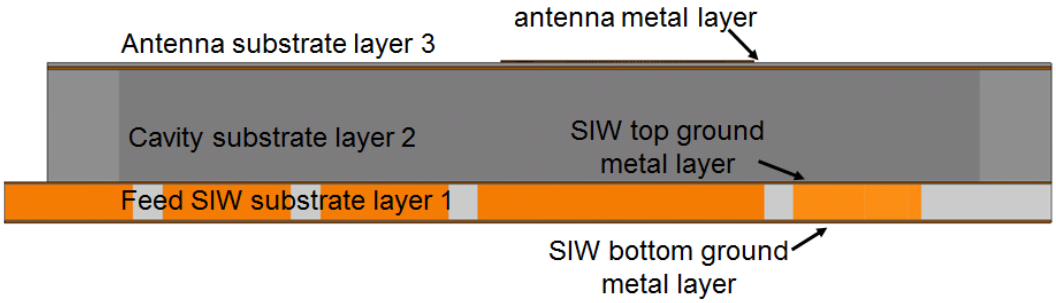

(c)

Figure. 4.1. CP antenna. (a) Top view, (b) exploded view and (c) cross section view. Where the parameter dimensions in mm are W_{via}= 0.25, R_{via}= 0.25, *Wa*=3.5, *Wb*=3.5 *Wv*=0.25, *Wcd*=0.3, *Wt*=0.3, *Lt*=0.375, *Wn*=0.4, *Ln*= 0.4, *R*=0.75, *Of*=0.49, *Ws*=0.33, *Ls*=1.9, and *Wsiw*=1.37.

At 60 GHz frequency, non-planar, 3-D architecture of 4 × 4 LP antenna array was proposed in [107]. In this work, a compact high efficiency CP antenna is proposed and fabricated in low-cost SIW technology. Simple aperture coupling method is used to excite each CP antenna and the array is isolated from its feeding network.

4.1.1 RHCP antenna Element

Radiating element performance at 60 GHz frequency range depends on the selection of feeding topology. In this work, metallic patch is selected as a radiating element and SIW is chosen as the feeding transmission line.

4.1.1.1 CP antenna architecture

As shown in Figure. 4.1, proposed antenna is stacked in three layers. SIW transmission line is drilled on layer 1, where a longitudinal slot with width *Ws* and length *Ls* is etched on the top ground plane. The slot is offset (*Of*) from the edge wall and three quarter wave lengths from the end wall. Layer 1 is on Rogers's 3006 substrate with $0.0508\lambda_o$ thickness. The slot position is optimized to match the input impedance of the antenna. Electric fields inside the slot are coupled to the patch antenna. The slot has a symmetric electric field distribution and is easy to characterize when compared to via fed patch. Layer 2 is on Rogers's 6002 substrate with 0.127λo thickness. Square cavity constructed with metallized vias is placed between layers 1 and 3. Substrate inside the cavity area is removed to have air space between slot and patch. Layer 3 is on Rogers's Ultralam substrate with 0.00508λo thickness. Radiating CP patch is integrated on layer 3. A thin antenna layer is selected to suppress a potential surface wave excitation in the radiating layer. As an initial step, a linearly polarized patch with radius R is optimized at 60 GHz. The patch is aperture-coupled through a slot etched on layer 1.

4.1.1.2 Antenna radiation performance

Notches with length *Ln* and width *Wn* are inserted on the circumference of the patch to create the CP mode. The AR bandwidth is further improved by adding two tuning stubs orthogonal to the notches. The variation of AR for three different values of tuning stub length Lt

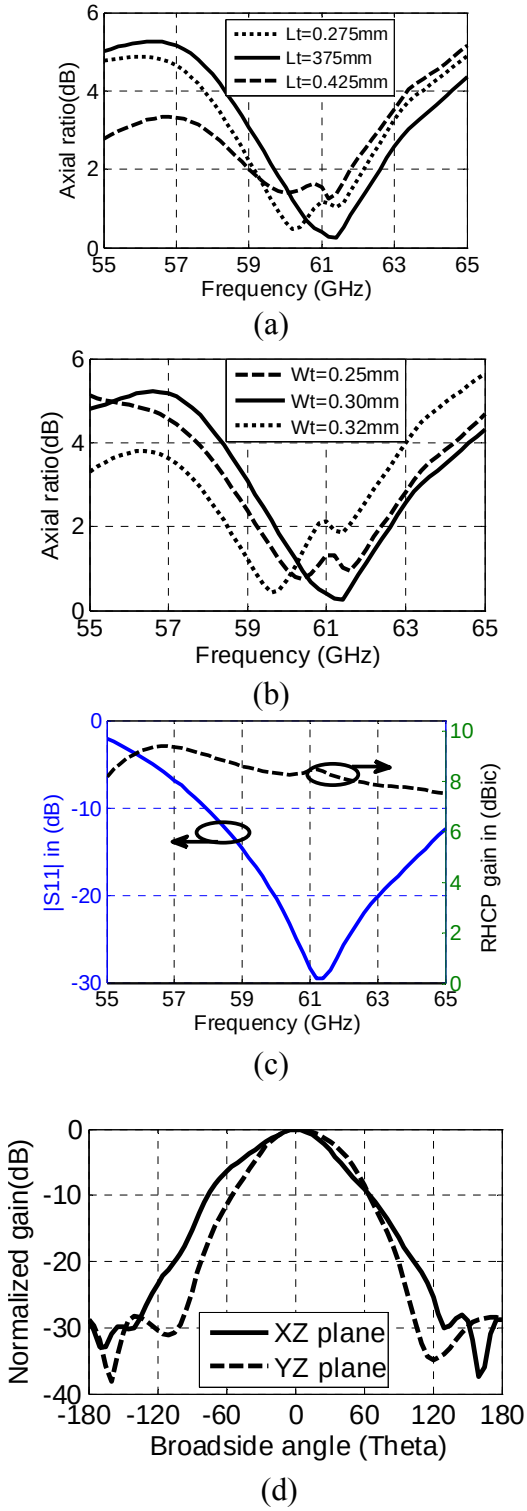

Figure. 4.2. Axial ratio as a function of frequency for different values of tuning stub (a) length, and (b) width, (c) magnitude of S11 and peak RHCP gain, and (d) antenna radiation pattern in standard cut at 60 GHz.

and width *Wt* is plotted in Figure. 4.2(a) and (b). The AR bandwidth of 6.6% is maximized at 60 GHz for Lt =0.375 mm and *Wt* =0.3 mm. Antenna input matching and RHCP gain as a function of frequency is plotted in Figure. 4.2(c). Antenna 2:1 VSWR bandwidth covers the frequency range from 57 GHz to 64 GHz. Average RHCP peak gain is 7.8 dBc with peak to peak gain variation that is less than 0.3 dB over the operating bandwidth from 57 GHz to 64. The antenna gain is almost constant and maximum gain direction varies from -2^o to +2^o over 58 - 62 GHz. Simulated radiation efficiency is over 95% in the entire frequency band. Co-polarized wide-beam radiation pattern in *XZ*-plane and *YZ*-plane is plotted in Figure. 4.2(d). Antenna physical size is 0.45λo × 0.7λo × 0.182λo. The RHCP antenna is used to implement 2 × 2 antenna array. The proposed the circular polarized radiating element has high aperture and radiation efficiency at 60 GHz frequency band. The small foot print allows designing a high performance phased array antenna for V-band frequency range.

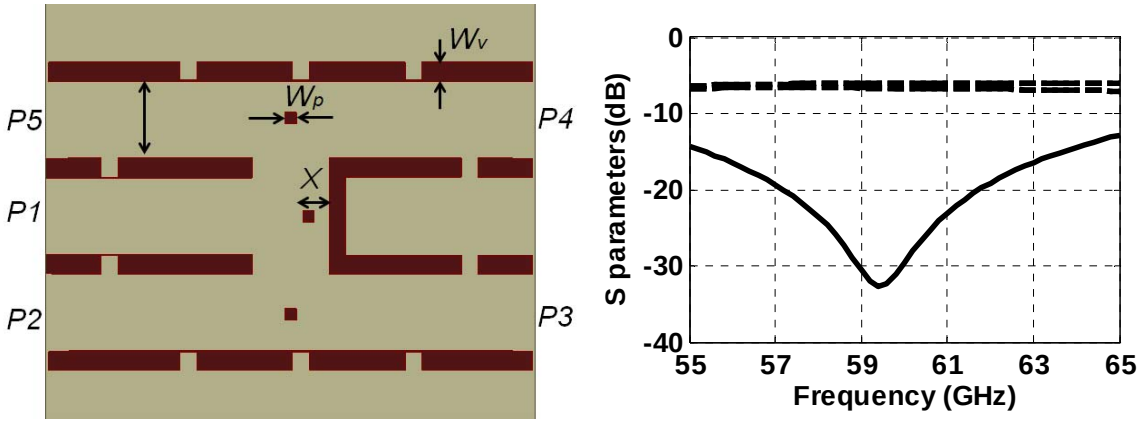

(a) (b)

Figure. 4.3. (a) Power dividing network for 2 × 2 patch array, (where W_p=0.25mm, W_v=0.27mm, *X*=0.3mm, *P*= port number), (b) S-parameters as a function of frequency (solid line: |S11|).

4.1.2 RHCP array

4.1.2.1 Array construction

SIW feeding mechanism is used to supply the required amplitude and phase distribution for an antenna array. The SIW power divider and physical parameters obtained in the simulation

are given in Figure. 4.3(a). When fed from port *P1*, the power is distributed uniformly among all the output ports *P2-P5*. Also, all the output ports are fed in phase, to obtain maximum

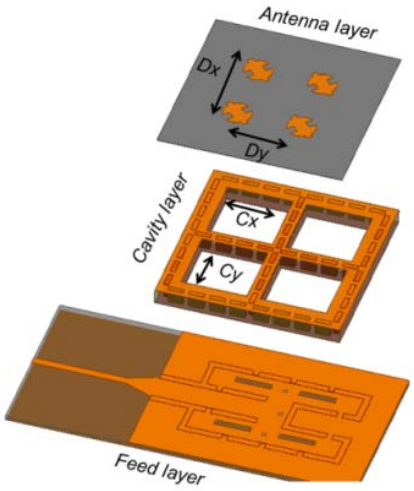

(a)

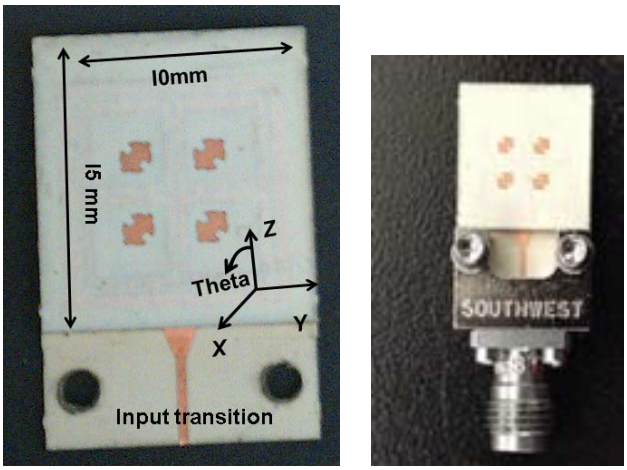

(b)

Figure. 4.4. RHCP array. (a) Three dimensional view, and (b) experimental prototype top view and with end launch connector.

peak gain. The exploded view of the antenna array is shown in Figure. 4.4(a). The metallic walls of the SIW are integrated on the feed layer 1. Four slots were etched on the top ground plane and also SIW to microstrip transition is used at the input port. An air cavity with metallic vias is integrated under each antenna element. The mutual coupling between antenna elements is

reduced, and hence gain is further enhanced in an array environment. The top most layer is antenna layer, where all the antenna elements are integrated on ultrathin substrate.

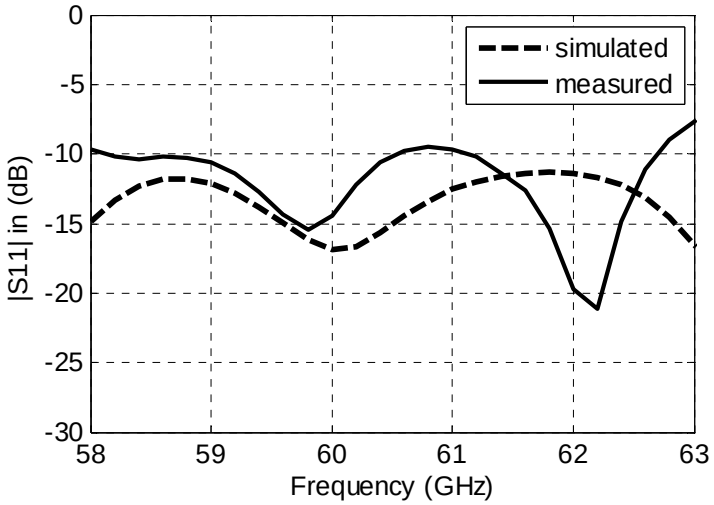

(a)

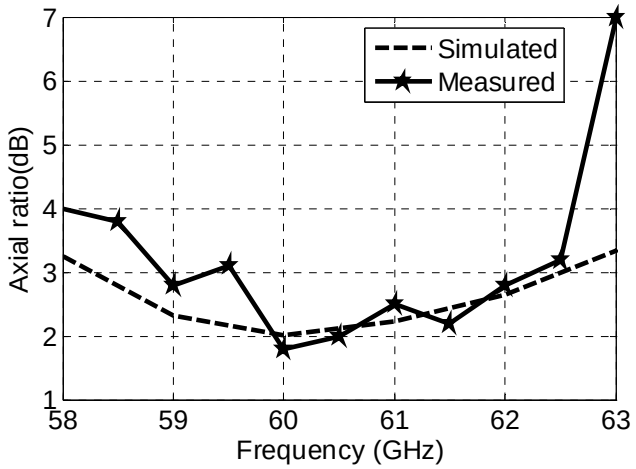

(b)

Figure. 4.5. Simulated and experimental prototype of (a) 2 × 2 patch array, (b) input matching as a function of frequency, and (c) axial ratio as a function of frequency.

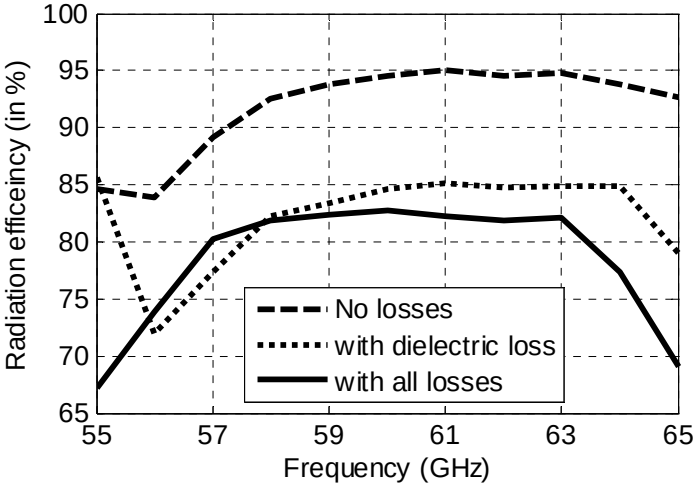

(a)

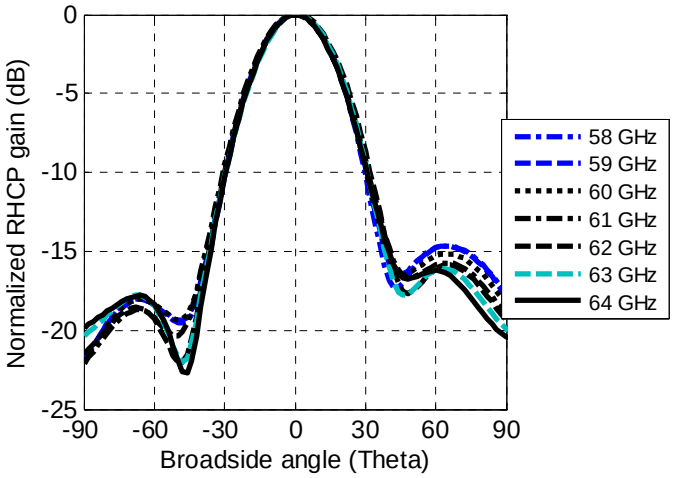

(b)

Figure. 4.6. Simulated (a) radiation efficiency as a function of frequency, and (b) RHCP gain in *XZ*-plane for frequency from 58 GHz to 64 GHz.

The selection of a feed substrate with permittivity of 6.3 allows to space antenna elements close to each other. The distance between antenna elements in *X*- and *Y*- directions is chosen as $D_x = 0.68\ \lambda_o$ and $D_y = 0.694\ \lambda_o$, respectively. The feed network printed on a high permittivity dielectric allows the freedom to choose a distance between antenna elements. The optimum spacing between antennas should sum up the individual element patterns to contribute to the maximum total gain.

4.1.2.2 Measured RHCP array performance

The 3 layers are fabricated individually and then glued together to realize the final array. The experimental prototype is shown in Figure. 4.4(b). A simple transition from microstrip to SIW is designed for array measurements. Simulated and measured input reflection coefficient is compared in Figure. 4.5(a). The magnitude of reflection coefficient is less than -10 dB over the 58-62 GHz frequency band. The frequency shift of 0.3 GHz between simulated and measured results is caused by the decrease in the effective width of fabricated SIW transmission line. Simulated and measured axial ratios as a function of frequency are compared in Figure. 4.5(b). The measured AR value is found less than 3.4 dB from 58.6 GHz to 62.7 GHz.

Simulated radiation efficiency as a function of frequency is plotted in Figure. 4.6(a). Copper layer thickness is 17 um and the vias are filled with copper to estimate the metallic loss. Simulated radiation efficiency by considering all loss factors is greater than 82% over the frequency band from 58 GHz to 62 GHz. Substrate losses decrease the antenna efficiency from 95% to 82%. Simulated normalized RHCP peak gain (in *XZ*-plane) as a function of broadside angle is plotted in Figure. 4.6(b). The array has a constant beam direction from 58 GHz to 64 GHz. The peak gain variation is less than 1 dB and the half power beam width (HPBW) variation is observed from 42^{o} to 38^{o}. Beam squint effect that normally occurs in a series feeding array is removed by replacing it with a parallel feeding power dividing network.

Far field radiation pattern is measured in our MI technology compact range anechoic chamber over 57 - 65 GHz with spacing of 0.5 GHz. The RHCP array is placed as a receiver and horn antenna is used as a transmitting antenna. Simulated and measured radiation patterns cut in *XZ* and *YZ* planes are compared in Figure. 4.7. The radiation patterns at three frequency points 59 GHz, 60 GHz and 61 GHz are compared to validate the simulation results. In the *YZ*- plane radiation pattern, added ripples from -90^{o} to -50^{o} stem from the height of the end-launch connector.

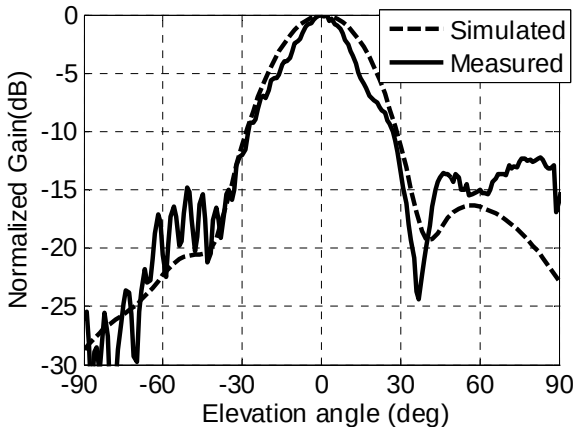
Simulated
Measured
Normalized Gain(dB)
Elevation angle (deg)
0
-5
-10
-15
-20
-25
-30
-90
-60
-30
0
30
60
90

(a)

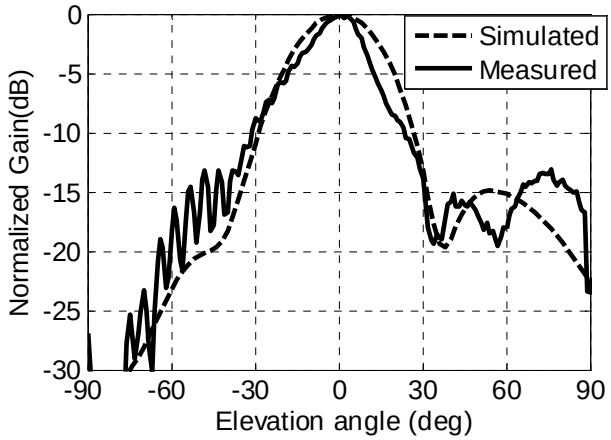
Simulated
Measured
Normalized Gain(dB)
Elevation angle (deg)
0
-5
-10
-15
-20
-25
-30
-90
-60
-30
0
30
60
90

(b)

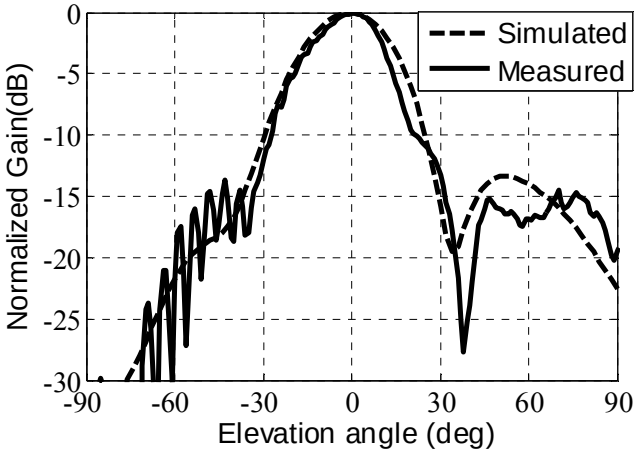
Simulated
Measured
Normalized Gain(dB)
Elevation angle (deg)
0
-5
-10
-15
-20
-25
-30
-90
-60
-30
0
30
60
90

(c)

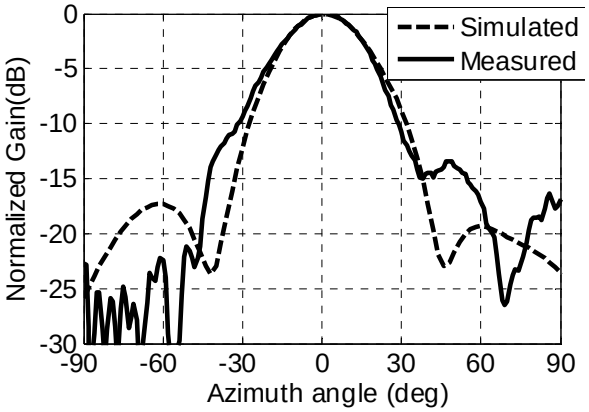

(d)

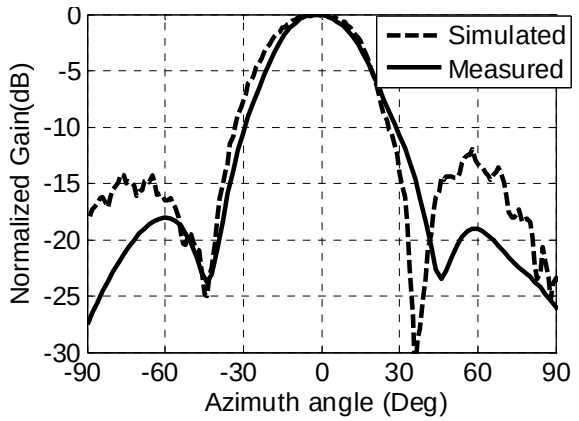

(e)

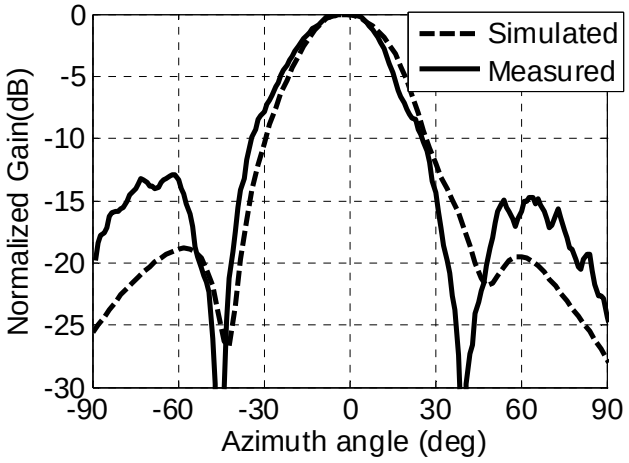

(f)

Figure. 4.7. Simulated and measured co-pol patterns in *XZ*-plane at (a) 59 GHz (b) 60 GHz (c) 61 GHz and in *YZ*-plane at (d) 59 GHz (e) 60 GHz (f) 61 GHz.

Measured RHCP gain is 12 dBic, 12.2 dBic and 12.5 dBic at 59 GHz, 60 GHz and 61 GHz, respectively. Although the gain is slightly lower than expected, both curves match with each other very well. The 1 dB drop in the measured gain is due to the imperfections of the compact range anechoic chamber and unaccounted losses such as surfaces waves, dielectric losses, and connector losses. The total size of the array excluding the input transition is $2\lambda_o \times 3\lambda_o \times 0.182\lambda_o$. Measured HPBW of the array is 42^o, 40^o and 39^o at 58 GHz, 60 GHz and 62 GHz, respectively. Simulated and measured results are in good agreement when beam width, side lobe levels and beam pointing direction are compared. The beam direction is in broadside for all the frequency range. Measured array side lobe levels are lower than -12 dB in both planes. The CP array has good radiation performance over 60 GHz frequency band.

4.2 Dual Circular polarization antenna element

The CP array discussed in the previous section is operating in RHCP mode only. New technique is proposed to radiate RHCP and LHCP with special feeding topology is proposed and validated in SIW technology at 60 GHz frequency.

In this work, SIW fed rod antenna [61] is used as radiating element and E-plane coupler[108] is used as a feeding topology. The DCP antenna is working in left-hand circularly polarized (LHCP) mode and right-hand circularly polarized (RHCP) mode for port 1 and port 2, respectively. First feeding network in 3D architecture is discussed and finally integrated along with dielectric rod antenna. The simulated and measured characteristics of scattering parameters, axial ratio and radiation are discussed in detail. The DCP antenna and feeding network are fabricated on Rogers 3006 substrate (10 mil thickness, $\varepsilon_r = 6.3$, $\tan\delta = 0.0025$).

4.2.1 Antenna element and feeding network design]

In the design DCP element, multi-layer E-plane coupler is used to feed two orthogonally polarized antennas. The physical parameters of the coupler are shown in the Figure. 4.8a. The 3-dB coupler isolation and reflection coefficient magnitudes are lower than -20 dB over the frequency range from 55 GHz to 64 GHz. An unequal length and unequal width zero degree phase shifter shown in the Figure. 4.8b, is integrated at the output ports of the coupler. As a final step,

coupler output ports are loaded with two different vertical interconnects. Side view and back view of the DCP feed network is shown in Figure. 4.8c, d.

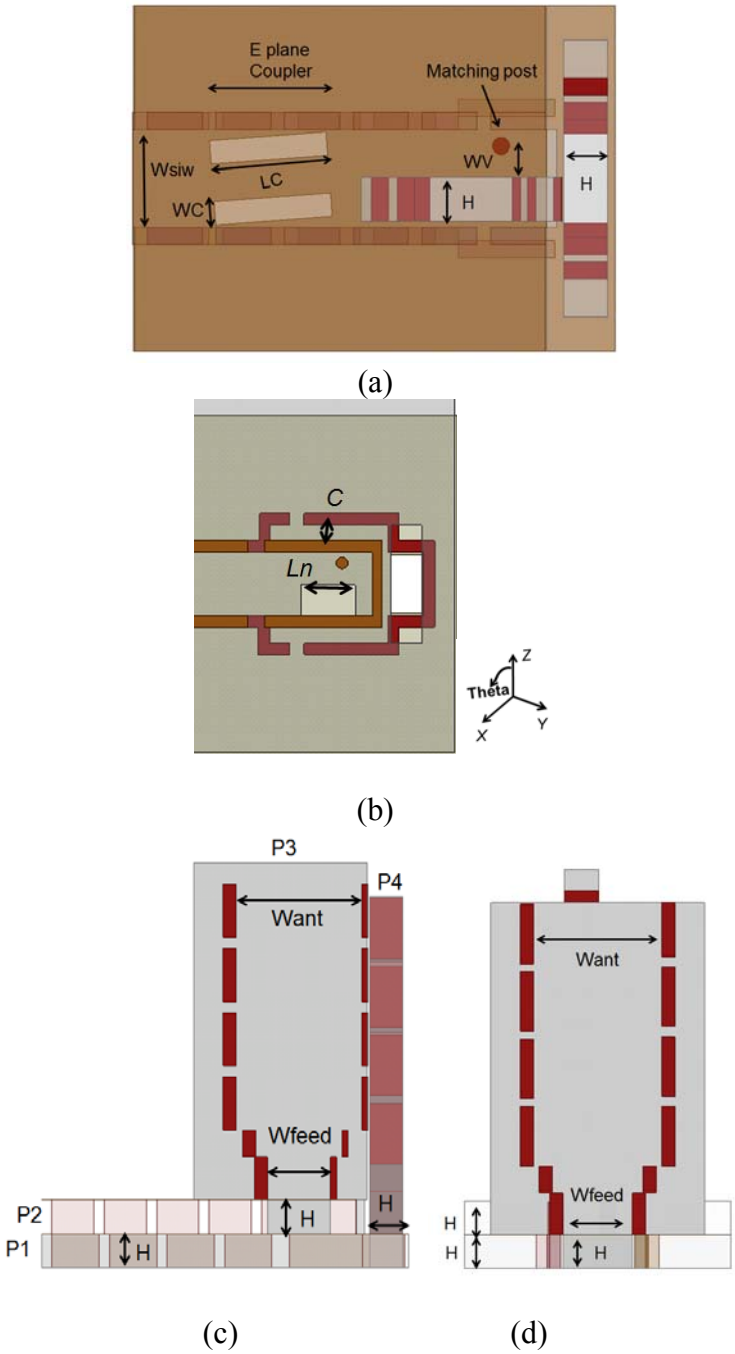

Figure. 4.8. SIW feed network architecture (a) top view with *E*-plane coupler, (b) zero degree phase shifter, (c) side view , and (d) back view,.(where the parameters (in *mm*) are *Ln*=1.2, *C*=0.35, W_{siw}=*1.4*, *WC*=0.34, *LC*=1.7, *H* = 0.635,*WV* =0.45, W_{ant}=2.4, and W_{feed}=1.2).

Simulated amplitude and phase performance as a function of frequency is plotted in Figure. 4.9a,

b. All interconnects are matched from input to output ports, so all the fields are coupled to the output ports. The magnitude of isolation coefficient between input ports and reflection coefficient of the input ports is lower than -13 dB over the desired frequency range. For port *P1*, differential phase shift between output ports varies from 77° to 91° and amplitude coefficient varies between -3.7 dB and -4.1 dB over the frequency range from 57 GHz to 65 GHz. Hence, the condition for circular polarization is satisfied in the proposed feed network.

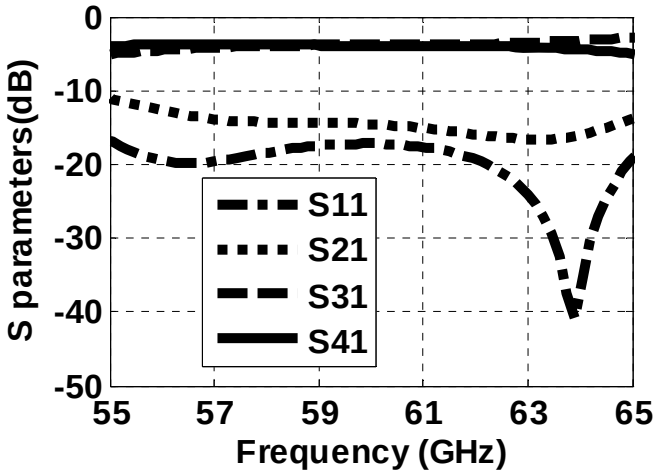

(a)

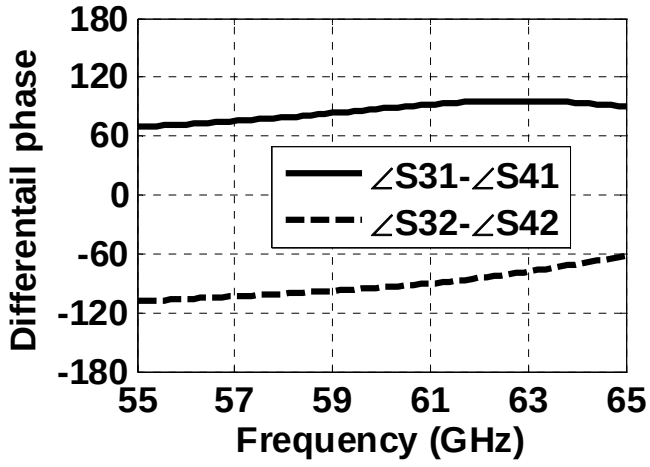

(b)

Figure. 4.9. DCP feed network (a) amplitude, and (b) phase performance.

The feeding network of DCP antenna and final experimental prototype is shown in the Figure. 4.10. Antenna is fabricated in two-steps printed circuit board (PCB) process. In the first step, two layer feed network is fabricated by using a multi-layer fabrication process. In the second step, antennas are fabricated individually and later integrated into the respective slots on the top and bottom layers of the feed network. Antenna feed points are soldered to avoid any significant leakage loss due to air gaps. Two port network S-parameters are measured by using Anritsu vector network analyzer 37397. Measured magnitude of reflection coefficients for both input ports (|S11| and |S22|)) is less than -10 dB and magnitude of isolation coefficient (|S21|) is less than -10 dB from 57 GHz to 63 GHz.

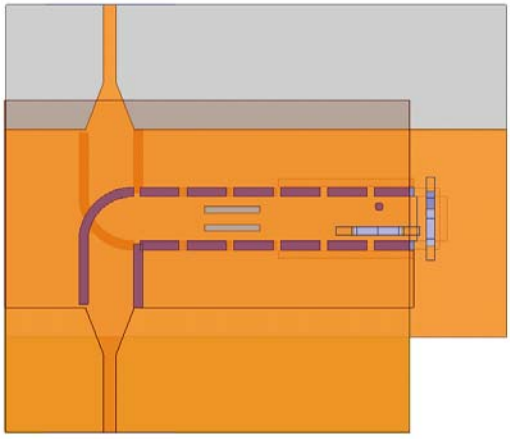

(a)

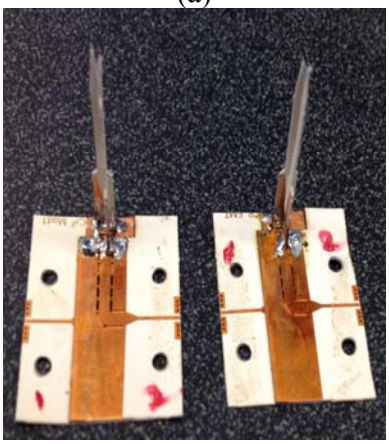

Figure. 4.10. Experimental prototype of the DCP antenna.

4.2.2 Axial ratio performance

When fed from port *P1*, AR as a function of frequency for three elevation angles (*theta*=-5^o, 0^o, +5^o) is shown in Figure. 4.11a. AR value is less than 2 dB from 57 GHz to 63 GHz and minimum at the broadside angle (theta=0^o). For input ports *P1* and *P2,* antenna is radiating in LHCP mode and RHCP mode, respectively. Simulated and measured AR as a function of frequency is compared in Figure. 4.11b. Due to the symmetry of feed network, similar behavior is obtained for *P2* also. Measured AR is less than 4 dB from 58 GHz to 64 GHz for both the input ports *P1* and *P2*. The observed increase in measured AR values is due to the fabrication tolerances introduced by the multi-layer fabrication process. Vias forming SIW side walls are drilled by using a laser micromachining. The laser beam has a fixed diameter of 2 mils, decreases the distance between SIW side walls about 4 mils. An observed shift in measured AR from the simulated counterpart is due to decreased effective width of the fabricated SIW line.

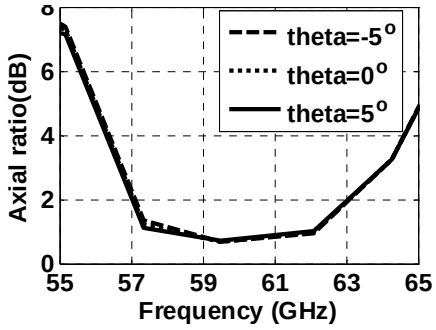

(a)

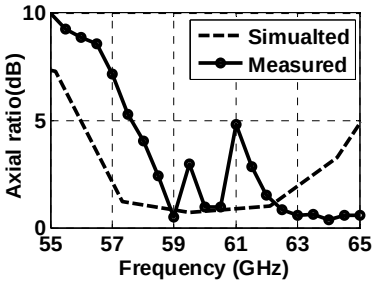

(b)

Figure. 4.11. Axial ratio as a function of frequency (a) for three radiating angles, and (b) in LHCP mode.

4.2.3 DCP element radiation performance

The DCP antenna radiation efficiency is simulated as a function of frequency. For including the metallic loss in the simulation, each copper layer thickness is considered as 17 um and all the vias are filled with copper. Radiation efficiency by considering all the losses is

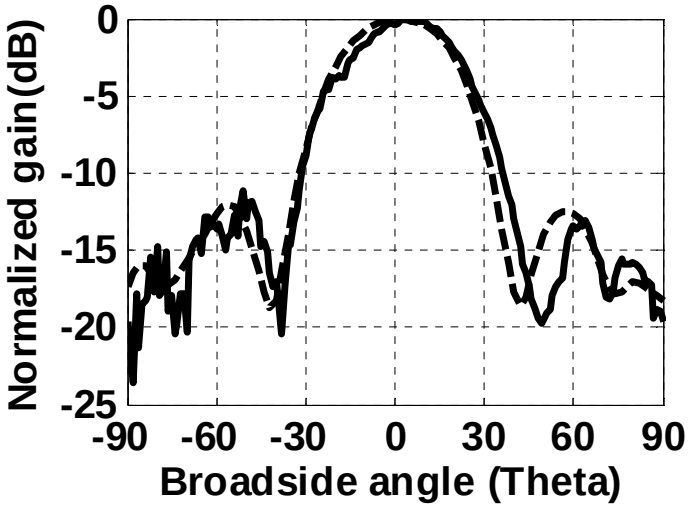

(a)

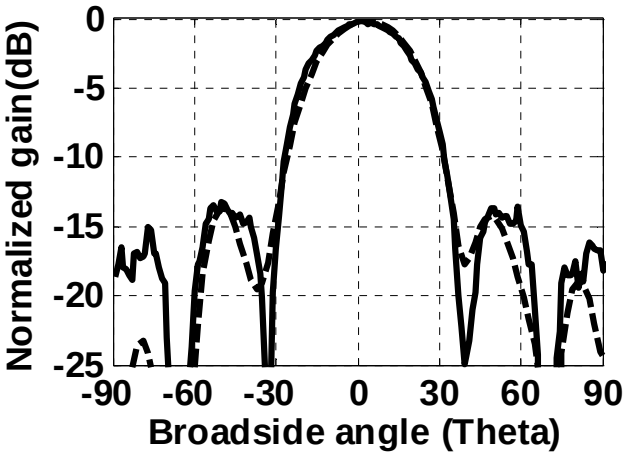

(b)

Figure. 4.12. Antenna LHCP gain at 60 GHz in (a) *xz*-plane, (b) *yz*-plane. Dash line: simulated, solid line: measured.

greater than 72% over the frequency band from 58 GHz to 64 GHz. Dielectric losses of the substrate and metallic losses inside the SIW sidewalls are dominant that reduce antenna efficiency from 95% to 72%. Far field pattern is measured inside our MI technology anechoic chamber in both *XZ* and *YZ*-planes for all the frequency range from 57 GHz to 64 GHz with spacing of 0.5 GHz. At 60 GHz, measured and simulated radiation pattern cuts are compared in Figure. 4.12. Measured beam pattern is overlapped with the corresponding simulated beam pattern.

Measured half-power beam width (HPBW) in both the pattern cuts is 39^{o} with side lobe levels lower than -10 dB for both input ports P1 and P2. Rod antenna inserted on bottom layer is over lengthier by value of 0.635 mm, than the antenna on the top layer. This additional value brings the two antennas to the same level of height. For port *P1*, LHCP antenna gain is measured as 11.5 dBc, 12 dBc and 12.5 dBc for 58 GHz, 60 GHz and 62 GHz, respectively. Measured radiation efficiency is extracted from simulated directivity and measured gain. This value is greater than 75% over the frequency band from 58 GHz to 64 GHz. Symmetry of the feeding network produces similar radiation behavior for ports *P1* and *P2*. Simulated and measured results are well in agreement when beam width, side lobe levels and maximum gain are compared.

4.3 Phase steered circularly polarized radiated beam in 2D scan space

The CP radiating aperture and folded Butler matrix in 3-D configuration are integrated in SIW technology to demonstrate 2-D scan CP phased array antenna.

4.3.1 Beam forming network design

The horizontal and vertical waveguides were connected by using vertical interconnects to build three-dimensional (3-D) antennas and phased array systems [23]. Similar principle is adopted in the design of a vertical interconnect shown in Figure. 4.13a, and used to implement a

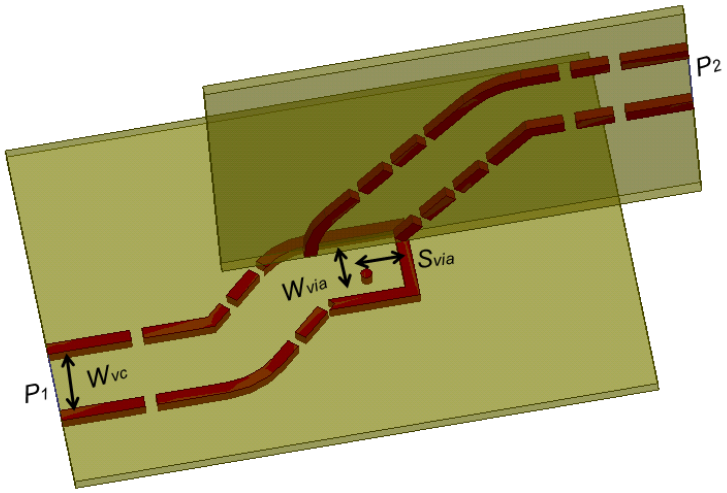

(a)

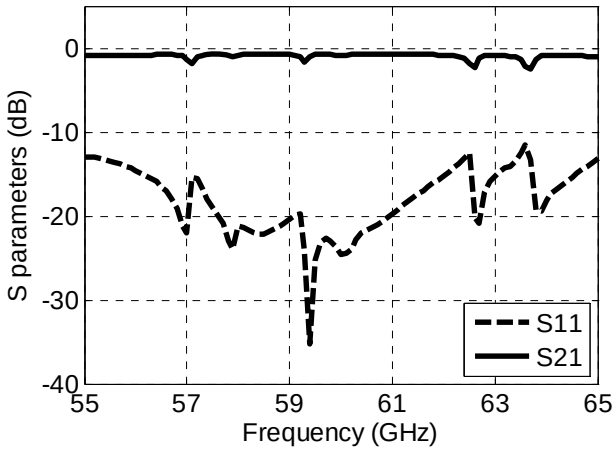

(b)

Figure. 4.13. (a) Proposed vertical interconnect, (W_{vc}=1.7mm, S_{via}=0.92mm, W_{via}=2.3mm), (b) frequency response,

space saving feeding network. The S-parameters as a function of frequency are shown in Figure. 4.13b. Magnitude of transmission coefficient (|S21|) is found to be greater than -1 dB and magnitude of reflection coefficient (|S11|) is less than -20 dB over the frequency band from 57 GHz to 64 GHz. The metallic post placed on the feeding transmission line improves the matching performance of the vertical interconnect.

The vertical interconnect is used as a basic building block to implement eight port phase shifting network. The cruciform coupler proposed in [24] is used as main coupling unit to implement the BFN. Figure. 4.14a, b depicts the proposed three-dimensional Beam forming network. When fed from port *P1* on the feed guide, field is smoothly coupled to the vertical

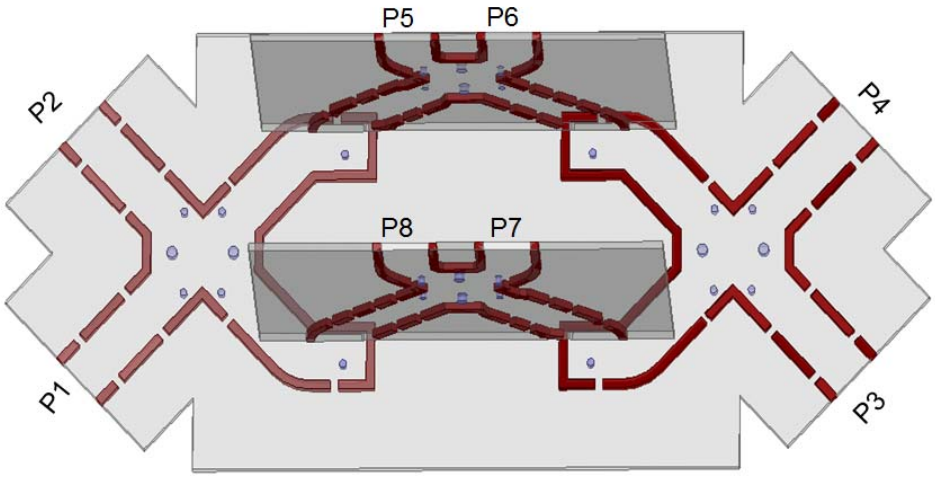

(a)

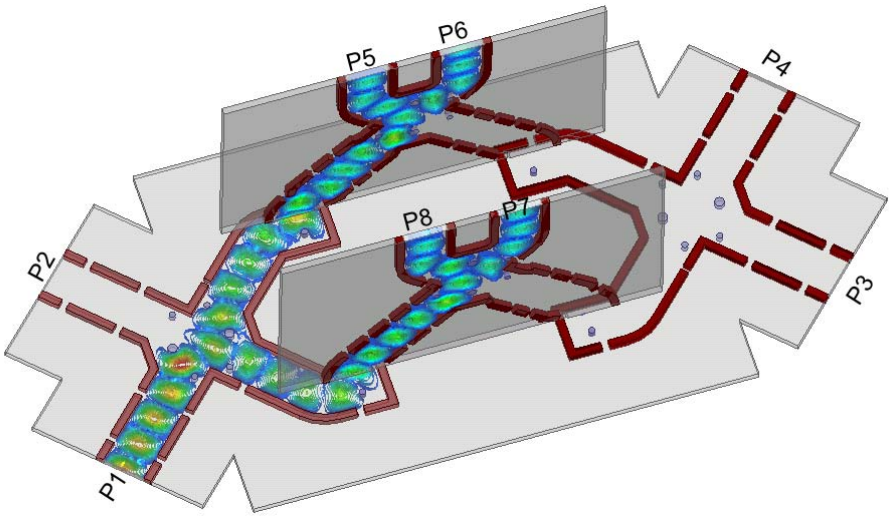

(b)

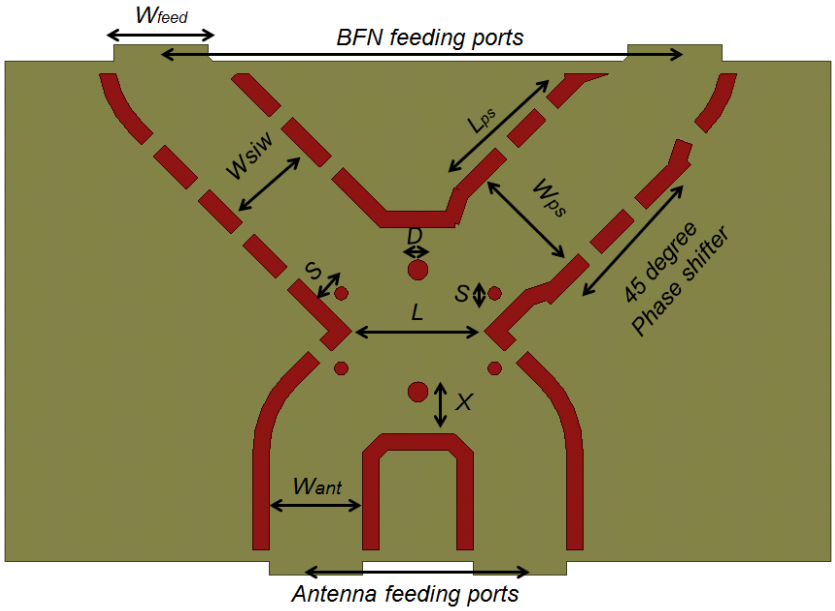

(c)

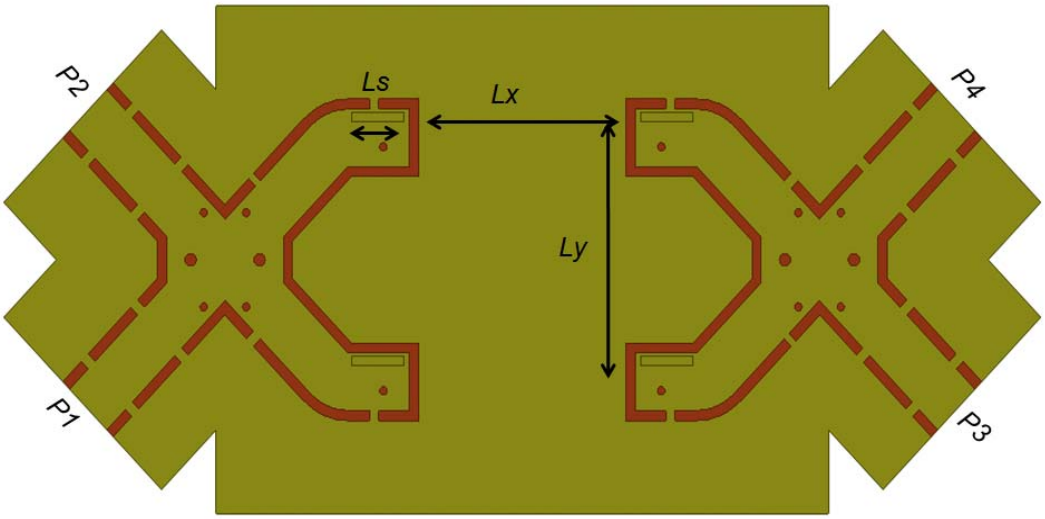

(d)

Figure. 4.14. (a) BFN 3-D architecture, (b) BFN field distribution inside the integrated waveguide topology when fed from port 1, BFN (c) vertical guide part (where W_{siw}=1.7 W_{feed}=1.7, W_{ant}= 1.7, S= 0.76,D=0.4, L=2.4, X=0.76, L_{ps}=2.1, W_{ps}=2.1, where all dimensions are in mm), and (d) horizontal guide part , (L_s=1.7,L_x=7.2,L_y=7.2, P=port number where all dimensions are in mm).

guide and uniformly distributed to the output ports with 45º phase gradient. Similar performance behavior is expected for remaining 2 ports, because of the symmetry of BFN. Butler matrix operation principle is obtained with four cruciform couplers and two 45º fixed phase shifters. The Butler matrix special topology is chosen to obtain scanned beams in the azimuth and elevation planes. The eight port network is modified to feed the planar array and to obtain beams in the two-dimensional scan space. The matrix is folded to reduce the size in the azimuth plane and also to feed the elements ports directly. Two directional couplers are located

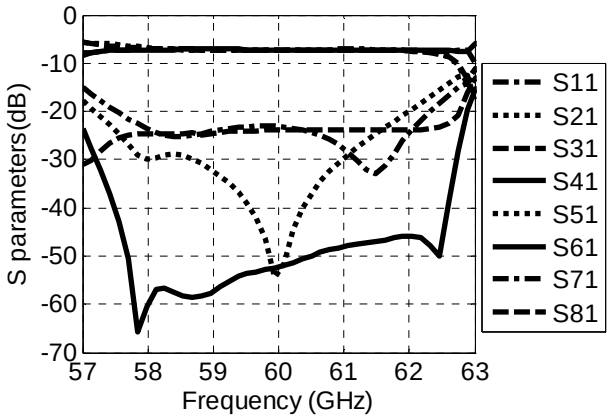

(a)

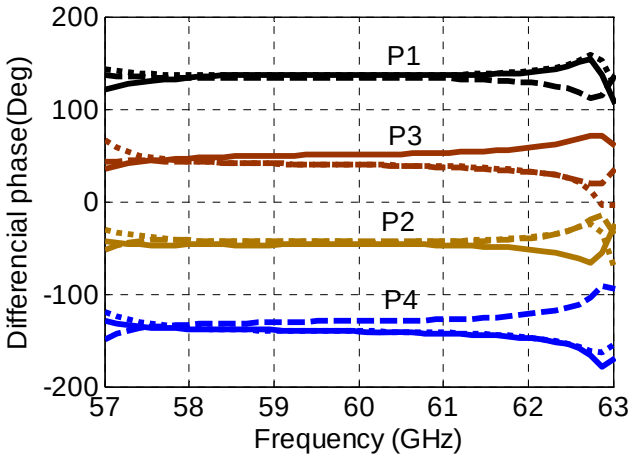

(b)

Figure. 4.15. BFN (a) amplitude performance and (b) phase gradient as a function of frequency, (solid $\angle S6p - \angle S5p$, dot $\angle S7p - \angle S6p$, dash $\angle S8p - \angle S7p$,where p=1, 2, 3 and 4,

on the feed guide and two couplers are on the vertical guide. As shown in Figure. 4.14c, 45º phase shifter is integrated on the vertical guide along the two branches of a coupler. Phase dispersion is reduced by using unequal length and unequal width phase shifter. The four input ports are located on the feed waveguide as shown in Figure. 4.14d.

The amplitude and phase performances of the BFN are shown in Figure. 4.15a, b. When fed from port *P1*, magnitude of transmission coefficients (|S51, |S61|, |S71 and |S81||) are less than -6.5 dB over the frequency band from 58 GHz to 62 GHz. The phase difference between the output ports is 135º, -45º, 45º, and -135º for four input ports *P1* to *P4*, respectively. The phase dispersion is less than 10º over the frequency band from 58 GHz to 62 GHz.

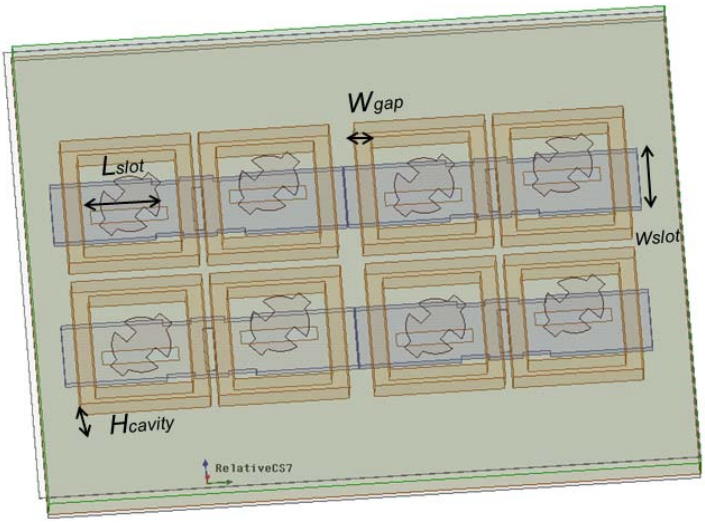

(a)

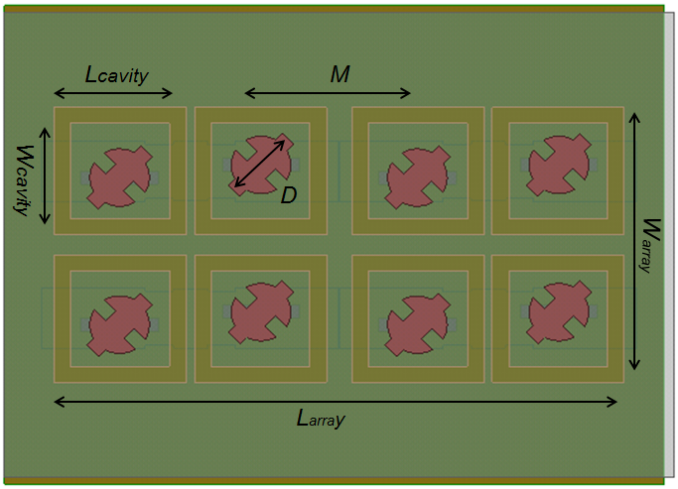

(b)

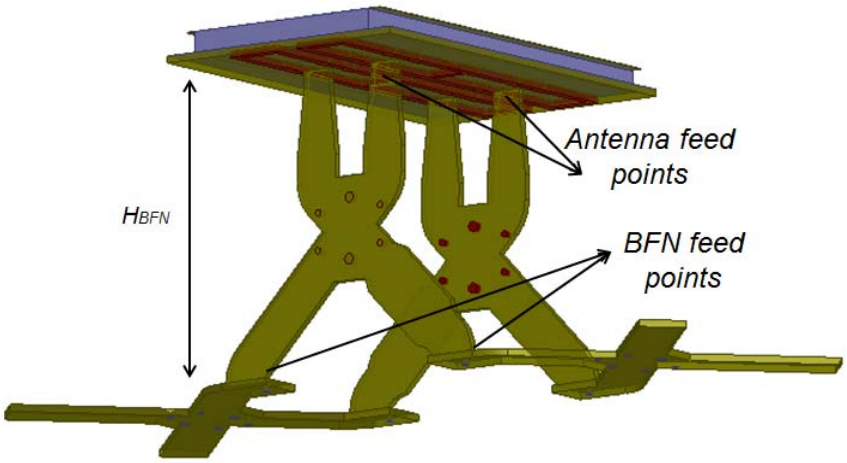

(c)

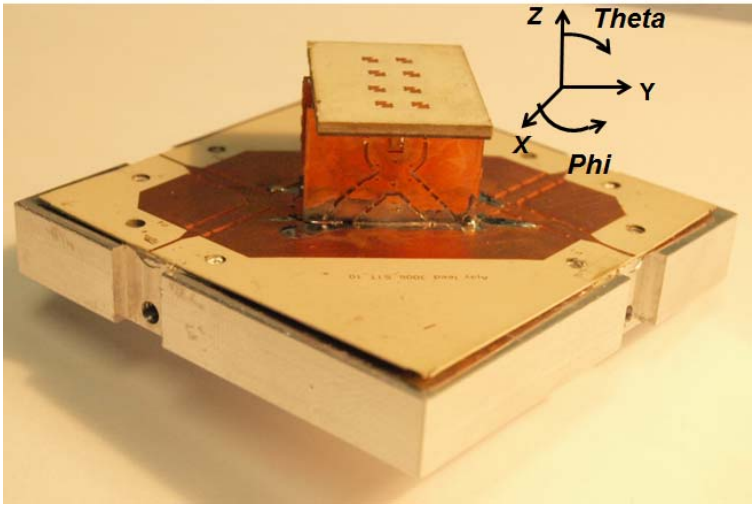

(d)

Figure. 4.16. Antenna array (a) transparent view, (b) top view, and phased array antenna (where W_{gap}=0.3, L_{slot}=1.87, W_{slot}= 1.52, H_{cavity}= 0.635, W_{cavity}= 2.9, L_{cavity}= 2.8, W_{array}= 8.6, D=1.84, M=4.1, L_{array}=15, and H_{BFN}=11 , where all dimensions are in mm), (c) simulated prototype, (d) experimental prototype.

4.3.2 Antenna array design

It is well-known that microstrip patch antennas are suitable for implementing compact and light weight phased array antennas. The antenna printed on dielectric substrate is suitable for mass production and can be integrated with any feeding network. Excitation of patch antenna is very critical at millimeter-wave frequency to reduce the radiation leakage and also to obtain good cross-polarization characteristics. In this work, an aperture coupling method is used for the

excitation and slot antenna is used as an excitation source to obtain good cross-polarization characteristics.

A circularly polarized radiating element is chosen to construct a radiating aperture [106]. Antenna has unidirectional radiation pattern characteristics and right hand circularly polarized (RHCP) gain of 7.5 dBc. The radiated beam direction is constant over the frequency band from

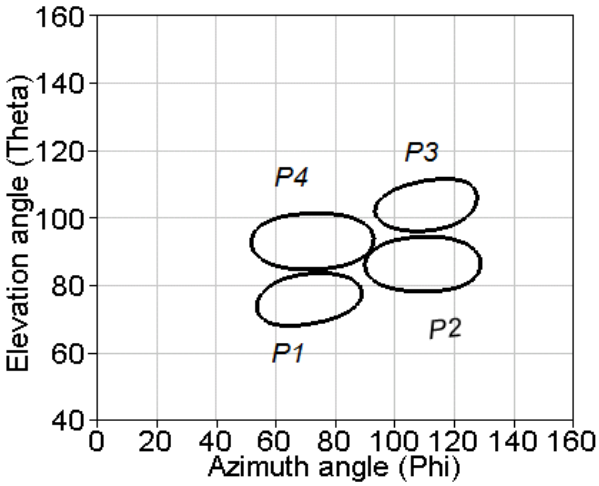

Figure. 4.17. Simulated HPBW for 2-D scan phased array antenna.

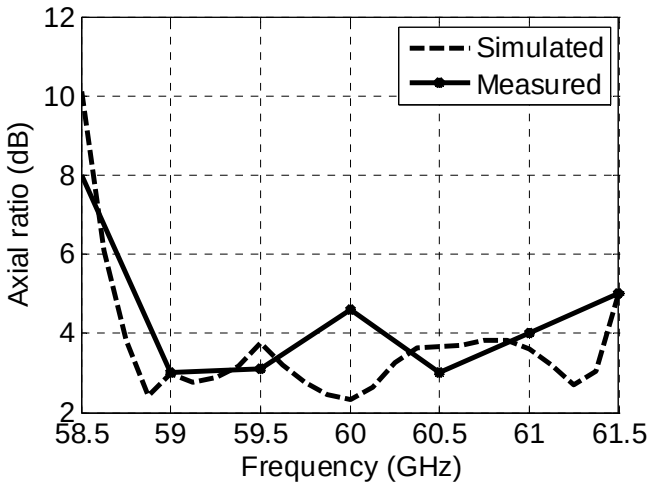

Figure. 4.18. Comparison between simulated and measured axial ratio as a function of frequency.

58 GHz to 62 GHz. As illustrated in Figure. 4.16, CP element is used to construct a three layered antenna array. Feeding layer (Rogers 3006 with $\varepsilon_r = 6.3$, 10 mil thickness) is an SIW transmission line where excitation slots are etched, the second layer (Rogers 5880 with $\varepsilon_r = 2.2$, 31 mil thickness) acts as an SIW cavity and air-gap, the third layer (Rogers 3850 with $\varepsilon_r=2.9$, 1 mil thickness) is antenna layer. The top and bottom metallic planes are connected through metallic filled vias, so that the antenna does not experience any back lobe radiation. The metallic cavities synthesized on the second layer are able to enhance the gain of antenna by suppressing higher order surface modes in the structure. The metallic walls are suppressing unwanted surface modes and also decreasing the mutual coupling between adjacent antenna elements. Each slot is etched at a distance of one quarter wavelength from the edge of a short circuited SIW line, so that maximum source excitation is obtained in the feeding network. Circularly polarized antenna impedance is matched to cover the frequency band from 58 GHz to 62 GHz. The spacing between antenna elements in *X*- and *Y*-directions is fixed at 0.7λ and 0.8λ, respectively. The radiating aperture is RHCP array with a simulated broadside gain of 13 dBc over the designed frequency band. Simulated HPBW plotted in Figure. 4.17, has four clearly defined beam forming directions in the 2-D scan space. When the input port is switched from port *P1* to *P4,* the outgoing beam direction is moving in the azimuth and elevation directions.

4.3.3 Measured phased array performance

The phased array prototype shown in Figure. 4.16d, is fabricated in two steps. In the first step, BFN parts are fabricated individually (Rogers 3006 with $\varepsilon_r = 6.3$, 10 mil thickness) and then vertical guide feed sections are inserted into the slots drilled along the horizontal guide. In the second step, the three layer antenna array is fabricated by using a multi-layer fabrication process and then the BFN output ports are inserted into the slots made on the SIW feeding layer of antenna array. 2-D scan phased array impedance and radiation pattern characteristics are measured by using four V-band connectors. Array impedance is matched in the scanned beam direction over the frequency range from 58 GHz to 62 GHz. Antenna far-field radiation pattern characteristics are measured in our compact range MI technology reverberation chamber and a linearly polarized V-band horn antenna is used as a radiating source.

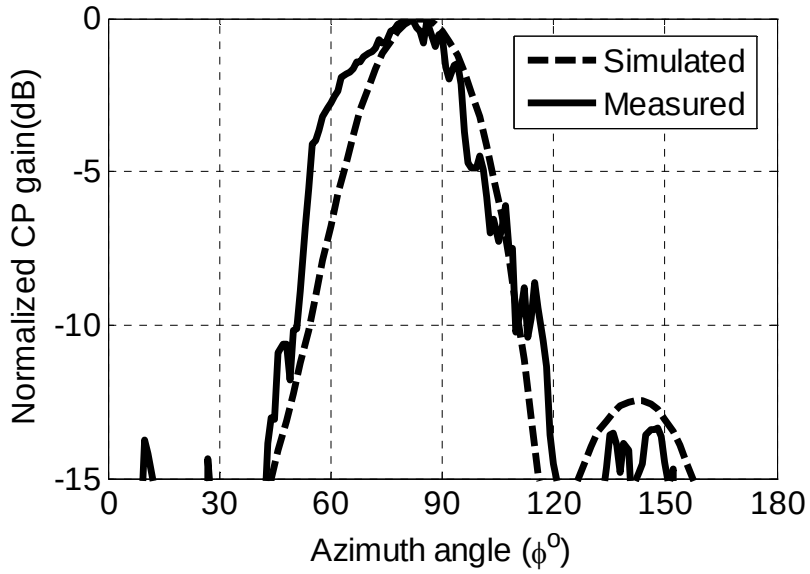

(a)

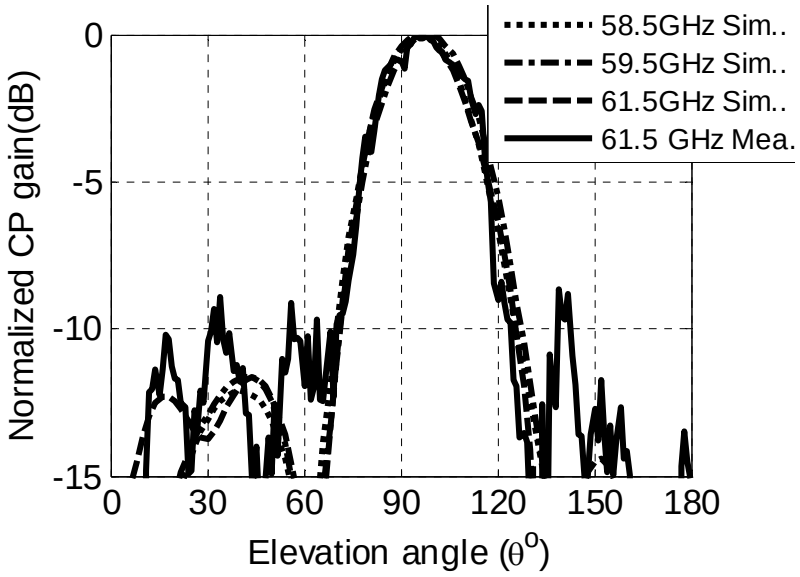

(b)

Figure. 4.19. 2-D scan phased array performance at 60 GHz frequency for (a) port 1 in azimuth plane (b) port 4 in elevation plane.

Figure. 4.19 plots the measured radiation pattern as a function of the azimuth angle (phi). For port 1 to port 4, the maximum gain is measured at an angle of ((phi, theta)) (70°, 75°), (70°, 95°),

(110°, 80°) and (110°, 100°). The simulated and measured beam patterns are compared and a good agreement is obtained for different frequency points. Each directive beam maximum gain is extracted after the calibration with two standard horn antennas. Axial ratio values are extracted from difference gain values of the azimuth and elevation gain patterns. As compared to Figure. 4.18, the measured axial ratio is less than 4.5 dB over the bandwidth from 58.8 GHz to 61.5 GHz for port P1. The measured axial ratio was extracted from the difference of amplitude received with the horizontal and vertical polarizations. The measured axial ratio values were higher than the simulated values, mainly because of fabrication tolerances and slight misalignment effects in the anechoic chamber. The antenna has a wide azimuth plane HPBW of 38º and a narrow elevation plane HPBW of 18º because the array construction is a rectangular planar array. The BFN phase and amplitude distributions are uniform over the frequency band and the measured side lobe levels (SLL) are -8 dB lower than the maximum beam in the scanned direction. As frequency increases, phase dispersion introduced in the BFN increases and subsequently SLL increases. The right-hand circularly polarized phased array peak gain is measured as 12.8 dBc for input ports over the frequency range from 58.5 GHz to 61.5 GHz. The maximum measured beam pointing error is 5º for edge scanned beams. The fabrication tolerances introduced by the laser perforating machine deviates the outgoing beam direction from the expected beam direction.

4.3.4 CONCLUSION

In this chapter, unlicensed frequency range from 57 GHz to 64 GHz was chosen to design single circular polarization, dual circular polarization and single circularly polarized phased array antenna systems.

In this chapter, quasi-planar array makes use of an SIW technology has been in the investigated. The array has compact size, high radiation efficiency and good radiation pattern performance. Integrated SIW cavity excites each patch with maximum radiation and also reduces the mutual coupling of antenna elements. The 2 × 2 planar array can be used as sub-array in the design of a high gain CP antenna array at 60 GHz frequency band and other millimeter-wave bands.

Furthermore, new technique was proposed to obtain DCP mode at 60 GHz frequency range. The gain enhancement is achieved without increasing any feed network size. The DCP antenna compact architecture allows designing higher order antenna arrays.

Finally, a circularly polarized phased array with 2-D scanning techniques are introduced and experimentally characterized over the 60 GHz frequency range.. The 2-D scan RHCP phase array antenna implemented by using 2 × 4 antenna array and folded Butler matrix. The feed network size in the azimuth plane is reduced by using a vertical interconnect and folded in half to feed planar array. The physical size is $6\lambda \times 3\lambda \times 2.2\lambda$ each phase steered CP beam has gain of 12 dBc. The single polarized (RHCP) phased array performance can be extended to dual polarized (LHCP and RHCP) phased array by using the folded BFN concept.

CHAPTER 5 PHASED ARRAY ANTENNA DESIGN WITH TWO DIMENSIONAL SCAN CAPABILITY

In this chapter, 2-D scan phased array antenna utilizing phase and frequency scanning is proposed to obtain multiple scanned beams in limited and wide scan region. At first, 2-D scan conformal phase fed frequency scan antenna system is proposed to cover limited scan region in elevation and in azimuth direction respectively. In the second prototype, Butler matrix based phase shifting network is chosen to cover 320^{o} scan region in azimuth and 20^{o} scan region in elevation respectively.

5.1 Conformal Multi-Beam Integrated Waveguide Array Antenna with Two-Dimensional Scanning Capability

In this work, a high-performance two-dimensional (2-D) scanning one-port leaky-wave antenna (LWA) is proposed, studied and implemented in substrate integrated waveguide (SIW) technology. A series-fed single-port planar transverse slot one-dimensional (1-D) leaky-wave antenna (LWA), which is composed of reflection cancellation slot pairs, is found to exhibit frequency dependent directional pattern characteristics from-37° to +18°(covering a bandwidth of 29%) including the broadside direction. This antenna structure is studied in the SIW technology. A periodic modulation of transverse slot on the broad wall of LWA spaced at one guided wavelength exhibits a frequency scanning behavior and also a wide impedance bandwidth due to in-phase addition of each excited slot. The natural open stop-band of the periodic LWA is suppressed with the reflection cancellation slot added at a distance of quarter wavelength from the excitation slot. The SIW-based vertical inter-connect from E-plane to H-plane (E2H) guide is proposed, validated, and used to feed each radiating element. Nine groups of these LWAs are integrated on a conformal array contour of the Rotman lens-based passive phase shifter, to design two-dimensional (2-D) scanning on-substrate multi-beam antenna (MBA) array. The phase-controlled seven radiating beams cover an azimuth scan angle of 71.8^{o} over an array bandwidth from 73 GHz to 78 GHz. In the perpendicular dimension, the frequency-controlled radiating beams for each port cover an elevation angle of 13.5^{o} during the experiments. Due to its attractive advantages, the proposed MBA system is suitable for

various scanning applications such as millimeter-wave automotive radar and RF switchable software-defined radio.

The operation principle of conformal arrays is illustrated in Figure. 5.1. In this case, they require a multiple pole multiple-throw switch, a Butler matrix or a lens to alter the excitation amplitude for the array elements, and amplitude or phase correction techniques to control the side lobe level [110-111].

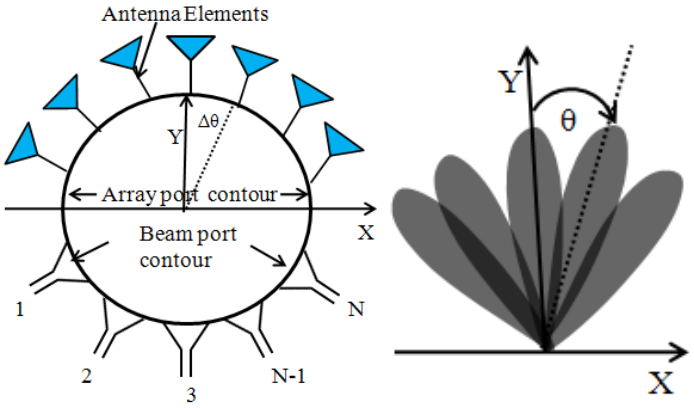

Figure. 5.1. Beam forming network (BFN) feeding conformal array for upper hemisphere coverage, where θ is the main beam steering angle, $\Delta\theta$ is the required phase shift, N=the number of beam ports.

Obviously, such resulting complex architectures are not suitable for cost-effective integration and implementation. The concept of phase-frequency scanning was introduced in [112-113]. This new class of scanning arrays is able to achieve scanning in two dimensions by creating a one-dimensional phased array of leaky-wave line-source antennas. The phase control of one-dimensional frequency scanning arrays has been realized by using a microstrip Rotman lens in [114] and by controlling of a free running frequency of voltage controlled oscillators in [115]. The 2-D beam scanning by using digital beam forming techniques has also been studied in [116-118]. Unfortunately, the feed network losses of the matured microstrip technology limit the use of the proposed methods over the millimeter-wave frequency range. The planar form of various beam forming network (BFNs) such as Butler, Blass, Nolen matrices, Rotman lens, and R-kR lens was studied in [119]to scan one dimensional (1-D) linear array only. To overcome the loss hurdles of the microstrip line and other planar techniques, the substrate integrated waveguide (SIW)

technology was used to implement passive phase shifter based on parabolic reflector principle in[120], to scan an array of leaky wave antennas. The proposed method has a full planar integration capability but occupies a relatively large size. A multilayer technology has been effectively used in [121, 122] to reduce the size of the MBA. The 2-D antenna array based on a

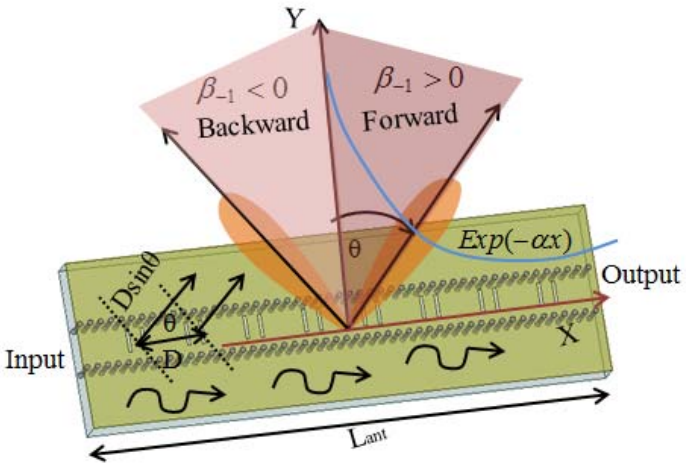

(a)

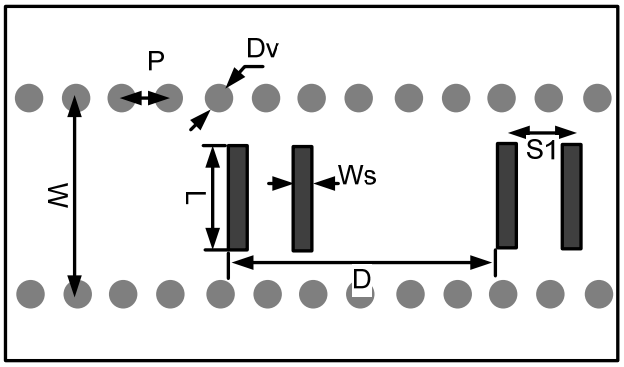

(b)

Figure. 5.2. (a) The reflection cancellation forward wave LWA, (b) Small Section of the LWA, where the parameters are defined as *W*= 2.1, *P*=0.52, *Dv*= 0.26, *L*=1.1, *Ws*=0.24, *D*=2.9, *S1*=0.6132 (all units are in mm).

multimode concept has been proposed in [123], where phase distribution has been obtained by using different SIW widths. However, all those cited solutions are concerned with the occupation

of a large space and they are not suitable for feeding conformal arrays, where 360° full space scan coverage is essential[124].

In this chapter, a high-performance 2-D scanning one-port leaky-wave antenna (LWA) is proposed and implemented in the SIW technology as the first step of achieving the desired 360° elevation and azimuth coverage. This LWA structure is steerable from backward to forward direction including the broad side. The azimuth plane scanning of MBA is obtained through the phase control of an array of nine 1-D elevation-plane frequency scanning LWAs, each fed through the E2H (from E-plane to H-plane) corner on the array port contour of the Rotman lens. The SIW technology is selected aiming at low-cost, light-weight, which is completely different from traditional coaxial cables used in [110]. This technology as demonstrated in this work presents an excellent solution for the design and development of cost-effective advanced phased array systems particularly for E-band automotive surveillance radar (73-78 GHz) applications.

The complete antenna prototype was fabricated on single Rogers RT/Duriod 6002 substrate with ε_r =2.94, tanδ=0.0028, thickness =0.508 mm and simulated in Ansoft HFSS.

5.1.1 SIW leaky wave antenna

The series-fed linear array presents a unique frequency scanning behavior, where the angle of main beam θ is a function of the operating frequency. SIW LWA based on this principle was studied in [125], where the leaky mode was radiated from the near broadside to end-fire direction. The periodic frequency scanning antenna generally has poor radiation efficiency around broad side due to the existence of open stop band in the narrow frequency band. The reason is due to the constructive addition of all series or shunt admittances along the transmission line forces input impedance to become zero. The addition of reflection cancellation stub at the distance of λ_g /4 from excitation slot avoids the undesired open stop-band [126]. The dual slot structure was proposed in [127], but the structure is of broadside nature only.

In this section, SIW LWA using the concept of reflection cancellation is proposed, and also demonstrated are the directional pattern characteristics from -37° to +18° by changing the frequency from 58 GHz to 78 GHz. The matched termination is designed, validated and integrated to realize single port LWA. The antenna working condition is validated through the experimental results.

5.1.1.1 Antenna Design and modeling

The operating principle of one-dimensional (1-D) SIW LWA array is demonstrated in Figure. 5.2a. Where the angle of radiation θ is a function of space harmonic β_n, if $\beta_{-1}<0$, the antenna radiates in backward direction, as frequency is increasing $\beta_{-1}>0$, antenna radiates in forward direction. Along the axis of propagation (X-axis) the available power decays as an exponential function of leakage factor α. (Two symmetrical beams around θ are due to two ports). The periodic array of eight radiating transverse slots embedded on the broad wall of the guiding structure. The distance (*S1*) between the excitation slot and reflection cancellation slot is approximately one quarter of a guided wavelength (λ_g). The total phase shift between the two slots is approximately 180°. Hence, the reflected waves from the two slots are added in out-of phase resulting in a very low reflection coefficient at the input. The slot pairs are periodically spaced at one λ_g, hence progressive phase is multiple of 2π, resulting in the fact that all the slot pairs are added in phase.

The chosen SIW width, post diameter, period and optimized slot dimensions are indicated in Figure. 5.2b and these SIW parameters will apply to all the results in this section. The antenna radiation behavior is explained by using the periodicity of the space harmonics.

According to Floquet's theorem, the infinite numbers of space harmonics of guided mode inside periodic LWA are related to,

$$\beta_n D = \beta_o D + 2n\pi \tag{1}$$

Where β_o is the fundamental space harmonic and n is the space harmonic index.

The first higher-order radiating space harmonic β_{-1} inside the dielectric filled rectangular waveguide for which $(\beta_n / K_o) \le 1$ is related as:

$$\frac{\beta_{-1}}{k_o} = \sqrt{\varepsilon_r}\sqrt{1-\left(\frac{c}{2a_{rwg} f\sqrt{\varepsilon_r}}\right)^2} - \frac{n\lambda_o}{D} \tag{2}$$

Where a_{rwg} is the SIW equivalent width (a_{rwg} =1.9473mm in our case), c is the velocity of light in free space, ε_r= dielectric constant of the substrate and D is the periodicity between array elements.

From the Snell's law of refraction, the angle of outgoing beam gets multiplied by a factor of $\sqrt{\varepsilon_r}$, and then the main beam pointing angle is given by the classical formula

$$\theta = \sin^{-1}\left(\frac{\sqrt{\varepsilon_r}\beta_{-1}}{K_o}\right) \quad . \qquad (3)$$

The total internal reflection occurs for angle of incidence

$\theta_i > \theta_c$, where

$$\theta_c = \sin^{-1}\left(\frac{1}{\sqrt{\varepsilon_r}}\right) \qquad (4)$$

Where θ_i is the incident angle inside the guide, θ_c is the critical angle. From (4), θ_c is calculated as 35.6° (for ε_r =2.94). From (3), the antenna scan range for first-order leaky mode is less than 30°, hence the condition for the total internal reflection is also satisfied.

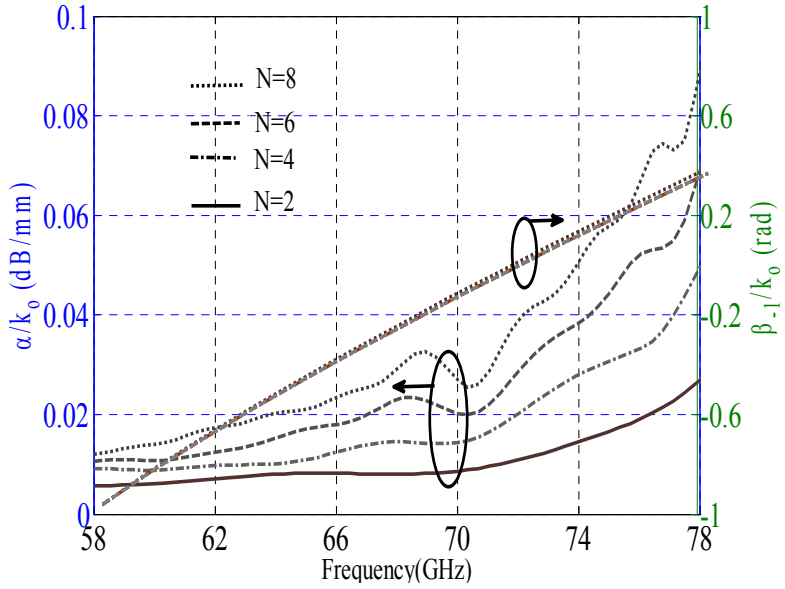

Figure. 5.3. The dispersion characteristics of LWA

The leakage power of the LWA is calculated by,

$$L_p = 1 - |S_{11}|^2 - |S_{21}|^2 \qquad (5)$$

The available power inside the guide is calculated as,

$$A_p = 10\log_{10}\left(|S_{11}|^2 + |S_{21}|^2\right)(\text{dB}) \qquad (6)$$

The leakage factor α is defined in terms of available power A_p,

$$\alpha = -\frac{8.686\ln(A_p)}{2L}(dB/mm) \tag{7}$$

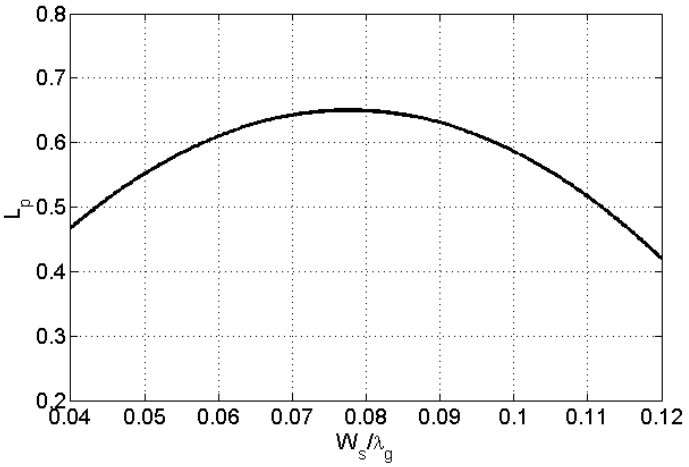

(a)

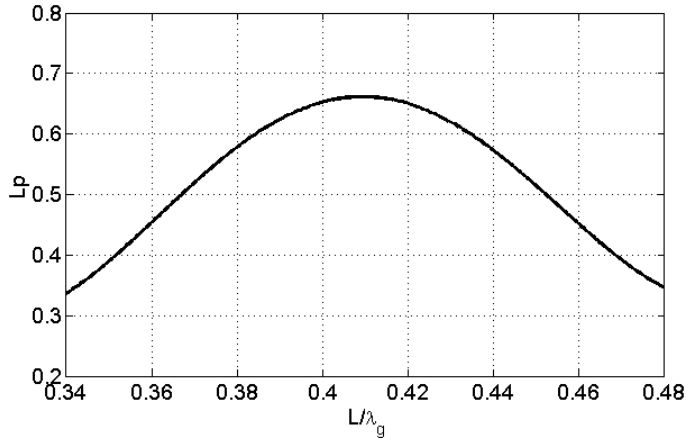

(b)

Figure. 5.4. The leakage power (equation (5)) variation with (a) slot width W_s (b) slot length L at 74.5GHz. (*Ws, L* are normalized to guided wave length).

The calculated normalized phase constant from (2) for the leaky mode and leakage factor from (7) as a function of frequency for different number of cells are plotted in Figure. 5.3. with the

increase in number of slot pairs(leakage factor on left side and first space harmonic normalized to free space wave-number on right side. where N is the number of slot pairs). N=2, 4, 6, 8. The term "Ko " is the free space propagation constant. the terms attenuation constantα and phase constant βinside the guide are normalized to "Ko. The value of β is constant for different number of cells N .The slope of phase constant is stable and non-zero. The normalized attenuation constant α/k0 increases linearly with frequency from 58 GHz to 78 GHz. It confirms that radiation is obtained including the broadside direction. The normalized leakage factor α/k0 does not experience any sharp drop over the wider operating bandwidth. The value of α is close to zero below 58 GHz due to the absence of radiation. Above 78 GHz, α is suddenly increased to higher value due to the presence of the immediate stop band.

It must be mentioned that the design of LWA for broadside radiation is dependent on the value of S (here 0.21λg@74 GHz). The initial design value of S=0.25 λg must be optimized to cancel the mutual coupling effects between the excitation and reflection cancellation slot. The variation of leakage power Lp (in HFSS assumed that zero conductor and zero dielectric loss) as a function of slot length L and width Ws is plotted in Figure. 5.4.

The initial design parameters for the slot length $L = \lambda_g / \sqrt{2(\varepsilon_r + 1)}$, width W_S $(\lambda_g / 20 << W_S << \lambda_g / 10)$ are optimized to yield the maximum amount of leakage power at 74.5 GHz. The final values are selected as W_s= 0.075λ_g (0.21 mm), L= 0.41λ_g (1.1 mm). The value of L_p is maximum under the resonant condition for selected values of slot length and width. The amount of leakage power can be increased by increasing the number of slot pairs. The calculated angle of the main beam from (3) and the simulated peak gain as a function of frequency is shown in Figure. 5.5. The gain increases with frequency due to a larger electrical length of antenna at a higher frequency. The gain variation is less than 2 dB over the targeted operating bandwidth from 73 GHz to 78 GHz.. The antenna impedance (return loss <-10 dB) is matched over a wide frequency range covering from 58 GHz to 78 GHz. It is observed that the open-stop band is suppressed over the frequency range. Figure. 5.6b plots the simulated radiation efficiency as functions of frequency from 58GHz to 78 GHz. Dielectric and metallic losses are included in the simulation to calculate the radiation efficiency. Dielectric loss tangent value is set to be $tan\delta$ = 0.0028@74GHz and all the vias are filled with copper. The value of radiation efficiency for eight pairs of slots is of 68% at 74 GHz.

The value is changing from 50% at 58 GHz to 78% at 78GHz. This is due to the increasing gain value at higher end of frequency band.

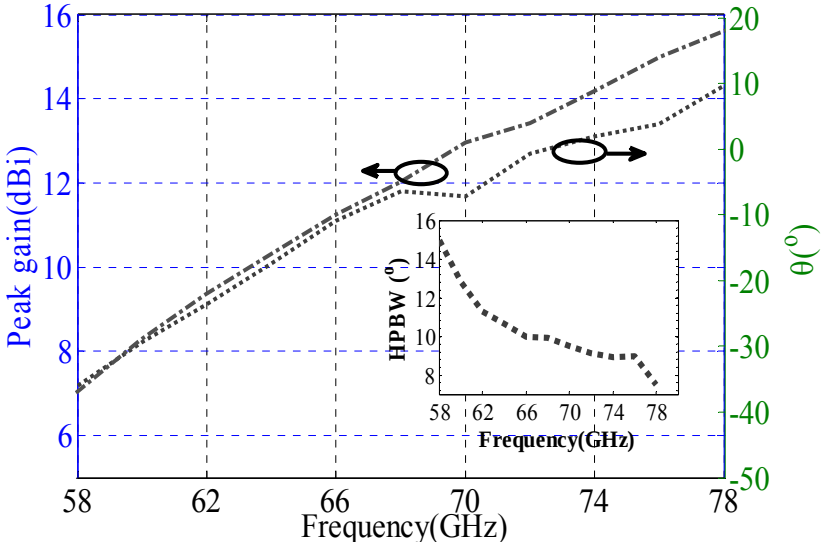

Figure. 5.5. The calculated scanning angle on the right side and simulated peak gain on the left side as a function of frequency. (The variation of HPBW with frequency is also shown in the inset).

The simulated frequency dependent H-plane normalized radiation pattern of the two port LWA for a frequency range from 58 GHz to 78 GHz is plotted in Figure. 5.6a. The antenna steers from -37° scan angle at 58 GHz in the backward direction, enters into broadside at 70 GHz and steers up to +18° scan angle in the forward direction. As frequency increases, the beam is steering towards the direction of the propagation of the leaky wave inside the guide. The side lobe levels are lower than -11dB for all the radiated beams. Electric field value is maximum in the aperture of slot. So, the amplitude coefficients are function of field distribution inside the slot. Side lobes can be shaped by following aperture synthesis method such as Taylor and chebyshev [37]. The corresponding theoretical beam directions from equation (3) are 8°, 13°, and 17°. Simulated peak gain is 13.1 dBi, 13.4 dBi, 14.32 dBi and the simulated beam direction is 9°, 14°, and 18° at 74 GHz, 76 GHz and 78 GHz respectively. The antenna radiation efficiency can be improved by increasing the number of slot pairs. It can be concluded that the calculated and simulated beam directions are well in agreement. As expected, the value of E-plane half power beam width (HPBW) is decreasing along with frequency.

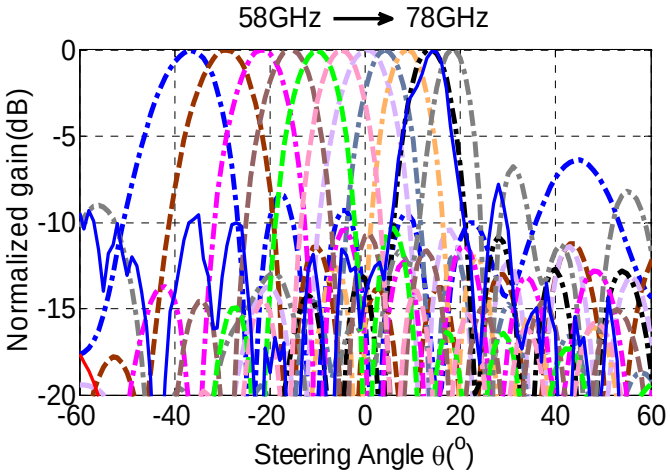

(a)

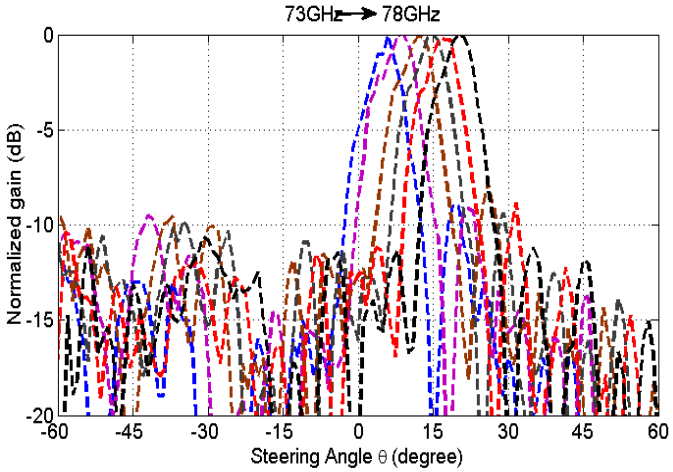

(b)

Figure. 5.6. (a) E-plane co-pol simulation (dotted) and measurement (solid blue) at 76 GHz for the LWA. The frequency is changing at an interval of 2 GHz. (b) measured E plane pattern for one-port LWA (input frequency changing from 73 GHz to 78 GHz at an interval of 1 GHz).

5.1.2 Input matching and Directional pattern measurements

For realizing one-port LWA, simple matched termination is designed by using SIW to microstrip transition. The *0201* package thick film resistor is soldered in between the open ended microstrip line and the quarter-wave length microstrip butterfly open stub. The fabricated

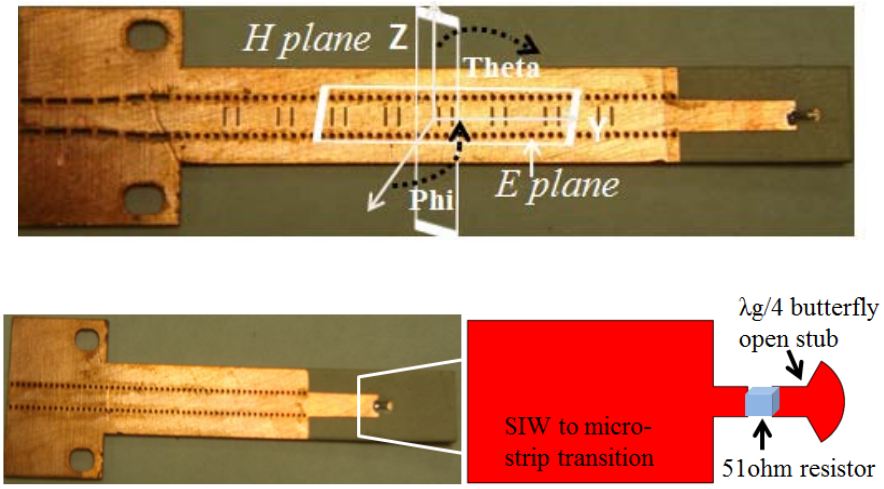

Figure. 5.7. The manufactured prototype of single port LWA and 75 GHz load used for matched termination. The detailed view of the matched termination is also shown here.

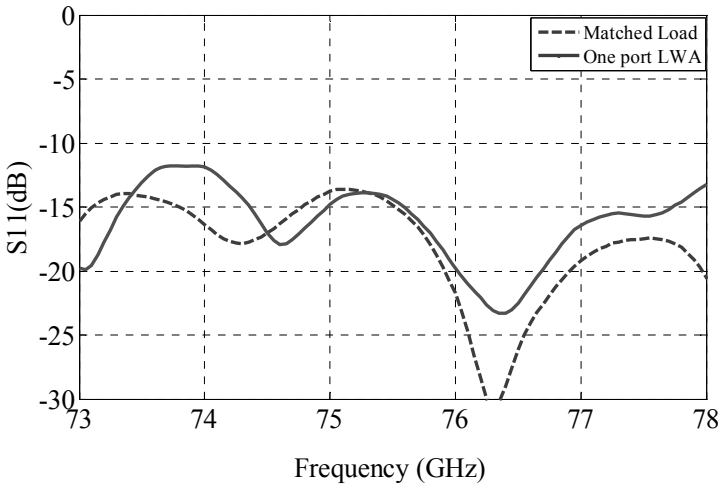

Figure. 5.8. Measured reflection coefficient for the one-port LWA and matched termination. The matching bandwidth of the load termination limits the LWA frequency of the operation.

circuits of the antenna and matched load are given in Figure. 5.7. As shown in Figure. 5.8, measured return loss of the matched termination is less than -13 dB and the measured reflection coefficient for the one port LWA is less than -10 dB in the targeted frequency range from 73 GHz to 78 GHz. The antenna is measured by using the multi-section transition between the standard WR10 waveguide and SIW. As a comparison, the measured radiation pattern at 76 GHz is plotted in Figure. 5.6b. The one-port LWA is designed for achieving maximum gain over the frequency band from 73 GHz to 78 GHz, since the BFN operation bandwidth is limited from 73 GHz to 78 GHz only. The peak gain directions are obtained as 6.5º, 10º, 11.8º, 15º, 17º and 20º with gains of 11.4 dBi, 12.1 dBi, 12.3 dBi, 12.4 dBi, 12.7 dBi and 12.8 dBi respectively. The proposed LWA covers 13.5º elevation solid angle with 8.2º HPBW for each frequency.

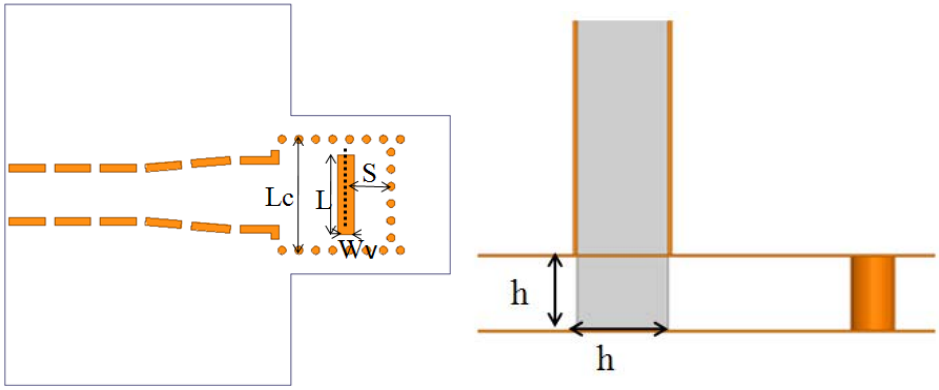

Figure. 5.9. The proposed E2H corner (a) The top view, here S=1.3, W_V=0.508, L=1.9783 L_C =3.5 (b) Side view, here h= 0.508 (all units are in mm).

5.1.3 SIW cavity coupled E to H plane bend

A vertical transition from horizontal plane to vertical plane in SIW technology is introduced in this section. Such as a transition is very useful in the size reduction of antenna feeds and also useful to connect two layers in a multi-layer environment. A transition from SIW to rectangular waveguide (RWG) is proposed in [128], and the achieved impedance bandwidth (≤-10 dB) is of 3.1% at 34.75 GHz. But the hybrid geometry is not suitable for complete SIW based circuits. The proposed idea is a direct transformation of the corner used in the convectional metallic waveguide-based magic T [129] to SIW corner. Figure. 5.9 describes architecture and dimensions of the

proposed wide-band transition from H-plane to E-plane guide. The feed guide has the square type SIW cavity where the electric field is maximum at the center. The vertical guide foot print is placed at a distance of *S* (approximately half-guided wavelength from the end wall of cavity).

Vertical guide is placed on the middle of a cavity in the end of feeding guide. Hence, the maximum power is coupled to the H-plane guide. The cavity's length determines the operating frequency range of the transition. Its width should be less than certain limit in order to avoid excitation of the undesired TE_{30} mode, whereas the TE_{20} mode is not critical because of the symmetry of the structure, this constraint define the parameters *Lc* =3.41mm. A circuit-equivalent model from [129] is the simplest approaches to define the initial values and if the performance are sufficient for our application. As shown in Figure. 12a, the model is composed of H-plane T-junctions used to interconnect the rectangular waveguides discontinuities: the main part is an open E-plane T-junction, one of the two H-plane branch is short-circuited at its extremity with length S and the other branch is a step. The parameter *S* is determined by the model is about 1.15 mm. The theoretical S-parameters of the Lumped equivalent model are plotted in Figure. 5.10. The substrate is considered as lossless in the above Lumped equivalent model. The model results show an attainable 15dB return loss bandwidth is 11.4% and the -20 dB is about 6.1% which is sufficient for our application.

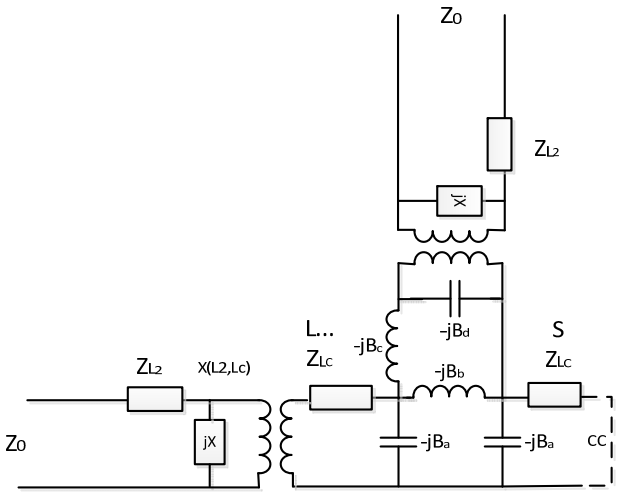

Figure. 5.10. (a) Lumped equivalent model for H2E corner.

The different dimensions are optimized, the variation of voltage standing wave ratio (VSWR) of the corner as a function of spacing S is plotted in Figure. 5.11, at 72 GHz, 74 GHz

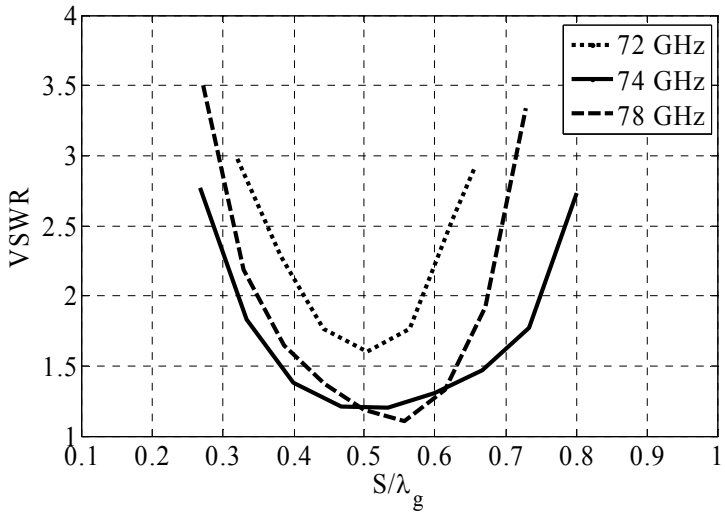

Figure. 5.11. The variation of port 1 VSWR inside the corner as a function of S normalized to the guided wavelength at the given frequency.

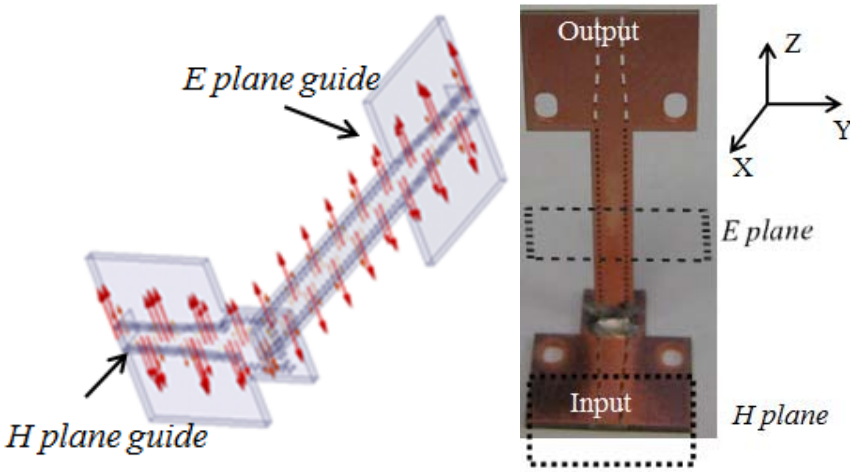

Figure. 5.12. H fields coupling through the corner for TE10 mode on the left side (plotted at 75 GHz) and the fabricated prototype of the E2H corner on the right side, here *YZ* plane is E plane and *XY* plane is H plane.

and 78 GHz. The final optimized S dimension for minimum reflections (of VSWR < 1.7) is selected as 0.5λg at the operating frequency. In fact, the 180° change the short circuit plane the vertical waveguide level constructing a corner. The guided magnetic field inside the corner is illustrated in Figure. 5.12, showing that the magnetic field inside the E plane guide excites the TE10 mode into the H plane guide. For the vertical footprint the length L is the equivalent rectangular waveguide width and the width Wv is the thickness of H-plane guide.

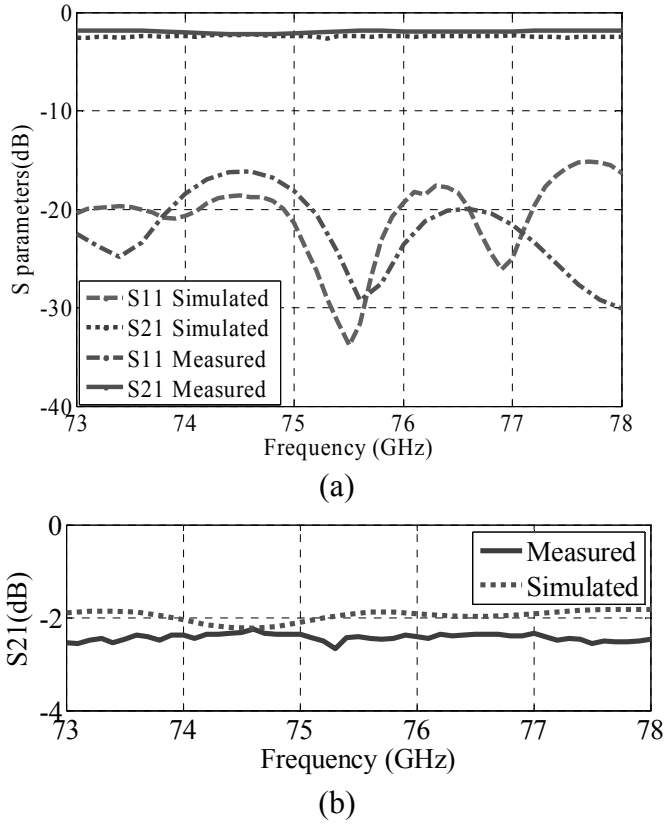

Figure. 5.13. The simulated (dashed line) and measured (solid line) scattering parameters of the E2H corner.

Fabricated prototype of the E2H corner is shown in Figure. 5.12. The circuit is measured by using an Anritsu 37397 vector network analyzer after standard TRL calibration. The transition is measured by using two simple multi-step transitions between standard WR10 waveguide and SIW cross-section. The comparison between simulated and measured scattering parameters is given in the Figure. 5.13. The measured bandwidth (return loss ≤ - 15dB) of 11.9% covers

frequencies from 71 GHz to 80 GHz as predicted by the model. The measured insertion loss is ≤ -2.3 dB over the entire bandwidth. The conductor, dielectric and leakage losses of the SIW add about 1.5 dB to the insertion loss of the corner. The E2H corner has a good agreement between its simulated and measured scattering parameters.

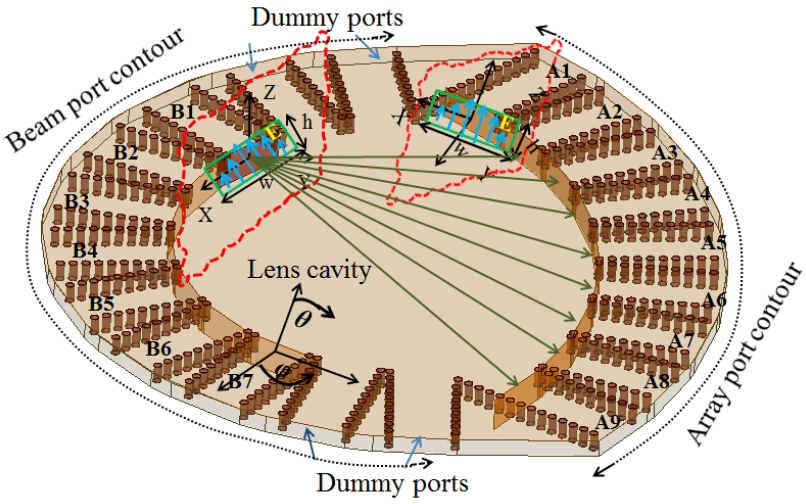

Figure. 5.14. Simulated SIW Rotman lens diagram in HFSS. The beam port contour has seven input ports *B1-B7* on the left side and array port contour has nine output ports *A1-A9* on the right side. The aperture cross-section for beam port *B1* and array port *A1* is shown. (Assuming half-cosine aperture distribution along the cross-section of the aperture).

5.1.4 2-D scan conformal antenna results

The 2-D scanning multi-beam conformal array is realized by utilizing Rotman lens as BFN and LWA as radiating element. The Rotman lens BFN is shown in the Figure. 5.14 is used as a phase shifting network. The whole 3-D circuit is built after fabricating nine LWAs and then inserted into the slots made on the Rotman lens BFN. The seven ports of BFN are used for E-plane steering and nine LWAs are used for H plane steering. The proposed LWA radiation pattern has a wideband bandwidth in the frequency range covering from 58 GHz to 78 GHz. The four dummy ports and all output ends of LWAs are terminated by the wideband matched termination described in section II. MBA is simulated by using the Ansoft HFSS software. BFN referenced in [130], provides the required amplitude and phase profile at the output contour of the Rotman

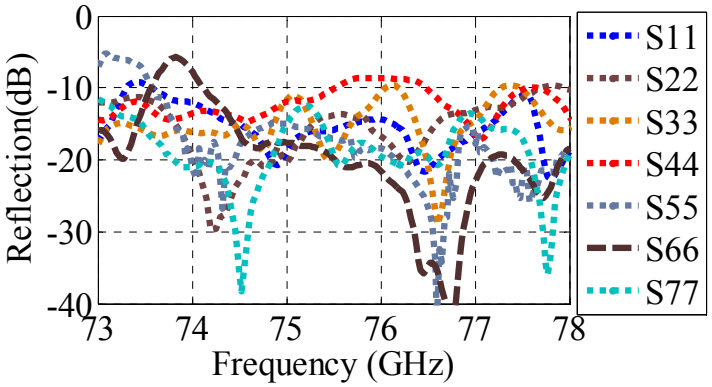

(a)

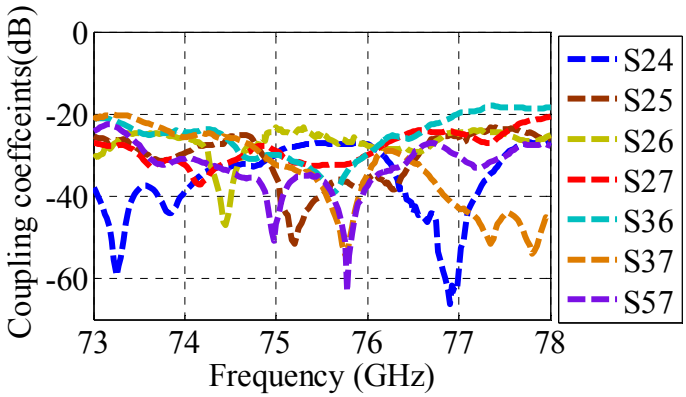

(b)

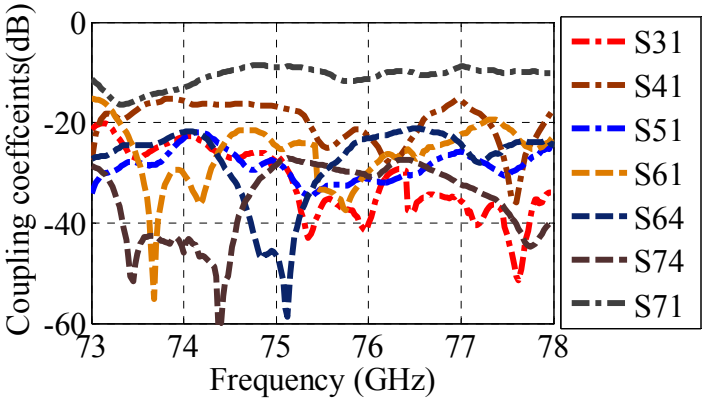

(c)

Figure. 5.15. Measured (a) return loss for beam ports *B1* to *B7,* (b) isolation from port 2, 3 to remaining ports, (c) isolation from port 1, 4 to remaining ports

As shown in Figure. 5.15, return loss and coupling coefficients are measured by using an Anritsu 37397 vector network analyzer after standard TRL calibration. Figure. 5.15a plots the measured return loss of ports *B1*, *B2*, *B3*, *B4, B5, B6* and *B7*. The return loss for all the ports is lower than 10 dB over the desired frequency band. Figure. 5.15b, c plots the measured isolation between all the beam-ports of the 2-D scan antenna. Port *B4* and the other input ports. The isolation between ports 2 and other ports is less than -20 dB. The isolation value between edge ports 1 and 7 is lower than -10 dB over the entire frequency range from 73 GHz to 78 GHz. The edge port that increases reflection and isolation is due to additive reflections and the array port aperture mismatch (as shown in Figure. 5.15).The isolation between the adjacent ports is not possible to measure in the present configuration due to the size of the transition used in this measurement.

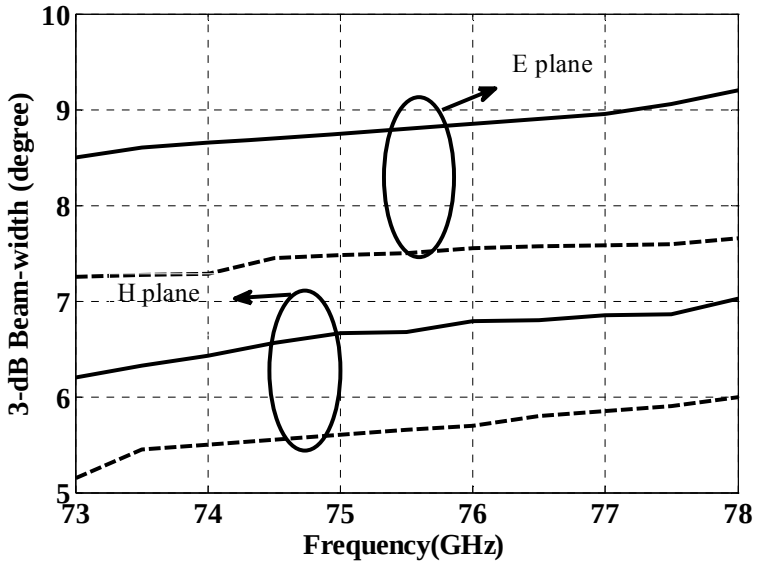

Figure. 5.16. Comparison between the simulated (dotted) and measured (solid) 3-dB beam-width in both E and H-planes when excited at the middle port 4.

The MBA forms two dimensional scanned patterns by changing input ports 1 to 7 and also by changing frequency from 73 GHz to 78 GHz. The exact symmetry between the ports is not obtained .The reason is due to proposed structure with radiation box is very large. The Tetrahedron Refinement in those regions is random. Until the structure is symmetric, after the mesh has been refined, the final meshing is not symmetrical. The gain of the MBA for edge ports B1, B7 is 3 dB less than the other ports due to the theoretical insertion loss increases with angle of incidence on

an aperture of the array ports. The difference of 2º beam-width is observed between both of the results. The inherent RF losses (dielectric and metallic) decreases measured peak-gain value by 2.5dB also increase beam-width. As frequency increases from 73 to 78 GHz, peak gain value is increasing approximately by 1dB value.

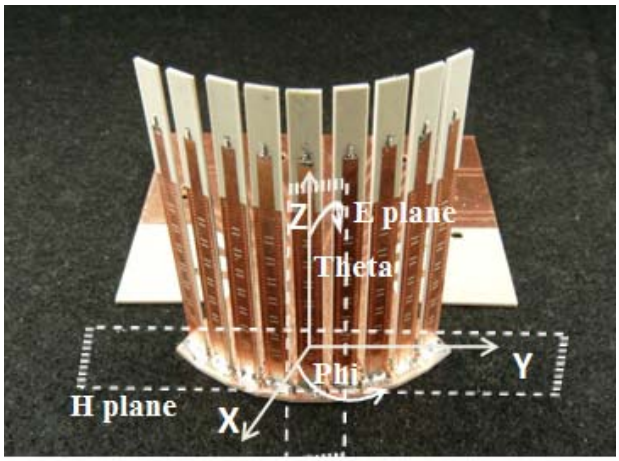

Figure. 5.17. Experimental prototype of the 2-D scan multi-beam antenna.

The directional pattern measurements are conducted in the MI technology anechoic chamber inside our Poly-Grames Research Centre. In this compact range setup antenna under test is used as a receiver sweeping in azimuth plane. Figure. 5.16 plots the beam variation as function of frequency for all the beam ports 1-7.The simulated and measured results are also compared. When operation frequency varies from 73 GHz to 78 GHz, such a 2-D multi-beam antenna can almost cover the angular region from (49°, 84.5°) to (120°, 70°) ((phi, theta)) having 3 dB beam width of 8.2° and

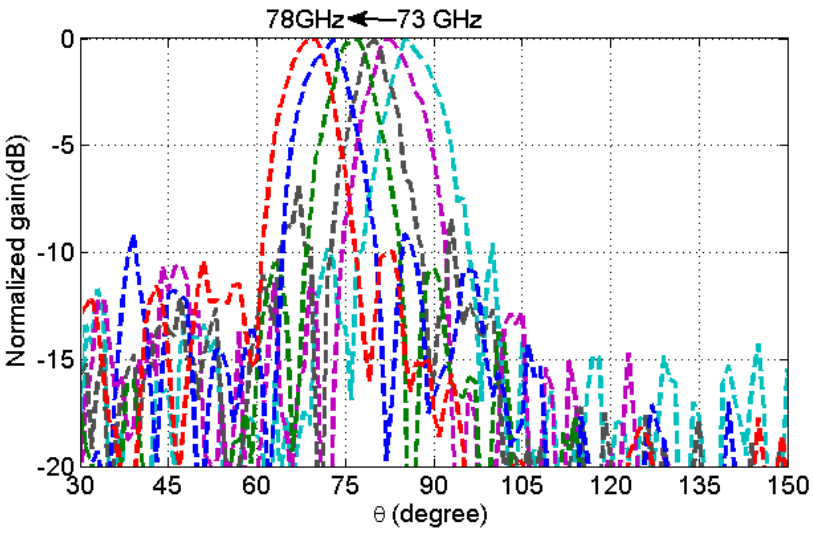

(a)

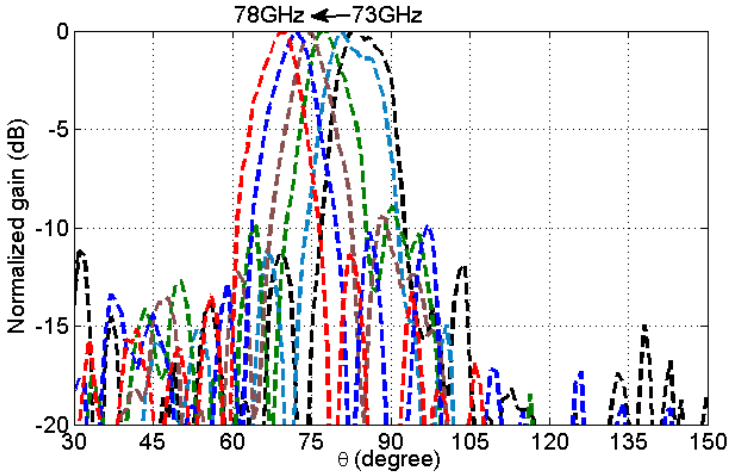

(b)

Figure. 5.18. Measured E-plane patterns excited at (a) at input port 1 versus frequency. (b) Input port 4 versus frequency.

7° in the H-plane and E-plane, respectively. The experimental prototype along with the original dimension is shown the Figure. 5.17. The E-plane and H-plane are also defined on the experimental prototype. Figure. 5.18a-b plots the measured E-plane directional patterns by changing frequency from 73 GHz to 78 GHz at an interval of 1 GHz when fed from port 1 and port 4 respectively. For port 1, the peak gains are measured to be 13.7 dBi, 14.1 dBi, 14.4 dBi, 14.8 dBi, and 15.2 dBi. The beam directions in H-plane at an E-plane angle of 49° are measured to be 85.1°, 83°, 81.2°, 78.2°,

and 70.2° .The side-lobe levels are measured to be less than -12 dB at 73, 74, 75, 76 and 78 GHz. For port 4, the peak gains are measured to be 15.4 dBi, 15.8 dBi, 16.8 dBi, 17.1 dBi, and 17.7 dBi. The beam directions in H-plane at an E-plane angle of 90° are measured to be 5.8°,82.7°, 81.9°, 80.2°, and 71.2°. The side-lobe levels are measured to be less than -14 dB at 73, 74, 75, 76 and 78 GHz.

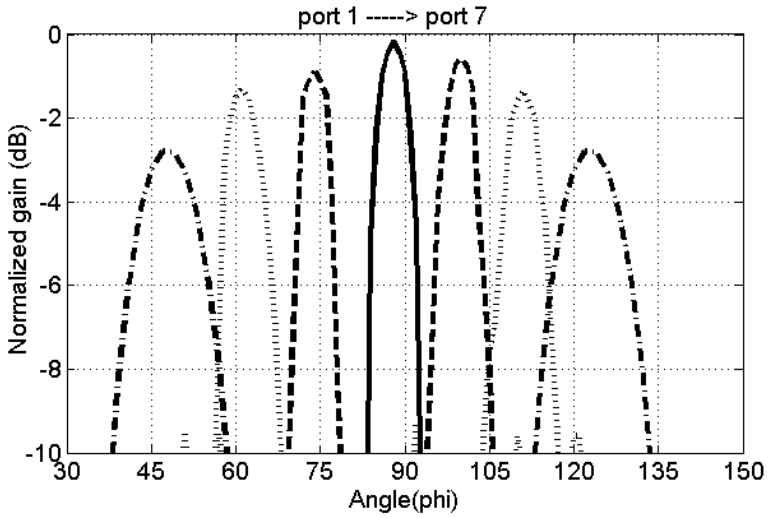

Figure. 5.19. Measured H-plane patterns excited from ports 1-7 at 74.5 GHz.

Figure. 5.19 plots the measured H-plane directional patterns at 74.5 GHz by changing the input from port 1 to port 7. The peak gains are measured to be 13.6 dBi, 15.3 dBi, 16.1 dBi, 17 dBi, 16.2 dBi, 15.2 dBi, 13.2 dBi, the beam directions in E-plane at H-plane angle of 80.2° are measured to be 49.3°, 60.6°, 75.1°, 88.5°, 101.2°, 110.5°, 119.1° and the side-lobe levels are measured to be –9.7 dB, –11.2 dB, –12.7 dB, –12.5 dB, –12.2 dB, –11.7 dB, –9.8 dB at 75 GHz. The MBA shows the same performance for other frequencies in the operation band.

The measured beam width obtained in H-plane is narrow because the antenna is using the 8 pair of slots and also narrow in E-plane Rotman lens is feeding the nine antenna elements. The increase in antenna elements contributes to high gain but antenna beam width becomes narrow. Finally, to obtain full 360º scan region following two methods are suggested [131]. Method 1 is to use low gain antenna element, so that wider beam angle coverage will be obtained. Method 2 is to increase the number of array ports on the output contour of the Rotman lens, so that it can be used to feed larger number of radiating elements and also to allow covering wide angular coverage.

5.2 Simultaneous Transmit/Receive Full-Space Scanning Phased Array System for Future Integrated High Data Rate Communication over E-band and Beyond

The limited scan region of 2-D scan conformal phased array antenna described in the previous section, is extended to obtain multiple beams to cover nearly 360^{o} scan region in azimuth and 20^{o} in elevation respectively. In this section, 45^{o} linearly polarized LWA array is used to implement multi-beam antenna array.

In this section, a novel technique for achieving simultaneous multiple scanned directional beams is introduced and its development is enabled by the substrate integrated waveguide (SIW) technology. The proposed phase-frequency scanning multi-beam antenna (MBA) array consists of four physical parts. In the first part, a two-port leaky-wave antenna (LWA) with 45º inclined polarization is proposed. The LWA with frequency scanning behavior scans over the beam angle from -30º to +30º covering the broad-side radiating beam. The output port is terminated by a matching load so to use as one-port LWA. In the second part, 4×4 Butler matrix, which is developed upon a short-short coupler technique, is proposed to design a space-saving beam-forming network (BFN). Differential phase between the output ports of the BFN is used to scan each beam of the frequency scanning LWA array. This judicious combination enables the development of a 2-D scan phased array system. Nevertheless, the MBA is able to operate as either transmit array or receive array. The third part, is composed of a simultaneous two-way transmit or two-way receive MBA array. Two-layered feed part is implemented by the combination of 90º H-plane coupler and two similar 4 × 4 Butler matrices. In this configuration, one of the beams can be used for transmit operation while the other beam can be used for receive operation simultaneously. Measured S-parameters and directional pattern measurements have confirmed multi-dimensional scanning capability of the proposed MBA. In the fourth part, the beam scanning range is further extended to cover the full-plane region by placing two independent MBAs orthogonal to each other. The proposed and demonstrated E-band phased array system can be used in future intelligent communication or transportation systems. This experimentally proven concept can easily be scalable for various system applications up to W-band frequency range and beyond.

The techniques proposed in [132, 133] were using metallic waveguide-based transmission line to obtain radiated beams over 360º scan range. Nevertheless, the design involved in those schemes

not suitable for implementing fully integrated electronically steerable phased array systems. BFN is essentially known to provide necessary amplitudes and phases to radiating elements in order to produce desired beams. All the planar forms of various phase scanning techniques like Butler, Blass and Nolen matrices can only produce one-dimensional (1-D) beam scanning with a fixed number of output beams, together with a fixed phase difference between the outputs. The technique for achieving the 2-D beam steering is by combining the frequency scanning arrays with the phase scanning technique.

The proposed technique in this work makes use of SIW technique to realize BFN, antenna array and also form directional beams in 2-D scan region. SIW is realized by synthesizing an array of metallic vias along the side walls in a longitudinal direction. BFN is integrated on azimuth plane and LWA is integrated in elevation plane to reduce size and loss of the phased array. The complete demonstration of the proposed method will be given below.

5.2.1 Two-port LWA with 45º inclined polarization

In this sub-section, a 45º polarized LWA is proposed and experimentally evaluated over a frequency range from 74 GHz to 90 GHz. As shown in Figure. 5.20, each reflection-cancellation slot-pair is inclined at an angle of 45º and then spaced periodically at a distance of one guided wavelength. Also, mutual coupling effect occurring in the case of a vertical polarized LWA is reduced by adding an offset *DD* in the transverse direction within each reflection cancellation slot pair. This antenna is designed to cover all the frequency from 74GHz to 90GHz. Each slot is excited through an aperture coupling method.

An experimental prototype of LWA is shown in Figure. 5.20. This is a 3-D antenna in physical architecture, where input and output are located on feeding SIW waveguides and the 45º polarized array is integrated on the bridge connecting between input waveguide ports. Each right angled corner is optimized to match the impedance over the entire band from 80 GHz to 90 GHz. The comparison between simulated and measured S-parameters is given in Figure. 5.21. Antenna bandwidth is reduced for the 3-D LWA, when compared to its planar counterpart. The circuit is measured by using an Anritsu 37397 vector network analyzer after using a standard TRL

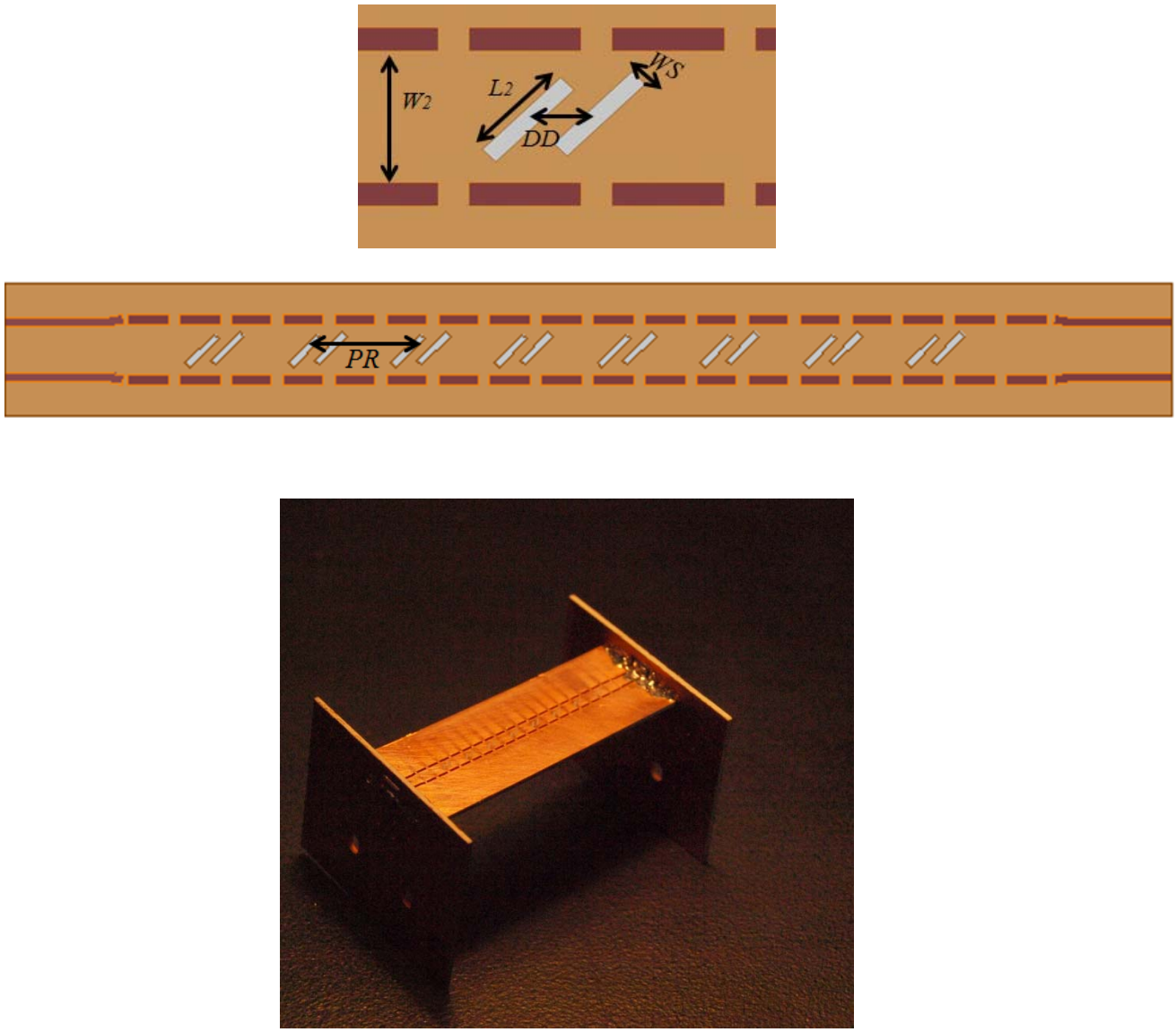

Figure. 5.20. Simulated and experimental prototype of two-port LWA with 45º inclined polarization and also shown single cell of an inclined slot-pair along with the dimension.

calibration. The transition is measured by using two simple multi-step transitions between standard WR10 waveguide and SIW cross-section. For measurement of S-parameters antenna physical architecture is changed, where two connecting waveguides are feeding from opposite sides. The measured bandwidth (return loss ≤ - 10 dB) of 11.7% covers frequency range from 80 GHz to 90 GHz as predicted by the model. The measured transmission loss is of -2.3 dB is adding over to the simulated transmission loss. This value is combined loss of two right angled corners and conductor,

dielectric and leakage losses of the SIW add up about 2.3 dB to the insertion loss of the corner. Simulated gain pattern for planar LWA is shown in the Figure. 5.22a, where antenna is covering from -30º to + 30º from 73 GHz to 90 GHz. But for 3-D LWA

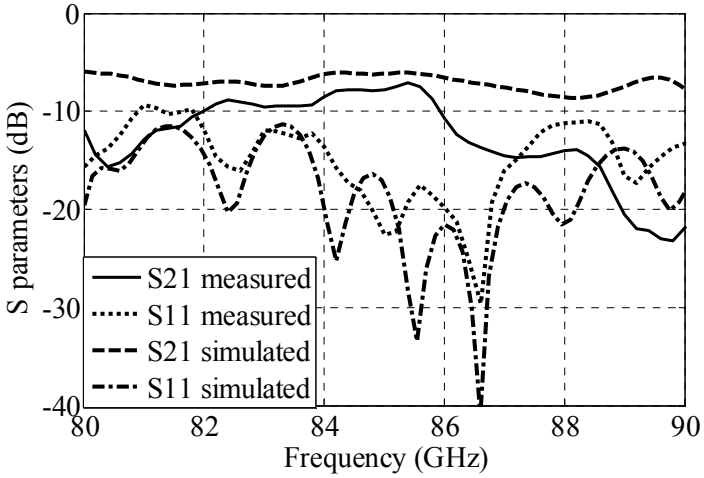

Figure. 5.21. Simulated and measured S-parameters of two-port LWA.

impedance and radiation bandwidth is reduced. Measured gain plot of the 3-D LWA is shown in Figure. 5.22b. LWA antenna is radiating from -15° to + 15° including the broadside direction when frequency. changes from 80 GHz to 90 GHz with approximately HPBW of 12° (in the YZ plane) for each beam The peak gain directions are obtained at 6.5o, 10o, 11.8o, 15o, 17o and 20o with gains of 11.4 dBi, 12.1 dBi, 12.3 dBi, 12.4 dBi, 12.7 dBi and 12.8 dBi, respectively. The proposed LWA covers 13.5o elevation solid angle with 8.2o HPBW for each frequency. Peak gain variation between lower and higher ends of frequency is lower than 3 dB. In the H-plane, LWA HPBW is calculated to be 78º at the frequency of 84 GHz. LWA is designed for achieving maximum gain over the frequency band from 82 GHz to 86 GHz. Longer antenna input ports in the measured plane are causing additional side lobe levels. LWA array uses four antenna elements of this type to implement a full-space scan antenna with multiple beams, each with 45º inclined polarization.

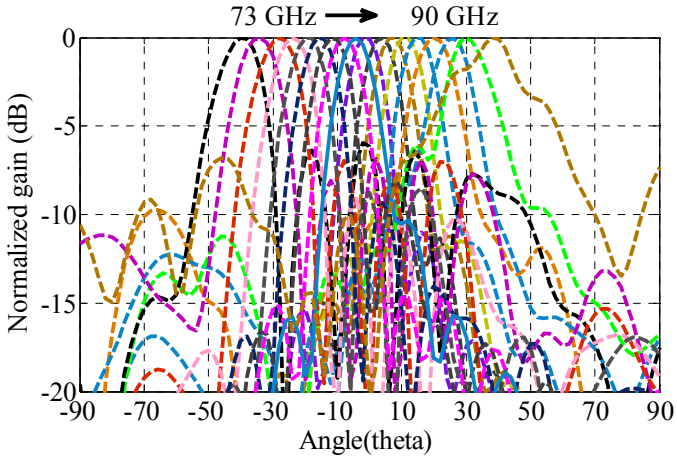

(a)

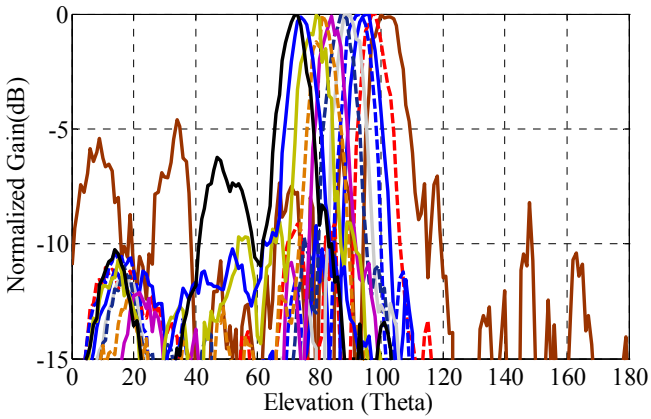

(b)

Figure. 5.22. (a)E-plane co-pol simulation radiation pattern (b) measured E plane pattern of two-port LWA (the input frequency varied from 80 GHz on left side to 90 GHz on right side at an interval of 1 GHz).

5.2.2 Millimeter-wave Crossover Structure Utilizing Simultaneous Electric and Magnetic Coupling

In this section, new cross over structure used in implanting full-spcae scan antenna system is discussed. The concept is experimentally verified at 35 GHz, and similar topology is adopted at 84 GHz range.

An ultra-compact wideband crossover is proposed and realized by using vertical coupling of both electric and magnetic fields simultaneously. The four port multilayered substrate integrated waveguide (SIW) crossover structure consists of two different types of 90^{o} hybrid coupler integrated at the same physical location. The magnetic field (H) is coupled through slots etched adjacent to the side walls of waveguide and the electric field (E) is coupled through slots etched on the middle of waveguide. Measured insertion loss is less than 0.9 dB over an operating bandwidth of 16.6% at 35 GHz. The experimental prototype occupies a compact size of $4.8\lambda_g$x$3.7\lambda_g$x$0.145\lambda_g$ including its input transitions.

The development of low-cost, high-performance, wide-band millimeter (mm) wave antenna arrays is urgently required for today`s high data-rate wireless radio links, automotive radar and mm-wave imaging, thanks to large spectral space available at these frequencies. The strength of mm-wave antenna array systems lies in the design of a beam forming network (BFN), to distribute the output signal power from the transmitter to radiating elements and to provide the required aperture amplitude and phase distribution for desired beam direction angle θ_0, beam shape, side lobe control. And also, it must be of low-cost, low-loss, wide-band, high-beam pointing accuracy and planar integration. As an example, the BFN based on theoretically lossless Butler matrix consists of a number of directional couplers and crossovers between the excitation ports and antenna array feed ports.

The ideal crossover shown in Figure. 5.23 can be represented either in planar or in multilayer structure. Various designs were proposed in [134-138] aiming at the development of compact and low-loss crossover junctions. A simple design of planar microstrip crossover junction was described in [134], where two 3dB hybrid couplers were cascaded in series manner. The design of various crossover junctions in microstrip technology was described in [134]. The miniaturization techniques for microstrip crossover structures based on concentric ring couplers were studied in [135]. The radiation loss of the traditional microstrip technology limits the use of the proposed methods for the mm-wave frequency band. The SIW version of the planar crossover structure was proposed in [136], where the four port junction is optimized to achieve 5% coupling bandwidth. The cross coupler proposed in [137], using edge slot coupler at 26 GHz, presents good results over 1 GHz (relative bandwidth of 3.8%). In [138], cruciform coupler is used to build the crossover at 12.5 GHz, achieves good performances over a relative bandwidth of 24%. However, the cascaded solution for such crossover structures occupies larger physical size.

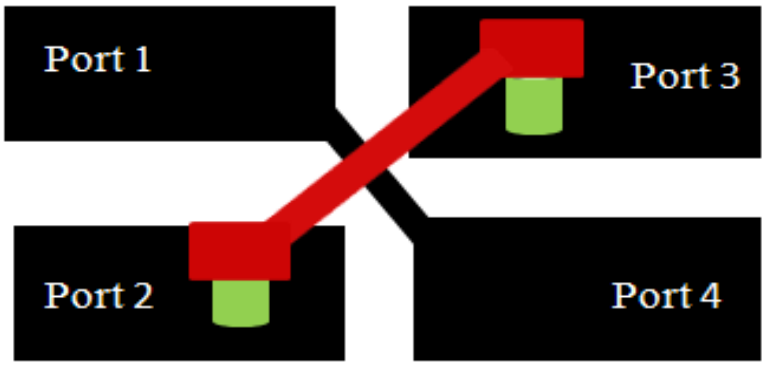

Figure. 5.23. Schematic representation of the ideal crossover junction, where ports 1 and 2 represent one transmission line and ports 3 and 4 represent the other transmission line.

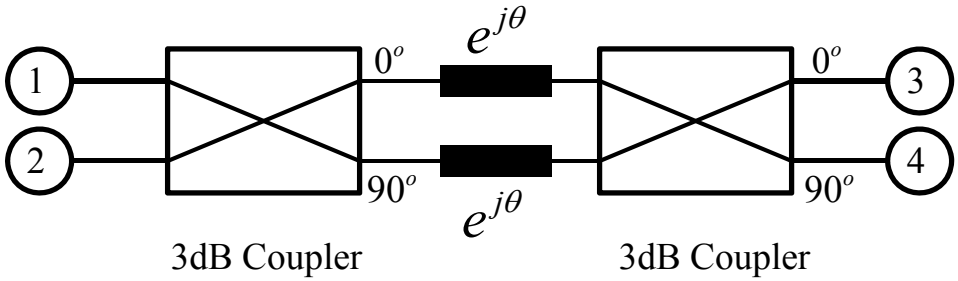

Figure. 5.24. The 0-dB coupler contains two 3-dB couplers separated with electrical distance θ where $\theta = (2n+1)\pi\lambda/4, n = 0,1,2..$

In this work, the development of two-layered SIW crossover junction is realized by integrating two different E-plane couplers at the same physical location aiming at achieving a wider bandwidth, low-loss and in particular miniaturization Physical dimensions of the coupler are obtained through Ansoft HFSS simulator and later experimentally validated on Rogers 6002 substrate with dielectric constant = 2.94, thickness = 20 mil.

5.2.2.1 Cascaded Coupler

The vertical coupling of electric fields in waveguide structure can be obtained either by using twin pair of slots [139] or by synthesizing an array of holes on the middle layer [140] of the two layer couplers. Figure. 5.24 shows a generalized block diagram to obtain the maximum amount of power in diagonal port 4 or 3 when fed from port 1 or 2. The two 3-dB coupling sections are

separated by electrical distance θ .To avoid a multi-reflection between the two stages, length θ has to be odd multiple of $\lambda g/4$. Coupler based on this topology is discussed in this section.

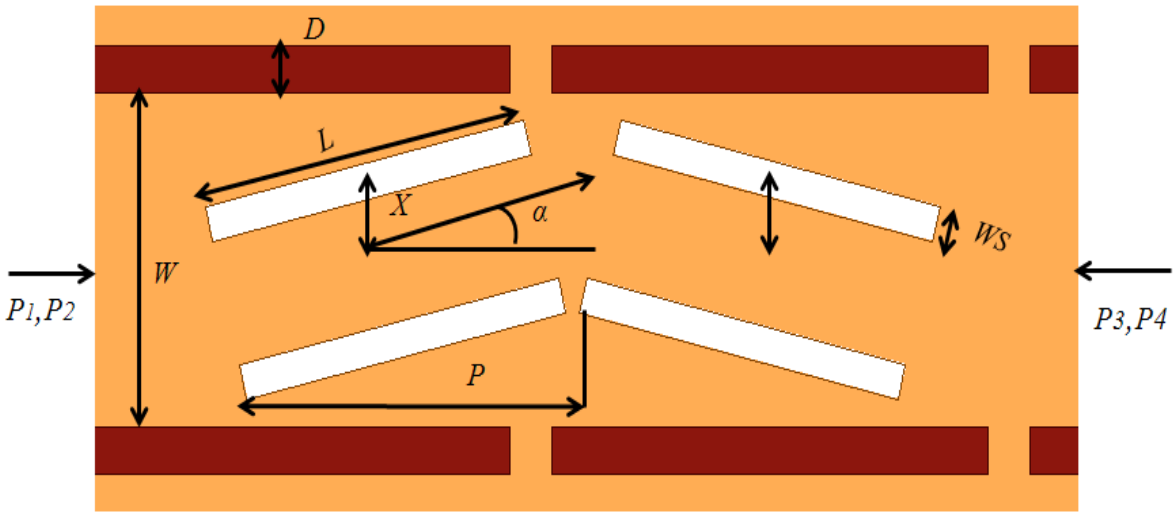

(a)

Figure. 5.25. Top view of (a) the cascaded two 3dB hybrid couplers, where *D*=0.5, *L*=4, *Ws*=0.38, *X*=0.83, α=14.2°, *P*=10, *W*=3.64, parameters for the SIW and the coupler are also shown. The slots are on the middle layer of the multi-layer structure where ports 1, 3 on the bottom layer and ports 2, 4 are on the top layer.

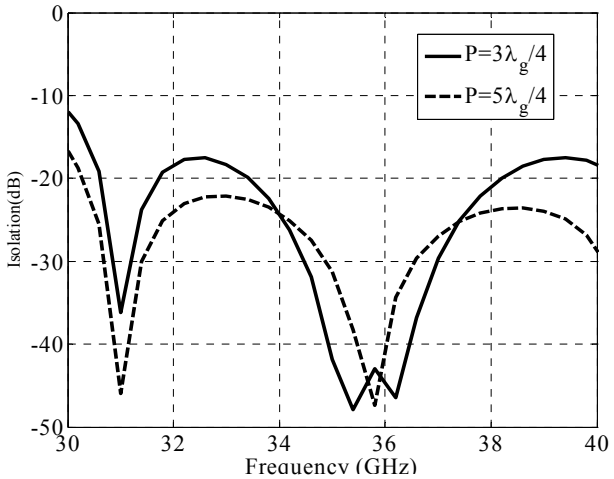

Figure. 5.26. The comparison between simulated S-parameters of the cascaded coupler with two different physical separation distances P.

The E-plane coupler with twin pair of slots offset from the centre of the waveguide axis and inclined at an angle of α with the centre of axis is proposed in [139]. Initially one E-plane 3-dB

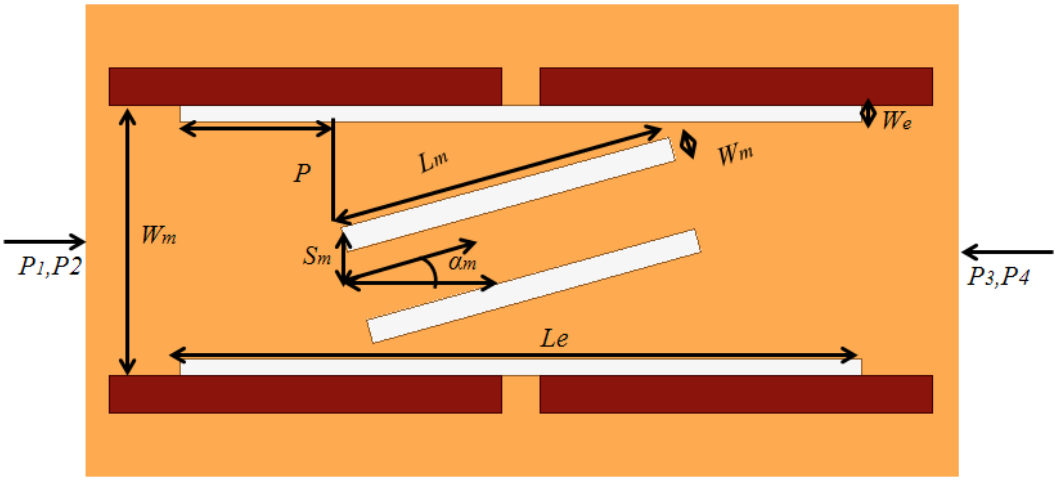

Figure. 5.27. Proposed two layered transition showing the E-plane and H-plane in the same physical distance. The slots are placed in the common layer between two substrates. The dimensions are: D=0.5, Lm=4, Ws=0.25, X=0.2, αm=10°, P=2, Wm=3.6, Le=8.5, Sm=1.5, We=0.2 (all dimensions are in mm).

directional coupler is designed and all the parameters are optimized to achieve 16% bandwidth at 35 GHz. The two designed 3-dB couplers are cascaded in series with slots inclined at an angle of 90° with each other, so that the 0-dB coupling is achieved over 28% of operating bandwidth. All the slot parameters are optimized and the physical parameters are given in Figure. 5.25. The coupling section occupies a physical length of 2.25λg at the operating frequency of 35 GHz. Figure. 5.26 plots the isolation from port 1 to port 2 for two different values of length P = 5mm, 11 mm. The coupler response is periodically repeated for each distance of one guided wavelength. The 20-dB isolation bandwidth of the coupler is of 28% at 35 GHz (from 29 GHz to 40 GHz).

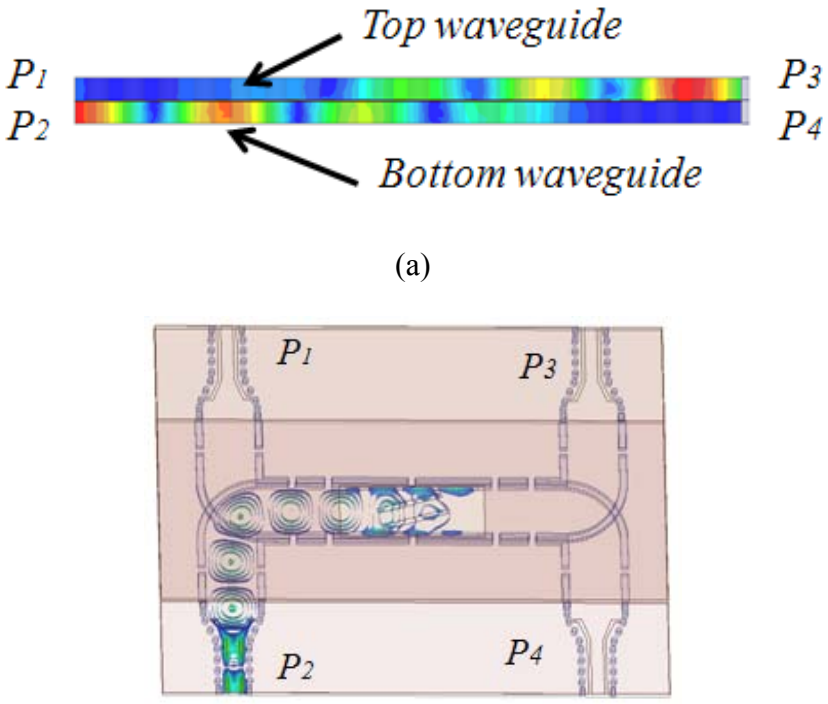

Figure. 5.28. The E-Field (at 35GHz) coupled through (a) the two-layer structure (b) the bottom waveguide.

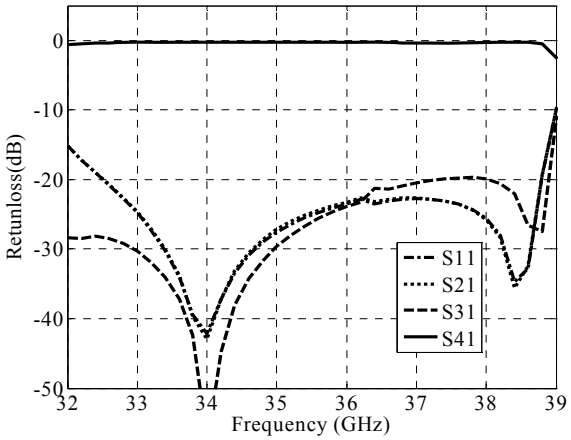

Figure. 5.29. The scattering parameters of the SIW cross over structure without the input transitions.

The 0-dB coupling can also be achieved when the physical distance *P* between different 3-dB hybrid couplers, is made equal to $\lambda_g/4$. To reduce the physical dimension of the cascaded coupler, a new configuration is proposed. As an example, one of the E-plane couplers (slot pair in the middle waveguide) is replaced with another E-plane coupler type (slot pair etched on the edge of the waveguide). We can control easily the length and the width of the slots to ensure the $\lambda_g/4$ criteria and to have the two couplers that are co-centered. The two E-plane coupler parameters are optimized to achieve a flat 0-dB coupling over 17.1% bandwidth. The physical dimensions of the proposed coupler are given in the Figure. 5.27. The power flow through the multi-layer coupling structure at the operating frequency of 35 GHz is illustrated in Figure. 5.28. The maximum amount of power is coupled to the diagonal port on the top waveguide with almost no power reaching the direct port.

When fed from port 1, Figure. 5.30 plots the coupler performance for power division among the other three ports. The coupling section occupies a physical length of $1.21\lambda_g$ at 35 GHz. The coupler transmission loss is less than 0.5dB over the operating bandwidth from 32 GHz to 38 GHz and the amplitude responses are symmetrical about the operating frequency. The 20-dB

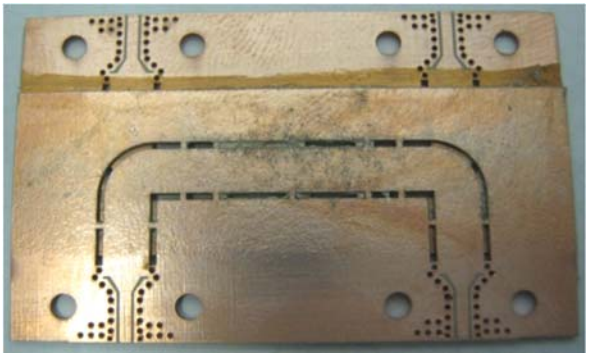

(a)

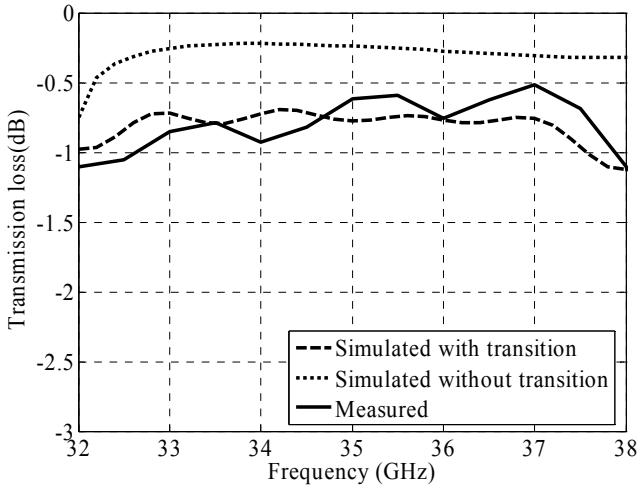

(b)

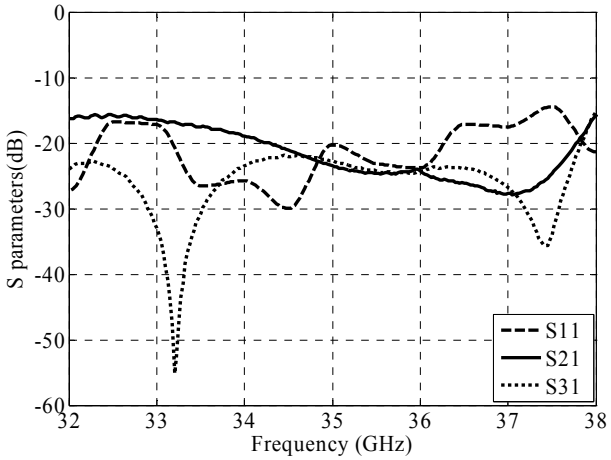

(c)

Figure. 5.30. (a) Experimental prototype of the 0-dB coupler, measured (b) transmission loss S_{41} and (c) return loss S_{11}, isolation S_{21}, and coupling S_{31}.

return loss and isolation bandwidth of the coupler is 17.1% over the operating bandwidth from 32 GHz to 38 GHz. The coupler band of operation shifts towards higher frequencies if the physical distance *P* is varied from zero to higher value. The coupler exhibits similar performance and also 47% of size reduction when compared with the cascaded coupling structure.

The designed coupler is then fabricated by using a multilayer fabrication process. The transition from the grounded coplanar waveguide to the SIW is made to measure the four port coupler. The fabricated coupling strucurer is depicted in Figure.5.30a. The top side of the bottom waveguide consists of four resonant slots and the bottom side of the top waveguide consists of a wider rectangular side covering an area larger than that of edge slot coupler. The two layers are fabricated individually and then glued together to realize the multi-layer coupler. The rectangular slots are metallized after drilled by using a laser micromachining. Simulated and measured insertion losses from port 1 to port 4 are compared and plotted in Figure. 5.30b. Simulated insertion loss is 0.5 dB and measured insertion loss is 0.75 dB at 35 GHz. The increased radio frequency loss is due to the inherent dielectric losses inside the substrate and the increased metallic losses in the process of metallization of the side walls of the SIW. The simulated and measured operating bnadwidths of the coupler are overlapped with each other. The measured retun loss, isolation and coupling values are lower than -17 dB over the bandwidth of 32 GHz-38 GHz. A slight increase regarding the levels of return loss and isolation is caused by a minor mismatch between the input K-connector and the GCPW line. The phyiscal size of the coupler including the input transitions is $4.8\lambda_g \times 3.7\lambda_g \times 0.145\lambda_g$. The size reduction of 53% is achieved over the cascaded version of the crossover structure.

5.2.3 Beamforming network design

Any Butler matrix prototype consists of four 3-dB 90º hybrid couplers and two 45º fixed phase shifters. Various configurations with and without cross-over junction were investigated in the SIW technology [39, 141]. Here, short slot H-plane coupler is chosen as key building block to

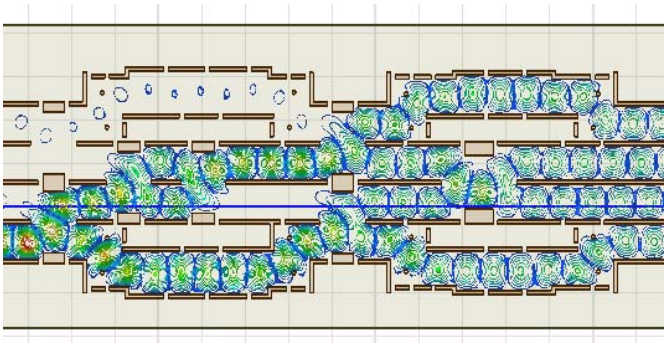

(a)

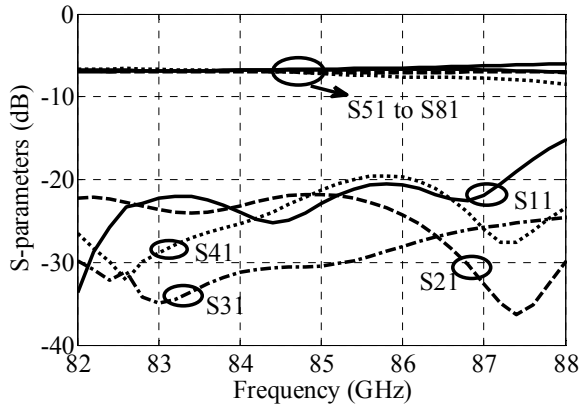

(b)

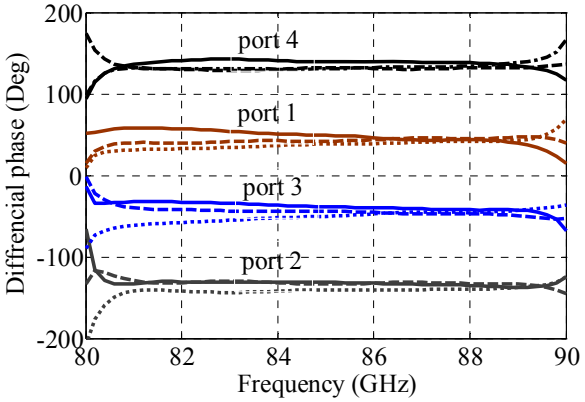

(c)

Figure. 5.31. (a) proposed planar Butler matrix (b) differential phase between the output ports of the Butler matrix,(solid $\angle S6p-\angle S5p$, dot $\angle S7p-\angle S6p$, dash $\angle S8p-\angle S7p$,where p=1,2,3 and 4 (c) S-parameters from port1 to port 5,6,7 and port 8,also coupling from port1 to port 2,3,4.

implement the Butler matrix technique. This type of topology is chosen to feed 4 element linear arrays from the output ends of BFN.

5.2.3.1 Single layer Butler matrix design

The planar H-plane coupler parameters are well optimized for equal power division with 90° phase shift between the coupled and direct ports and achieved 30% bandwidth over which isolation between the coupling ports is better than -20 dB and return loss for input ports below -25 dB. Linear phase progression at the output ports is obtained by arranging four couplers in the planar structure. Two unequal length and unequal width 45º fixed phase shifters are also integrated in the same structure. The planar Butler matrix to feed 1 × 4 linear array is illustrated in Figure. 5.31a. The horizontal to vertical plane interconnect is designed in the SIW technology. The feed guide has a rectangular slot (near to the shorted end of waveguide wall) and then vertical guide is inserted through this rectangular slot. The simulated bandwidth covers over E-band frequencies from 78 GHz to 90 GHz. The simulated insertion loss is ≤ -1.7 dB over the entire bandwidth. The transition allows for a smooth flow of the power from the feed guide to the vertical guide. The BFN matrix has the four input ports 1-4 on input side and the four output ports 5-8 on the output side. The planar BFN is supplying the required theoretical amplitude and phase distribution of -6.01 dB and 45°,-135°,-45°, 135° when fed from ports 1, 2, 3 and 4, respectively. Simulated transmission magnitude and phase parameters versus frequency are shown in Figure. 5.31b, c. Matrix has good amplitude and phase behavior from 81 GHz to 87 GHz, while covering the useful frequency range from 82 GHz to 86 GHz. The transmission parameter magnitudes are -7.7 dB without considering the transition effects. The amplitude difference of 1.7 dB between simulated and measured transmission coefficient is mainly due to the dielectric losses of the substrate and also insertion loss of each coupler is 0.2 dB. The phase dispersion with peak to peak error of 12° less than theoretical values. The phase difference between the theoretical and simulated values is caused by the phase dispersion of unequal length and unequal width phase shifter in the horizontal plane. The maximum amplitude dispersion is within + 1.1 dB over the frequency range of 82 GHz - 86 GHz. The coupling coefficient between input ports P1 to P4 is also shown in the Figure. 10b.From port 1 to port 2,3,4 coupling is less than -20dB over the desired frequency range of 82 GHz to 86 GHz. As shown in Figure. 10c, the optimized peak-to-peak phase dispersions of each port is less than 12° over the frequency range of 82 GHz - 86 GHz. Impedance differences at each interface of the BFN are

minimized to reduce reflections and to maximize the power transfer through the each part of the array.

The BFN is maintaining a compact size and also can feed 1×4 linear array of LWA sources. The spacing between the output ports is less than 0.6λo, so that the array can have scanned beam patterns without any grating lobes in the scan region. The whole size of BFN is 30mm × 14mm × 0.508mm.This BFN can be used to scan quarter part of full space scan region. The matrix scan capability is further extended by using the dual layer feed network.

5.2.3.2 Dual layered Butler matrix design

The transmit/receive modules in any phased array radar system were using circulators to enable the antenna system for simultaneous operation [142]. The lossy and expensive circulators can be replaced by simple cross-over-junction to realize the working principle of the circulator. When the two 3-dB 90º couplers are cascaded in a series manner, the signal enters at one port will exit through the diagonally located port. The combination will work as 0-dB coupler. This is a type of topology that has been used in many applications to realize the cross-over junction [135, 136]. The dual-lens structure loaded with 3-dB hybrid couplers was proposed in [131] to use the lens as a simultaneous transmit and receive antenna. However, only theoretical aspects are discussed. The lens type of BFNs requires a careful design of beam port and element port contour to minimize the phase and amplitude errors. The coupler isolation between the adjacent ports is less than -25 dB from 75GHz to 100GHz..From port 1 power is transferring to diagonal port with almost no power is being coupled to other remaining two ports. Impedance is well matched over the frequency band from 75 GHz to 90 GHz.

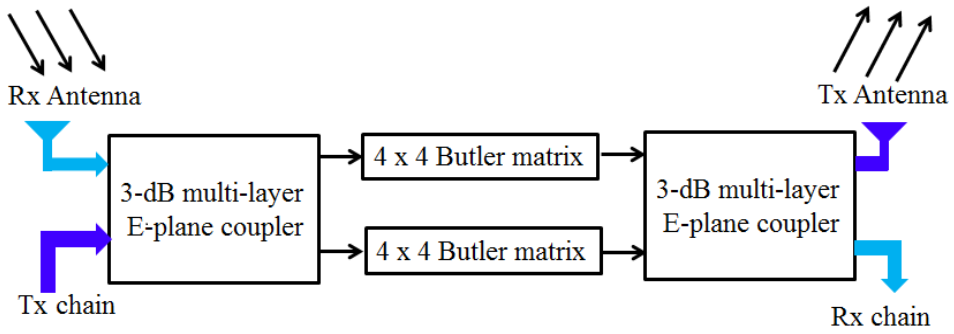

Figure. 5.32. Proposed circuit diagram for feeding transmit and receive arrays.

The proposed feed network schematic is explained in Figure. 5.32. A 3-dB coupler is realized by etching slot pair near the edge of the waveguide wall [26]. A 4×4 Butler matrix based BFN is chosen to obtain the desired phase and amplitude profile. The design complexity for the Butler matrix based BFN is reduced when compared to lens based BFN. The two BFNs are duplicated and placed one below the other. For example, a signal available at the output of the power amplifier in the transmitter chain will pass through the two 3-dB couplers and two Butler matrices and then transmitted by the antenna element. In the similar manner, the signal received at the receiver antenna is collected by the receiver port placed diagonally and then later processed in the receiver chain. The same operation is visualized in Figure. 5.33. Here, the antenna elements can be used for simultaneous transmission and reception without using any circulators. The beam and element ports are defined in the Figure. 5.34.

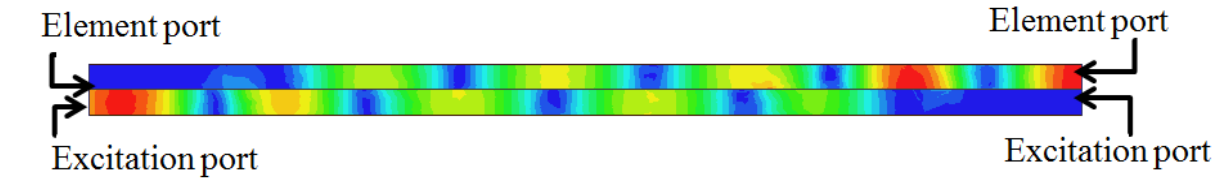

(a)

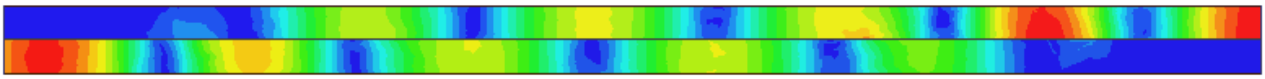

(b)

Figure. 5.33. The Tx chain and Rx chain are connected to the excitation ports located on the bottom layer. Signal flow through the dual-layered feed for (a) Rx case and (b) Tx case

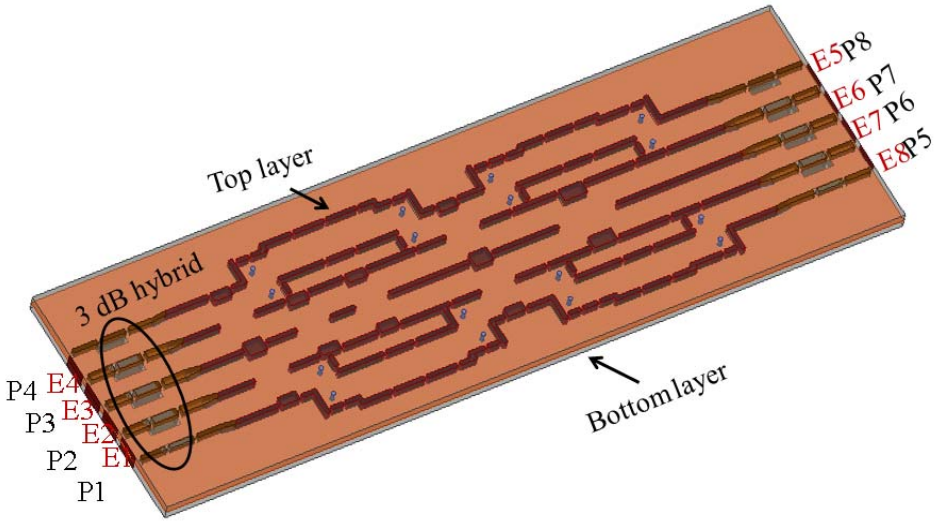

Figure. 5.34. A feed network showing two similar 4 x 4 Butler matrices in two layers.

5.2.3.3 Dual layer BFN simulated S-parameters

The simulated reflection, transmission and coupling coefficient magnitude parameters versus frequency are shown in Figure. 5.35a, b. Transmission parameters are shown from port 1 to element ports E5, E6, E7 and E8. The transmission parameter magnitudes are close to 7.5 dB. The value is similar to the value obtained for single BFN. All the reflection and coupling coefficients are lower than -20 dB over the operating bandwidth from 82 GHz to 86 GHz. The phase performance versus frequency is not affected by the input 3-dB hybrid couplers at the both ends. The phase dispersion between element ports of the two layered BFN with peak-to-peak error of 15° around the theoretical values of 45°, 135°, 45° and -135°, respectively. The differential phase between the output ports of the cross-over junction is less than 5º, hence, it does not affect the phase profile of the two layered BFN. The matrix phase behavior is flat over the entire frequency band. So, when the array is fed by this BFN beam, the deviation with

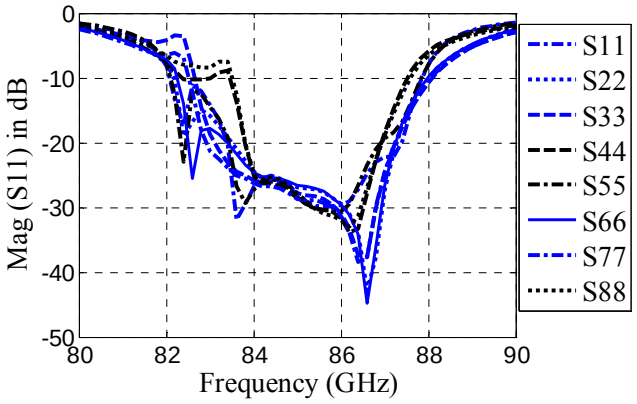

(a)

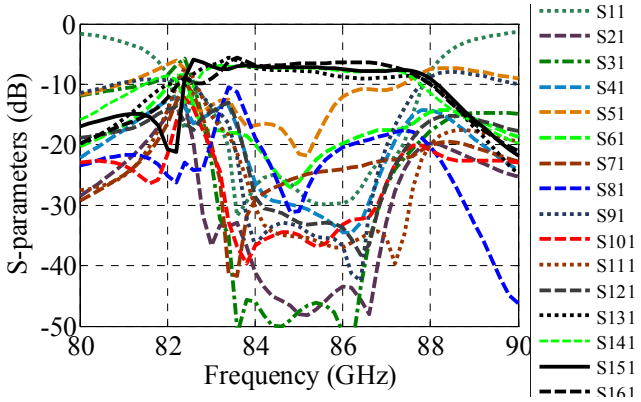

(b)

Figure. 5.35. Simulated (a) return loss and (b) coupling coefficients of proposed multi-dimensional phased array scanning system.

reference to operating frequency will be small. A similar performance is obtained for remaining beam-ports P5-P8 due to the nature of geometrical symmetry.

5.2.4 Simultaneous transmit/receive operation

The combination of frequency scanning antenna and phase scanning BFN produces multiple beams only in a limited scan region. The MBA is useful only for transmitting or only for receiving power at a given time [39]. The scan region is limited only to the right half of the sphere. To further extend the MBA capability to be used as simultaneous transmit and receive functions, a dual layered feed matrix is used to obtain the phase steered beams in the orthogonal plane. The MBA can also able to cover a full sphere scan region. Complete design

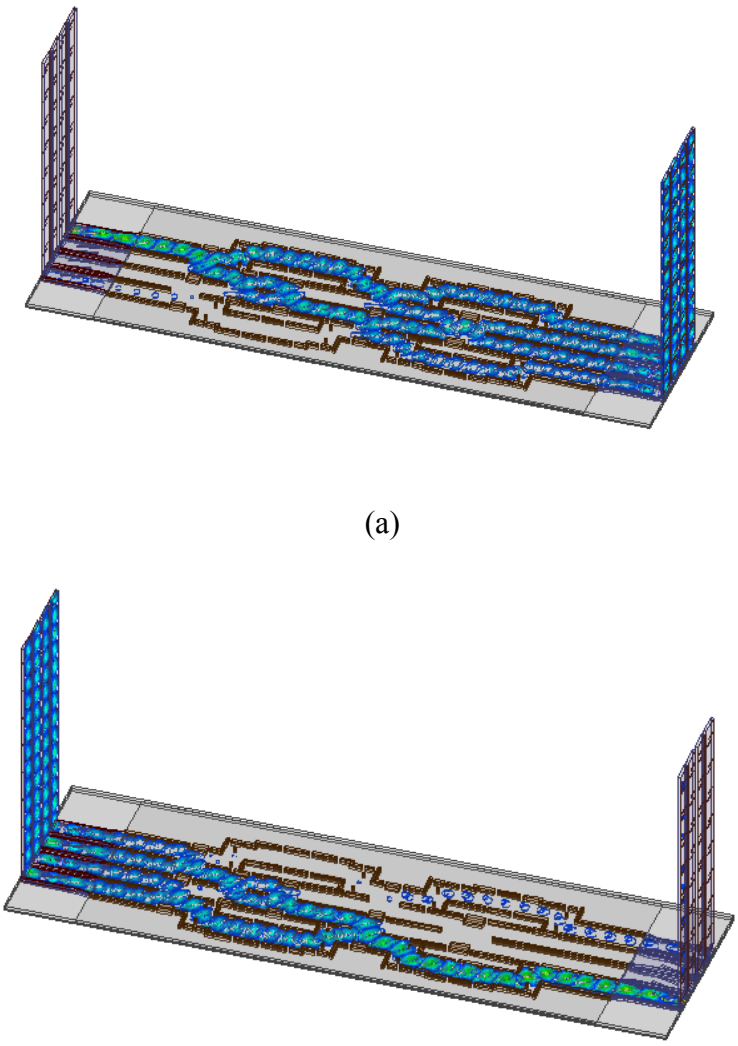

(a)

(b)

Figure. 5.36. Proposed multi-dimensional phased array scanning system (a) in transmitting mode and (b) in receiving mode.

of the proposed two layered feed network and increased frequency scan capability LWA is discussed in this section.

As a proof-of-concept, Butler matrix BFN is chosen and realized in the standard topology. The matrix scanning performance was experimentally proved for 60 GHz smart antenna system [23]. Continuous aperture H-plane coupler, cross-over junction, and 45º fixed phase shifters are

used together to design the BFN operating frequency at 84 GHz. Each of the Butler matrix input and output ports are loaded with 3-dB hybrid coupler.

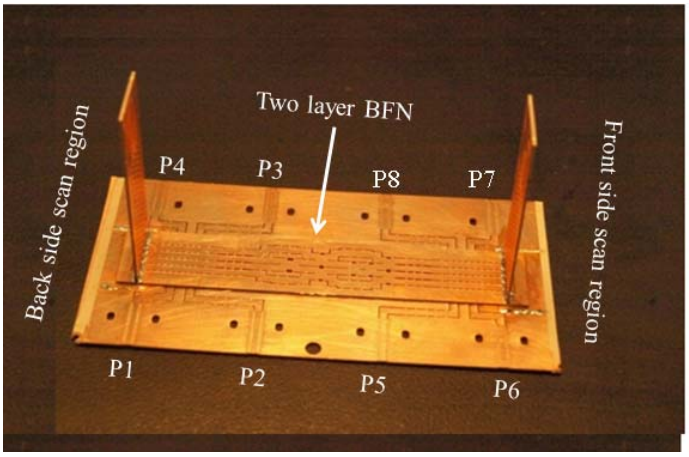

Figure. 5.37. Proposed multi-dimensional phased array scanning system, where excitation ports on the bottom layer, for Tx array from P1-P4 are on the left side and for receive array from P5-P8 are on the right side.

The power flows smoothly over the two layered structure and feeds the transmitting array. The power leakage into the array ports and also into the excitation ports P5-P8 is almost negligible. An array can transmit phase scanned patterns by changing the excitation ports also frequency scanned patterns by changing the input frequency. The operation for simultaneous transmitting/receiving array can be understood from the electric field visualization shown in Figure. 5.36. Experimental prototype of the MBA is shown in Figure. 5.37, where eight input ports from P1-P8 are located on the bottom layer of BFN and eight output ports on the top layer of BFN are feeding two arrays of LWA sources. The array scanned performance in terms of scan range and gain is discussed below. The complete array is free from any grating lobes in the scan region. Calculated peak gain for different operating frequency and for different input ports is calculated to be close to 14.5 dB. The beams-scanned away from the broadside are experiencing a gain loss of 2.8 dB.

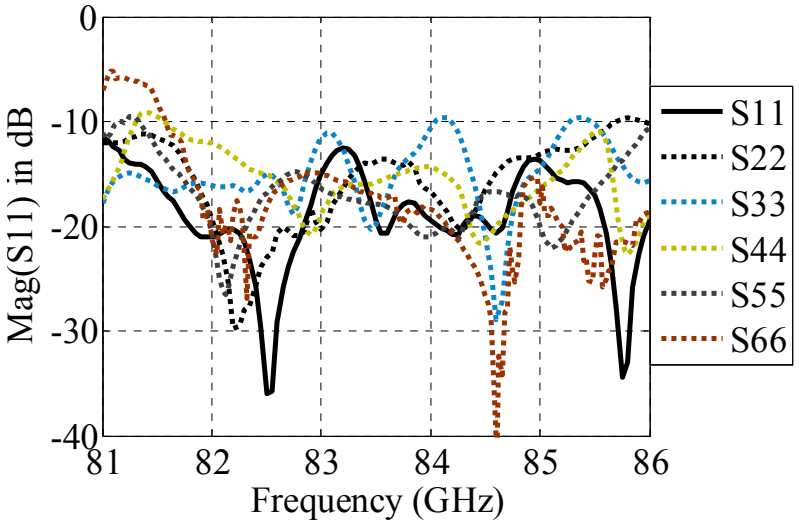

(a)

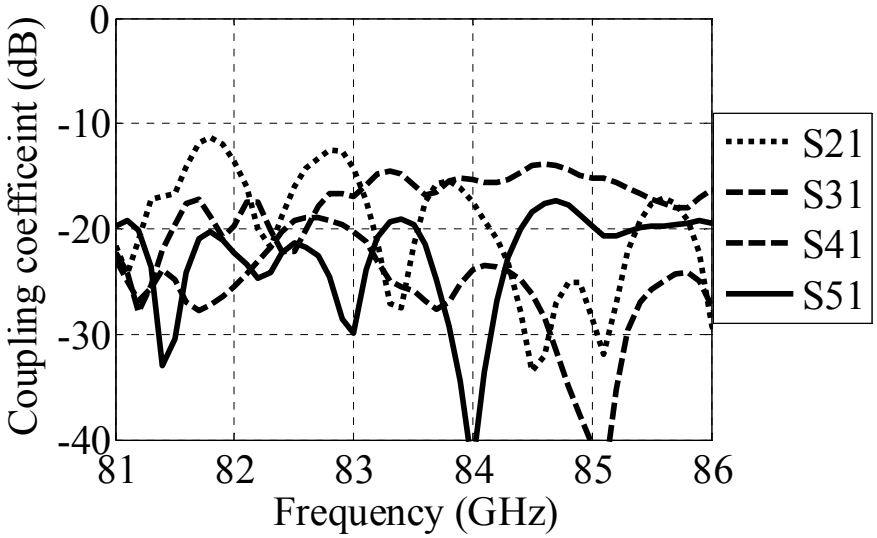

(b)

Figure. 5.38. Measured S-parameters (a) when excited at port P1, P2, P3 and P4 (b) when excited at port P1 and collected at P4, P5 and P6.

5.2.4.1 Measured S-parameters

The MBA input reflection coefficient and coupling coefficients are measured by using an Anritsu 37397 vector network analyzer after the use of a standard TRL calibration. Figure. 5.38a plots the measured reflection coefficient of the beam-ports *P1*, *P2*, *P3*, *P4, P5, P6* and *P7*. The

return loss for all the ports is lower than 10 dB over the desired frequency band from 82 GHz to 86 GHz. Figure. 5.38b plots the measured isolation between the beam-ports of the 2-D scan antenna. All the isolation coefficients are lower than -15dB over the operating bandwidth from 82 GHz to 86 GHz. An increased isolation from P1 to P2 is due to the minor mismatch between the coupler ports and excitation ports. Graphical visualization of electric fields given in Figure. 5.36 shows that most of the power coupling to desired ports. The S-parameters are also behaving in the similar manner as in the case of the transmitting array. The isolation value between transmitting and receiving ports is less than 20 dB.

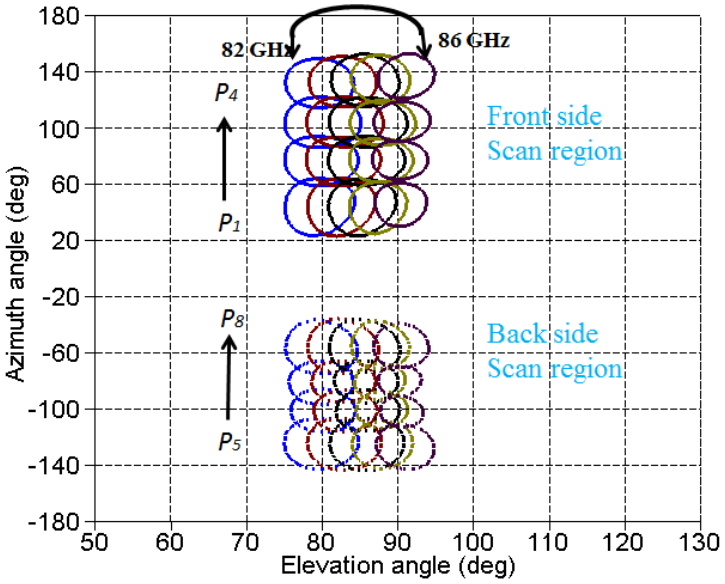

Figure. 5.39. HPBW plot showing all the 16 phase-steered beams and also four frequency-steered beams.

5.2.4.2 HPBW plot of the scanned beams

The simulated 2D contour plot of half-power beam-width (HPBW) is shown in Figure. 5.39. The MBA is able to form multiple beams covering the scan range from is from ((phi, theta)) (50°, 90°) to (120°, 90°) for *P1-P4* with four phase steered beams and from (-50°, 90°) to (-123°, 90°) for *P5-P8* with four phase steered beams. These azimuth scanning beams are at a fixed frequency point and MBA covers an elevation angle of 19º from (-50°, 75°) to (-50°, 94°) by sweeping frequency over a fixed input port *P1*. The right part of the scanned beams corresponds to excitation ports *P1-P4* and left part of the scanned beams corresponds to excitation ports *P5-P8*. As frequency

is sweeping from 82 GHz to 86 GHz, beams are moving close to each other with narrowing the HPBW, because array spacing is normalized to the frequency of 82 GHz. The HPBW for the frequency scanning arrays is calculated to be 7º and for phase steered array is calculated to be 28º for each beam port.

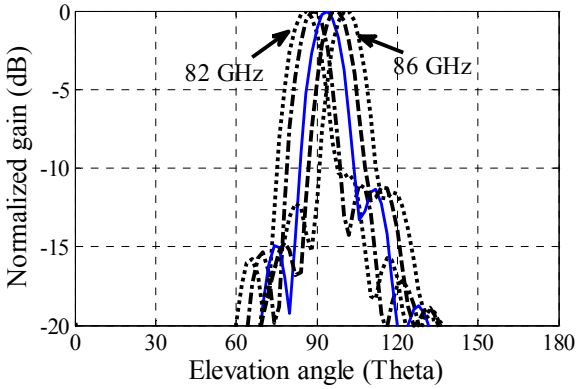

(a)

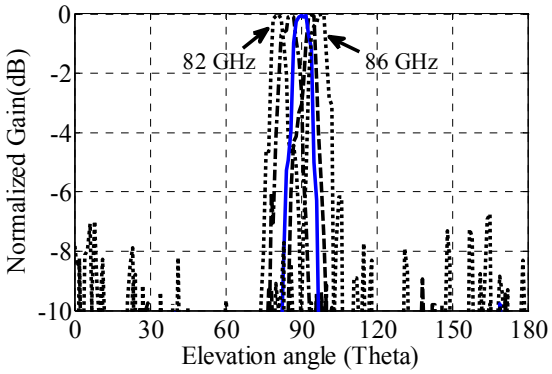

(b)

Figure. 5.40. (a) Simulated elevation plane pattern using one-port LWA (input frequency changing from 83 GHz to 86 GHz at an interval of 1 GHz) when fed from P1.(b) Measured elevation plane pattern using one-port LWA (Beam port is changed from P1 to P4) when source frequency is set at 84 GHz.

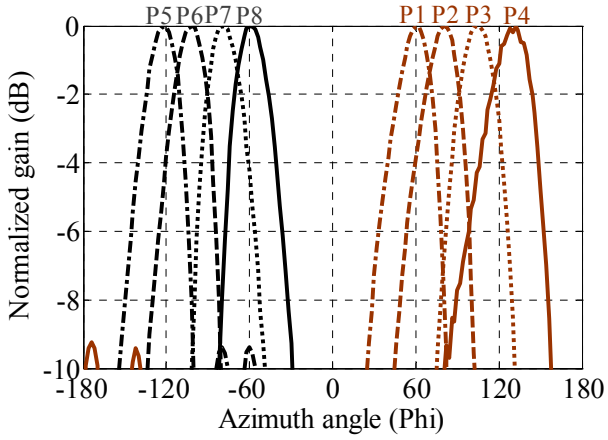

(a)

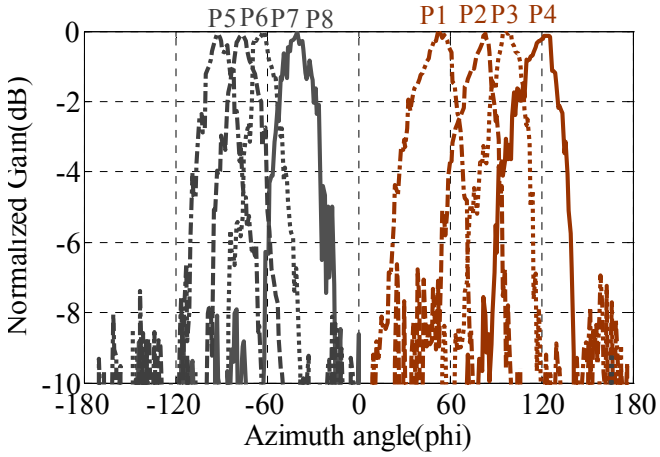

(b)

Figure. 5.41. (a) Simulated azimuth plane pattern using one-port.(b) Measured elevation plane pattern using one-port LWA (when fed from P1, Beam port is changed from P1 to P4) when source frequency is set at 84 GHz).

5.2.4.3 Two way Tx or Rx MBA radiating performance

The LWA is acting as radiating array to design two ways transmit or receive array. The spacing between the array elements is chosen to be 0.6λ at 84 GHz. The LWA array is combined with two layered BFN to show a multi-dimensional phased scanned array system for both transmit and receive operations. The directional pattern measurements are conducted in the MI technology

anechoic chamber inside our Poly-Grames Research Centre. In this compact range setup antenna under test is used as a receiver sweeping in azimuth plane.

Figure. 5.40a, b plots the simulated measured E-plane directional patterns by changing frequency from 82 GHz to 86 GHz at an interval of 1 GHz when fed from port 1. For port 1, the peak gains are measured to be 14.7 dBi, 15.1 dBi, 15.4 dBi, 15.8 dBi, and 16.2 dBi at 82, 83, 84, 85 and 86 GHz. The beam directions in E-plane at an H-plane angle of 54° are measured to be 80°, 84°, 89°, 94.7°, and 99° . For port 4, the peak gains are measured to be 13.5 dBi, 14.3 dBi, 14.9 dBi, 15.1 dBi, and 15.8 dBi at 82, 83, 84, 85 and 86 GHz. The beam directions in E-plane at an H-plane angle of 125° are measured to be 80°, 84°, 89°, 94.7°, and 99° at 82, 83, 84, 85 and 86 GHz.

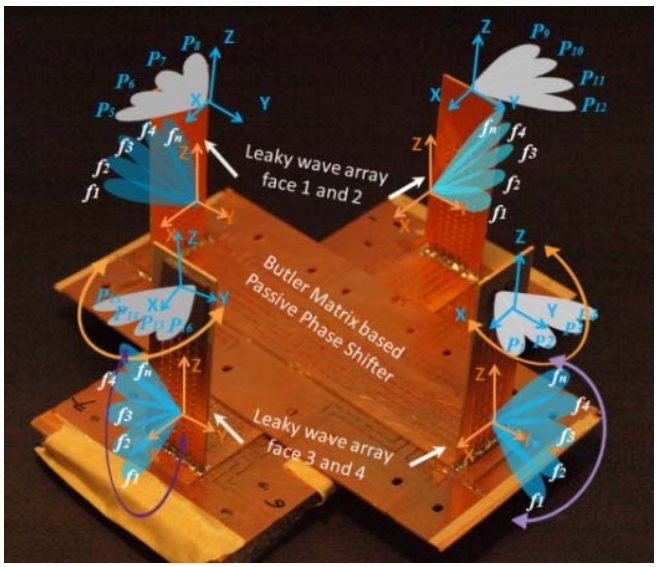

Figure. 5.42. Experimental prototype of the multi-beam antenna forming 2-D scanned patterns

Figure. 5.41a, b plots the simulated and measured H-plane directional patterns at 84 GHz by changing the input from port 1 to port 8. The peak gains are measured to be 13.6 dBi, 14.1 dBi, 14.2 dBi, 13 dBi for port 1 to port 4. The same value peak-gain values are noted for other four ports P5 to P8. The beam directions are measured in H-plane at E-plane angle of 85°. The beam directions for P1 to P4 are measured to be 54°, 83°, 97°and 125°, respectively. The beam directions for P5 to P8 are measured to be -93°, -76°, -63°and -40°respectively. Beams shapes are symmetrical in nature due to the symmetry of BFN topology. MBA is having measured 3 dB beam width of 25° and 8° in the azimuth-plane and elevation-plane, respectively. The beam direction agreement between simulated and measured result is obtained for all the ports.

5.2.5 Full-space scan array with simultaneous transmit/receive operation

The MBA discussed in section 5.2.4, is acting as simultaneous Tx or Rx in only two directions. The scan capability can be extended to cover full space region by placing two MBA orthogonal to each other. The final experimental prototype of the proposed full-space scan phased array system is shown in Figure. 5.42. The MBA functioning as four way transmitter or receiver with multiple scanned patterns in all four facets of the full sphere. Here, two independent MBA are placed orthogonal to each other. Each beam of leaky wave array is phase-steered by using the

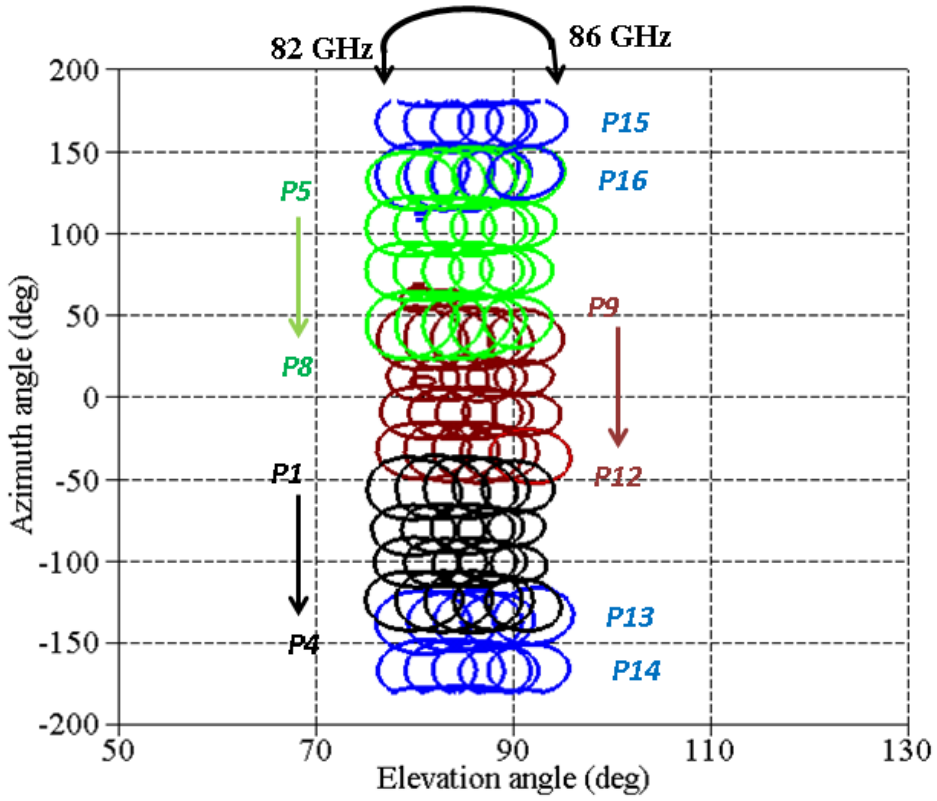

Figure. 5.43. HPBW plot showing all the 16 phase-steered beams and also five frequency-steered beams.

Butler matrix. Total numbers of inputs are 16 and output end of LWA is match-terminated Preliminary results are reported in [28], but here the complete design details and measured performance are given and discussed. This section demonstrates the complete performance of the full space scan performance by comparing simulated and measured results.

.

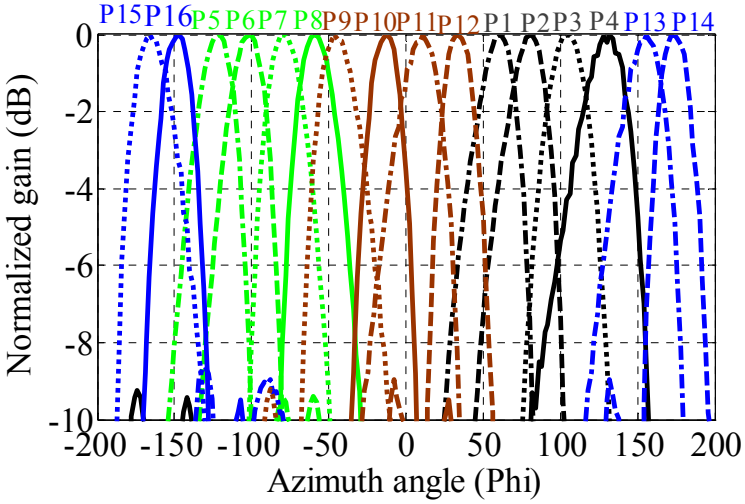

(a)

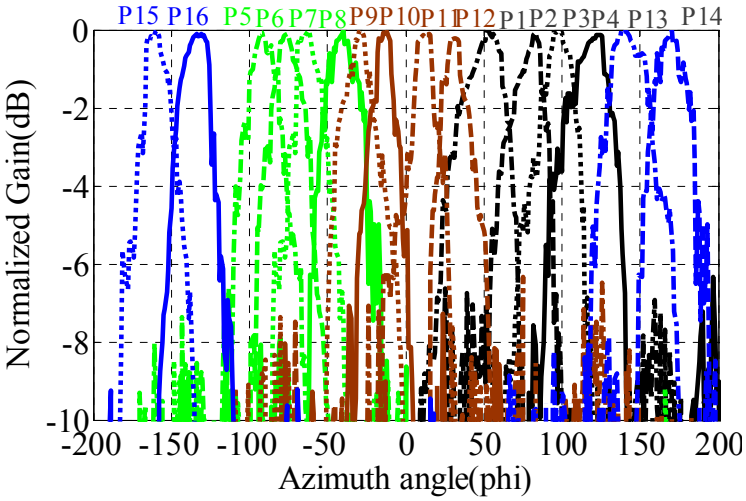

(b)

Figure. 5.44. (a) Simulated and (b) measured azimuth plane pattern of the phase-steered beams for 16 inputs.

5.2.5.1 HPBW plot

The simulated 2D contour plot of HPBW is shown in Figure. 5.43. The MBA is able to form multiple beams covering the scan range from ((phi, theta)) (-160, 90°) to (160°, 90°) for P1-P16 and at a fixed frequency point of 84 GHz. For each port by sweeping frequency, MBA scans

an elevation region of 20º scan angle. Azimuth region is densely covered with phase steered beams of BFN and elevation is covered with frequency steered beams of the LWA

5.2.5.2 Full plane scan measured performance

The MBA is measured in MI technology anechoic chamber over the frequency range from 82 GHz to 86 GHz. MBA radiation pattern is measured in each half planes for beam ports *P1-P16*. The entire array elements are fed with equal power distribution and constant phase profile supplying by corresponding beam port. Figure. 5.44a plots the simulated azimuth plane pattern of the MBA for all the 16 beam ports, when input frequency is fixed at 84 GHz. Figure. 5.44b plots the measured azimuth plane pattern of the MBA for all the 16 beam ports, when input frequency is fixed at 84 GHz. The measured elevation plane for each port when frequency is changed from 82 GHz to 86 GHz is similar as shown in Figure. 5.40.

5.3 Conclusion

In this chapter, two types of 2-D passive phased array with phase scan in one plane and frequency scan in the orthogonal plane are demonstrated.

In the first prototype, 2-D scan conformal array is realized by feeding LWA with the Rotman lens based phase shifter in the SIW technology. The wideband matching condition (28.5% of 2:1 VSWR bandwidth) is achieved at 70 GHz for the LWA by adding reflection cancellation stub. It is expected that with increase in number of slots the maximum amount of power gets radiated from LWA, so that the reflection from the matched termination becomes insignificant. The multi-beam antenna can efficiently cover the solid angle of (49°,84.5°) to (120°, 70°) ((phi, theta)) by multiple beams. The whole array including beam forming network and radiating elements has been benefiting from the advantages of low-cost SIW technology. An inexpensive wideband matched termination with satisfactory performance is integrated for sidewalls and also for LWA. The demonstrated antenna system is readily usable particularly for E-band (73GHz-78GHz) low-cost commercial automobile applications. The antenna steering capability can be extended to full 360° scan by making use of multiple lenses.

Furthermore, a novel crossover junction is studied and realized by using two proposed methods each using the vertical coupling of electromagnetic fields within the multi-layer structure. The simultaneous electric and magnetic field coupling is effectively used for the miniaturization of the

first method. The SIW technology is used to implement the mm-wave multi-layer transition. A low-loss and wideband behavior of the miniaturized coupler is very useful in the size reduction of larger beamforming networks such as 8 × 8 Butler matrix.

Finally, full space scan phased array system is demonstrated in SIW technology. Butler matrix-based passive phase shifting is used to scan a 1×4 array of one-port leaky-wave antennas. The proposed LWA can also radiates in bi-directional , by etching slots 45º inclined slots on the top and bottom ground planes, produces two directional radiated beams with equal power. The dedicated channel for transmit and receive arrays allows send/receive power simultaneously in multiple directions. The MBA is free from expensive circulators, which are normally used to realize T/R module. The proposed scheme will provide a technique to develop a low-cost microwave and millimeter-wave full-plane scanning systems or simultaneous transmit/receive platforms. The demonstrated antenna system is readily usable particularly for E-band (82GHz-86 GHz) low-cost commercial automobile applications.

CHAPTER 6 CONCLUSIONS AND FUTURE WORK

6.1 Conclusions

The frequency spectrum over the mm-wave frequency range offers numerous advantages when compared to the lower end of frequency spectrum. In particular, at mm-wave frequency, antenna system is smaller in footprint, and offers a higher data-rate transfer capability. However, radiation efficiency decreases because of feeding network losses and mutual coupling effects at mm-wave frequencies. In this PhD research, new solutions were proposed to solve some of bottle-neck problems of the mm-wave antenna front end systems such as efficiency, polarization diversity, compact feeding geometry and full system integration.

Radar systems require advanced phased array technologies in order to obtain rapid beam scanning, transmit and receive functions at multiple simultaneous scan angles, and capabilities to distinguish between targets of various polarization signatures. In this PhD thesis, new phased array antenna techniques have been investigated and developed to steer the radiated beam electronically in multiple directions to be used in advanced radar systems.

The main high lights addressed in this PhD thesis are summarized through a flow chart below, and each component is discussed in detail.

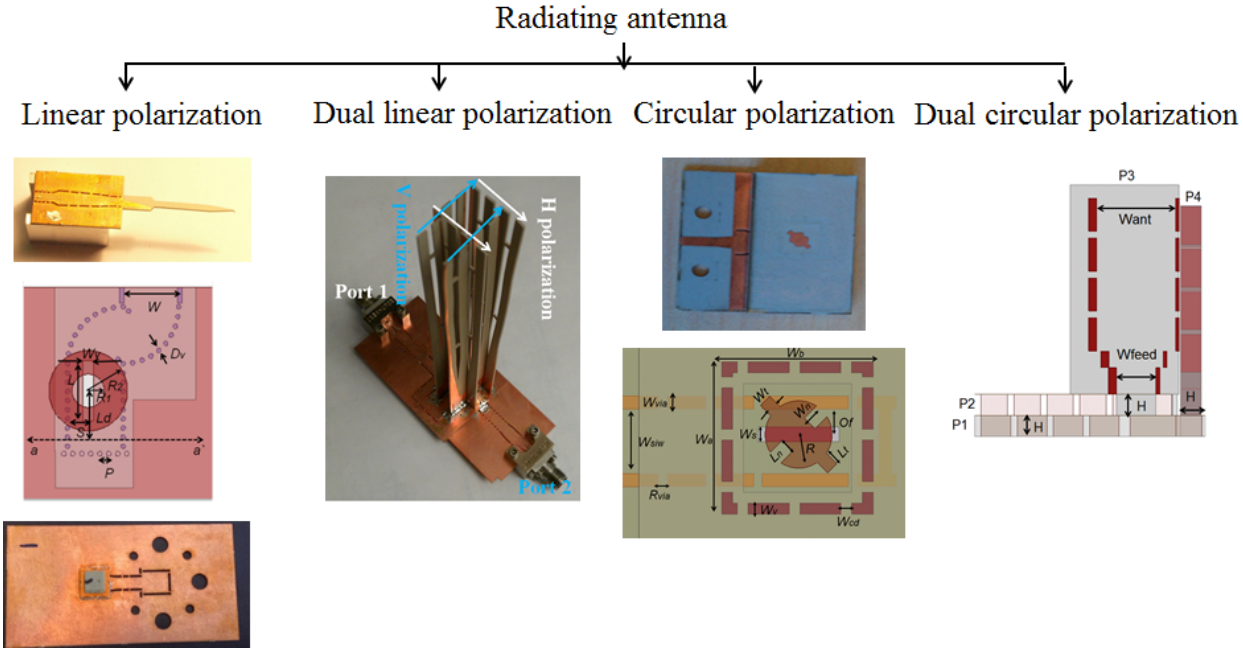

Figure 6.1: Different types of radiating elements.

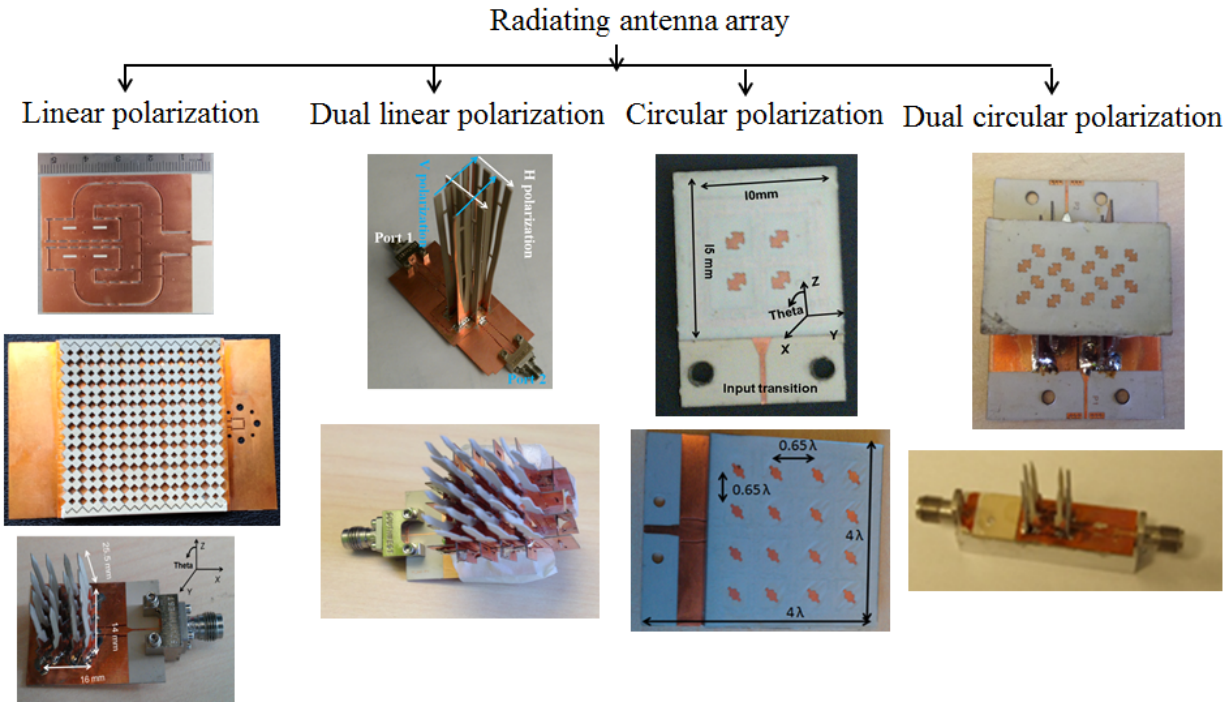

Figure 6.2: Different types of antenna arrays

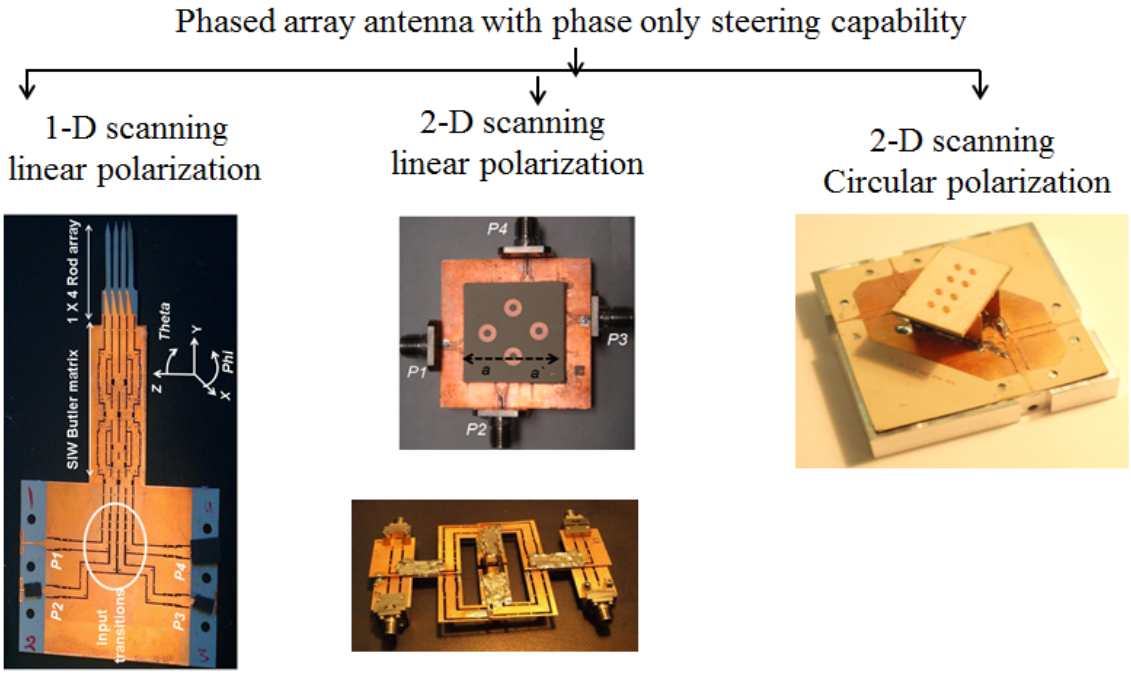

Figure 6.3: Different types of 1-D and 2-D scan phased array antennas with limited scan range using phase only technique

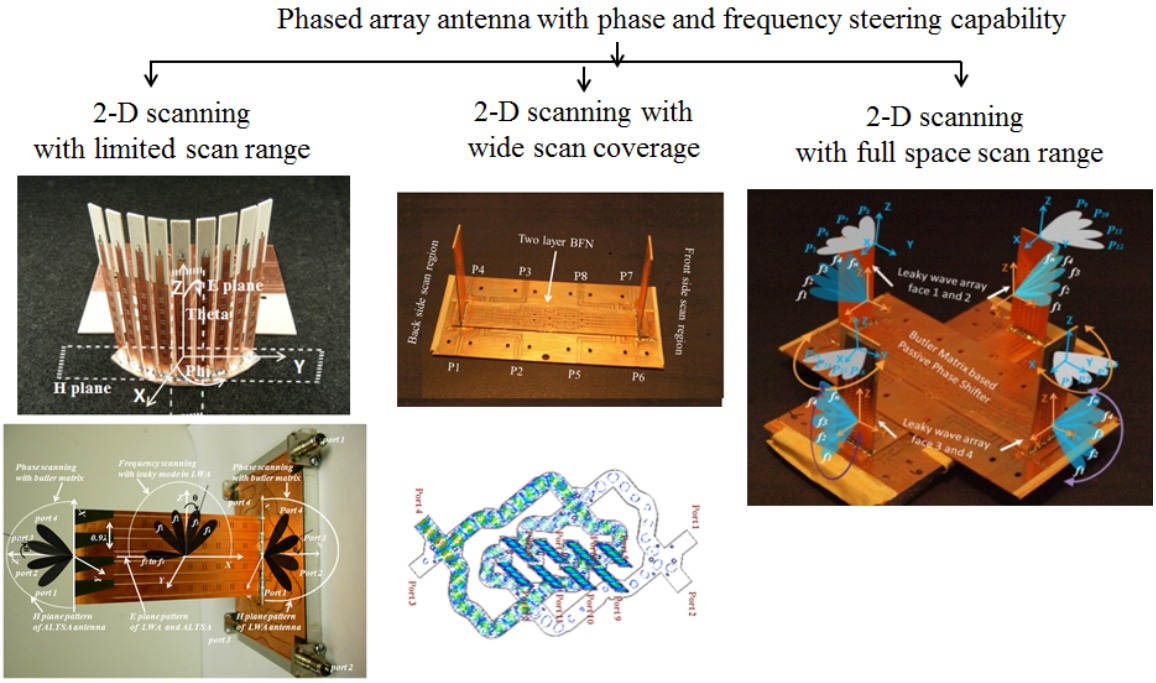

Figure 6.4: Different types of 1-D and 2-D scan phased array antennas with wide scan range using phase and frequency scanning technique

The highlights of the antenna front-end systems investigated in this thesis work are summarized as follows:

In fixed beam antenna array techniques,

- High aperture and radiation efficiency dielectric rod antenna is proposed, which is driven by a low-cost and low-loss SIW structure. The simple architecture of antenna allows more freedom in designing high-gain antenna arrays with multiple polarization signatures. The designed antenna can be readily combined with any beam-forming technique to achieve multi-dimensional scanning patterns with polarization agile capability.

- In advanced radar system, 45^{o} polarization is advantageous then 0^{o} or 90^{o} polarization. For this purpose, 45^{o} linearly polarized antenna array is proposed and implemented at 60 GHz frequency range. Antenna occupies a volume of 14 mm × 16 mm × 25.5 mm. The average measured peak gain of 17.5 dBi is obtained with 16 rod antenna elements. The gain enhancement is achieved without increasing any feed network size. Gain can

be further increased by utilizing the rod antenna length in the third dimension. The array gain is enhanced without increasing the size of feeding network.

- A simple technique is studied to implement higher order dual linearly polarized (DLP) antenna array with high gain and acceptable radiation characteristics at 60 GHz frequency. The feeding network effectively utilizes inter-element spacing between antennas and excites two orthogonal polarized components simultaneously. The techniques proposed are easily scalable to higher mm-wave frequency. The three-dimensional antenna is integrated in SIW technology and fabricated in low-cost fabrication process.

In scanned beam antenna array techniques, we proposed new methods to steer the beam in one and two dimensional scan space with linearly polarized and circularly polarized radiated beams.

- The 2-D scan 2 × 2 planar array fed by an eight port hybrid BFN for four independent orthogonal beams is proposed, studied, fabricated and validated. The conductor, dielectric and metallic losses of the dielectric substrate are responsible for a significant RF loss inside SIW BFN, hence the radiation efficiency and gain are reduced. The GCPW to SIW transition for BFN allows measurements of antenna through a K-connector as an interface. The proposed 2 × 2 planar array can effectively scan in four quadrants with four independent orthogonal beams.
- The 2-D passive phased array with phase scan in one plane and frequency scan in the orthogonal plane is obtained by feeding LWA with the Rotman lens based phase shifter in the SIW technology. The whole array including BFN and radiating elements benefits from the advantages of low-cost SIW technology. An inexpensive wideband matched termination with satisfactory performance is integrated for sidewalls and also for LWA. The demonstrated antenna system is readily usable particularly for E-band (73-78 GHz) low-cost commercial automobile applications. The proposed conformal phased antenna array systems and deployed low-cost technologies can easily be expandable to any other mm-wave and terahertz frequency ranges.
- Butler matrix-based passive phase shifting is used to scan a 1×4 array of one-port leaky-wave antennas. Efficient phased array system is designed on low loss substrate and

fabricated in the SIW technology. The proposed LWA can also radiate bi-directionally, by etching slots 45º inclined slots on the top and bottom ground planes, producing two directional radiated beams with equal power. The array scan region is extended to the full space by placing two MBA orthogonal to each other. The measured results confirm the multi-dimensional scanning capability of the proposed system in four half plane. The MBA is free from circulators, which are normally used to realize T/R module. The proposed scheme provides a technique to develop a low-cost microwave and mm-wave full-plane scanning systems or simultaneous transmit/receive platforms.

High data rate communication systems rely upon phased arrays for adaptive beam forming and improved system capacity. The advanced phased array systems are rapidly replacing traditional mechanically controlled array systems in part due to their higher reliability and recent trend in more affordable costs. The beam forming is one of the important features of the phased array system, where the generation of multiple beams, the electronic control of phase, and the adaptive tuning of beam are three important characteristics of the system. The benefits of beam-forming are the increase of signal gain from a constructive combination of the output signal and the reduction of multipath fading effect.

6.2 Future work

The research work and contributions summarized in this thesis can further be explored in the following mentioned areas:

- The single circularly polarized (RHCP) phased array antenna data handling capability can be further extended to dual circularly polarized (LHCP and RHCP) phased array by using the folded BFN concept.
- High gain dual linear and dual circular polarization antenna arrays with pencil beam radiation characteristics can be obtained by extending SIW corporate feeding network to feed higher order antenna arrays.
- The 3-D SIW feeding antenna and phase shifting network proposed in this PhD thesis are scalable and can be extended to implement high efficiently antenna arrays in sub-THz frequency regime.

- The dielectric rod antenna is excellent choice to implement broadband and high efficiency antennas. Rod antenna can also be designed on silicon wafer for realizing low-cost on-chip antenna for mass production.
- The fixed beamforming smart antenna system can be made continuously steerable by integrating the active component in phase shifting network paths.
- The SIW technology supress the substrate modes, mutual coupling between closely spaced transmission lines is negligible and hence highly dense feeding network can be built to feed higher order dual-polarization antenna arrays
- The proposed techniques play vital roles in the implementation of mm-wave wireless power transmission techniques.

REFERENCES

[1] Z. Yu, L. Sun, and P. Yue, "Keynote address II Towards sub-millimeter wave CMOS circuits," *11th IEEE International Conference on Communication Technology*, pp. 10-12, Nov. 2008.

[2] T.Y.J Kao,Y. Yan, T.M. Shen, A.Y.K Chen, and J.Lin, "Design and Analysis of a 60-GHz CMOS Doppler Micro-Radar System-in-Package for Vital-Sign and Vibration Detection," *IEEE Transactions on Microwave Theory and Techniques*, vol.61, no.4, pp.1649,1659, April 2013

[3] T.M. Shen, T.J. Kao, T.Y. Huang, J. Tu, J. Lin, R.B. Wu, "Antenna Design of 60-GHz Micro-Radar System-In-Package for Noncontact Vital Sign Detection," *IEEE Antennas and Wireless Propagation Letters*, vol.11, pp.1702-1705, 2012.

[4] K.K.M. Chan, A.E. Tan, and K. Rambabu, "Circularly Polarized Ultra-Wideband Radar System for Vital Signs Monitoring," *IEEE Transactions on Microwave Theory and Techniques*, vol.61, no.5, pp.2069-2075, May 2013

[5] X. Y. Bao, Y. X. Guo, and Y. Z. Xiong, "60-GHz AMC-based circularly polarized on-chip antenna using standard 0.18 m CMOS technology," *IEEE Trans. Antennas Propag*., vol. 60, no. 5, May 2012.

[6] T. Paing, E. Falkenstein, R. Zane, and Z. Popovic, "Custom IC for ultra-low power RF energy harvesting," *Twenty-Fourth Annual IEEE Applied Power Electronics Conference and Exposition*, pp.1239-1245, Feb. 2009

[7] T. Paing, E. Falkenstein, R. Zane, and Z. Popovic, "Custom IC for ultra-low power RF energy harvesting," *Twenty-Fourth Annual IEEE Applied Power Electronics Conference and Exposition*, pp.1239-1245, Feb. 2009

[8] P.R.Rao,"Role of mm-waves in terrestrial and satellite communications" *Int. Journal of Systems and Technologies*. 2010. Vol. 3, No.1. pp. 25-34.

[9] Z. Yuan, Z. Liu, and J. Zhang, "Inter-satellite link design for the LEO/MEO two-layered satellite network," *International Conference on Wireless Communications, Networking and Mobile Computing*, vol.2, pp.1072-1075,Sept.2005

[10] N. Shinohara, "Recent wireless power transmission via microwave and millimeter-wave in Japan," *42nd European Microwave Conference (EuMC), 2012*, vol., no., pp.1347-1350, October 2012.

[11] C.T. Rodenbeck, Ming-Yi Li, and K. Chang, "A phased-array architecture for retrodirective microwave power transmission from the space solar power satellite," *IEEE MTT-S International Microwave Symposium Digest, 2004*, vol.3, no., pp.1679-1682 Vol.3, 6-11 June 2004 .

[12] N. Shinohara, "Beam Control Technologies with a High-Efficiency Phased Array for Microwave Power Transmission in Japan," *Proceedings of the IEEE*, vol.101, no.6, pp. 1448-1463, June 2013.

[13] N. Shinohara, "Development of high efficient phased array for microwave power transmission of Space Solar Power Satellite/Station," *Antennas and Propagation Society International Symposium (APSURSI), 2010 IEEE* , vol., no., pp. 1-4, July 2010.

[14] G. Oliveri, L. Poli, and A. Massa., "Maximum Efficiency Beam Synthesis of Radiating Planar Arrays for Wireless Power Transmission," *IEEE Transactions on Antennas and Propagation,* vol.61, no.5, pp. 2490-2499, May 2013.

[15] H.H. Meinel, "Commercial Applications of Millimeter waves – History, Present Status and Future Trends", *IEEE Trans. Microw. Theory Tech.*, vol. 43, no. 7, pp. 1639–1653, Jul. 1995.

[16] Mitola, J., Maguire, G. Q.: 'Cognitive radio: Making software radios more personal'*, IEEE Personal Communications*, 1999, 6, (4), pp.13-18

[17] Hall, P. S., Gardner, P., Faraone, A.: 'Antenna requirements for software defined and cognitive radios', *Proc. IEEE*, 2012, 99, pp.1-9

[18] Tawk, Y., Bkassiny, M., El-Howayek, G., *et al.*: 'Reconfigurable front-end antennas for cognitive radio applications', *IET Microw. Antennas Propag.*, 2011, 5, (8), pp. 985-992

[19] Kenington, P.B.: 'Emerging technologies for software radio', *Electronics & Communication Engineering Journal* ,11,(2), pp.69-83, Apr 1999

[20] Guntupalli, A.B.,Wu, K.: 'Multi-dimensional scanning multi-beam array antenna fed by integrated waveguide Butler matrix', *IEEE MTT-S Int. Microwave Symp*., June 2012, pp.1-3

[21] Cheng, Y.J., Bao, X.Y., Guo, Y.X.: '60-GHz LTCC miniaturized substrate integrated multibeam array antenna with multiple polarizations', *IEEE Trans. Antennas Propag.*, 2013, 61, (12), pp.5958-5967

[22] Guntupalli, A.B., Djerafi, T., Wu, K.: 'Two dimensional scan antenna array fed by the integrated waveguide phase shifter', *IEEE Trans. Antennas Propag*, 2014, 62,(3), pp.1117-1124

[23] Guntupalli, A.B., Wu, K. "60 GHz circularly-polarized smart antenna system for high throughput two-dimensional scan cognitive radio," *IEEE MTT-S Int. Microwave Symp*., June 2013, pp. 1-3

[24] Guntupalli, A.B., Wu, K.: 'Millimeter-wave phased array antenna for high throughput two-dimensional scan cognitive radio', *IEEE Int. Wireless Symp.(IWS),* April 2013, pp. 1-4

[25] R.J. Mailloux, "Phased array theory and technology," *Proceedings of the IEEE* , vol.70, no.3, pp. 246- 291, March 1982.

[26] G.C. Sole, M.S. Smith, "Multiple beam forming for planar antenna arrays using a three-dimensional rotman lens," *IEE Proceedings H Microwaves, Antennas and Propagation*, vol.134, no.4, pp.375-385, August 1987.

[27] W.H. Kummer, "Basic array theory," *Proceedings of the IEEE*, vol.80, no.1, pp.127-140, Jan 1992.

[28] Balanis, C. A.: '*Antenna Theory: Analysis and Design*' (New York: Wiley, 3rd edn. 2005)

[29] B. Sheleg, "A matrix-fed circular array for continuous scanning," *Proceedings of the IEEE*, vol.56, no.11, pp. 2016- 2027, Nov. 1968.

[30] F. Watanabe, N. Goto, A. Nagayama and G. Yoshida, "A pattern synthesis of circular arrays by phase adjustment," *IEEE Trans. Antennas Propagat*., vol. AP-28, pp. 857-863, Nov. 1980.

[31] Bozzi, M., Georgiadis, A., Wu,K.: 'Review of substrate-integrated waveguide circuits and antennas', *IET Microw., Antennas Propag*., 2011, 5, (8), pp. 909–920

[32] Gentile, G., Jovanovic, V., Pelk, M.J., *et al. :*'Silicon-filled rectangular waveguides and frequency scanning antennas for mm-wave integrated systems," *IEEE Trans. Antennas Propag.*,2013, 61, (12), pp.5893-5901

[33] M. C. Kemp, "Millimetre wave and terahertz technology for detection of concealed threats-a review," *Proc. SPIE*, vol. 6402, pp. D01-D19, 2006

[34] H.H. Meinel, "Commercial Applications of Millimeter waves – History, Present Status and Future Trends", *IEEE Trans. Microw. Theory Tech.*, vol. 43, no. 7, pp. 1639–1653, Jul. 1995.

[35] P. F. Goldsmith, C.T. Hsieh, G. R. Huguenin, J. Kapitzky, and E. L. Moore, "Focal plane imaging systems for millimeter-wave lengths," *Trans. Microw. Theory Tech.*, vol. 41, no. 10, pp. 1664–1675, Oct. 1993.

[36] N. A. Salmon, “Scene simulation for passive and active millimetre and sub-millimetre wave imaging for security scanning and medical applications,” *Proc. SPIE*, vol. 5619, pp. 129–135, 2004.

[37] P. S. Hall and S. J. Vetterlein, “Review of radio frequency beamforming techniques for scanned and multiple beam antennas,” *Proc. Inst. Elect. Eng.*, pt. H, vol. 137, no. 5, pp. 293–303, Oct. 1990.

[38] M. Shahabadi, D. Busuioc, A. Borji, and S. Safavi-Naeini, "Low-cost, high-efficiency quasi-planar array of waveguide-fed circularly polarized microstrip antennas," *IEEE Transactions on Antennas and Propagation,* vol.53, no.6, pp. 2036- 2043, June 2005.

[39] A. Borji, D. Busuioc, and S. Safavi-Naeini, “Efficient, Low-Cost Integrated Waveguide-Fed Planar Antenna Array for Ku-Band Applications," *IEEE Antennas and Wireless Propagation Letters*, vol.8, no., pp.336-339, 2009.

[40] M.H. Awida, A.E. Fathy, "Substrate-Integrated Waveguide Ku-Band Cavity-Backed 2 × 2 Microstrip Patch Array Antenna," *IEEE Antennas and Wireless Propagation Letters*, vol.8, no., pp.1054-1056, 2009.

[41] Y. Zhang, Z.N. Chen, X. Qing, and W. Hong , "Wideband Millimeter-Wave Substrate Integrated Waveguide Slotted Narrow-Wall Fed Cavity Antennas," *IEEE Transactions on Antennas and Propagation*, vol.59, no.5, pp.1488-1496, May 2011.

[42] W.M.A. Wahab, S. Safavi-Naeini, and D. Busuioc, " Wide-Bandwidth 60-GHz Aperture-Coupled Microstrip Patch Antennas (MPAs) Fed by Substrate Integrated Waveguide (SIW)," *IEEE Antennas and Wireless Propagation Letters*, vol.10, pp.1003-1005, 2011.

[43] W.F. Moulder, W. Khalil, and J.L. Volakis, "60-GHz Two-Dimensionally Scanning Array Employing Wideband Planar Switched Beam Network," *IEEE Antennas and Wireless Propagation Letters*, , vol.9, no., pp.818-821, 2010.

[44] Y. J. Chen, W. Hong, and K. Wu , "Millimeter-Wave Multibeam Antenna Based on Eight-Port Hybrid," *IEEE Microwave and Wireless Components Letters*, vol.19, no.4, pp.212-214, April 2009.

[45] Y. Shiau, “Dielectric rod antennas for millimeter-wave integrated circuits,”*IEEE Trans. Microw. Theory Tech*., vol. 24, no. 11, pp. 869–872, Nov.1976.

[46] C. Chi-Chih, R.R. Kishore and R Lee, "A new ultra wide-bandwidth dielectric-rod antenna for ground-penetrating radar applications," *IEEE Transactions on Antennas and Propagation*, vol.51, no.3, pp. 371- 377, March 2003.

[47] T Tomur, Y.Miura, Z. Miao, J. Hirokawa and M. Ando, "A 45º Linearly Polarized Hollow-Waveguide Corporate-Feed Slot Array Antenna in the 60-GHz Band," *IEEE Transactions on Antennas and Propagation*, vol.60, no.8, pp.3640-3646, Aug. 2012.

[48] X.-P. Chen, K. Wu, L. Han and F. He "Low-cost high gain planar antenna array for 60-GHz band applications*", IEEE Trans. Antennas Propag*., vol. 58, pp.2126 -2129 2010.

[49] A. Patrovsky and K. Wu, "94-GHz planar dielectric rod antenna with substrate integrated image guide (SIIG) feeding," *IEEE Antennas Wireless Propag. Lett.* , vol. 5, pp. 435–437, 2006.

[50] N. Ghassemi and K. Wu, "Planar Dielectric Rod Antenna for Gigabyte Chip-to-Chip Communication," *IEEE Transactions on Antennas and Propagation*, vol.60, no.10, pp.4924-4928, Oct. 2012.

[51] R. Kazemi, A.E Fathy and R.A Sadeghzadeh, "Dielectric Rod Antenna Array with Substrate Integrated Waveguide Planar Feed Network for Wideband Applications," *IEEE Transactions on Antennas and Propagation,* vol.60, no.3, pp.1312-1319, March 2012.

[52] S. Mei, Q. Xianming and C. Zhi Ning, "60-GHz antipodal Fermi antenna on PCB," *Proceedings of the 5th European Conference on Antennas and Propagation (EUCAP)*, vol., no., pp.3109-3112, 11-15 April 2011.

[53] L. Wang, Y.-X. Guo, and W.X. Sheng, "wideband high-gain 60-GHz LTCC L-Probe patch antenna array with a soft surface*," IEEE Trans. Antennas Propag*, vol.61, no.4, pp.1802-1809, April 2013.

[54] T.M. Shen, T.J. Kao, T.Y. Huang, J. Tu, J. Lin, R.B. Wu, "Antenna Design of 60-GHz Micro-Radar System-In-Package for Noncontact Vital Sign Detection," *IEEE Antennas and Wireless Propagation Letters*, vol.11, pp.1702-1705, 2012.

[55] Y. Li, Z. N. Chen, X. Qing, Z. Zhang, J. Xu, and Z. Feng, "axial ratio bandwidth enhancement of 60-GHz substrate integrated waveguide-Fed circularly polarized LTCC antenna Array," *IEEE Trans. Antennas Propag*, vol.60, no.10, pp.4619-4626, Oct. 2012.

[56] X. P. Chen, K. Wu, L. Han, and F. H. , "Low-cost high gain planar antenna array for 60-GHz band applications," *IEEE Trans. Antennas Propag*., vol. 58, no. 6, pp. 2126–2129, Jun. 2010.

[57] M. Ohira, A. Miura and M. Ueba “60-GHz wideband substrate-integrated-waveguide slot array using closely spaced elements for planar multisector antenna", *IEEE Trans. Antennas Propag*., vol. 58, no. 3, pp.993-998, 2009.

[58] Y. Zhang, Z.N. Chen, X. Qing, and W. Hong, "Wideband Millimeter-Wave Substrate Integrated Waveguide Slotted Narrow-Wall Fed Cavity Antennas," *IEEE Transactions on Antennas and Propagation*, vol.59, no.5, pp.1488-1496, May 2011.

[59] O. Kramer, T. Djerafi, and K. Wu, “Very small footprint 60 GHz stacked Yagi antenna array,” *IEEE Trans. Antennas Propag.*, vol. 59,no. 9, pp. 3204–3210, Sep. 2011.

[60] B.Y. El Khatib, T. Djerafi, and K. Wu, "three-dimensional architecture of substrate integrated waveguide Feeder for fermi tapered slot antenna array applications," *IEEE Trans. Antennas Propag.*, vol.60, no.10, pp.4610-4618, Oct. 2012.

[61] A.B. Guntupalli, and K. Wu, "Polarization-Agile millimeter wave antenna arrays" *Proceedings of Asia-Pacific Microwave Conference, APMC 2012*, Kaohsiung, Taiwan, pp. 148-150, Dec. 4-7, 2012.

[62] A.B. Guntupalli, and K. Wu, " Milli-meter wave antenna arrays for high performance Radar/Radio Systems at 60 GHz" *Proceedings of International symposium on antennas and propagation, ISAP 2013*, Nanjing, China, pp. , Oct. 23-25, 2013.

[63] T.P. Budka, "Wide-bandwidth millimeter-wave bond-wire interconnects," *IEEE Transactions on Microwave Theory and Techniques*, vol.49, no.4, pp.715-718, Apr 2001.

[64] F. Gargione, T. Iida, F. Val doni, and F. Vata1aro, "Services, technologies, and systems at Ka band and beyond-a survey," *IEEE j. Sel. Areas in Comm*., vo1.17, Feb. 1999, pp. 133-144.

[65] Rusek, F.; Persson, D.; Buon Kiong Lau; Larsson, E.G.; Marzetta, T.L.; Edfors, O.; Tufvesson, F., "Scaling Up MIMO: Opportunities and Challenges with Very Large Arrays," *IEEE Signal Processing Magazine*, vol.30, no.1, pp.40,60, Jan. 2013.

[66] M. Bockmair and J. Detlefsen, "A Multistatic Two-Dimensional Millimeter Wave Imaging System at 35 GHz," *13th European Microwave Conference*, pp.540-545, 3-8 Sept. 1983.

[67] A. Doghri, A. Ghiotto, T. Djerafi, and K. Wu, "Early demonstration of a passive millimeter-wave imaging system using substrate integrated waveguide technology," *11th Mediterranean Microwave Symposium (MMS),* vol., no., pp.215-218, 8-10 Sept. 2011.

[68] M.H. Awida, S.H. Suleiman, and A.E. Fathy, "Development of a substrate-integrated Ku-band cavity-backed microstrip patch sub-array of dual linear/circular polarization for DBS

applications," *IEEE Radio and Wireless Symposium (RWS), 2010,* vol., no., pp.92-95, 10-14 Jan. 2010.

[69] R.K. Shaw, K. Patel, B.R. Schaffer, J.MacGahan, and S.Dhanjal, "Waveguide feed network producing dual-linear and dual-circular polarizations for satellite applications," *IEEE International Symposium on Antennas and Propagation (APSURSI), 2011*, vol., no., pp.2165-2167, 3-8 July 2011.

[70] P.Sehyun, Y.Okajima, J .Hirokawa, and M.Ando, "A slotted post-wall waveguide array with interdigital structure for 45° linear and dual polarization," *IEEE Transactions on Antennas and Propagation*, vol.53, no.9, pp. 2865- 2871, Sept. 2005.

[71] D. Kim, J. W. Lee, T. K. Lee, and C. S. Cho, "Design of SIW cavity backed circular-polarized antennas using two different feeding transitions*," IEEE Trans. Antennas Propag*., vol. 59, no. 4, pp. 1398–1403,Apr. 2011.

[72] Y.J. Ren and K. Chang, "5.8 GHz circularly polarized dual-diode rectenna and rectenna array for microwave power transmission," *IEEE Trans. Microw. Theory Tech.*, vol. 54, no. 4, pp. 1495–1502, Apr. 2006.

[73] A. Massa, G. Oliveri, F. Viani, and P. Rocca, "Array Designs for Long-Distance Wireless Power Transmission: State-of-the-Art and Innovative Solutions," *Proceedings of the IEEE*, vol.101, no.6, pp. 1464-1481, June 2013.

[74] K.I. Pedersen, P.E. Mogensen, and B.H. Fleury, "Dual-polarized model of outdoor propagation environments for adaptive antennas," *49th IEEE vehicular technology conference*, vol.2, no., pp.990-995 vol.2, Jul 1999

[75] A.P. Garcia Ariza, R. Muller, F. Wollenschlager, A. Schulz, M. Elkhouly, Y. Sun, S. Glisic, U. Trautwein, R. Stephan, J.Muller, R.S. Thoma, and M.A. Hein, "60 GHz Ultrawideband polarimetric MIMO sensing for wireless multi-gigabit and radar", *IEEE Transactions on Antennas and Propagation*, pp. 1631-1641,vol. 61, no. 4, April 2013

[76] G.Virone, R. Tascone, O.A. Peverini, and R.Orta, "Optimum-Iris-Set concept for waveguide polarizers," *IEEE Microwave and Wireless Components Letters*, vol.17, no.3, pp.202-204, March 2007

[77] L. Juan, F. Guang, and Y. Lin, "Design of a dual-polarised wideband short backfire antenna with high gain," *IET Microwaves, Antennas & Propagation*, vol.7, no.9, pp.735-740, June 2013

[78] M. Esquius-Morote, M. Mattes, and J.Mosig, "Orthomode transducer and dual-polarized horn antenna in substrate integrated technology," , *IEEE Transactions on Antennas and Propagation*, vol.PP, no.99, pp.1-1

[79] D. Kim, M. Zhang, J. Hirokawa, M. Ando,"Design and fabrication of a dual-polarization waveguide slot array antenna with high isolation and high antenna efficiency for the 60 GHz band," *IEEE Transactions on Antennas and Propagation*, vol.62, no.6, pp.3019-3027, June 2014

[80] S. Park, Y. Okajima, J. Hirokawa, and M. Ando, "A slotted post-wall waveguide array with interdigital structure for 45° linear and dual polarization*," IEEE Transactions on Antennas and Propagation*, vol.53, no.9, pp.2865-2871, Sept. 2005

[81] B.Y. El Khatib, T. Djerafi, and K. Wu, "Substrate-integrated waveguide vertical interconnects for 3-D integrated circuits," *IEEE Transactions on Components, Packaging and Manufacturing Technology*, vol.2, no.9, pp.1526-1535, Sept. 2012

[82] He,F. F., Wu, K., Hong, W., *et al* : 'Low-Cost 60-GHz smart antenna receiver subsystem based on substrate integrated waveguide technology', *IEEE Trans. Microw. Theory Tech.,*2012, 60, (4), pp.1156-1165

[83] M. C. Kemp, "Millimetre wave and terahertz technology for detection of concealed threats-a review," *Proc. SPIE*, vol. 6402, pp. D01-D19, 2006

[84] H.H. Meinel, "Commercial Applications of Millimeter waves – History, Present Status and Future Trends", *IEEE Trans. Microw. Theory Tech.*, vol. 43, no. 7, pp. 1639–1653, Jul. 1995.

[85] P. F. Goldsmith, C.T. Hsieh, G. R. Huguenin, J. Kapitzky, and E. L. Moore, "Focal plane imaging systems for millimeter-wave lengths," *Trans. Microw. Theory Tech.*, vol. 41, no. 10, pp. 1664–1675, Oct. 1993.

[86] N. A. Salmon, "Scene simulation for passive and active millimetre and sub-millimetre wave imaging for security scanning and medical applications," *Proc. SPIE*, vol. 5619, pp. 129–135, 2004.

[87] P. S. Hall and S. J. Vetterlein, "Review of radio frequency beamforming techniques for scanned and multiple beam antennas," *Proc. Inst. Elect. Eng.*, pt. H, vol. 137, no. 5, pp. 293–303, Oct. 1990.

[88] M. Shahabadi, D. Busuioc, A. Borji, S. Safavi-Naeini, "Low-cost, high-efficiency quasi-planar array of waveguide-fed circularly polarized microstrip antennas," *IEEE Transactions on Antennas and Propagation,* , vol.53, no.6, pp. 2036- 2043, June 2005.

[89] A. Borji, D. Busuioc, S. Safavi-Naeini, “Efficient, Low-Cost Integrated Waveguide-Fed Planar Antenna Array for Ku-Band Applications," *IEEE Antennas and Wireless Propagation Letters*, vol.8, no., pp.336-339, 2009.

[90] W.M.A. Wahab, S. Safavi-Naeini, D. Busuioc," Wide-Bandwidth 60-GHz Aperture-Coupled Microstrip Patch Antennas (MPAs) Fed by Substrate Integrated Waveguide (SIW)," *IEEE Antennas and Wireless Propagation Letters*, vol.10, pp.1003-1005, 2011.

[91] W.F. Moulder, W. Khalil, J.L. Volakis, "60-GHz Two-Dimensionally Scanning Array Employing Wideband Planar Switched Beam Network," *IEEE Antennas and Wireless Propagation Letters*, , vol.9, no., pp.818-821, 2010.

[92] Y. J. Chen, W. Hong, K. Wu , "Millimeter-Wave Multibeam Antenna Based on Eight-Port Hybrid," *IEEE Microwave and Wireless Components Letters*, vol.19, no.4, pp.212-214, April 2009.

[93] O. Kramer, T. Djerafi, and K. Wu, “Very Small Footprint 60 GHz Stacked Yagi Antenna Array,” *IEEE Trans. Antennas Propag*., vol.59, no.9, pp.3204-3210, Sept. 2011.

[94] N.Ghassemi, K. Wu, S. Claude, X. Zhang, and J. Bornemann, “Low-cost and high-efficient W-band substrate integrated waveguide antenna array made of printed circuit board process” *IEEE Trans. Antennas Propagat*., vol. 60, No. 3, March. 2012.

[95] T. Djerafi and K. Wu, “Super-compact substrate integrated waveguide cruciform directional coupler,” *IEEE Microw. Wireless Compon. Lett.*,vol. 17, no. 11, pp. 757–759, Nov. 2007.

[96] T. Djerafi, N. J. G. Fonseca, and K. Wu, (2011),"Design and Implementation of a Planar 4×4 Butler Matrix in SIW Technology for Wide Band High Power Applications” *Progress In Electromagnetics Research B*, Vol. 35, pp.29-51, 2011.

[97] K. Murai, H. Ikeuchi, T. Kawai, M. Kishihara, I. Ohta, "Broadband design method of SIW directional couplers," *China-Japan Joint Microwave Conference Proceedings* (CJMW), 20-22 April 2011, pp: 1 – 4.

[98] T. Djerafi, and K. Wu., “Multilayered substrate integrated waveguide 4 × 4 butler matrix". *Int J RF and Microwave Comp Aid Eng*, 22: 336–344. 2012.

[99] T. Sarrazin, H.Vettikalladi, O. Lafond, M. Himdi, and N. Rolland, “60 GHz membrane antennas fed by substrate integrated waveguide," *2012 International Symposium on Antennas and Propagation (ISAP)*, pp.70-73, Oct. 29 2012-Nov. 2 2012.

[100] T. Y. Yang, W. Hong, and Y. Zhang, "Wideband millimeter-wave substrate integrated waveguide cavity-backed rectangular patch antenna," *IEEE Antennas Wireless Propag. Lett*., vol.13, pp. 205-208, 2014.

[101] D.-Y. Kim, and J.–W. Lee, T.K. Lee, C.-S. Cho, "Design of SIW cavity-backed circular-polarized antennas using two different feeding transitions," *IEEE Trans. Antennas Propag*., vol.59, no.4, pp.1398-1403, April 2011.

[102] A. Borji, D. Busuioc, S. Safavi-Naeini, "Efficient, low-cost integrated waveguide-fed planar antenna array for Ku-band applications," *IEEE Antennas Wireless Propag. Lett*., vol.8, pp.336-339, 2009.

[103] H. Sun; Y.-X. Guo, and Z. Wang, "60-GHz Circularly Polarized U-Slot Patch Antenna Array on LTCC," *IEEE Transactions on Antennas and Propagation,* vol.61, no.1, pp.430, 435, Jan. 2013.

[104] C. R. Liu, Y. X. Guo, X. Y. Bao and S. Q. Xiao "60-GHz LTCC integrated circularly polarized helical antenna array",*IEEE Trans.Antennas Propag.*, vol. 60, no. 3, pp.1329 -1335 2012.

[105] Q. H. Lai, C. Fumeaux, W. Hong, and R. Vahldieck, "60 GHz aperture-coupled dielectric resonator antennas fed by a half-mode substrate integrated waveguide," *IEEE Trans. Antennas Propag*., vol. 58, no. 6, pp. 1856–1864, Jun. 2010.

[106] A.B. Guntupalli, and K. Wu, " Substrate integrated waveguide antenna arrays for high performance Radar/Radio Systems at 60 GHz" *Proceedings of International symposium on antennas and propagation, ISAP 2013*, vol.01, pp.589-592, Oct. 23-25, 2013.

[107] A.B. Guntupalli, and K. Wu, "45^{o} linearly polarized high-gain antenna array for 60-GHz radio," *IEEE Antennas Wireless Propag*., vol.13, pp.384-387, 2014.

[108] Ali, A., Aubert, H., Fonseca, N., and Coccetti, F.: 'Wideband two-layer SIW coupler: design and experiment', *Electron. Lett*, 2009, 45, (13), pp. 687–689.

[109] Li, D. X., Zhang, Y.P.: 'Integration of array antennas in chip package for 60-GHz radios', *Proceedings of the IEEE*, 2012, 100, (7), pp.2364-2371

[110] B. Sheleg, "A matrix-fed circular array for continuous scanning," *Proceedings of the IEEE*, vol.56, no.11, pp. 2016- 2027, Nov. 1968.

[111] F. Watanabe, N. Goto, A. Nagayama and G. Yoshida, "A pattern synthesis of circular arrays by phase adjustment," IEEE Trans. Antennas Propagat., vol. AP-28, pp. 857-863, Nov. 1980.

[112] A. A. Oliner, “A new class of scannable millimeter wave antennas,” in Proc. 20th European Microwave Conf., Budapest, Hungary, Sept. 1990, pp. 95–104.

[113] A. Oliner, “Leaky-wave antennas,” in Antenna Engineering Handbook, 3rd ed, R. C. Johnson, Ed. New York: McGraw-Hill, 1993, ch. 11.

[114] L. Dongkyu, L. Sanghyo , C. Changyul, K. Youngwoo , "A Two-Dimensional Beam Scanning Antenna Array Using Composite Right/Left Handed Microstrip Leaky-Wave Antennas," *IEEE/MTT-S International Microwave Symposium,* 2007. , vol., no., pp.1883-1886..

[115] C.-C. Hu, C.F. Jou, J.-J. Wu, "Two-dimensional beam-scanning linear active leaky-wave antenna array using coupled VCOs," IEE Proceedings Microwaves, Antennas and Propagation, vol.147, no.1, pp.68-72, Feb 2000.

[116] K.Shinho, Y.Wang, "Two-Dimensional Planar Array for Digital Beamforming and Direction-of-Arrival Estimations," *IEEE Transactions on Vehicular Technology*, vol.58, no.7, pp.3137-3144, Sept. 2009.

[117] J. D. Fredrick, Y. Wang, and T. Itoh, “A smart antenna receiver array using a single RF channel and digital beamforming,” *IEEE Trans.Microw.Theory Tech*., vol. 50, no. 12, pp. 3052–3058, Dec. 2002.

[118] J. D. Fredrick, Y. Wang, and T. Itoh, “Smart antenna based on spatial multiplexing of local elements (SMILE) for mutual coupling reduction,”*IEEE Trans. Antennas Propag.*, vol. 52, no. 1, pp. 106–114,Jan. 2004.

[119] K. Wu, Y.J. Cheng, T. Djerafi, X.P. Chen, N. Fonseca, W. Hong, "Millimeter-wave integrated waveguide antenna arrays and beamforming networks for low-cost satellite and mobile systems," *Proceedings of the Fourth European Conference on Antennas and Propagation (EuCAP),* 2010, vol., no., pp.1-5.

[120] Y.J. Cheng, W. Hong, K. Wu, Y. Fan, "Millimeter-Wave Substrate Integrated Waveguide Long Slot Leaky-Wave Antennas and Two-Dimensional Multibeam Applications," *IEEE Transactions on Antennas and Propagation,* , vol.PP, no.99, pp.1-1.

[121] M. Ettorre,R. Sauleau, L. Le Coq, L. , "Multi-Beam Multi-Layer Leaky-Wave SIW Pillbox Antenna for Millimeter-Wave Applications," *IEEE Transactions on Antennas and propagation*, vol.59, no.4, pp.1093-1100, April 2011.

[122] M. Ettorre, R. Sauleau, L. Le Coq, and F. Bodereau, "Single-folded leaky-wave antennas for automotive radars," *IEEE Antennas Wirel. Propag. Lett.,* vol. 9, pp. 859-862, 2010.

[123] Y.J. Cheng; W. Hong; K. Wu, "A two-dimensional multibeam array antenna based on substrate integrated waveguide technology," *APMC 2008 Asia-Pacific Microwave Conference*, 2008, vol., no., pp.1-4, 16-20 Dec. 2008.

[124] M.S. Smith, "Phased array fundamentals," *IEE Tutorial Meeting on Phased Array Radar*, vol., no., pp.1/1-133, Sepetember 1989.

[125] L. Juhua , D.R. Jackson,, L. Yunliang , "Substrate Integrated Waveguide (SIW) Leaky-Wave Antenna With Transverse Slots," *IEEE Transactions on Antennas and Propagation*, , vol.60, no.1, pp.20-29, Jan. 2012.

[126] S. Paulotto, P. Baccarelli, F. Frezza, D.R. Jackson, "A Novel Technique for Open-Stopband Suppression in 1-D Periodic Printed Leaky-Wave Antennas," *IEEE Transactions on Antennas and Propagation,* , vol.57, no.7, pp.1894-1906, July 2009.

[127] S. Yamamoto , J. Hirokawa and M. Ando "A beam switching slot array with a 4-way Butler matrix installed in a single layer post-wall waveguide", Proc. IEEE AP-S Int. Symp., vol. 1, pp.138 2002.

[128] L. Lin, X. Chen, R. Khazaka, K. Wu, "A transition from substrate integrated waveguide (SIW) to rectangular waveguide," *Asia Pacific Microwave Conference, 2009*, *APMC 2009*., vol., no., pp.2605-2608, 7-10.

[129] N. Marcuvitz, *Waveguide Handbook*, 1986, *IEE ElectromagneticWave Series*, vol. 21, Peter Peregrinus, London.

[130] Y. Cheng, W. Hong; K. Wu; Z.Q. Kuai, , Y. Chen ; J.X. Chen, J.Y. Zhou, H.J. Tang, ,"Substrate Integrated Waveguide (SIW) Rotman Lens and Its Ka-Band Multibeam Array Antenna Applications," *IEEE Transactions on Antennas and Propagation*, , vol.56, no.8, pp.2504-2513, Aug. 2008.

[131] R. Clapp, "Extending the R-2R lens to 360°," *IEEE Transactions on Antennas and Propagation,* vol.32, no.7, pp. 661- 671, Jul 1984

[132] J.J. Lee, R.S.Chu, S.Livingston, and R.Koenig, "Ultra wide band cylindrical array and 360-degree beam scan system," *IEEE International Symposium, Antennas and Propagation Society,* 2002 , pp. 212- 215 vol.4, 2002.

[133] K.J. Keeping, D.S. Rogers, and J.C. Sureau, "A Scanning Switch Matrix for a Cylindrical Array," *IEEE MTT-S International Microwave Symposium Digest,* vol., no., pp.419-421, 15-19 June 1981.

[134] Wight, J.S.; Chudobiak, W.J.; Makios, V.; , "A Microstrip and Stripline Crossover Structure (Letters)," *Microwave Theory and Techniques, IEEE Transactions on* , vol.24, no.5, pp.270, May 1976.

[135] Tzyy-Sheng Horng; , "A rigorous study of microstrip crossovers and their possible improvements," *Microwave Theory and Techniques, IEEE Transactions on* , vol.42, no.9, pp.1802-1806, Sep 1994.

[136] Djerafi, T.; Ke Wu; , "60 GHz substrate integrated waveguide crossover structure," *Microwave Conference, 2009. EuMC 2009. European* , vol., no., pp.1014-1017, Sept. 29 2009-Oct. 1 2009.

[137] Yamamoto, S., J. Hirokawa, and M. Ando, "A beam switching slotarray with a 4-way Butler matrix installed in single layer post-wallwaveguide," *IEICE Transactions on Communications*, Vol. E86-B, No. 5, 1653-1659, May 2003.

[138] T. Djerafi, N. J. G. Fonseca, and K. Wu, "Design and implementation of a planar 4x4 butler matrix in SIW technology for wide band high power applications," *Progress In Electromagnetics Research B*, Vol. 35, 29-51, 2011.

[139] Ali, A.; Aubert, H.; Fonseca, N.; Coccetti, F.; , "Wideband two-layer SIW coupler: design and experiment," *Electronics Letters*, vol.45, no.13, pp.687 -689, June 18 ,2009.

[140] Labay, V.A.; Bornemann, J.; , "E-plane directional couplers in substrate-integrated waveguide technology," *Microwave Conference, 2008. APMC 2008. Asia-Pacific* , vol., no., pp.1-3, 16-20, Dec. 2008.

[141] F. F. He, K. Wu, W. Hong, L. Han, and X.P. Chen , "Low-Cost 60-GHz Smart Antenna Receiver Subsystem Based on Substrate Integrated Waveguide Technology," *IEEE Transactions on Microwave Theory and Techniques,*vol.60, no.4, pp.1156-1165, April 2012.

[142] P. Schuh, R. Rieger, A. Fleckenstein, M. Oppermann, B. Adelseck, H. Mussig, and H. Brugge, "T/R-module technologies today and possible evolutions," *RADAR. International Conference - Surveillance RADAR for a Safer World,*, vol., no., pp.1-5, 12-16 Oct. 2009.

APPENDIX I

SMALLEST FOOT PRINT PENCIL BEAM ANTENNA ARRAY

In this work, we proposed to further simplify the fabrication time, enhance 3-dB gain bandwidth and the technique is scalable to milli-meter wave frequency range. The DRA array is constructed by simply connecting edges of the individual DRA elements, where one single air hole is used.. The DRA functionality is experimentally verified on Rogers's 6002 substrate with 120 mil thicknesses to realize 16 × 16 array size and then similar concept is extended for larger array of size 32 × 32 DRA array at 60 GHz frequency range. In our work, DRA feed is supplied through a slot etched beneath the first patch antenna element. Although DRA shape is independent on the performance, rhombus shape is suitable to manufacture DRA for mass production. The combined array of using parasitic patches and DRA array is suitable to realize the compact, low profile and high gain antenna in multi-layer configuration.

I. Single antenna element performance

The choice of radiating element is extremely important to realize pencil beam antenna arrays at milli-meter wave frequency band. The element must maintain low-profile, compact foot print, high gain, broadband feeding network and low radiation loss transmission line to realize high performance antenna arrays of 32 x 32 size at 60 GHz frequency. In this work, dielectric resonator antenna is chosen to implement high gain antenna array, because of its broadband impedance and radiation behaviour.

A. Proposed architecture

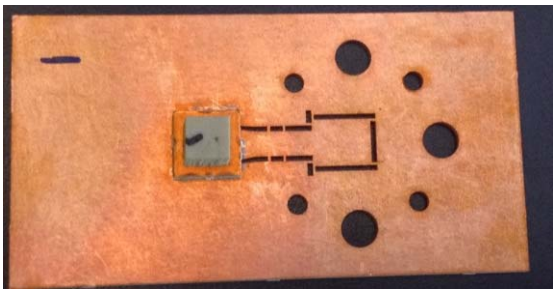

Fig. 1: Dielectric resonator antenna front and back side of the experimental prototype.

The dielectric resonator antenna (DRA) element is shown in the Fig. 1a, is without input WR15 to SIW transition. At the input side, WR15 to SIW transition is integrated for the measurement of single antenna element. As shown in the Fig. 1b, transition is integrated from the bottom ground plane of the SIW feeding transmission line. The antenna fabricated using multi-layer fabrication process is shown in the Fig. 1.

B. Input matching and radiation pattern

The far-field radiation pattern is measured in the MI technology anechoic chamber. The DRA radiation pattern in the standard cut planes is measured from 57 GHz to 66 GHz with 0.1 GHz frequency spacing and 1^{o} broadside angle interval from -90^{o} to $+90^{o}$ on the front side. The measured co-polarization and cross-polarization components are compared with simulated counterpart and both the results are well in agreement.

II. 2 x 2 sub array architecture

A. Feeding network architecture

At first, feeding network for 2 x 2 sub arrays is designed in a compact 3 layer configuration. The `SIW feeding network is shown in the Fig. 2. The field from layer 1to layer 3 is coupled through a slots etched on intermediate layers. The input excitation is on layer 1 and four output ports ae located on the top layer. When fed from port 1, all the four ports are in phase with unequal amplitude distribution.

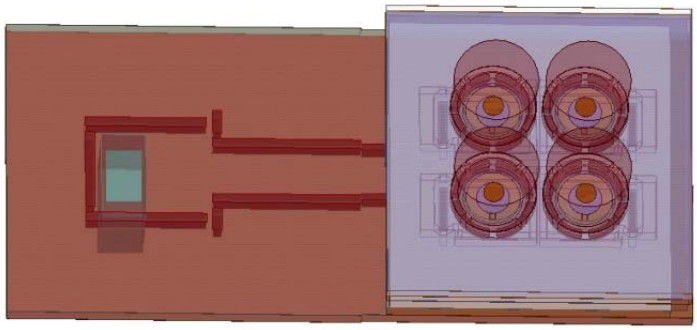

Fig.2: 2 x 2 antenna array top loaded with cylindrical dielectric substrate

III. 16 x 16 antenna array performance with uniform distribution

The dielectric resonator antenna (DRA) shown in the Fig. 8a, consists one dielectric cylindrical cube for each antenna. The peak gain and pattern bandwidth enhancement are achieved covering desired frequency band from 57 GHz to 66 GHz. However, extra fabrication processing time increases the manufacturing cost of the DRA. The accurate alignment of each dielectric cube poses limitation on mass production of the DRAs. The fabrication problem is solved with the DRA topology shown in the Fig. 8b. The rhombic shape of dielectric cube is loaded on each parasitic patch and the edges are connected to realize single dielectric cube. The DRA array is extended to implement large antenna aperture area . As an example, 16 x 16 array is designed and simulated to validate the proposed concept. The experimental prototype of DRA array is shown in Fig. 3.

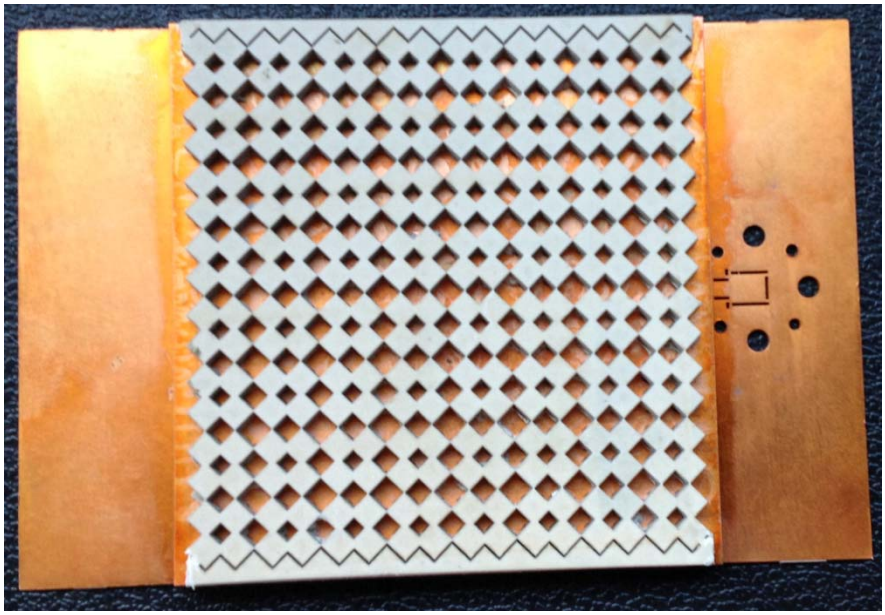

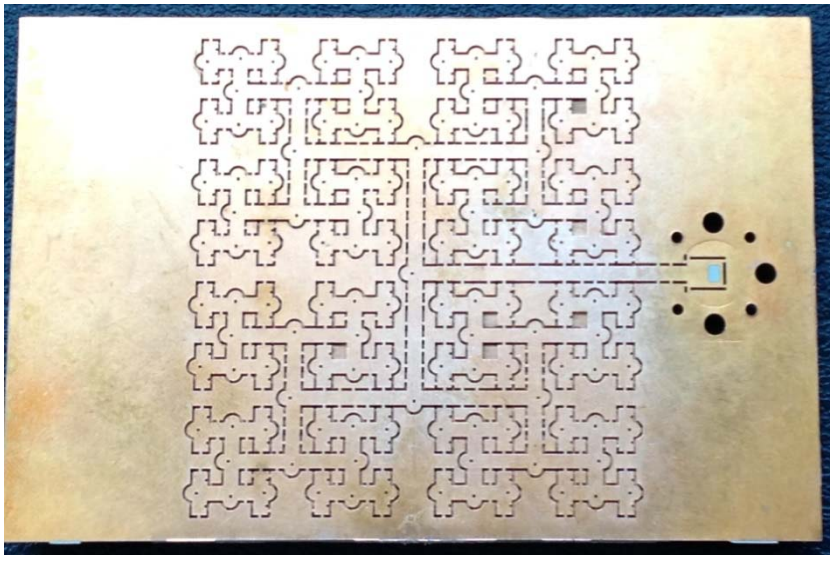

Fig. 3: Experimental prototype of 16 x 16 antenna array with uniform distribution

Fig. 4 compares simulated and measured radiation pattern in principal XZ-plane and YZ-plane. Antenna measured half power beam width is 4^{o} and 4.5^{o} in XZ-plane and YZ-plane respectively. The array is having equal beam-width in both planes. The array is fed with uniform distribution and hence the side lobes are -13 dB lower than main lobe. The array is combined with WR 15 waveguide to SIW transition to measure input impendence and radiation pattern.

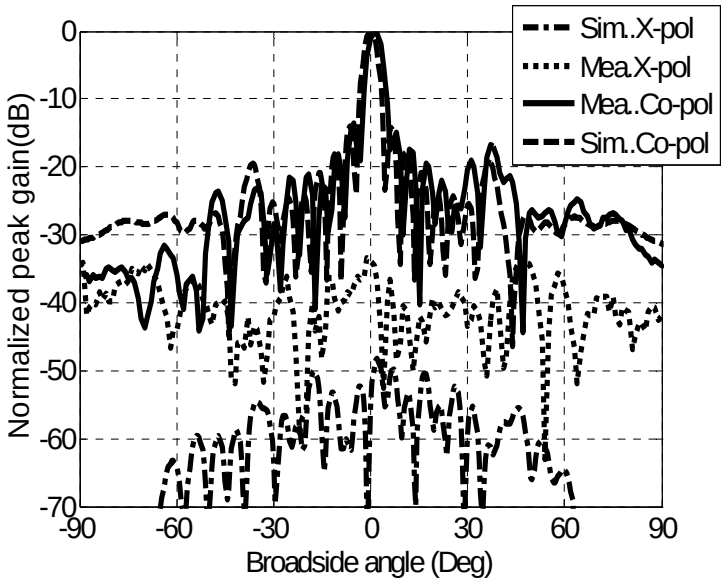

(a)

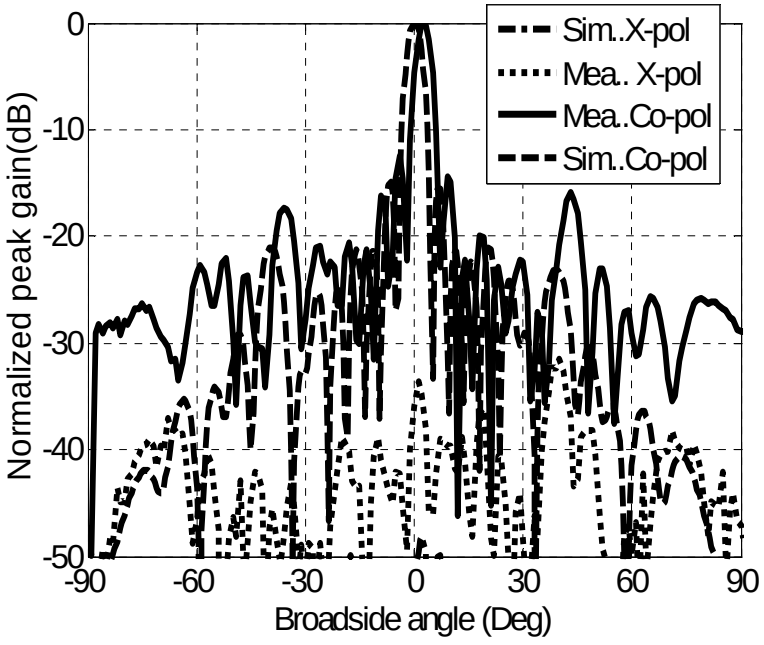

(b)

Fig. 4: 16 x 16 antenna array with uniform distribution measured radiation pattern in (a) gain_E_plane_58 GHz, (c) gain_H_plane_60 GHz, (d) gain_E_plane_60 GHz, (e) gain_H_plane_65 GHz, (f) gain_E_plane_65 GHz.

IV. 16 x 16 antenna array performance with non-uniform distribution

The feeding for uniform and non-uniform array is different in architecture and design. The uniform array feeding network has equal branch length and power is dividing equally at each intersection point. The non-uniform power division is achieved by offsetting the matching post at each intersection and the corresponding phase is compensated by using unequal length feeding network branches.

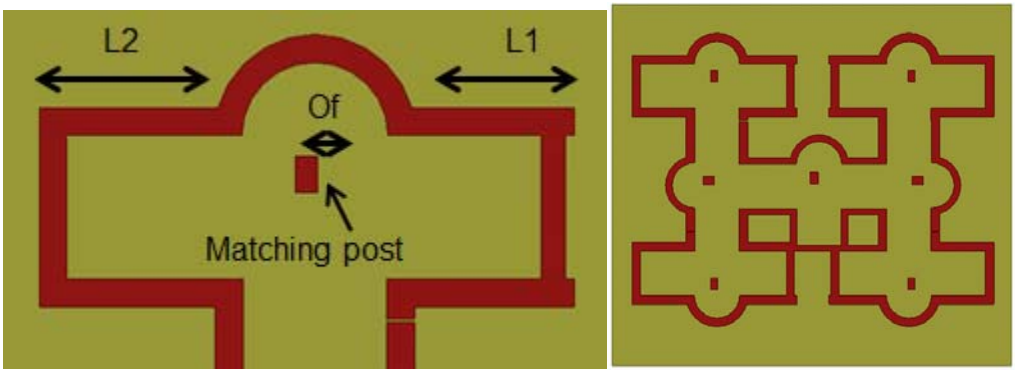

(a)

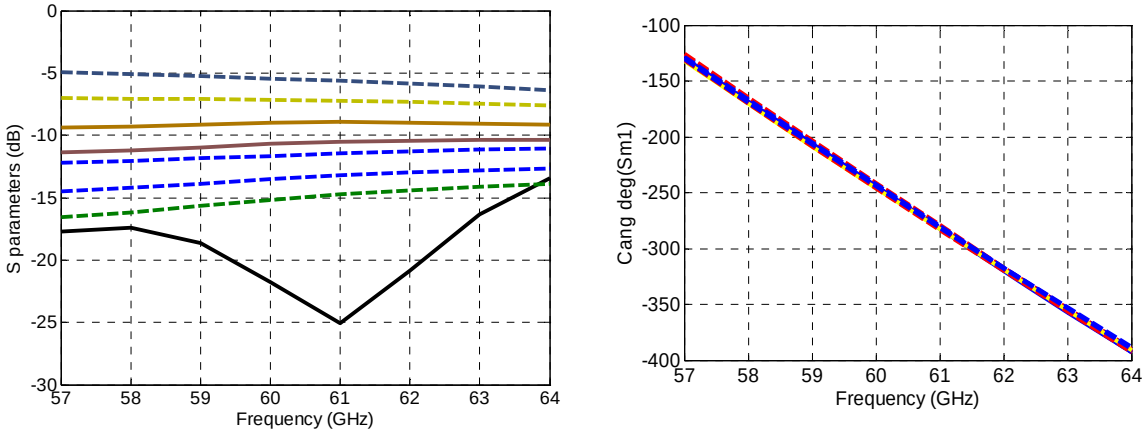

(c)

Fig.5: Non-uniform power divider architecture and scattering parameters as a function of frequency (a) One small branch, 1 x 9 power divider architecture (b) S21 to S91 when fed from port 1, phase of S21 to S91 when fed from port 1.

A. 16 × 16 antenna array performance with non-uniform distribution

The non-uniformly fed antenna of 16 × 16 array size is designed and simulated in HFSS. The ideal power dividing ratio calculated in MATLAB for achieving low SLL in an array. The radiation pattern shown in the Fig. 6, has side lobe levels lower than -20 dB in both the principal planes. The array is currently being optimized to further improve the radiation performance.

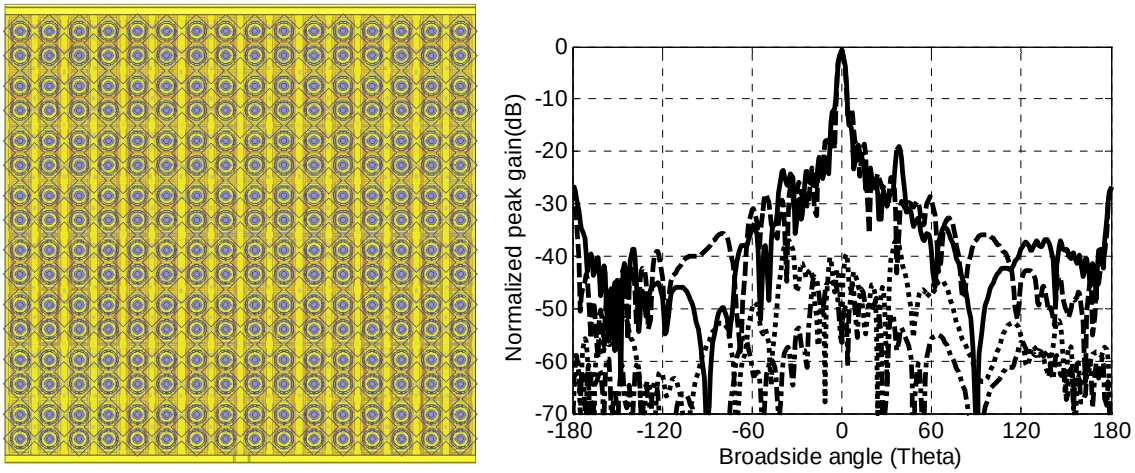

Fig. 6: 16 x 16 antenna array with non-uniform distribution

V. 32 x 32 antenna array performance with non-uniform distribution

The 32 × 32 array is constructed using four 16 x 16 sub arrays to reach the peak gain of 32 dBi at 60 GHz frequency. The corporate feeding network and array architecture is shown in the Fig. 8. The feeding network is designed in two layers. The final feeding network of the array is distributed into four layers. The complete feeding architecture is designed on RT 6002 substrate with 30 mil thickness for each layer. The final lay out of the array in layers S1 to S7 is shown in the Fig. 9 . The feeding network is designed to integrate in S1 to S4, the radiating patch array is integrated on layers S5 to S6, and the DRA is integrated on layer S7. The final array is occupying foot print of 135 mm x 135 mm x 7.5 mm. The simulated far-field radiation pattern of non-uniform fed 32 x 32 array is plotted in Fig. 10.

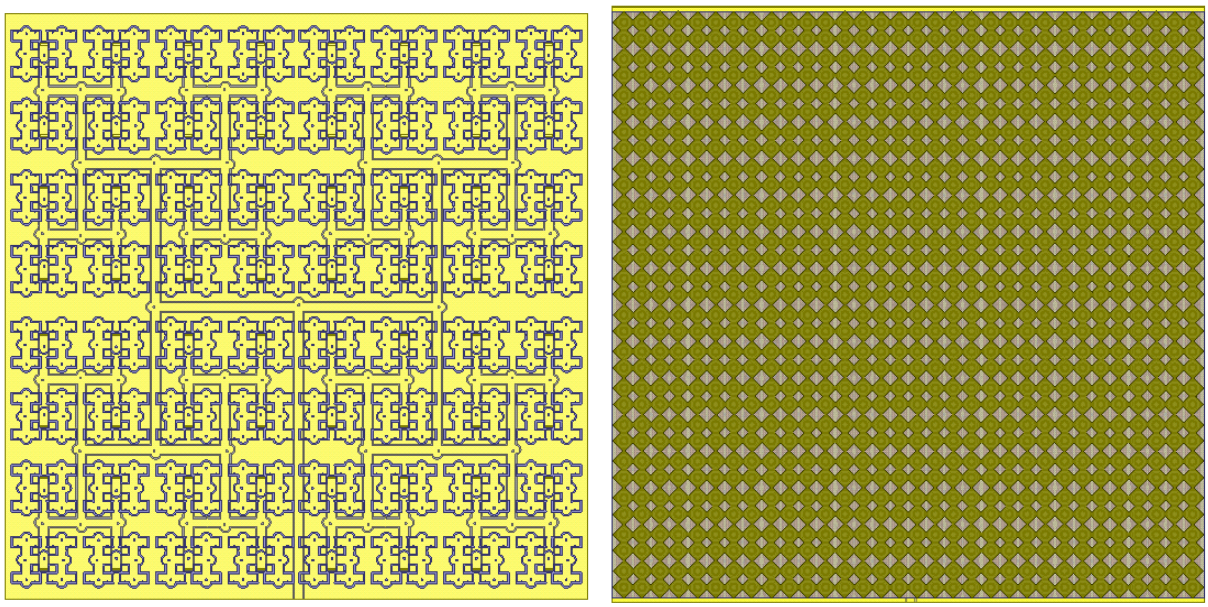

(a) (b)

Fig. 8: 32 x 32 antenna array (a) feeding network with non-uniform distribution, (b) radiating aperture.

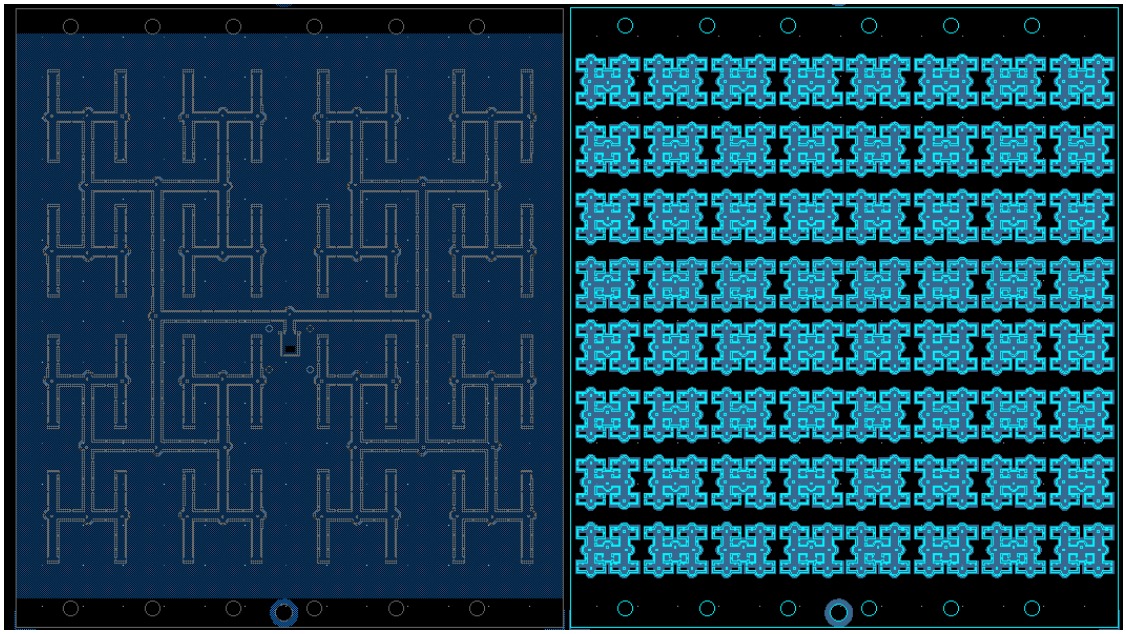

(a) (b)

Fig. 9: 32 x 32 antenna array in (a) S1, (b) S2, (c) S3, (d) S4, (e) S5, (f) S6,

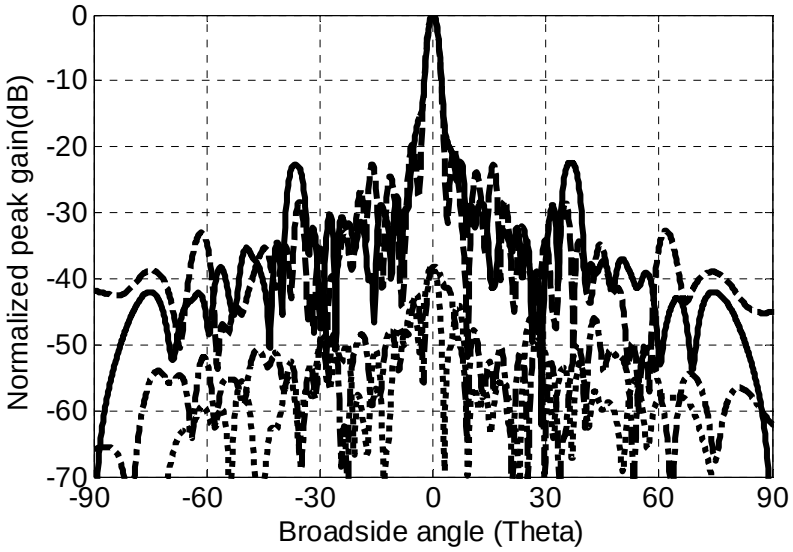

Fig. 10: 32 x 32 antenna array radiation pattern in standard cut planes.

VI. Conclusion

The singe DRA element is designed and experimentally characterized to verify the proposed concept. The DRA is used as a radiating element to implement 16 x 16 uniformly fed DRA array. The array impedance and radiation pattern are experimentally characterized at 60 GHz frequency range. The low SLL power divider is designed to reduce the side lobe levels of uniform-fed array. In the final stage, 32 x 32 array is designed and simulated to reach the peak gain around 32 dBi. The low SLL 32 x 32 array lay-out is sent for fabrication.